Quantum Barrier Devices for Sub-Millimetre Wave Detection

Viktor Doychinov

Submitted in accordance with
the requirements for the degree of
Doctor of Philosophy

The University of Leeds
School of Electronic and Electrical Engineering
August 2015

Declaration

The candidate confirms that the work submitted is his own, except where work which has formed part of jointly authored publications has been included.

The contribution of the candidate and the other authors to this work has been explicitly indicated below.

The candidate confirms that appropriate credit has been given within the thesis where reference has been made to the work of others.

The work in Chapter 3 of the thesis has appeared in publication as follows:

- V. Doychinov and D. Steenson, "Quantum barrier devices for efficient sub-harmonic sub-millimeter wave mixing," in *The 5th UK/Europe-China Workshop on Millimeter Waves and Terahertz Technologies*, Sept 2012, pp. 1-5.

- D. Steenson, V. Doychinov, L. Li, E. Linfield, and H. Patel, "W-band sub-harmonic mixers based on quantum barrier devices with low local oscillator power requirements," in *Millimeter Waves and THz Technology Workshop (UCMMT)*, 2013 6th UK, Europe, China, Sept 2013, pp. 1-2.

In both papers I was responsible for developing device models, circuit design and optimisation, setting up simulation models, processing the results, and producing a written description of these steps. Mr Patel fabricated the devices used, Prof Li and Prof Linfield kindly provided the semiconductor wafers used for device manufacture, and my supervisor Dr Steenson proposed the idea and initial design for the circuits presented, provided guidance, valuable discussions, and edited the final text of both papers.

The work in Chapter 4 of the thesis has appeared in publication as follows:

- V. Doychinov, D. Steenson, and H. Patel, "Resonant-tunneling diode based reflection amplifier," in *22nd European Workshop on Heterostructure Technology (HETECH)*, Sept 2013, pp. 1-2.

I was responsible for designing the amplifier circuits, running the simulations, processing the results, preparing the graphs, and writing a description of the design process. Mr Patel fabricated the devices used, and my supervisor Dr Steenson proposed the concept, provided guidance and valuable discussion of results, and edited the final text of the paper.

This copy has been supplied on the understanding that it is copyright material and that no quotation from the thesis may be published without proper acknowledgement

©2015 The University of Leeds and Viktor Doychinov

The right of Viktor Doychinov to be identified as Author of this work has been asserted by him in accordance with the Copyright, Designs and Patents Act 1988.

To my parents and grandparents,

for instilling in me the virtues of scholarly study.

Acknowledgements

First and foremost, I would like to sincerely thank my supervisor, Dr David Paul Steenson, for his guidance, help and support over the last four years. I would not have been able to make this journey without his patience, understanding, and encouragement.

Special thanks go to Dr Li Chen and Mr Geoff Butterworth for the invaluable cleanroom training and assistance with device and circuit fabrication. Furthermore, to Prof Lianhe Li and his team for growing the semiconductor layers used for the devices presented in this thesis, and to Mr Hamza Patel for making the devices themselves. I am grateful to Mr Richard Clarke for the help and discussions about microwave measurements and waveguide technology.

I would like to also thank Mrs Susan Hobson, Mrs Clair Atkinson, Ms Sian Owen, and Ms Louise Redmonds for their help with administrative matters. My gratitude goes to Mr John Sheard and the IT personnel at the School of Electronic and Electrical Engineering for their quick and friendly assistance with various hardware and software issues.

I am quite happy to have shared a fun, friendly, and creative office environment with Manoj Kumar, Reshma Mohandas, Mussa Elsaadi, Jay Keeley, Siddhant Chowdhury, Iman Kundu, Dong Rui, David Bacon, and last but not least, Susan Riley. Thank you for being the best office mates I could wish for.

On a more personal level, I am thankful to all my friends from the LUU Sci-Fi and Fantasy society for the unforgettable moments that enriched my student life here at the University of Leeds, and provided much needed respite every now and then.

Thank you to my lovely girlfriend Kate, for all her support and understanding during the final stages of my study.

Abstract

Resonant-Tunnelling Diodes (RTDs) are a specific class of Quantum Barrier Devices, which offer a lot of potential for customisation through careful engineering of their semiconductor layer structure. They exhibit characteristics that make them good candidates for use in both sub-harmonic mixers and signal amplifiers, that operate at millimetre and sub-millimetre frequencies.

In this thesis RTDs fabricated at the University of Leeds from three different layer structures are investigated. Initially, device measurements are presented along with a device model for use in circuit simulation software. Planar transmission media circuits were designed for sub-harmonic mixers and two types of amplifiers, all using these devices. Additional circuits, implemented in waveguide technology, were also studied in preparation for realising the RTD based amplifiers at sub-millimetre and terahertz frequencies.

The sub-harmonic mixer circuits were simulated at microwave, millimetre, and sub-millimetre frequencies. Best predicted conversion loss performance is on the order of 20 dB. It was found that amongst the devices used an optimum size exists, offering best trade-off between junction capacitance and current density.

The amplifier circuits are divided into two groups, reflection based amplifiers and active transmission line. Their purpose would be to complement the mixers towards eventually building a receiver with low power requirements and low overall conversion loss. The former were found to either exhibit high narrow-band gain, while the latter had low wide-band gain, with an additional, resonant peak at frequencies in the sub-millimetre wave region.

The project was primarily a parametric design study, rather than a build and test project. Therefore, the simulation results are used to determine what characteristics of the devices studied would make them suited for use in circuits at high frequencies; and to come up with recommendations for future optimum RTD layer design.

Table of Contents

List of Figures

List of Tables

List of Symbols and Abbreviations

Symbols

E_{kin}	Longitudinal kinetic energy
E_F	Energy difference between Fermi level and conduction band minimum
f_c	Cut-off frequency
$\hbar$	Reduced Planck constant, $\approx 4.136 \cdot 10^{-15} \frac{eV}{s}$
J_V	Current density
k	Boltzmann's constant, $1.37 \cdot 10^{-23} \frac{J}{K}$
λ_g	Guide wavelength
λ_0	Free-space wavelength
m^*	Effective mass
q	Electron charge, $\approx 1.602 \cdot 10^{-19} C$
T	Temperature in Kelvin

Abbreviations

ADS	Advanced Design System
BJT	Bipolar Junction Transistor
CL	Conversion Loss
CPW	Coplanar Waveguide
CPWG	Coplanar Waveguide with Ground plane
DC	Direct Current
DSB	Double Side Band
EBL	Electron-beam Lithography
ECM	Electronic Countermeasures
EDA	Electronic Design Automation
EM	Electromagnetic
EU	European Union
FEM	Finite Element Method
FET	Field Effect Transistor

FM	Frequency Modulation
FWHM	Full-Width Half-Maximum
HDTV	High Definition TV
HEMT	High Electron Mobility Transistor
IF	Intermediate Frequency
IEEE	Institute of Electrical and Electronics Engineers
ITU	International Telecommunications Union
I-V	Current-Voltage
LNA	Low-noise amplifier
LO	Local Oscillator
MBE	Molecular Beam Epitaxy
MESFET	Metal-Semiconductor FET
MIMO	Multiple-Input Multiple-Output
MOSFET	Metal-Oxide-Semiconductor FET
NDR	Negative Differential Resistance
NF	Noise Figure
PDR	Positive Differential Resistance
PVCR	Peak-to-Valley Current Ratio
PWL	Piece-Wise Linear
QBD	Quantum Barrier Device
QCL	Quantum Cascade Laser
RF	Radio Frequency
RTD	Resonant-Tunnelling Diode
SDD	Symbolically Defined Device
SEM	Scanning Electron Microscope
SFDR	Spurious-Free Dynamic Range
SHM	Sub-harmonic Mixer
SMU	Source Measurement Unit
SSB	Single Side Band
SSE	Sum of Squared Errors
TE	Transverse Electrical mode
TRL	Thru, Reflect, Line
VNA	Vector Network Analyser
VSWR	Voltage Standing Wave Ratio
WLAN	Wireless Local Area Network

Chapter 1

Introduction

The goal of this thesis is to present and discuss the results of a study into the possible applications of Quantum Barrier Devices (QBDs) for the purpose of millimetre and sub-millimetre electromagnetic (EM) wave detection. This was a complex and multi-faceted undertaking, requiring investigation of several major aspects. The work reported here focuses on frequency downconversion through the use of sub-harmonic mixers (SHMs), and later, on signal amplification.

Chapter 1 serves as both a starting point and a roadmap for this thesis. The Chapter begins with an explanation of the motivation for this study, complete with possible applications, and a list of issues that the work addresses. Following that, a brief overview of the rest of the Chapters in the thesis is given, with key topics covered by each Chapter mentioned.

The last part of this Chapter introduces the concept of frequency mixing, providing a brief summary of the theoretical foundation for the circuits used later in the thesis. Different types of mixers are discussed, along with their characteristics and most widely used figures of merit. Finally, an overview of the different semiconductor devices used in frequency mixers is presented, leading into Chapter 2.

1.1 Motivation

The main drive for the work carried out was to investigate the performance of a certain class of QBDs, called Resonant-Tunnelling Diodes (RTDs), and their suitability as a non-linear element in a sub-harmonic frequency mixer. A secondary research interest was the potential use of an RTD's Negative Differential Resistance (NDR) region in amplifier circuits.

The reason for the interest in these devices lies within the shape and controllability of their current-voltage characteristic (I-V), and the possibility to influence it through careful design of their semiconductor layer structure. The I-V characteristic of an RTD under direct current (DC) measurement conditions, in the case of symmetric semiconductor layer structure, is close to being perfectly anti-symmetric[1, 2, 3], as illustrated in Fig 1.1. As explained later in this Chapter, this is an important prerequisite for building efficient sub-harmonic mixers. Currently, such an I-V characteristic is achieved by using two Schottky diodes in an anti-parallel diode pair (APDP) configuration[4, 5], shown in Fig 1.2. However, this imposes strict requirements on the diodes, mainly that their individual I-Vs should be virtually identical. Furthermore, because the devices are connected in parallel, their respective junction capacitances are added together. The total capacitance of an APDP, combined with the series resistance of whichever diode is conducting at any given time, is the main factor that limits the maximum operating frequency of a mixer[6, 7].

In contrast, by using just a single RTD, the need for completely identical devices is eliminated in the case of a symmetrical semiconductor layer composition. Additionally, for devices of comparable size, the overall capacitance is halved, leading to a potential doubling of the maximum operating frequency[8]. Another interesting fact about the resonant-tunnelling diodes is that they can exhibit strong non-linearity at low voltage levels[9, 10]. As will be discussed later, this can result in a lower power consumption when RTDs are used as part of a mixer circuit, while maintaining good

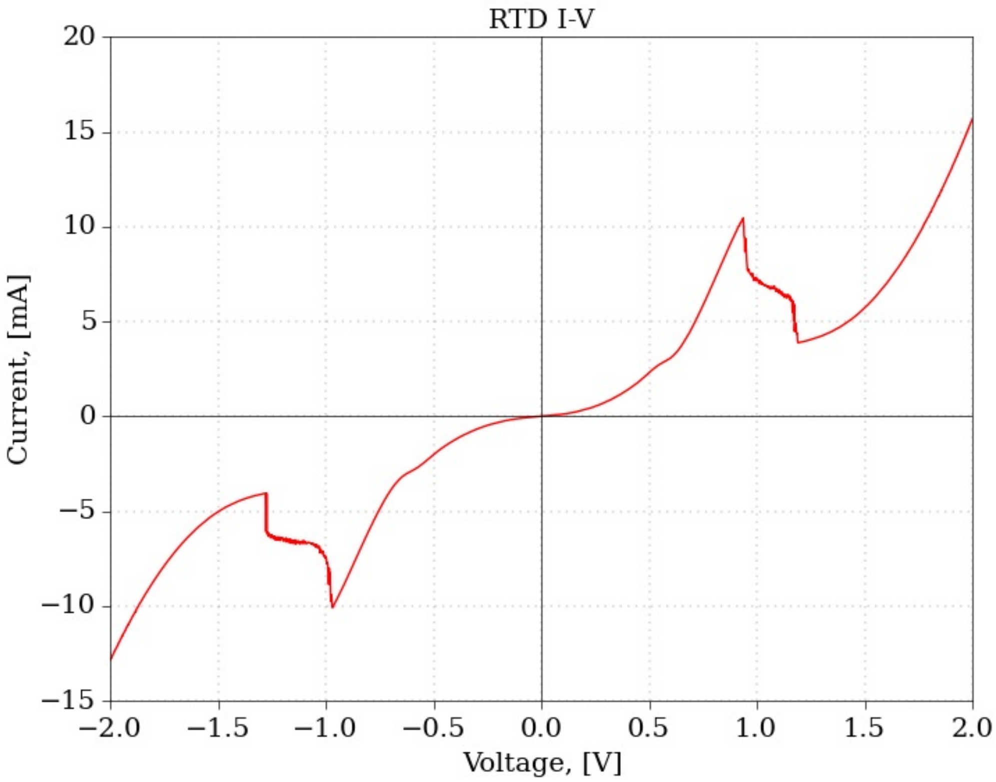

Figure 1.1: A current-voltage characteristic of an RTD with an area of $225 \mu m^2$, measured under DC conditions.

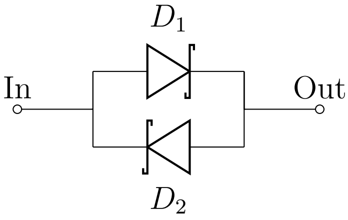

Figure 1.2: Anti-parallel diode pair (APDP), consisting of two Schottky diodes.

performance.

The final reason for the interest in RTDs is the possibility for developing small devices with high current density, which can be done via semiconductor layer engineering[11, 12, 13]. The multitude of physical parameters that can be tuned means that devices with I-V for specific needs can be designed and fabricated.

All these properties combine to make resonant-tunnelling diodes a potentially suitable candidate for a building block of a sub-harmonic mixer[14, 15, 16]. The option for devices with small capacitance, and yet high current density means that they can be particularly suited to operation at millimetre and sub-millimetre wave frequencies. The various applications for systems operating at these frequency ranges are discussed next.

1.1.1 Applications

There are three main organisations that are involved in the regulation of the electromagnetic spectrum, and allocation of frequency bands. These are the Institute of Electrical and Electronics Engineers (IEEE), International Telecommunication Union (ITU), and the European Union Electronic Countermeasure (EU ECM) designations. The frequency bands are split in a different, and not always overlapping way. This could sometimes lead to confusion as to what ranges are addressed when using the terms *millimetre wave*, *sub-millimetre wave*, and *terahertz*. The different band designations and corresponding frequency ranges are summarised in Table 1.1.

IEEE		ITU		EU ECM	
Name	Range [GHz]	Name	Range [GHz]	Name	Range [GHz]
Ka	27 – 40	*11*	30 – 300	*K*	20 – 40
V	40 – 75	*12*	300 – 3000	*L*	40 – 60
W	75 – 110			*M*	60 – 100
mm	110 – 300				

Table 1.1: A summary of the frequency bands defined by three governing organisations[17, 18, 19].

In this thesis, the ITU radio band designation is adopted, meaning that *millimetre wave* refers to the frequency range 30 – 300 GHz, and both *sub-millimetre wave* and *terahertz* refer to 300 – 3000 GHz. Furthermore, the IEEE's designation of *W-band* is used to refer to the frequency range 75 – 110 GHz. The relative position of these bands in the overall EM spectrum is shown in Fig. 1.3. The areas in which EM waves in the above-mentioned frequency ranges are used can be broadly categorised as security, medical, scientific research, and telecommunications. For each of these,

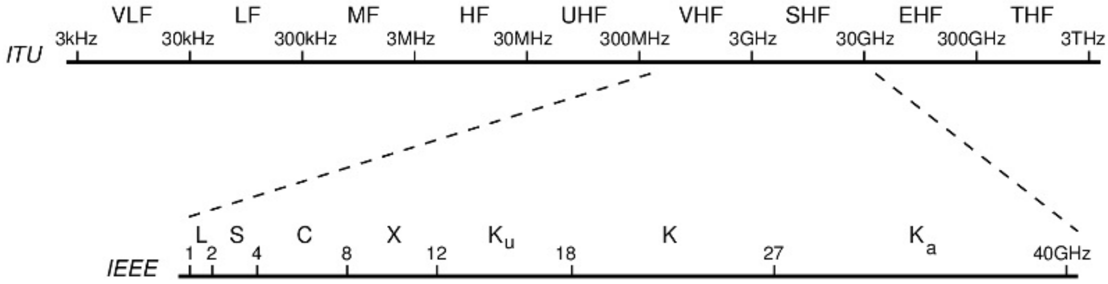

Figure 1.3: Spectrum of radio frequencies, with ITU and IEEE band designations.

detailed examples are given below.

Security

The main applications for millimetre wave and sub-millimetre wave signals in the area of physical security mainly revolve around imaging[20] in reflection mode. Airport safety agencies are some of the potential users of such technology[21]. For example, it has been demonstrated that different types of explosives have absorption lines in the terahertz frequency range[22]. Furthermore, because sub-millimetre wave radiation can penetrate clothing, but at the same time gets absorbed in the human body, these systems can be used to detect concealed firearms, bottles and liquid, and other metal and non-metal items[23]. Another reason to use terahertz frequencies for these tasks is that it is non-ionising radiation, and is therefore safer than the currently used X-ray backscatter equipment[24].

Medicine

Medical, biological, and biomedical uses of EM radiation in the millimetre and sub-millimetre range also focus on imaging[25]. Terahertz radiation can be used for tissue imaging, and can help in the identification and differentiation of tumour tissue[26]. These all rely on water absorption in said tissues. Being a non-ionising radiation is also helpful in this regard[27].

Scientific research

The usage of millimetre and sub-millimetre wave signals for scientific research has to do mainly with remote sensing of gases and water in both the Earth's atmosphere and other celestial bodies[28]. Many gas absorption lines fall into the frequency range between 30 GHz and 3 THz, and having the ability to correctly identify and quantify these gases is significant to fields such as climate modelling and meteorology[29]. Detection of ice crystals and water vapour can also be achieved via terahertz waves, and is of similar scientific importance. When such equipment is used as a scientific payload on board a spacecraft, it can help with identifying the composition of other celestial bodies' atmosphere[30, 31]. Finally, in the field of radio astronomy, signals received at millimetre and sub-millimetre wave frequencies can provide an insight into the formation of stars and the Universe[32].

Telecommunications

There are many bands available for communication use in the spectrum above 30 GHz, especially in W-band[33]. This available spectrum can provide usable bandwidth on the order of tens of Gbps. This can be used for HDTV data transmission and gigabit WLAN. It can also be used as an alternative to fibre optic cables in densely-built areas to provide short distance point-to-point links for traffic backhaul[34]. The main issue with these applications are the free space loss and water absorption loss, however there are ways of combating these. One such way would be to use Multiple-Input Multiple-Output (MIMO) technology both in receivers and transmitters[35]. Additionally, due to the high frequency of operation, even a small sized antenna can provide a lot of gain[36]. Finally, the millimetre wave range has also been explored as a potential candidate for 5G mobile communications[37].

1.1.2 Issues

As was mentioned in Section 1.1, the use of RTDs in sub-harmonic mixers, operating at millimetre and sub-millimetre wave frequencies, is meant to address a couple of issues which appear when these mixers are designed to work with Schottky diodes.

In no particular order, these are:

Device capacitance

The cutoff frequency of a diode-based mixer can be defined as $f_c = \frac{1}{2\pi R_s C_{j0}}$, where R_s is the diode's series resistance, and C_{j0} is the diode's junction capacitance at zero bias[38, 6]. In the case of an APDP, the Schottky diodes' individual capacitances add together, thereby increasing the overall C_{j0}.

The use of a single RTD, which has the same I-V shape as an APDP, could lead to the fabrication of mixers operating at higher frequencies, because of the reduced junction capacitance[39, 40].

Power requirement

Typically, the I-V characteristics of a Schottky diode exhibit a non-linear curvature, also known as a *knee*, around 0.7 V, while RTDs have a similar feature in their I-V characteristic at 0.5 V and below[41, 1, 42]. Usually, the voltage required to drive the quiescent point of a mixer circuit into this non-linear region is supplied by the Local Oscillator (LO) input of the mixer [6]. Given that mixers are dependent on that non-linearity to function properly, the existence of such a non-linearity at a lower voltage can directly translate to lower power requirements posed by circuits using resonant-tunnelling diodes. This would be particularly beneficial at millimetre-wave and sub-millimetre wave frequencies, where the available power is already low, and especially when receiver arrays are used, as whatever power is available would need to be distributed amongst many junctions[43]. A snapshot of the amount of power produced by different sources in 2012 is summarised in Fig. 1.4. Since then, significant breakthroughs have been reported, namely a Quantum Cascade Laser (QCL) operating at 3.4 THz with an output power of 1 W[45], as well as RTD based oscillators at up to 1.46 THz with 0.75 μW output power[46]. Additionally, RTD based oscillators have been reported in the W-band, with one example of -0.2 dBm at 75 GHz [47]

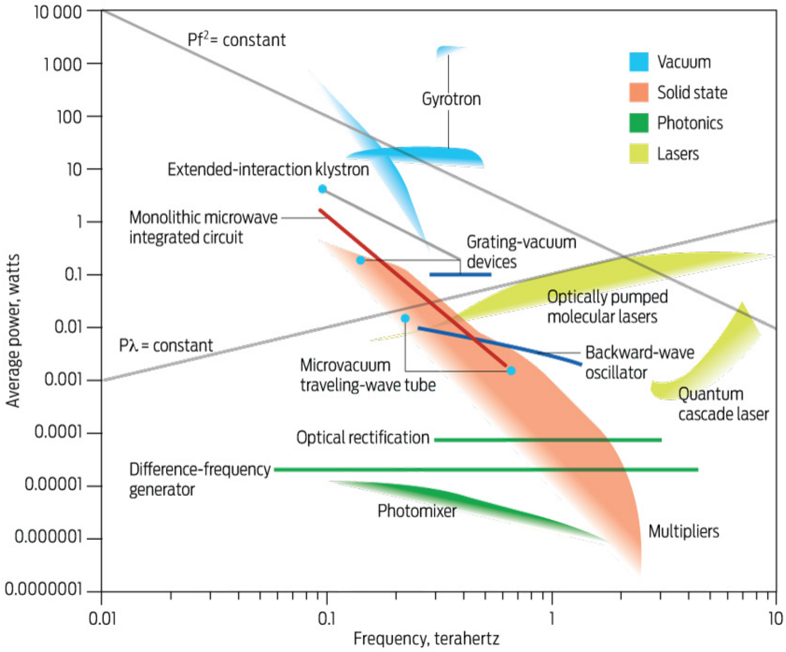

Figure 1.4: Power generated by different technologies at different frequency ranges[44].

However, in the region beyond 100 GHz and below a few THz the power available from solid-state sources rapidly decreases to the milliwatt, or even microwatt, range. Vacuum-based power sources exist that can provide more than a watt, however these are expensive, inefficient, and are short-lived. This is often referred to as the *terahertz gap*, and there is ongoing research to produce more powerful and efficient power sources[48].

Having described the motivation for the work behind this thesis, the next step is to present an overview and describe how the thesis is structured.

1.2 Thesis Overview

The remainder of Chapter 1 consists of a thorough introduction to the concept of frequency mixing, complete with mathematical background, different types of mixers, and ways of characterising and comparing them. Special attention is paid to the sub-harmonic mixer, which is of primary research interest due to its potential ability to operate at high frequencies with low power requirements. To round off the mixer introduction, the current state of their performance is reported. Finally, some more details on what devices are used in mixer circuits are given.

In Chapter 2 resonant-tunnelling diodes are reviewed in greater depth. The physical process behind the devices and the way they operate are explained. Following that, the influence of different parameters on their electrical characteristics is examined. The history and development of RTDs, as well as their use throughout the years is explored. Finally, the devices fabricated at the University of Leeds are presented. Both their measured I-Vs, and calculated capacitance characteristics are discussed.

Chapter 3 & Chapter 4 present the majority of the work conducted here at the University of Leeds. Chapter 3 explores in greater detail the use of RTDs in subharmonic mixers at various frequency ranges. It introduces the simulation model used for representing RTDs in EDA software. The overall mixer design procedure is explained in a step-by-step fashion. Circuits designed, as well as fabricated, here at Leeds are presented and discussed. Arguments for the different design choices are given. In a similar fashion, Chapter 4 deals with the application of RTDs in amplifiers. Design procedure and circuits tested are discussed for two separate amplifier topologies.

The results presented in these two Chapters cover the investigation into some of the many different parameters that are believed to affect either mixing or amplifying performance, such as device size, semiconductor layer composition, and the various properties of transmission line media that would eventually be used to physically implement the circuits. Since the overall aim of this study was to determine what combination of these parameters would result in RTDs optimally suited for SHMs and amplifiers, the results presented are simulation results obtained from the Agilent ADS and Ansoft HFSS software packages.

Chapter 5 focuses on exploratory work for sub-millimetre wave frequency range components. It presents designs developed for waveguide implementation of couplers at frequencies above W-band, in the form of waveguide split blocks. This work had two main motivations. On one hand, couplers and filters themselves can be used independently in receivers. On the other hand, these couplers can be used as part of the reflection-based RTD amplifiers, discussed in Chapter 4. Finally, this was done in order to explore the possible use of a newly acquired, at the University of Leeds, water jet guided laser, for the purposes of rapid manufacture. The long-term goal of this waveguide related work would be making SHMs in finline technology, which is standard practice at terahertz frequencies.

Chapter 6, the final chapter, presents a concise summary of the work reported in this thesis, along with conclusions from the simulations and measurements performed. Ideas and directions for future work, building on the results obtained, are also discussed.

1.3 Frequency Mixers

Frequency mixers, and more specifically, sub-harmonic frequency mixers, were the main focus of the work presented in this thesis. As such, a thorough introduction to their fundamentals is given in this section. Following a brief description, their principle of operation is laid out. The metrics and important properties by which mixers are characterised are explained afterwards. Next, the different types of mixers are listed, along with their specific traits. Finally, the current best reported performance of sub-harmonic mixers operating at millimetre and sub-millimetre frequencies is summarised.

1.3.1 Brief Description

A frequency mixer is defined as a three port device, with two inputs and one output. In an ideal mixer, the output is the product of the two input signals. The input ports are the radio frequency (RF) port, and the local oscillator (LO) port, while the output is known as the intermediate frequency (IF) port[6]. An illustration of an ideal mixer is given in Fig. 1.5. In case of harmonic input signals, the IF product consists of two signals, one with a frequency equal to the sum of the frequencies of the RF and LO signal, and one equal to the difference. Usually only one of these is the wanted one, and the other is filtered out. One of the advantages of subharmonic mixers is that they simplify this filtering, since the sum and the difference frequencies are much further apart than for a fundamental mixer. In the case of an *upconverter* the difference is discarded, while a *downconverter* filters out the sum. In principle, any non-linear device can be used as a mixer[7].

Figure 1.5: Ideal mixer

Mixers are used as an integral block in modern radio transmitters and receivers. In transmitters, they shift the low frequency, information carrying signal, to a higher frequency, used for transmission. On the other hand, in receivers, mixers reverse this process and bring the received radio signal down to lower frequencies, where it is easier to amplify and process it[49]. A block diagram of a simple radio receiver, showing the position of a mixer in the signal chain, is shown in Fig 1.6. A more detailed description of the frequency mixing process, along with the mathematical equations behind it, is presented in the next section.

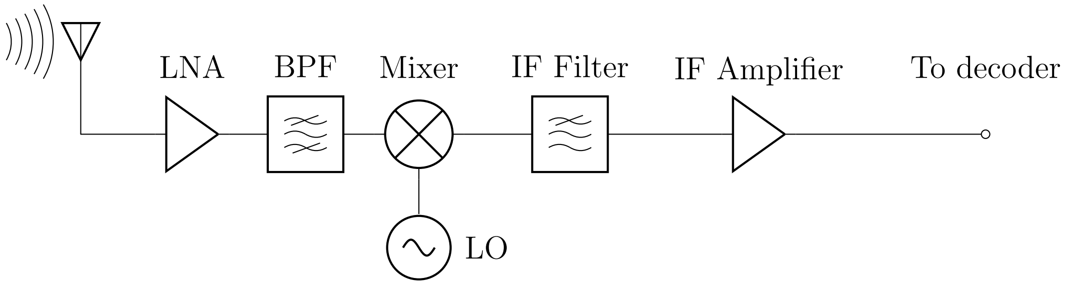

Figure 1.6: A simple radio receiver, illustrating the use of a mixer.

1.3.2 Mathematical Background

The signals applied to the two input ports of the frequency mixer can be written down in general form as

$$y_{LO}(t) = A_{LO}(t)\cos(\omega_{LO}t) \tag{1.1a}$$

$$y_{RF}(t) = A_{RF}(t)\cos(\omega_{RF}t) \tag{1.1b}$$

i.e. two harmonic signals, where $\omega_{LO} = 2\pi f_{LO}$ and $\omega_{RF} = 2\pi f_{RF}$. For example, in the case of FM radio transmission, f_{RF} can be between 88 MHz and 108 MHz[50], whereas f_{LO} will vary between 98.7 MHz and 118.7 MHz[51].

As was previously mentioned, an ideal mixer is a multiplier, and from trigonometry[52]:

$$\begin{aligned} y_{IF}(t) = y_{LO}(t) \cdot y_{RF}(t) = \\ = \frac{A_{LO}(t)A_{RF}(t)}{2}\left[\cos(\omega_{LO}+\omega_{RF})t + \cos(\omega_{LO}-\omega_{RF})t\right] \end{aligned} \tag{1.2}$$

This is the resulting output in the case of an ideal multiplier. Again, depending on whether the mixer is used as an upconverter or downconverter either the sum $\omega_{LO} + \omega_{RF}$ or the difference $\omega_{LO} - \omega_{RF}$ will be discarded via the use of a filter. However, in practice, the non-linear component would not be an ideal multiplier and would have an I-V characteristic that can be represented via an infinite power series[6]:

$$I(V) = \alpha_0 + \alpha_1 V + \alpha_2 V^2 + \alpha_3 V^3 + \ldots \tag{1.3}$$

Due to this, additional frequency products will be generated at the output, generally having the form $\pm n\omega_{LO} \pm m\omega_{RF}, n, m = 0, 1, 2, \ldots$. If the RF signal's power level is significantly lower than the LO one, usually by at least 20 dB, the output has the form $\pm n\omega_{LO} \pm \omega_{RF}, n = 0, 1, 2, \ldots$[6, 7]. The resulting spectrum is illustrated in Fig. 1.7. Another important product of the way frequency mixing works is the

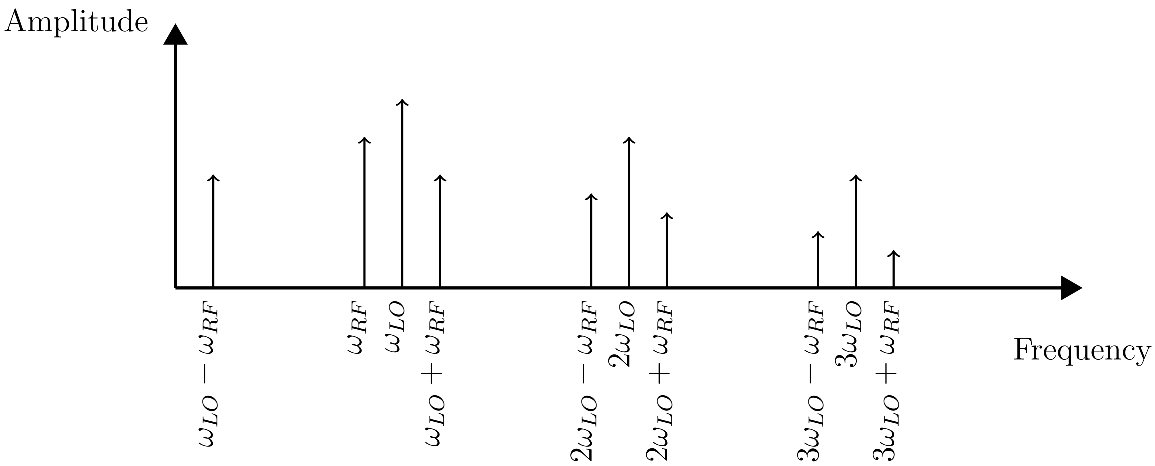

Figure 1.7: Output spectrum of a non-ideal mixer. RF signal is assumed to be significantly lower than LO.

presence of the *mirror image* frequency[38]. The mixer can produce an output at the desired frequency in response to two different RF inputs, one at $\omega_{LO} + \omega_{IF}$ and one at $\omega_{LO} - \omega_{IF}$. The undesired one is called the mirror image, and is filtered out.

Finally, it should be noted that the maximum power of the output IF signal would be nearly always at least 3 dB lower than that of the input signal. This comes as a direct result of Eqn. 1.2, which shows that the RF power is split between the $\omega_{LO} + \omega_{RF}$ and the $\omega_{LO} - \omega_{RF}$ frequency products.

1.3.3 Characteristics

There are several performance indicators that are used to characterise and compare frequency mixers. Some of them are used more commonly and more frequently than others. These performance metrics are as follows[6, 49, 52].

Conversion loss

Conversion loss (CL) is the most widely used performance indicator when characterising mixers. It is defined as the ratio of the input RF signal's power to that of the output IF signal's, measuring how much the frequency shifted signal has been attenuated or amplified:

$$CL = \frac{P_{in}(RF)}{P_{out}(IF)} \tag{1.4}$$

The conversion loss is usually given in dB, in which case the equation takes the form:

$$CL_{dB} = P_{in,dB}(RF) - P_{out,dB}(IF) \tag{1.5}$$

The conversion loss can be both positive, meaning that the input signal has been attenuated in the mixer; and negative, signifying that the mixer is also providing some amplification. Multiple factors can contribute to the conversion loss of a mixer, such as type of device, amplitude of LO and RF signals across said device, port impedance mismatch, insertion loss, etc.

LO power level

Another important characteristic of a mixer is the power level of the local oscillator. The other performance metrics, such as conversion loss, voltage standing wave ratio (VSWR), port isolation, are often dependent on LO power supplied and are usually specified for certain values of LO drive level[53, 54]. This level also often sets the quiescent impedance seen at the mixer ports, which is used when designing matching circuits. The power requirements of a mixer depend on what and how many devices are used as a non-linear element. For example, in diode based mixers, the LO signal is used to *drive* the diodes as close as possible to the non-linear part of their I-V, thereby ensuring optimum mixing with the RF signal would occur. The LO power level is measured and given in dBm.

Noise characteristics

The mixer, like any other component in a system, contributes noise to the output signal[55]. There are a few ways to quantify the noise of a mixer, via the use of the *noise temperature* and *noise factor* metrics. The noise factor F can be defined as $F = \frac{N_{in}+N_{addedd}}{N_{in}}$, and can be expressed in dB as a *noise figure* $NF = 10\log_{10} F$. The noise temperature gives the magnitude of the total noise generated by the mixer, while the noise factor shows the degree to which a mixer's noise contribution degrades the noise floor[56, 57].

There are different contributors to the overall noise of a mixer, such as flicker noise, white noise, shot noise, insertion loss, noise introduced by port terminations, noise from the LO source, phase noise, etc. Furthermore, noise at the different frequency components of the RF, LO, and IF signals is often different and can be attributed to different sources. There is also a distinction between Single Side Band (SSB) and Double Side Band (DSB) noise, depending on whether the noise present at the mirror image frequency is taken into account. Noise levels are also dependent on mixer operating conditions, such as ambient temperature and LO drive level.

When characterising a mixer's noise performance, it is usually modelled as a *black box* and there is only interest in its overall noise contribution. For design purposes, the noise arising from different processes in the non-linear semiconductor devices needs to be modelled and understood[58]. Later on, when discussing devices used in mixers, their noise properties will be also be presented.

There is an inherent relationship between CL and noise metrics, though a diode mixer may not exhibit a low CL and low noise temperature at the same time[6]. Noise temperature and noise factor tend to be used more in radio astronomy, where the RF signals are very low in power, and when giving an idea of a mixer's overall performance. For the rest of the thesis, as well as in Chapter 3, conversion loss will be used as the primary metric.

Port-to-port isolation

Isolation between ports in a mixer is the value, usually in dB, which shows how much a signal coming from one port is attenuated at the other ports. The most important of these are the LO to RF and LO to IF port isolation, due to the high relative power level of the LO signal. A potential LO signal leakage to the other ports can lead to problems with the RF and IF amplifiers, and transmission of the LO frequency by the antenna. Good isolation can be achieved in a few different ways, such as using transmission line stubs to create virtual grounds, using more than one non-linear device in a balanced configuration, and applying the LO and RF signals to different terminals of the device; or any combination of these.

Port VSWR

The impedances that are presented by the mixer on its three ports are different for different LO power levels and RF and LO frequencies. As such, there is a varying degree of impedance mismatch that is always present. This in turn leads to power being reflected by the mixer back to the signal sources, which could cause interference problems with previous stages in the receiver or transmitter chain. Impedance mismatch is usually characterised by either the VSWR, or by the reflection coefficient Γ. The relationships between them and the different impedances are defined through the following equations:

$$\Gamma = \frac{Z_{PORT} - Z_0}{Z_{PORT} + Z_0} \tag{1.6}$$

$$\text{Return Loss (RL)} = -20\log_{10}\Gamma \tag{1.7}$$

$$VSWR = \frac{1+\Gamma}{1-\Gamma} \tag{1.8}$$

Here $\Gamma \in [0, 1]$ and VSWR $\in [1, \infty)$. In order to mitigate this mismatch, impedance matching circuits may be employed. Quite often, owing to their inherent narrow bandwidth, these are designed for a particular LO power level and a specific LO and RF frequency. Using such circuits, target VSWRs of 3 or less are possible.

Linearity indicators

Being inherently non-linear circuits, mixers can cause distortion in their output signals, and there are a few ways to quantify this. The values for the *1 dB compression point, spurious-free dynamic range*, and *3rd order intercept point* are often used when characterising a mixer. A quick definition list of these indicators:

- 1 dB compression point: This metric measures the amplitude non-linearity of the mixer. It is defined as the input power level at which the output power has fallen 1 dB below the expected linear output, i.e. the CL has degraded by 1 dB. In the case of a mixer, the input is the RF signal.
- Spurious-free dynamic range (SFDR): Defined as the difference between the 1 dB compression point and the lowest input signal power level that produces a discernible output, both expressed in units of dBm. Higher dynamic range is always preferable, however a trade-off must be made against cost and complexity of the mixer.
- 3^{rd} order intercept point: This refers to undesired mixing products of the input RF signal with other signals at adjacent frequencies, i.e. signals such as $(2\omega_{RF1}\pm\omega_{RF2})\pm\omega_{LO}$. The 3^{rd} order intercept point is then defined as the RF input power at which the output power of these products is the same as the output power of the desired output signal. This metric is more important for upconversion mixers than it is for downconversion ones.

Mixers usually operate at room temperature, and all the performance metrics are quoted with that in mind. It is also possible to cryogenically cool the mixers using cryostats[59]. Doing so results in better performance, however this comes at the price of additional complexity and expensive components.

1.3.4 Mixer Types

There are many different types and categories of mixer circuits. They all provide different performance according to the previously discussed metrics, and have different advantages. On the other hand, they also have different downsides and trade-offs must be made. An important distinction, and the one used to classify mixers into two large categories, is that between active and passive mixers.

Passive mixers perform frequency conversion without manipulating the amplitude of the IF signal, save for introducing some unavoidable attenuation, expressed as the conversion loss of the mixer. Passive mixers are implemented using diodes, be they junction, Schottky, or other types. Quite often, the terms *passive mixers* and *diode mixers* are used interchangeably[6]. Passive mixers are usually cheaper and easier to make, and take up less space. Additionally, they seldom, require any external DC power source, since they usually have no need for biasing. This is not always the case, as Schottky diodes can be biased in the middle of the *knee* of their I-V characteristic, especially at sub-millimetre frequencies. Other advantages of passive mixers include their lower noise figure and high dynamic range. Passive mixers can also, because of their simple device geometries, operate at higher frequencies, up to a few THz. Downsides include the need for a separate IF amplifier, and the higher LO power requirements[49].

Active mixers, in contrast, intrinsically amplify the IF component, and as a result have conversion gain rather than conversion loss. They are most often made using bipolar junction transistors (BJTs) and field effect transistors (FETs), including high electron mobility transistors (HEMTs), which is why *transistor mixers* can be used to mean *active mixers.* Besides offering conversion gain, other advantages of active mixers are the better LO-to-IF port isolation, and overall reduced sensitivity to port terminations. These are balanced by the need for biasing circuits and therefore more space on a circuit board, DC power supply, and increased cost and complexity of circuits[7]. Last but not least, transistors operating at frequencies above W-band are not generally available. Transistor amplifiers operating at 1 THz have recently been reported, however the technology is extremely expensive and uncommon[60].

Another regularly used distinction is that of unbalanced (single device), single balanced, and double balanced mixers. Again, all of these offer different performance and have different niche uses.

An example of each of these types will be presented, along with a short discussion about their specifics. This presentation and argumentation generally follows [6], [7], [49], and [52]. Special attention will be paid to the sub-harmonic mixer, which will be described in a separate subsection.

Single diode mixer

The single diode mixers, like the one shown in Fig. 1.8, are the simplest possible diode mixer circuits. Here, both the LO and the RF signal are applied to one terminal of the diode, while the IF output is taken from the other terminal. Because the two input signals are added together before the non-linear element, this is also known as additive mixing. This type of mixer has generally poor performance, as a result of using a single diode. Furthermore, without the use of filters there is no way to isolate the RF and LO inputs.

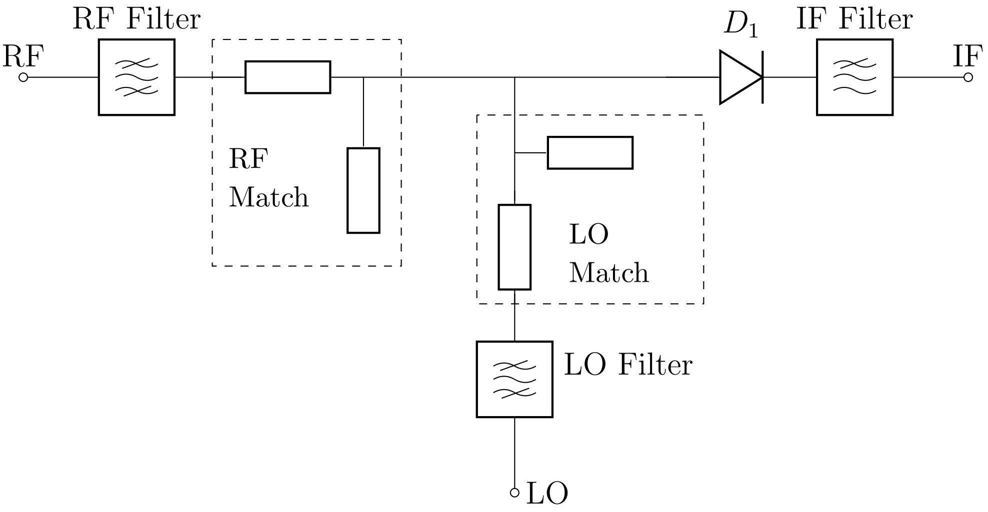

Figure 1.8: Single diode mixer, with filters and port impedance matching circuits.

Overall, single diode mixers have very narrow bandwidth and their CL and NF metrics vary greatly with the amount of LO power provided.

Single diode mixers do however find application at higher frequencies, towards the end of the millimetre wave range and over the sub-millimetre one, due to their simple design. They are also easy to make and have low overall cost.

Single balanced diode mixer

Single balanced diode mixers employ two diodes and either a balun or a hybrid coupler. Both the balun, which name is a shorthand for *balanced-unbalanced*, and the hybrid coupler, are used to convert a signal between being balanced and unbalanced. Balun circuits are more common when coaxial circuits are used, whereas hybrid couplers are implemented in planar transmission media. In this case, the balun or the hybrid coupler are used to convert the LO signal from potentially being unbalanced, into a balanced input, applied to the diode pair. The hybrid could be either a 90° or a 180° one, and is usually a branch line coupler, a Lange coupler, or a rat-race hybrid. As the RF increases into the W-band region and above, it becomes increasingly difficult to realise these hybrids and to ensure good power split and phase shifts. An example of a single balanced diode mixer using a 180° hybrid is shown in Fig. 1.9. The hybrid helps improve the port-to-port isolation between the LO and RF inputs. Additionally, filters might be used to further increase this isolation.

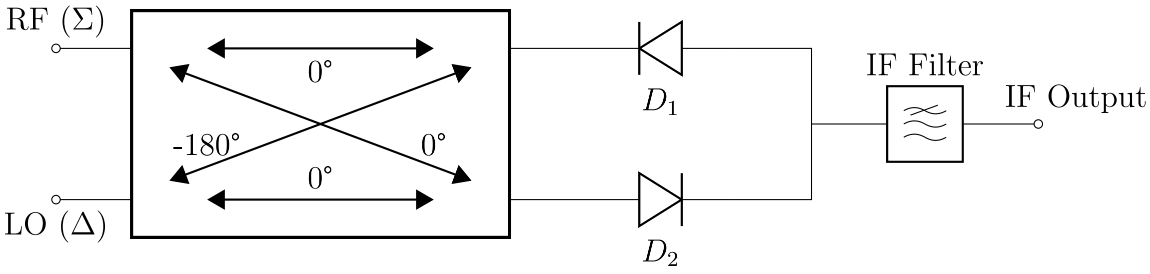

Figure 1.9: Single balanced mixer, using two junction diodes and a 180° hybrid.

In addition to better port isolation, a single balanced diode mixer has a greater dynamic range, due to the RF signal being split between the two diodes; wider operational bandwidth; LO noise rejection; and frequency products of the form $n\omega_{RF} + m\omega_{LO}$, where n and m are even, are suppressed.

These improvements come at the price of increased CL and higher LO requirements, as the two diodes need to be driven by the same source. Placement of the diodes, specifically their polarity, is important to ensure the IF signals produced by them do not cancel each other out. The increased complexity of the mixer is also reflected in its increased relative cost.

Finally, it should be mentioned that because the RF and LO signals are applied to different ports, this circuit performs multiplicative mixing.

Double balanced diode mixer

A double balanced mixer in a diode ring configuration is shown in Fig. 1.10. This type of mixer is most commonly used in the microwave region, and requires four diodes and two hybrids or baluns. In comparison to the single balanced mixer, the double balanced one has an even wider bandwidth, better LO to RF port isolation, and higher 3rd order intercept point. A double balanced mixer also suppresses frequency components of the form $n\omega_{RF} + m\omega_{LO}$, with even n and m.

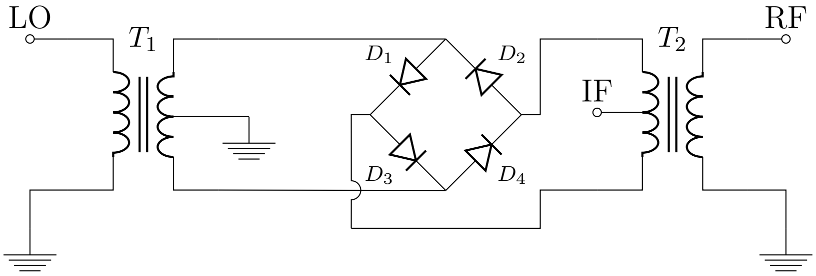

Figure 1.10: Double balanced mixer in a ring configuration, using junction diodes and a transformer balun.

Double balanced mixers however require even higher levels of LO power, and exhibit even greater CLs. Additionally, the hybrids/baluns need to be as close to perfectly symmetrical as possible; as should be the four diodes used.

Single transistor mixer

Similarly to diode mixers, the simplest active mixer is the one consisting of just a single transistor with accompanying circuits. Fig. 1.11 shows two examples of such a mixer, using different types of transistor. A common element for all transistor mixers is the need for biasing circuits, usually a base/gate one and a drain/collector one. The single ended transistor mixer can be viewed as a combination of a pre-amplifier and a single diode mixer, offering relatively good noise and CL performance. However, because both the RF and LO signals are applied together to the gate/base of the transistor, there is no inherent isolation between them. The use of filters is therefore necessary in order to provide some separation.

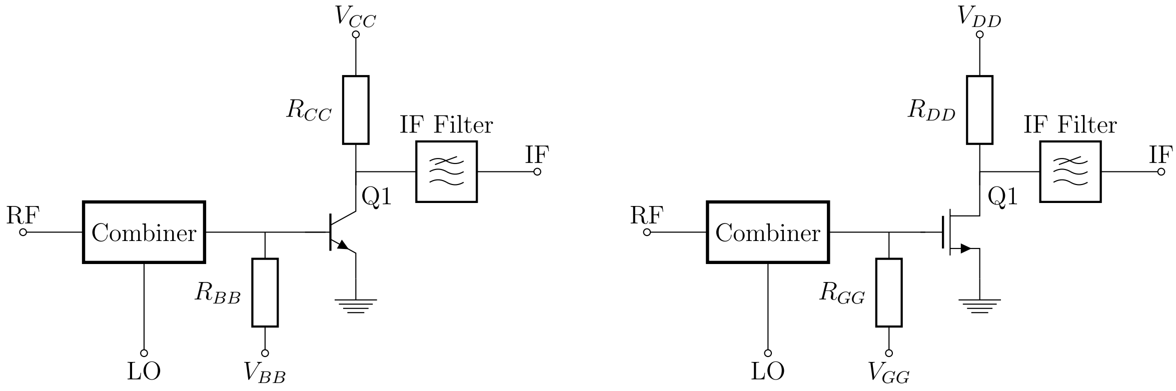

(a) NPN BJT.

(b) N-channel MOSFET.

Figure 1.11: Single ended active mixer, using different transistors as non-linear element.

A variant of the single transistor mixer, providing some RF to LO port isolation, is shown in Fig. 1.12. Here, the LO signal is applied to the source terminal of a FET, achieving some separation between the two signals. Even though this variant requires a larger LO drive signal, it has comparable performance to the one in Fig. 1.11.

Another variant with an even better RF to LO port isolation is the one using a dual-gate FET, shown in Fig. 1.13. Here, the dual-gate device is shown as two single gate FETs, connected in series. Applying the RF and LO signals to

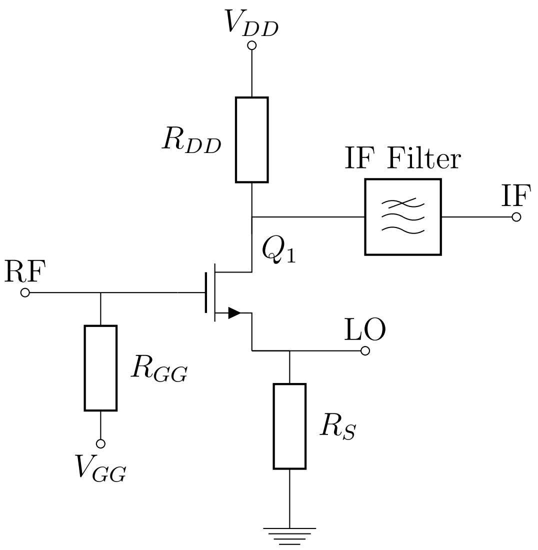

Figure 1.12: Single ended active mixer with LO injection at source terminal, providing better RF-to-LO isolation.

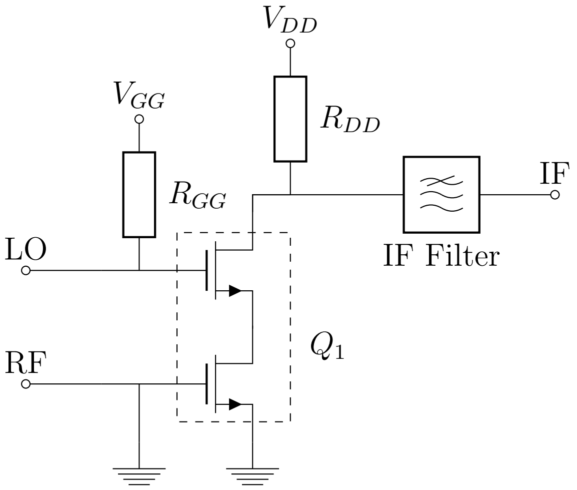

Figure 1.13: Dual-gate FET mixer, LO and RF signals applied at different gates. Good RF-to-LO isolation.

the two different gates is what provides the port-to-port isolation. This type of mixer also requires less LO power, and imposes fewer constraints on LO and RF filtering. It is, however, less stable than other single transistor mixers, and care must be taken when designing it.

The final single transistor variant discussed in this thesis is the resistive FET mixer, shown in Fig. 1.14. The resistive mixer can also be realised as a balanced mixer. The most distinguishing feature of a resistive mixer is the

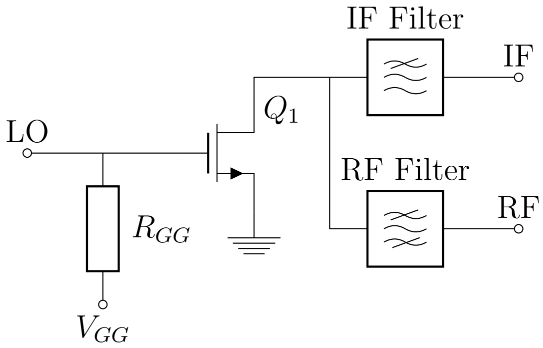

Figure 1.14: Resistive MOSFET mixer. Both RF and IF signals present at drain terminal. No drain bias necessary.

lack of drain bias. Instead, the RF signal is applied at the drain of the FET device, and filtering is used to separate and extract the IF output. As a result, the resistive mixer is a low-noise, low-distortion mixer with a low LO power requirement. Its CL performance is similar to that of single diode mixers.

Single balanced transistor mixer

The single balanced transistor mixer is similar to the single balanced diode mixer in that it uses two devices along with either hybrids or baluns. An example circuit is presented in Fig. 1.15, using single gate FETs, though in practice dual-gate devices can also be used. In a similar fashion to single balanced diode mixers, these mixer have better RF to LO isolation, and improved linearity and noise performance. Their CL performance is the same as that of single transistor active mixers. However, unlike their diode counterpart, single balanced transistor mixers require a hybrid or a balun to combine the IF outputs of the two individual transistors.

Gilbert cell mixer

The Gilbert cell mixer, an example of which is shown in Fig. 1.16, is the most advanced active mixer circuit type. Even though the circuit in Fig. 1.16 uses FETs, the Gilbert cell can also be realised with BJTs. The Gilbert cell mixer offers excellent port isolation and reduction of spurious frequency products. It also needs very low LO power, and it is often used at low frequencies and can

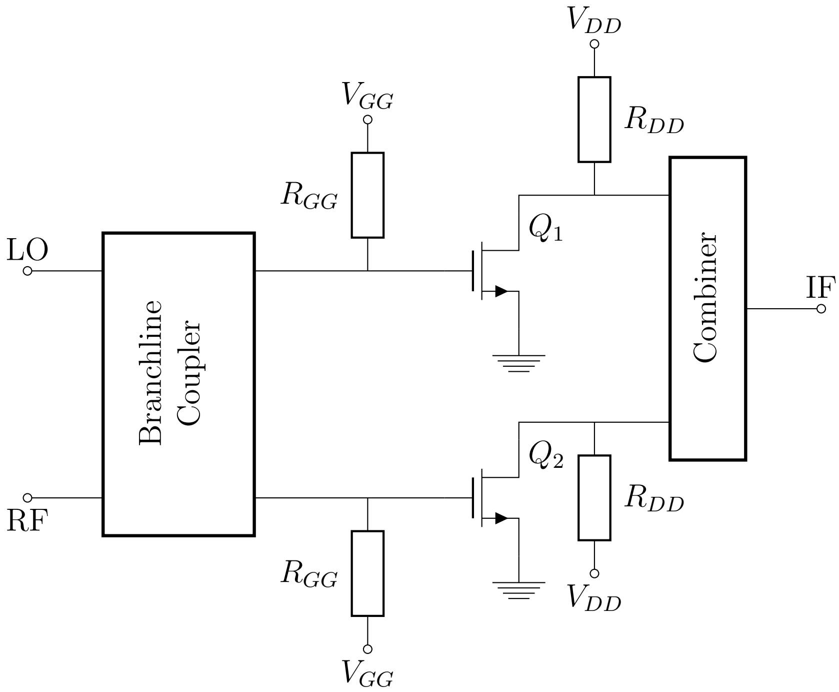

Figure 1.15: Single balanced active mixer, using FET devices. Resistive variants also possible.

easily be integrated in a monolithic fabrication process. The differential input and output ports also provide good linearity. Its only downside is the poor noise performance.

These are the standard mixer circuits, used both in everyday radio receivers and in specialised equipment. Each of these can be used as a part of an image reject mixer, like the one in Fig. 1.17. As the name suggests, this type of mixer can suppress the mirror image frequency component. Using phase shifts provided by the 90° hybrids, the image reject mixer separates the signals with frequencies $\omega_{LO}+\omega_{IF}$ and $\omega_{LO}-\omega_{IF}$ and outputs them to different ports. This is incredibly useful in cases where due to low IF the narrowband image product filters are difficult to realise.

1.3.5 Sub-Harmonic Mixers

As was previously mentioned, sub-harmonic mixer design constitutes the bulk of the work reported in this thesis. Therefore, a more detailed description of them is

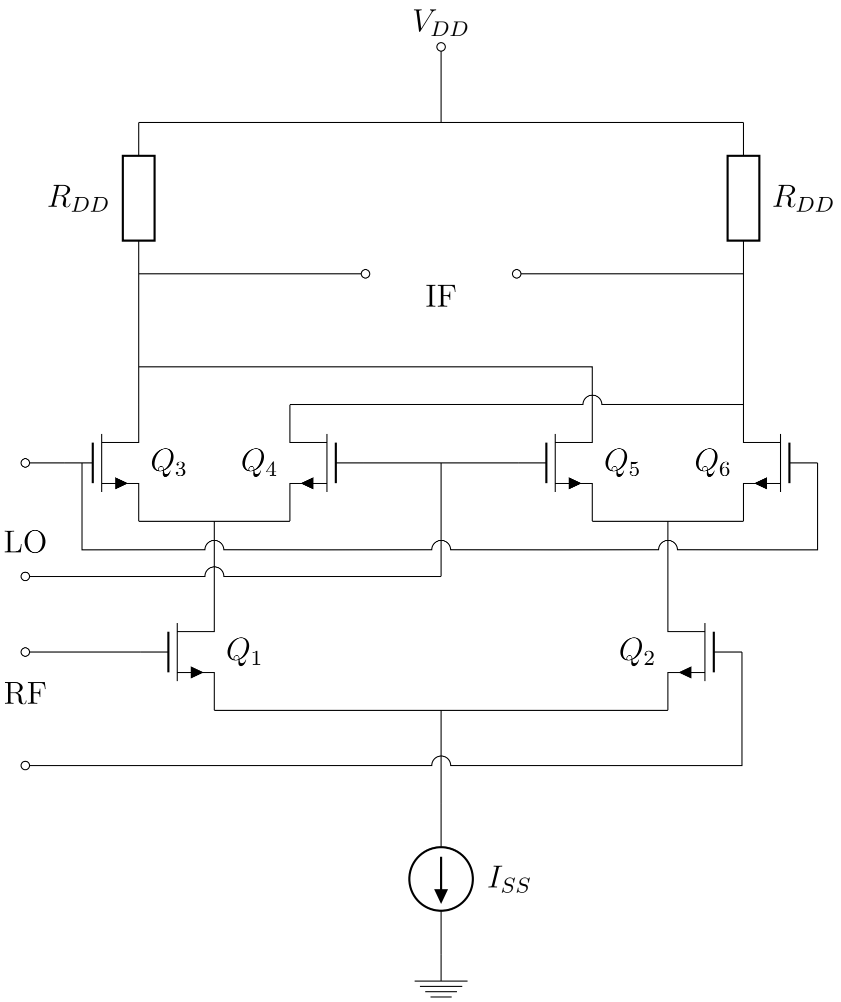

Figure 1.16: Gilbert cell mixer, using FETs. Differential IF output, possible to implement with BJTs instead.

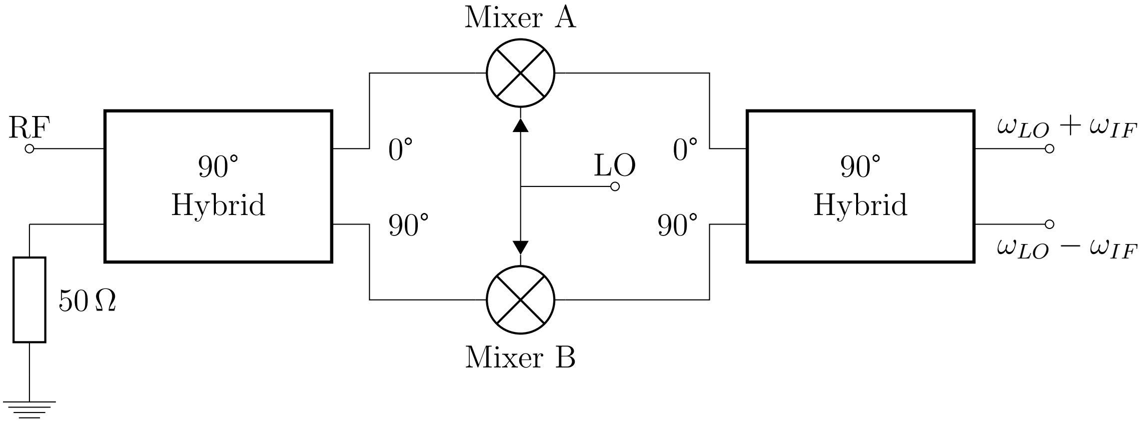

Figure 1.17: Image reject mixer, separating the real and the image signals. Mixers A and B can be of any type.

presented here.

Sub-harmonic mixers differ from regular harmonic mixers in that they most commonly use the 2nd harmonic of the LO signal, having an IF output of the form $2\omega_{LO} \pm \omega_{RF}$[5]. Some sub-harmonic mixers use the 4th harmonic instead[61, 62]. These types of mixer circuits are primarily used in the millimetre and sub-millimetre frequency ranges, where the LO power available is simply not enough to efficiently drive a fundamental mixer[40, 63]. Their CL performance is often worse than that of a fundamental mixer by a few dB, though this may be acceptable. Some advantages of using SHMs are the simplified filter design for the different ports, as well as the inherent high LO to RF port isolation[6].

While it is possible to use a single diode to perform sub-harmonic mixing, it is not advisable to do so as the mixing with the fundamental harmonic of the LO is a big source of performance loss. In practice, SHMs are often realised with an anti-parallel diode pair of Schottky diodes[4]. Such a pair has a composite anti-symmetric I-V characteristic, and it can be demonstrated that the total current of the pair contains only products of the form $m\omega_{LO} \pm n\omega_{RF}$, where $m + n$ is an odd integer. The fundamental and the odd harmonic mixing products are suppressed by the pair. In order to obtain good suppression, the two diodes need to be as identical as possible, and any difference in their parameters, including their parasitics, leads to performance degradation[5, 64, 65]. This is one of the reasons to investigate the resonant-tunnelling diode as a substitute, as it is a single device with an anti-symmetric I-V[66, 67, 39].

A typical SHM circuit, using an APDP is presented in Fig. 1.18[68]. While it omits components such as filters and matching circuits, it is still a functioning example of what SHMs look like, and forms the basis for the designs presented later in Chapter 3. The transmission line stubs are essential to the proper operation of a SHM. They function as virtual grounds and help provide port-to-port isolation. The $\frac{\lambda_{LO}}{4}$ stub terminates the diode pair with a short circuit at the LO frequency,

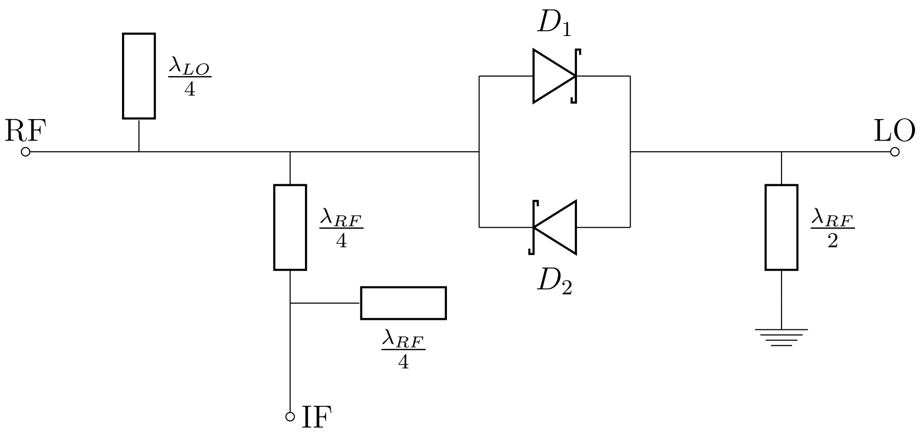

Figure 1.18: Sub-harmonic mixer, consisting of a Schottky anti-parallel diode pair and terminating transmission line stubs.

while leaving the RF input signal unaffected. In a similar fashion, the $\frac{\lambda_{RF}}{2}$ short circuits the RF signal to ground, without affecting the LO. The couple of $\frac{\lambda_{RF}}{4}$ stubs prevent leakage of the RF signal to the IF port, by presenting a virtual ground to the RF signal[6, 69].

1.3.6 Overview of Sub-Harmonic Mixers

Schottky-based sub-harmonic mixers operating at millimetre wave frequencies have been around for many years, and a lot of research and development has gone into optimising the diodes and the circuits for best performance and minimal conversion loss. Mixers operating at close to 1 THz have been reported, and performance in other frequency ranges is constantly being improved. A quick baseline summary of some of these reports is given in Table 1.2. It should be noted that these have been reported throughout the years, and are for different Schottky geometries, diode sizes, and surrounding circuits. They are given here to give a fuller perspective of what typical sub-harmonic mixer performance is across the spectrum, and to setup a benchmark against which the circuits based on RTDs will be compared.

These reported results can be further aggregated by frequency range, as shown in Table 1.3: As research into Schottky diodes and SHMs continues over the years, their performance improves, and it is reasonable to expect circuits in the near future

Frequency [GHz]	Conversion loss [dB]	Required LO [dBm]	Reported in
23	9.4	13	[70]
37	12	13	[70]
60	11.3	3 [$n = 4$]	[71]
60	8.3	5.5	[72]
90	10	11	[64]
94	10	8.5	[63]
183	6.85	7	[73]
183	4.9	7	[74]
215	10.9	7	[75]
330	6.3	4.7	[76]
330	10	2	[77]
361	15	6	[78]
366	6.9	8.5	[74]
380	8	2	[79]
420	8	7	[80]
520	7.7	15	[81]
540	12	15	[81]
590	14	9.5 [Biased]	[82]
600	15	13 [$n = 4$]	[83]
614	12	10	[84]
640	9	6	[85]
650	10	7	[86]
664	8	6	[87]
874	12	7 [Biased]	[88]

Table 1.2: A summary of the reported performance of Schottky-based SHMs for different frequency ranges.

Frequency range [GHz]	Typical conversion loss [dB]
30 – 300	5 – 10
300 – 600	7 – 12
600+	12 – 15

Table 1.3: Performance breakdown by frequency range.

to have CL of less than 10 dB in the millimetre and sub-millimetre wave ranges.

1.4 Devices Used

Mixers nowadays use either diodes or transistors as their non-linear element, depending on various design requirements and constraints. The characteristics and peculiarities of the different types of diodes and transistors used are discussed next.

1.4.1 Diodes

The diodes usually used in mixers are junction and Schottky diodes[6]. They both derive their characteristics from the barrier effect that occurs at the interface of two different types of semiconductor (junction), or semiconductor and metal (Schottky)[41]. Junction diodes are typically used at lower frequencies, while Schottky diodes are the workhorse of mixers operating at microwave, millimetre, and sub-millimetre frequency ranges[6]. Therefore, subsequent discussion will focus on them.

The capability of a Schottky diode to operate at higher frequencies comes from the fact that it is a single charge carrier device, i.e. there are no minority carriers, and as a result it offers faster switching and quicker recombination times[89].

The current-voltage characteristic of a Schottky diode is given by the well-known Shockley equation[41]

$$I\left(V\right) = I_s\left[\exp\left(\frac{qV}{\eta kT}\right) - 1\right] \tag{1.9}$$

where I_s is the small reverse saturation current, q is the electron charge, k is Boltzmann's constant, T is temperature in Kelvin, and η is the Schottky diode's ideality factor. With a higher ideality factor, the non-linear behaviour of the diode decreases, changing the gradient of the I-V curve; and as a consequence the overall performance of a mixer using a Schottky diode is reduced.

The contact between a metal and a semiconductor can be thought of as an abrupt(step) junction, and the capacitance associated with it can be expressed via:

$$C_j\left(V\right) = \frac{C_{j0}}{\left(1 - \frac{V}{\phi}\right)^{\gamma}} \tag{1.10}$$

where C_{j0} is the junction capacitance at zero bias, ϕ is the built-in potential, and γ is a coefficient dependent on the semiconductor doping profile[41].

There are many Schottky diode models used in circuit analysis, such as large- and small-signal SPICE models, equivalent circuits, etc. A simplified equivalent circuit is shown in Fig. 1.19[7]. Here R_s is the series resistance, which can be considered a constant, and R_j models the variable resistance of the Schottky junction.

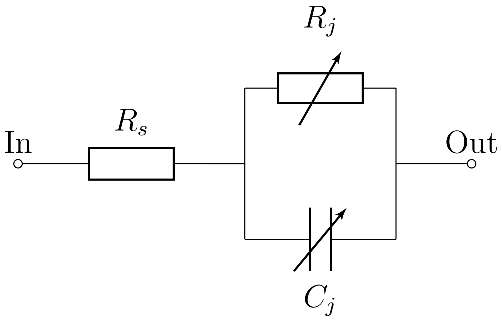

Figure 1.19: A simplified Schottky diode equivalent circuit, not taking into account packaging and other parasitics.

The series resistance is the major contributor of thermal noise, while random charge carrier flow is responsible for the presence of shot noise[6].

There are several trade-offs that need to be considered when designing Schottky diodes for sub-millimetre frequency mixer use[86]. First of all, it is difficult to make diodes with low R_s, and that is one of the major contributors to mixer conversion loss. Next is the question of junction area. On one hand, larger area leads to larger C_{j0}, which restricts the range of impedances that can be presented to the mixer ports, makes impedance matching difficult, and increases losses; on the other hand larger areas can support larger current and provide better power handling capabilities[75].

Finally, Schottky diodes intended for mixer use at millimetre and sub-millimetre frequencies are usually fabricated out of GaAs or InGaAs, because of the mature technology and lower resulting R_s[89].

1.4.2 Transistors

Unlike passive mixers, where Schottky diodes are predominantly used, several different types of transistors are used in active mixers. Silicon-based BJTs were traditionally used at RF frequencies, i.e. up to a few GHz[6]. However, circuits based on Si MOSFETs[90], GaAs MESFETs[91], and HEMTs[92], are currently preferred. In addition to this, FETs are better suited for monolithic integration. Regardless of what technology the transistors are, they are always either n-type or n-channel[7, 93].

In modern mixers, Si MOSFET are used for microwave applications, up to a few GHz. Above 1 GHz, GaAs and other III-V compound semiconductors are used in MESFETs, which have no shot noise, but higher flicker noise[6].

HEMTs offer superior performance than MESFETs, due to their ability to support higher current, and the fact that carrier transport occurs in buried layers (HEMT), as opposed to surface contact between metal and semiconductor (MESFET). HEMTs can also be used in mixers up to W-band[52]. This class of transistors offers more degrees of freedom in design and customisation. The main trade-off that is made is that of gate length against noise performance, frequency of operation, and conversion loss[94].

The non-linear characteristic of transistors that is used to provide frequency mixing is the transconductance g_m, which itself is a function of gate voltage.

There are multiple SPICE and equivalent circuit models of the different types of transistors, with varying degrees of accuracy and detail. However, since the work in this thesis focuses on passive sub-harmonic mixers using diodes, further discussion of transistor devices is beyond the scope of this work.

1.4.3 Resonant-Tunnelling Diodes

Resonant-tunnelling diodes have several properties that make them potentially useful competitors to Schottky diodes in sub-harmonic mixers operating at millimetre and sub-millimetre frequencies[14, 16, 95]. The main one is the anti-symmetric I-V, presented by a single device, which importantly is associated with smaller overall junction capacitance and no need for careful selection of identical diodes. The RTDs are also less dependent on surface interface quality, since, just like HEMTs, the actual non-linear device is formed by buried semiconductor layers. In addition, a single diode is much more compact, a consideration at THz frequencies where λ can be less than 300 μm. Finally, there are more parameters that can be tuned at a semiconductor layer level in order to obtain better performance.

RTDs are usually fabricated from layers of GaAs and AlGaAs, though other compound semiconductors can be used[96, 12, 97]. The work in this thesis will focus on GaAs and AlGaAs as this material system is readily available at the University of Leeds, however the conclusions in terms of design choices can be carried across to different material systems in the future. Unfortunately, while some exact models that tie an RTD's I-V with its physical parameters exist, such as SILVACO[98] and Quant ST[99], these require extensive calibration and may not always result in good agreement between predicted and observed performance. There are, however, several approximate models that are used in circuit design[100]. Resonant-tunnelling diodes are discussed in greater depth in the next Chapter.

Chapter 2

Resonant-Tunnelling Diodes

The performance of resonant-tunnelling diodes as potential non-linear elements in sub-harmonic mixers at millimetre and sub-millimetre frequencies is the main focus of this thesis. In addition, there is also interest in their possible use in low-gain amplifiers at the same frequency ranges to complement mixers by compensating for their inherent conversion loss.

One of the reasons for this interest is the multitude of parameters that can be optimised in a resonant-tunnelling diode to achieve a desired current-voltage characteristic, coupled with its low specific capacitance.

The first part of this Chapter provides a thorough introduction to the RTD. After a brief description of the history and development of the RTD, the physical principles behind its operation are presented. This includes a brief discussion on how adjusting the different physical dimensions of the diode affect its I-V.

The second part introduces the devices made here at the University of Leeds, along with their measured and calculated parameters. Following that, the reasons for their use in sub-harmonic mixers will be reviewed again, and the RTDs' current use in various circuits will be reported. Finally, an overview of the models used in circuit design and simulation will be given, together with the model that was used in the work presented in this thesis.

2.1 History

The quantum tunnelling phenomenon was first predicted and studied during the early part of the 20th century, but it was not until 1973 when Leo Esaki and Raphael Tsu first theoretically investigated tunnelling in a finite multi-barrier structure. In their seminal paper[1] the pair presented calculations for both the transmission probability $T(E, V)$ in such a structure, and the current density $J(V)$. This formed the foundation for analysis of periodic quantum barrier structures and hinted at the electrical properties they might have.

In the following year, 1974, the same team, together with L L Chang, published the first experimental evidence of resonant tunnelling in a double quantum barrier device[101]. The paper included experimental data at both room and liquid nitrogen temperatures, and presented for the first time the measured I-V of an RTD, showing a negative differential resistance (NDR) region.

From then, the use of RTDs in a variety of circuits has been studied. During the 1980s a lot of research and development went into improving the analytical models[102, 103, 42]. Research into RTDs is still ongoing today, with new materials being tested, and new ways of modelling and analysing the diodes being developed[10, 104, 97].

2.2 Physics Background

The physical principles of operation of the resonant-tunnelling diode are briefly summarised in this section. Starting with the semiconductor layer composition and resultant energy band diagram, the shape of the RTD's current-voltage characteristic is explained. Following that, a brief discussion on the effects of the different layer parameters on the I-V is presented.

2.2.1 Double Quantum Barrier

An RTD is in essence a double quantum barrier device, at its most basic form composed of three layers of undoped semiconductor material. Compound III-V semiconductors are most often used, and the thickness of these layers is no greater than several nanometres, i.e. smaller than the de Broglie wavelength of an electron, which is about 30 nm in GaAs[105]. Two of these layers have a different bandgap, forming two quantum barriers, with a quantum well in-between them[102]. A conduction band diagram is shown in Fig. 2.1. The layers labelled *Emitter* and *Collector* are usually doped, with dopant concentrations on the order of $10^{16}/cm^3$ – $10^{17}/cm^3$, and are of the same material as the well[2, 12]. Additional undoped spacer layers can be added between these two regions and *Barrier 1* and *Barrier 2* to prevent dopant diffusion and tailor the current-voltage and capacitance-voltage characteristics[106, 10]. The width of the barriers does not need to be the same, and asymmetrical layer structures are employed in some specific cases, such as devices used in oscillators[96, 107].

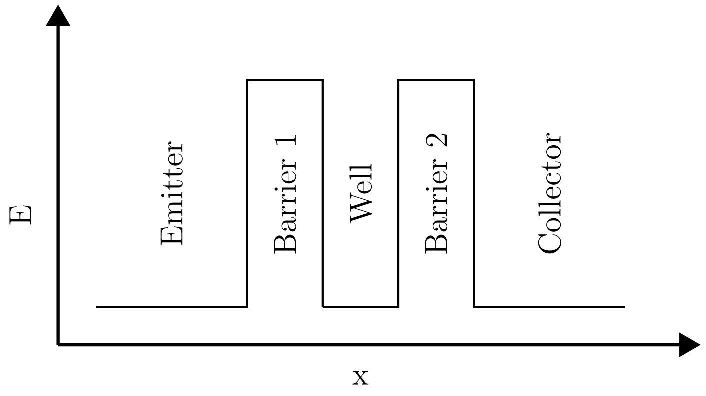

Figure 2.1: A conduction band diagram of a the conduction band edge in a typical RTD device. Shown are the two barriers, well, and emitter and collector regions.

It is known from quantum mechanics that inside a quantum well charge carriers can occupy discrete energy levels. Solving Schrödinger's equations simultaneously in the three regions leads to a tunnelling probability function which exhibits sharp peaks. These occur when the energy of charge carriers coming from the *Emitter* coincide with one of the energy levels inside the well, allowing them to tunnel through the structure, and giving these devices the name *Resonant-Tunnelling Diodes*[41, 103].

The energy of the emitter charge carriers, relative to these allowed states in the well, is controlled by external voltage bias. The following series of graphs (Fig. 2.2a – Fig. 2.2f) describes how applying different levels of bias results in the different regions of an RTD's current-voltage characteristic. At low levels of applied bias, the current flowing through the device is dominated by non-resonant and scattering assisted tunnelling, as well as thermionic emission over the finite-height barriers. This forms the first region of an RTD's I-V, the *Positive Differential Resistance (PDR)* region[101, 108]. As the bias increases, the energy of the carriers in the emitter gets closer and closer until it eventually matches one of the allowed energy

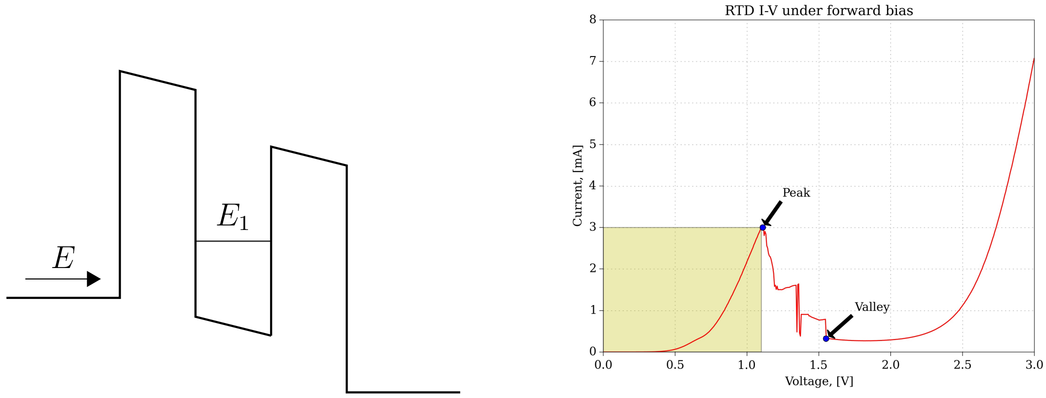

(a) Low levels of bias

(b) First PDR region

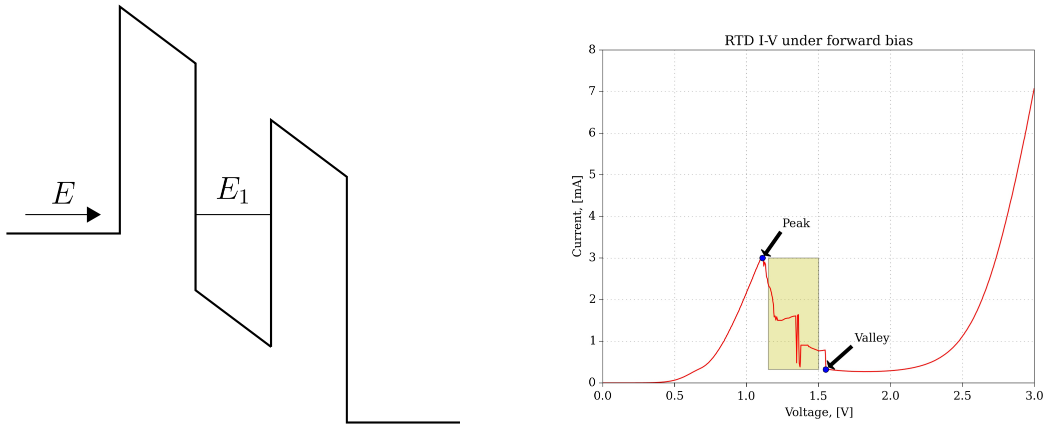

(c) Increased bias, resonant condition

(d) Subsequent NDR region

levels inside the quantum well. This corresponds to a local maximum in the I-V, known as the *peak*. However, with further increase, the incoming charge particles have energies that do not match any of the levels inside the well, leading to a decrease in the overall current. This gives rise to the second region of interest in the RTD's current-voltage characteristic, the *Negative Differential Resistance (NDR)* one[109]. At some point, either due to sufficient lowering of the barriers by the applied bias, or due to alignment with another allowed energy level, current through the diode increases again. The voltage at which this happens, and the associated current with it, are known as the *valley*. The parameter *Peak-to-Valley Current Ratio* (PVCR) is often used when characterising RTDs[13].

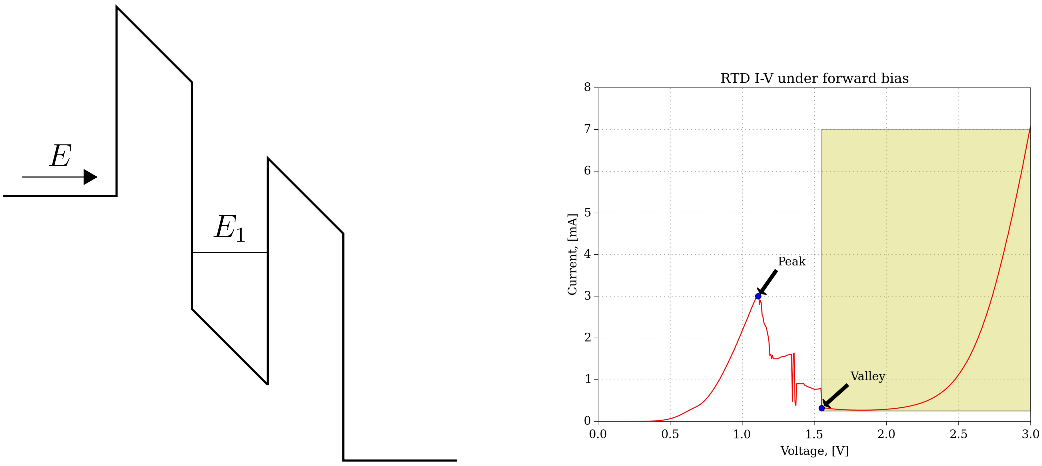

(e) Further increased bias

(f) Second PDR region

Figure 2.2: Diagrams showing the relationship between the RTD's band diagram, levels of applied voltage, and corresponding regions in its I-V characteristic.

The next section will introduce the different qualitative effects of the various physical parameters on the device's electrical behaviour and performance.

2.2.2 Effect of Physical Parameters on I-V

The ability to individually control the thickness and height of the two barriers, as well as the thickness of the quantum well, offers a lot of design flexibility when tailoring the semiconductor layer composition for a specific application. Furthermore, different spacer layers can be added to the quantum barrier structure to allow for even greater design freedom.

The thickness of the barriers, as well as the width of the well, are the main influencing factor on the current density J_V of a particular resonant-tunnelling diode. The relationship is inversely proportional, i.e. devices with thinner barriers tend to exhibit higher current densities[42, 110, 111]. This thickness can easily be controlled during the Molecular Beam Epitaxy (MBE) growth process[112].

The barrier height, on the other hand, determines a practical limit to the allowed energy states inside the well. This can be exploited to fabricate RTDs with PDR region spanning a wide voltage range, which would be very useful when designing mixers with large input signal dynamic range. The barrier height is determined by the compound semiconductor material used for it, and can be tuned by adjusting the ratio of the individual elements, e.g. the amount of Al in a AlGaAs barrier[41].

Another parameter influenced by the barriers is the PVCR, as well as the position of the valley point. In a similar manner to RTDs tailored towards mixers, carefully designing the barriers can result in devices with large PVCR over an extended voltage range[109, 3]. This type of RTDs find application in oscillators[96, 113, 114].

The quantum well width is used to manipulate the position of the resonant current peak, with shorter wells resulting in a peak at a higher voltage[102].

Undoped spacer layers are usually added between the barriers and the emitter and collector to prevent dopant diffusion. It has been shown that these spacer layers can lead to a decrease in the overall capacitance of the RTDs[106].

2.3 Leeds Devices

Currently, there are no RTD devices that are commercially available and already packaged. Therefore, for the the needs of the project, custom resonant-tunnelling diodes had to be fabricated on site at the University of Leeds. This was an iterative process, using different device shape and different semiconductor layer composition. The details of the these layers, their physical size, as well as their electrical characteristics are described in this section.

2.3.1 Layer Details

Devices were fabricated in a cleanroom environment from several different semiconductor layers. Initially, layers grown at the University of Nottingham by Dr M Henini, to a design by Dr DP Steenson, were used to make diodes in the form of a cylindrical mesa structure. Current-voltage measurements of these diodes at DC were used to develop an initial circuit model for an RTD and to obtain a first approximation of expected performance as a sub-harmonic mixer element. A top-down reflected light microscope photograph, along with a sketch of its cross-section, of such a diode are shown in Fig. 2.3. These layers are designated as NU-455, NU-462, and NU-469. The specifics of the semiconductor composition of these are given in Table 2.1. Layer NU-469, due to its extra layer, does not exhibit an anti-symmetric I-V characteristic, as it was originally intended for oscillator use. However, by numerically selecting one half of its I-V and mirroring it around the origin, such a characteristic can be achieved.

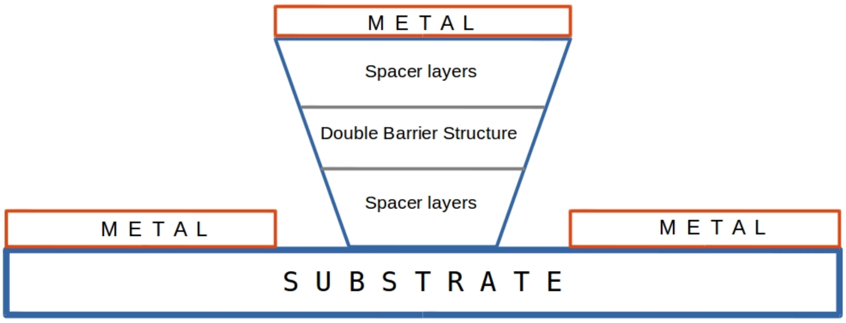

(a) Cross-section sketch

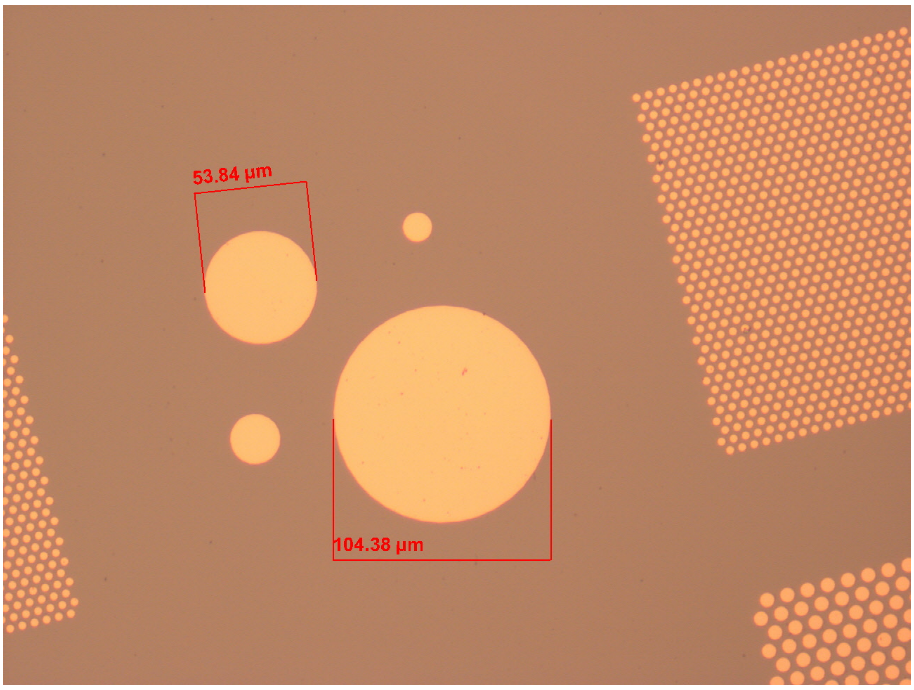

(b) Microscope photograph

Figure 2.3: Cylindrical RTD devices, fabricated from NU layers. Approximate device diameter measurements included.

NU-455		NU-469	
Thickness	Material	Thickness	Material
0.5 μm	GaAs $(1 \cdot 10^{18}/cm^3)$	0.5 μm	GaAs $(1 \cdot 10^{18}/cm^3)$
0.1 μm	GaAs $(1 \cdot 10^{17}/cm^3)$	0.1 μm	GaAs $(1 \cdot 10^{17}/cm^3)$
51 Å	$GaAs\,(UD)$	51 Å	$GaAs\,(UD)$
43 Å	$Al_{0.4}Ga_{0.6}As\,(UD)$	43 Å	$Al_{0.4}Ga_{0.6}As\,(UD)$
51 Å	$GaAs\,(UD)$	51 Å	$GaAs\,(UD)$
43 Å	$Al_{0.4}Ga_{0.6}As\,(UD)$	43 Å	$Al_{0.4}Ga_{0.6}As\,(UD)$
51 Å	$GaAs\,(UD)$	51 Å	$GaAs\,(UD)$
0.1 μm	GaAs $(1 \cdot 10^{17}/cm^3)$	0.1 μm	GaAs $(2 \cdot 10^{16}/cm^3)$
0.5 μm	GaAs $(1 \cdot 10^{18}/cm^3)$	0.1 μm	GaAs $(1 \cdot 10^{17}/cm^3)$
Substrate	GaAs (N^+)	2 μm	GaAs $(1 \cdot 10^{18}/cm^3)$
		Substrate	GaAs (N^+)

(a) Layers with AlGaAs barriers. Layer NU-469 has an extra layer, indicated by grey text background.

Three more layers, designated L938, L939, and L940, were grown at the University of Leeds using Molecular Beam Epitaxy (MBE) technology by a team lead by Dr L Li, again to Dr DP Steenson's specifications. Beam lead RTDs, i.e. devices

NU-462	
Thickness	Material
600 Å	GaAs ($2 \cdot 10^{16}/cm^3$)
0.5 μm	GaAs ($2 \cdot 10^{17}/cm^3$)
25 Å	$GaAs\,(UD)$
17 Å	$AlAs\,(UD)$
42 Å	$GaAs\,(UD)$
17 Å	$AlAs\,(UD)$
25 Å	$GaAs\,(UD)$
0.4 μm	GaAs ($2 \cdot 10^{17}/cm^3$)
1 μm	GaAs ($1 \cdot 10^{18}/cm^3$)
Substrate	GaAs (N^+)

(b) Layer with pure AlAs barriers.

Table 2.1: Details for semiconductor layers grown at the University of Nottingham, including quantum barrier structure and doped layers for ohmic contact. Quantum barrier structure layers are italicised.

with protruding metal contacts from both electrodes, were fabricated using these layers, and the resulting devices were used for more extensive modelling, simulation, and design work. An SEM photograph, and a corresponding cross-section sketch, of one of these devices are shown in Fig 2.4, and the layer details are summarised in Table 2.2. The difference in barrier height and barrier material leads to a difference in the transmission probability function $T(E)$ for the different layers. Another distinction between L938 and L940 is the type of molecular As used, with As_2 for L938 and As_4 for L940. Given that layers L938 and L940 have the same parameters for their barriers, they would have identical transmission probability functions. The transmission probabilities for all layers grown at the University of Leeds are calcu-

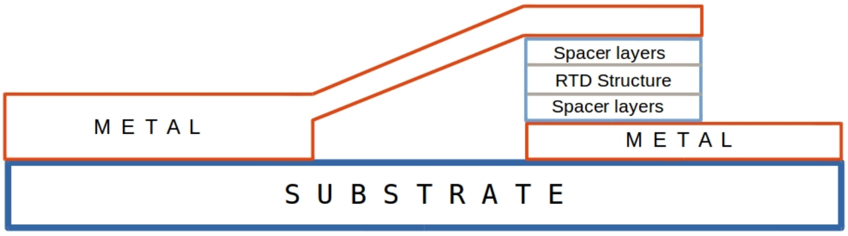

(a) Cross-section sketch

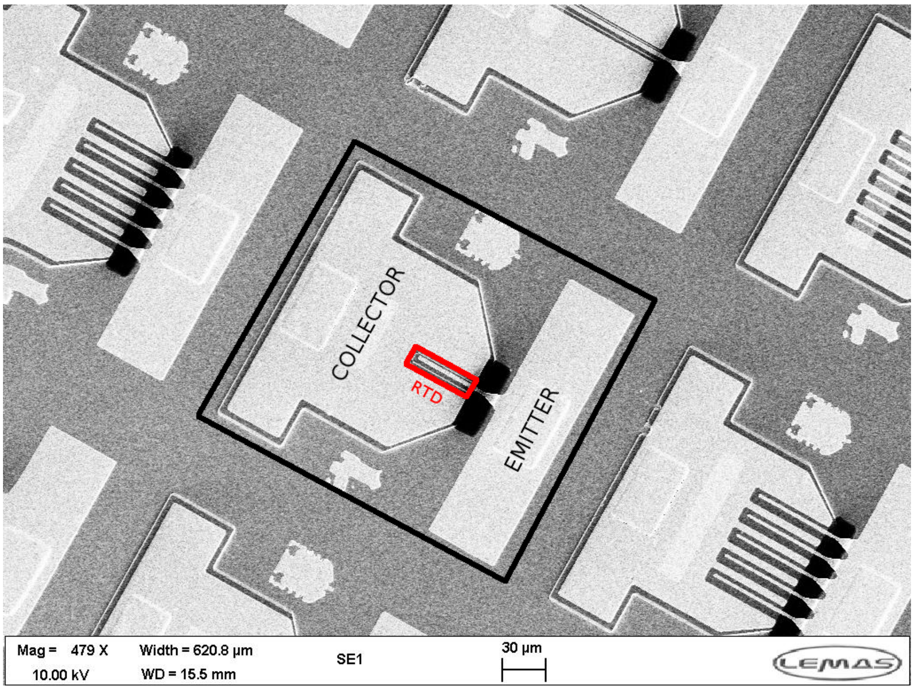

(b) SEM photograph

Figure 2.4: An SEM photograph of beam lead RTDs, made from University of Leeds grown layers on semi-insulating GaAs, with active area in the shape of a finger structure. A black box surrounds a single device.

L938 and L940		L939	
Thickness	Material	Thickness	Material
0.5 μm	GaAs $(2 \cdot 10^{18}/cm^3)$	0.5 μm	GaAs $(2 \cdot 10^{18}/cm^3)$
0.1 μm	GaAs $(2 \cdot 10^{16}/cm^3)$	0.1 μm	GaAs $(2 \cdot 10^{16}/cm^3)$
100 Å	$GaAs\,(UD)$	100 Å	$GaAs\,(UD)$
50 Å	$Al_{0.4}Ga_{0.6}As\,(UD)$	17 Å	$AlAs\,(UD)$
50 Å	$GaAs\,(UD)$	50 Å	$GaAs\,(UD)$
50 Å	$Al_{0.4}Ga_{0.6}As\,(UD)$	17 Å	$AlAs\,(UD)$
100 Å	$GaAs\,(UD)$	100 Å	$GaAs\,(UD)$
0.1 μm	GaAs $(2 \cdot 10^{16}/cm^3)$	0.1 μm	GaAs $(2 \cdot 10^{16}/cm^3)$
0.5 μm	GaAs $(2 \cdot 10^{18}/cm^3)$	0.1 μm	GaAs $(2 \cdot 10^{18}/cm^3)$
0.1 μm	GaAs (UD)	0.1 μm	GaAs (UD)
Substrate	GaAs	Substrate	GaAs

Table 2.2: Details for semiconductor layers grown at the University of Leeds, including quantum barrier structure and doped layers for ohmic contact. Quantum barrier structure layers are italicised.

lated using a FORTRAN program developed by Dr DP Steenson, the source code of which is given in Appendix B. The program computes $T\left(E\right)$ by solving the general equation

$$T = M_{11} - \frac{M_{12}M_{21}}{M_{22}} \tag{2.1}$$

where M_{ij} are the elements of the transfer matrix, which relate the amplitude of the wave functions of incident and reflected electrons in the emitter region, and the transmitted ones in the collector region[103]. The resulting graph is given in Fig 2.5. These illustrate how the layer structures will likely affect the current-voltage characteristic - L939's first resonant energy level occurs at a higher incident energy than L938 and L940, meaning that L939's NDR would occur at a higher applied voltage. Furthermore, L939 has a larger full-width at half maximum (FWHM), meaning a higher current density should be expected from devices made from it.

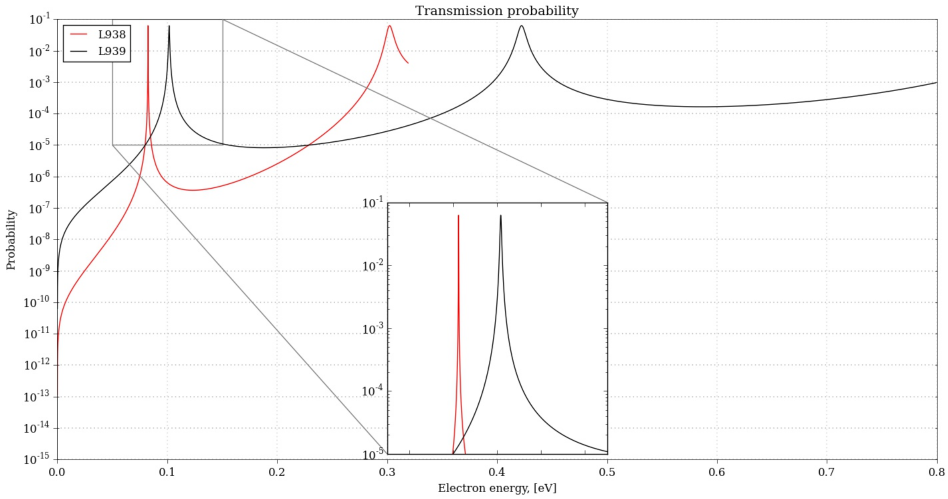

Figure 2.5: Transmission probability graph for layers L938 and L939, showing first two resonant energy levels.

2.3.2 Device Dimensions

The first devices fabricated at the University of Leeds were in the shape of cylindrical dot diodes, as illustrated in Fig. 2.3. The diameter of these ranged from 100 μm for the largest devices down to 5 μm for the smallest. All devices had the same height, determined by the semiconductor layer composition given in Table 2.1.

These diodes were useful as a technology demonstrators and ensuring that RTDs can be reliably made and measured at Leeds. However, this type of structure was found to be unsuitable for packaging and use in a circuit. Furthermore, problems with metallisation, specifically metal creeping down the cylinder and shorting out the quantum well structure, meant that yield was low, especially on devices with small diameter.

To solve this, a mask set, originally developed by Dr DP Steenson, was adapted and used by Mr H Patel to make beam lead RTDs with finger-shaped active area. One SEM photograph of these devices is shown in Fig. 2.4, and a close-up on the finger area is given in Fig. 2.6. Using this mask set, devices of five different sizes were fabricated. The length of the finger area is the parameter being varied, with the width being kept the same. The values for the width and length of the fingers

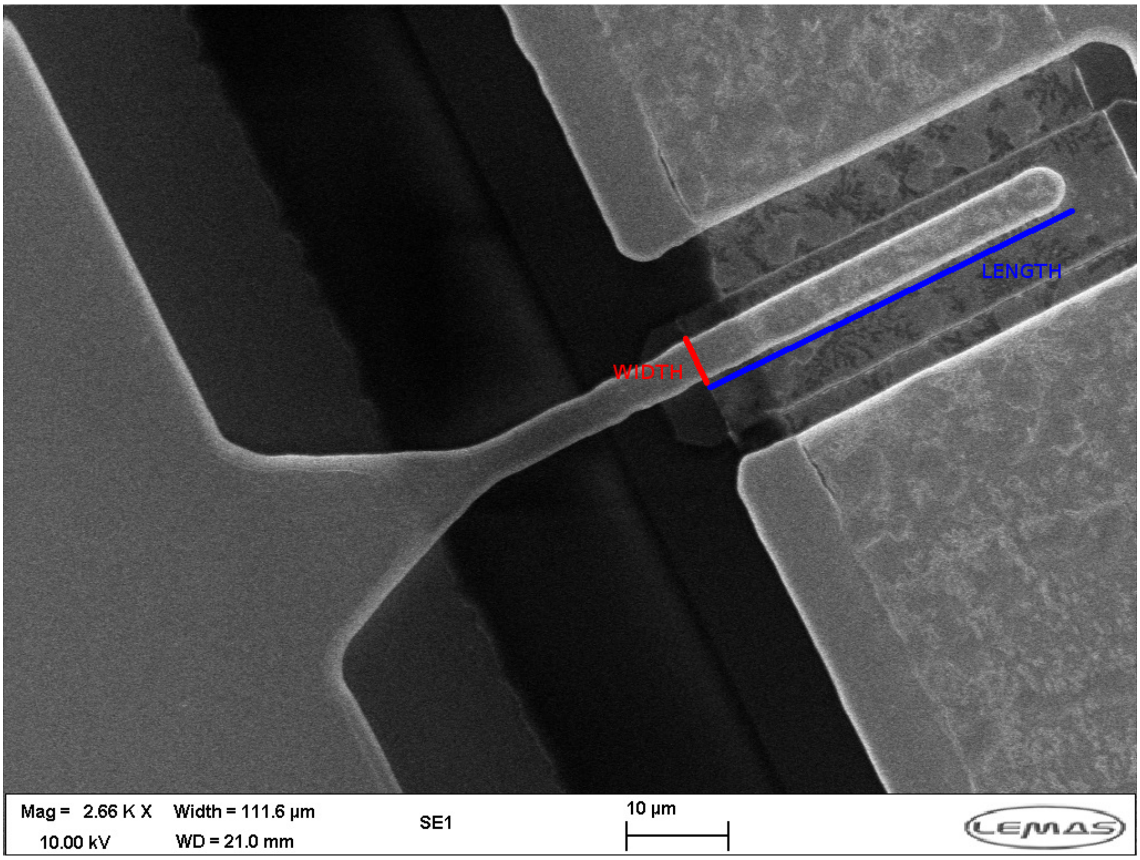

Figure 2.6: A close-up of the finger area of a beam lead resonant-tunnelling diode.

are given in Table 2.3, along with device size designation. The height of active area is constant, and is defined by the thickness of the different layers, as given in Table 2.2. These planar devices are more suitable for use in microstrip or coplanar waveguide circuits, which are the technologies used in this thesis. Better yield and repeatability was also achieved, meaning RTDs could be reliably manufactured at the University of Leeds.

Size Designation	D1	D2	D3	D4	D5
Length [μm]	6	12	22	45	90
Width [μm]	5	5	5	5	5
Area [μm^2]	30	60	110	225	450

Table 2.3: RTD device size, for diodes fabricated from L938, L939, and L940 material.

2.3.3 Measured and Calculated Parameters

To accurately model an RTD device and use said model in circuit design software, both its current-voltage characteristic and its C_{j0} are required.

The I-V of the manufactured devices was measured at DC frequency. To do so, a Keithley Instruments 2636A Source Measurement Unit (SMU) was used. The instrument was driven by a LabVIEW program, developed by the author for this specific task. To measure the I-V, a couple of needle probes were used, which were in turn connected to the terminals of the SMU. Voltage was applied across the RTD device, sweeping between a minimum and a maximum value. At the same time, the current passing through it was measured by the Keithley SMU and recorded by the LabVIEW software. The SMU itself was configured to be in current-limited mode so as to avoid burning out the diodes. This approach also made it possible to read out the I-V data in text format, which made consequent data handling operations easier.

Devices of all sizes, made from all three layers were measured in two large batches, from two different fabrication runs. Most of the measurements were made at room temperature, i.e. 290 K. Some devices were selected and measured at liquid nitrogen temperature, i.e. 77 K.

Detailed plots of these measurements are presented in Fig. 2.7 through Fig. 2.14. While only comparative plots are presented in this Chapter, individual I-V plots are included in Appendix A. Additionally, Appendix A has plots of devices that were not used for modelling or simulations purposes. These are included for completeness. The plots in Fig. 2.7 – Fig. 2.13 are all room temperature measurements. Diodes were fabricated from two different parts of the same wafer, with the individual layers grown on them. Devices from both production runs have very pronounced NDR regions, as well as highly non-linear I-Vs close to the origin. The I-Vs are also nicely anti-symmetric, leading to expectations of good frequency mixing performance. As for the effect of device size, an increase of up to ten times in amount of current conducted is observed between the smallest and the largest devices. However, the ratio of areas between the smallest and largest device is fifteen, showing imperfect scaling. It should also be noted that the position of the NDR region is roughly the same for all devices and both wafer samples for devices manufactured from the same semiconductor layers.

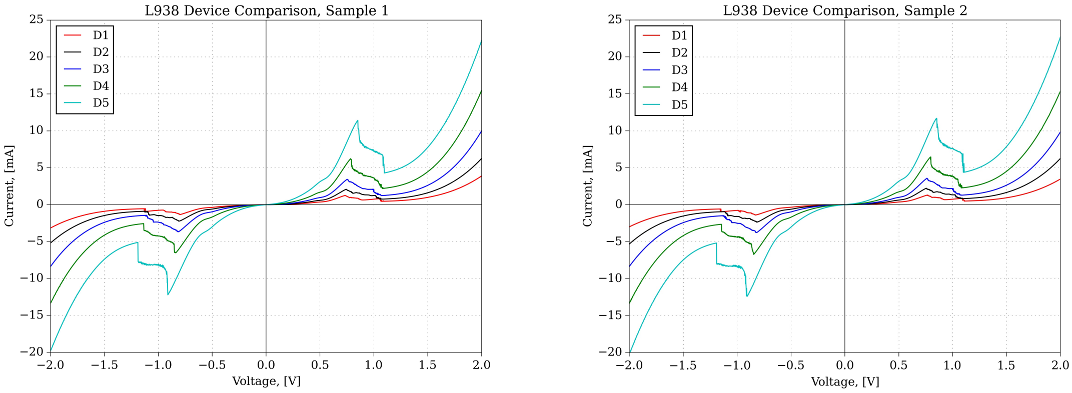

(a) Sample 1

(b) Sample 2

Figure 2.7: Measured current-voltage characteristics of L938 RTD devices.

Another comparison can be made between devices with the same active area and layer composition, and coming from different parts of the same wafer. Such a comparison for devices made from L938, with area of $30\mu m^2$ and $450\mu m^2$, are shown in Fig. 2.8a and Fig. 2.8b, respectively. These graphs show that devices from different parts of the same wafer have virtually identical current-voltage characteristics, meaning that good yield can be expected.

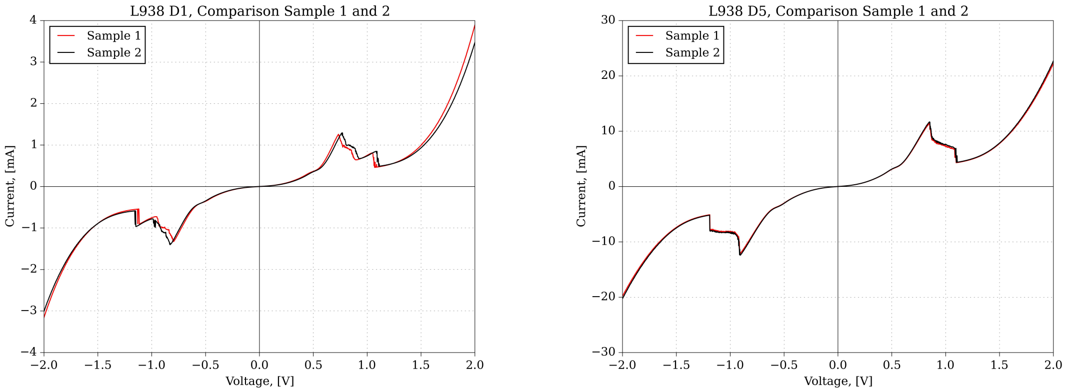

(a) Device Size 1, area of $30\mu m^2$

(b) Device Size 5, area of $450\mu m^2$

Figure 2.8: Comparison of current-voltage characteristics of L938 RTD devices.

L940 has the same layer structure as L938, and the corresponding graphs showing the I-Vs of L940 devices are given in Fig. 2.9 and Fig. 2.10. The conclusions that can be drawn from these graphs are the same as those for L938, i.e. excellent sample processing and good expected wafer yield, well distinguished NDR region and strong non-linearity close to zero bias. A direct comparison between devices

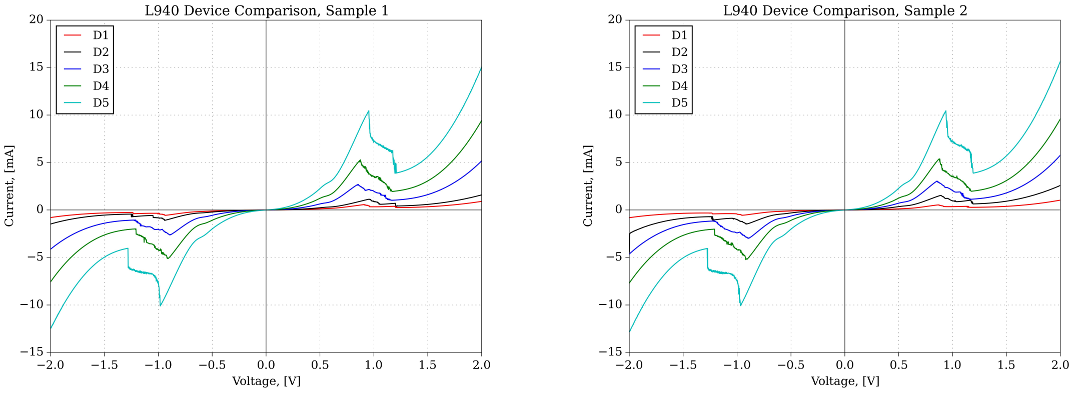

(a) Wafer Sample 1

(b) Wafer Sample 2

Figure 2.9: Measured current-voltage characteristics of L940 RTD devices.

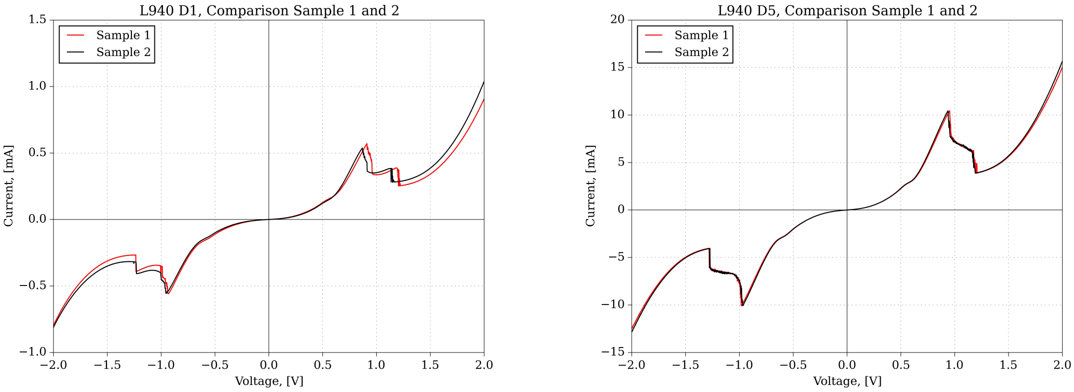

(a) Device Size 1, area of $30 \mu m^2$

(b) Device Size 5, area of $450 \mu m^2$

Figure 2.10: Comparison of current-voltage characteristics of L940 RTD devices.

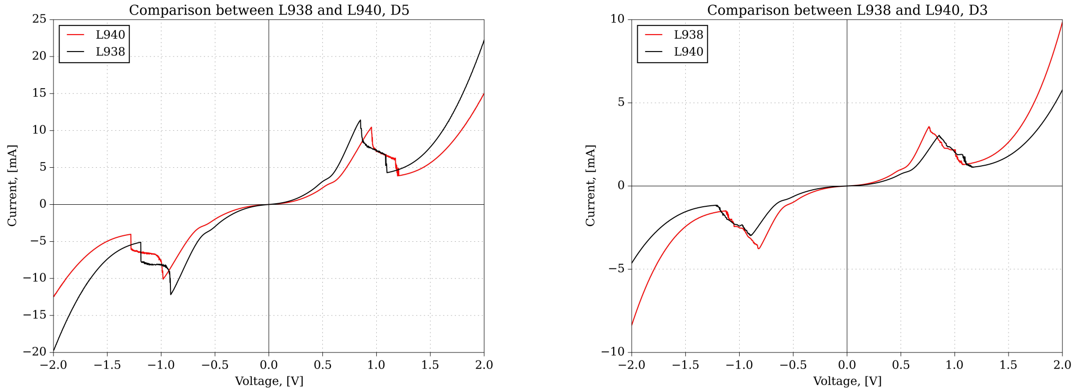

(a) Device Size 3, area of $110 \mu m^2$

(b) Device Size 5, area of $450 \mu m^2$

Figure 2.11: Comparison between D3 and D5 from L938 and L940, illustrating effect of MBE growth parameters.

of same size from the two layers is given in Fig. 2.11. It can be seen that even though the I-V characteristics are identical when the applied voltage is less than $0.1V$, L938 can conduct larger current, and has an NDR at slightly lower voltages. These differences, despite the same semiconductor layer structure, illustrate how sensitive the double-barrier quantum well devices are to variations in MBE growth parameters.

The third semiconductor layer composition which was used for device fabrication, L939, differs from L938 and L940 by having a thinner barrier, $17\mathring{A}$ vs $50\mathring{A}$, and different barrier material composition, $AlAs$ vs $Al_{0.4}Ga_{0.6}As$.

During the initial manufacturing and measuring run, devices were only measured between -2 V and 2 V, leading to the I-Vs in Fig 2.12a. These I-Vs do not show an NDR region, just typical anti-symmetric diode behaviour. However, during subsequent measurements the voltage range was expanded, and the obtained results are presented in Fig 2.12b. The devices now show an NDR region, though notably only the smaller sized ones. Self-heating from the large current passing through is the most likely reason for the diminished tunnelling current and straightening of the NDR region. While the measurements confirm the expectations for an NDR at higher voltages and higher current density, the much higher position of the peak can also be partially attributed to poor metal contact, resulting in large contact resistance. As can be seen from Fig. 2.13, which shows the comparison between same sized devices from all layers, L939 offers up to 10 times larger current density than L938 and L940, as a result of its much thinner AlAs barriers. Finally, the effect of temperature on the devices' I-V was examined by cooling down a few samples using liquid nitrogen to about 77 K during measurement. The results of these measurements, compared to room temperature I-Vs of the same devices, are shown in Fig. 2.14.

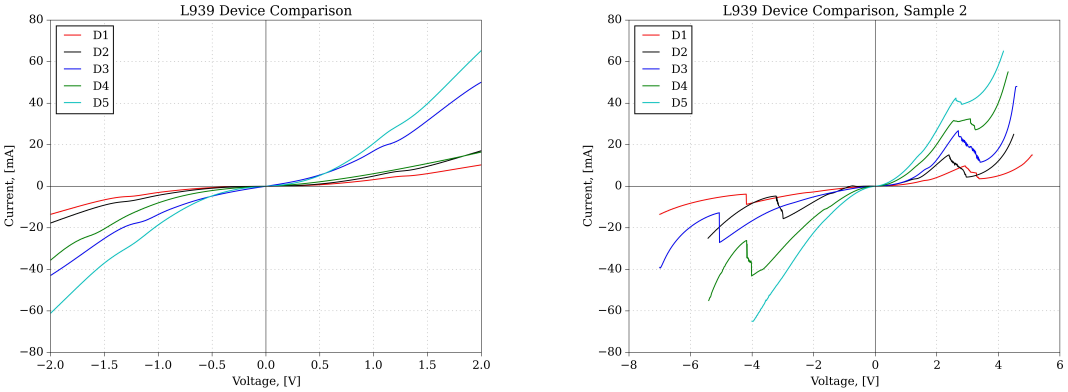

(a) First batch of L939 devices

(b) Second batch of L939 devices

Figure 2.12: Measured current-voltage characteristics of L939 RTD devices.

It should be noted that the L939 devices do not exhibit NDR, because the liquid nitrogen measurements were conducted before expanding the voltage range, as dis-

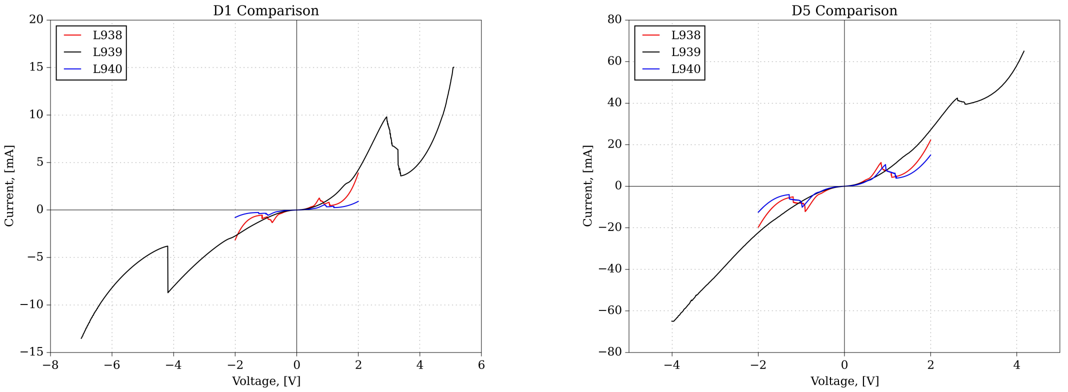

(a) Device Size 1, area of $30\mu m^2$ (b) Device Size 2, area of $60\mu m^2$

Figure 2.13: Comparison between devices of same size from L938, L939, and L940.

cussed previously. These measurements show that the liquid nitrogen cooling has several effects on the RTDs. There is a larger portion of the I-V where the RTD is effectively *off* and does not conduct current, followed by a more pronounced non-linear *knee*. In addition to this, the L940 sample has increased current density, along with larger peak-to-valley ratio, when compared to the room temperature one.

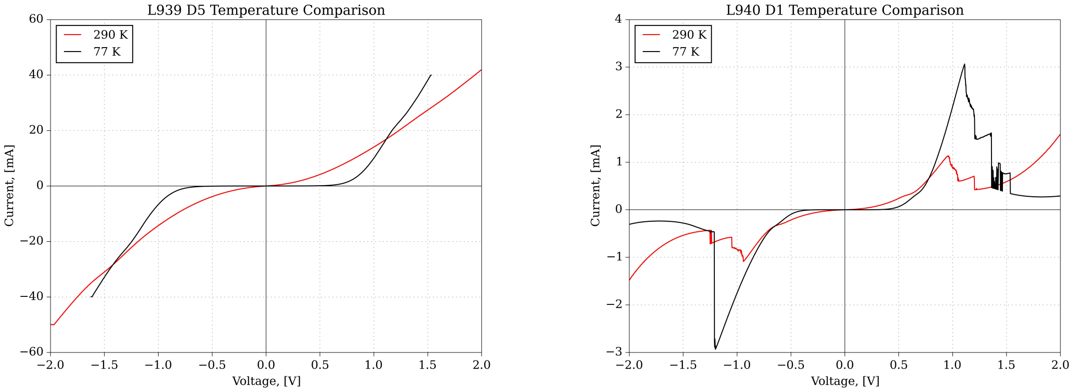

(a) L939 Device Size 5, area of $450\mu m^2$ (b) L940 Device Size 1, area of $30\mu m^2$

Figure 2.14: Current-voltage characteristics of devices measured at 77 K, compared to I-Vs measured at 290 K.

The effect of these changes and the extent to which they are beneficial for frequency mixing and amplification is investigated in Chapter 3 and Chapter 4.

Another important characteristic of the RTDs is the capacitance-voltage characteristic, and more precisely, the zero-bias junction capacitance C_{j0}. Unfortunately, since we were unable to directly measure this value with the equipment available at the University of Leeds, the C_{j0} had to be estimated from the physical parameters of the fabricated diodes. Therefore, using an abrupt junction assumption, the C_{j0} was calculated as a parallel-plate capacitor with a thickness of 100 nm. This thickness was based on a Debye length of 30 nm, added to the overall thickness of the undoped layers of the RTDs[41]. The results for the C_{j0} of the different sized devices are given in Table 2.4. These calculations suggest an average C_{j0} of about $2.75 fF/\mu m^2$, which can be used to estimate the capacitance of future smaller devices, fabricated from the same material system and having similar geometry.

Size Designation	D1	D2	D3	D4	D5
C_{j0} $[fF]$	81	163	308	651	1300
Area $[\mu m^2]$	30	60	110	225	450

Table 2.4: Zero bias junction capacitance C_{j0} for the different device sizes.

Now that both the I-V data and the C_{j0} values are available, all the necessary elements to create a model for use in mixer and amplifier simulations are present. The model used in this thesis is covered in greater detail later in this Chapter, as well as in Chapter 3.

2.4 Potential Uses as Sub-Harmonic Mixer

Several properties of RTDs point to potential good performance as a non-linear element in a sub-harmonic mixer circuit. Resonant-tunnelling diodes may also find application in oscillator and amplifier circuits. The reasons for these expectations can be summarised as follows:

Shape of current-voltage characteristic

Symmetrical semiconductor layer structure results in an anti-symmetric current-voltage characteristic. Since such an I-V is a prerequisite and is what makes efficient sub-harmonic mixing possible in the first place, as explained in Chapter 1, it stands to reason that an RTD device is perhaps a natural candidate for such a mixer. In addition to having such a shape, the RTD devices' I-V characteristic exhibit strong non-linearity at low voltage level, which can be varied during growth. Finally, the ability to engineer the barriers' material composition and thickness presents an ability to control the current density somewhat independently of its contact doping, which determines C_{j0} and R_s. The combination of these points to several possible benefits of RTDs over the use of anti-parallel Schottky diode pairs. Firstly, even a small difference in the two Schottky diodes of an APDP leads to a degradation in performance. On the other hand, being a single device with a symmetric layer structure, an RTD does not suffer from this. Furthermore, its junction size can be significantly smaller which aids THz applications. Next, the presence of a non-linear region at lower voltage levels should lead to a lower LO power requirement. This would be incredibly beneficial at higher frequencies (hundreds of GHz) where power is at such a premium.

A whole other unique aspect of the RTD's I-V that can be explored is the negative differential resistance region. Since this can be accurately modelled as a negative resistor, an RTD biased anywhere in that region can be used in amplifier or oscillator circuits. Again, the possibility to tailor the semiconductor layer composition means that the slope of this NDR region, as well as the peak-to-valley ratio and position can be adjusted to suit a specific design need.

Device capacitance

Another potential benefit of using an RTD is the reduced overall capacitance. For simulation purposes, a diode, be it a Schottky or a resonant-tunnelling one, can be represented by a current source connected in parallel to a capacitor. This capacitance is one of the limiting factors for the maximum frequency at which devices can operate. Therefore, by using one RTD diode instead of two Schottky diodes, we can halve that capacitance, and hypothetically construct similar mixers with diodes with similar sized junctions, operating at a higher maximum frequency.

2.5 Current State of RTD Use

Resonant-tunnelling diodes have been the subject of extensive research in the past, and their performance in various applications is still being investigated. Due to their unique properties, they could be used in a variety of circuits. While the current thesis deals with their application in mixers and amplifiers, examples of use in other circuits will also be given.

Mixers

The suitability of RTDs for sub-harmonic mixer use has been long recognised, and as a result studied throughout the years[14, 115]. Other research teams have theoretically investigated how RTDs perform at a wide range of frequencies, up to the THz region. Exploiting the transition curvature in the I-V between the first PDR region and the NDR region, researchers have discussed an active mixer based on an RTD[116]. Furthermore, designs of low-noise mixers have also been explored[15].

Similarly to the devices used in this thesis, most of the RTDs investigated in published articles use GaAs/AlGaAs semiconductor layer structure. Other reported material combinations used to fabricate a double quantum barrier structure include GaN/AlGaN[97], InAs/AlSb[96], AlGaAs/InGaAs/GaAs, and InGaAs/InAlAs[11].

Oscillators and Amplifiers

Having an NDR region, the RTD is a natural candidate for use in amplifiers and oscillators[7]. Previous work has looked at the construction of an active transmission line using resonant-tunnelling diodes, as well as other distributed amplifier circuits[117, 118, 119].

RTDs have proven themselves capable of generating power beyond 1 THz, even though the amount of power is significantly less than 1 mW[113]. However, these have found application in the emerging field of short-range, high-capacity wireless communication, as even a few 100 μW would suffice to drive a low power SHM using RTDs[120].

The principle of self-oscillating mixers has been investigated, but ideally the high current required of the oscillatory junction should be separated from the mixing element. This in principle can be done using RTDs, but requires two different co-joined devices, a potentially unique advantage of RTD based THz circuits.

Other Uses

Apart from being used as oscillators, RTDs have also been demonstrated to work well as detectors in wireless communication systems[40].

Another use of RTDs is as frequency multipliers, again taking advantage of their I-Vs' strong non-linearity at low voltage levels[14].

Resonant-tunnelling diodes have found use in digital circuits, such as analogue-to-digital converters, logic gates, memory circuits, inverters, and others. RTDs are uniquely suited for use in three-state circuits. Examples have been proposed where the use of an RTD reduced circuit complexity and power usage. In digital circuits, RTDs are often used in conjunction with transistors[121].

2.6 RTD Models

For the successful design and simulation of the various circuits incorporating resonant-tunnelling diodes, a suitable device model is needed. Such a model should be able to accurately and precisely capture and represent the RTDs' non-linear behaviour.

Ideally, the model should not be too computationally intensive and should provide a way to easily alter the device's I-V as a way to emulate changes in the physical parameters of said device. Finally, a way to model device parasitics is also required.

There are a few different categories of RTD models, each with different intended applications and limitations. These are presented and discussed here, along with some words on the model chosen for use in the design of the circuits presented in Chapter 3 and Chapter 4.

2.6.1 Equivalent Circuit Models

This type of models aim to represent the intrinsic diode device and the various parasitics associated with it via a combination of standard circuit elements, such as resistors, inductors, etc[122, 123].

The equivalent circuit representation of an RTD was originally based on that of an Esaki tunnel diode[124, 125]. A simplified version of such a circuit is presented in Fig. 2.15. This circuit does not feature packaging or other parasitics, and the element G is used to represent the NDR region. Additional resistors and capacitors can be included for more accurate modelling.

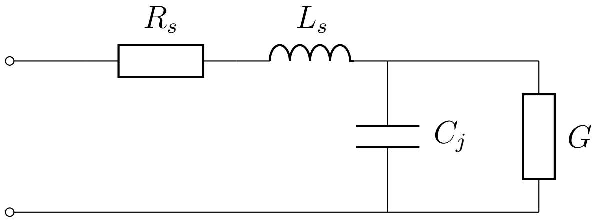

Figure 2.15: A simplified tunnel diode equivalent circuit, not taking into account packaging and other parasitics.

Such a circuit needs to be fit to some RTD impedance and/or small-signal S-parameter measurements, and is not an universal way of representing a device[126, 127]. This fitting process can be difficult in some cases. Another limitation is that this model is valid over a limited frequency range.

2.6.2 SPICE Models

These are usually modelled as large-signal equivalent circuit using the SPICE programming language. They can be generally divided into piece-wise linear (PWL) or non-PWL models[128, 129]. Regardless of the type, the I-V curve is divided into regions, and different circuits are used for each region, depending on the applied voltage. Furthermore, the parameters of the SPICE circuits are also extracted from RTD measurements[130].

As can be inferred from the name, the PWL models linearise the I-V curve and represent it as a combination of straight lines. A current source is used to model the NDR region. While unsuitable for non-linear circuits such as frequency mixers, PWL models find use in digital circuit design.

The other class of SPICE models include diodes in the circuit representation of the RTD, along with Gaussian and exponential functions, to preserve the non-linear behaviour of the resonant-tunnelling diode[131]. It is also possible to use look-up tables, directly based on RTD measurements[123].

2.6.3 Physics Based Equations

Analytically modelling the physical processes behind the resonant-tunnelling diode is a very extensive field. Numerous models exist, each with different approximations and assumptions. This is due to the many elements that need to be accounted for, such as quantum tunnelling effects, operating conditions, material properties[132, 133, 134].

Using these models is more suited to semiconductor physics simulations, and exploring the effect of different structure parameters on the RTD's I-V, than it is for high frequency circuit design and simulation[135, 134]. Physics based equations are, however, the method that provides better fits than the other approaches, though they need slight adjustments to perfectly match individual devices.

The gist of this approach is to solve the Schrödinger and Poisson equations to obtain a self-consistent expressions for the potential and charge distribution across a resonant-tunnelling diode device[126]. However, while solving these equations, convergence problems might arise, due to the presence of an NDR region. It can be shown that the overall shape of an RTD's current density can be expressed via the following equation[132]:

$$J\left(V\right)=\frac{2qm^{*}kT}{\pi^{2}\hbar^{3}}E_{kin}T\left(E\right)\ln\left\{\left[1+\exp\left(\frac{E_F-E_{kin}}{kT}\right)\right]/\right.$$
$$\left.\left[1+\exp\left(\frac{E_F-E_{kin}-qV}{kT}\right)\right]\right\} \tag{2.2}$$

This can be subsequently parametrised as to allow for compensation of approximations and for producing better fits. The symbols used in the above equation are defined in the List of Abbreviations and Symbols.

Overall, using physics based equations is a very computationally intensive method, and is not suitable for direct inclusion in present circuit simulation tools.

2.7 Polynomial Representation

The polynomial representation is the preferred method and the one used in this thesis to capture and represent the non-linear RTD characteristics. It has been used with success by other researchers[136, 137].

This method works by fitting a polynomial of sufficiently high degree to the RTD's current-voltage characteristic. A polynomial can be used to represent either the entirety of the I-V, or just particular parts of it, such as the NDR region. This fit is usually done using a computational package such as Matlab. A custom-made Python script, written by the author, was used in the thesis to produce the polynomial coefficients, the source code of which is included in Appendix B.

Once a suitable polynomial has been found, the next step is include it in a circuit simulator tool. The software package used to design the circuits presented in this thesis is Agilent Advanced Design System (ADS), which natively supports polynomial representation via the so-called Symbolically Defined Devices (SDD). A further discussion of SDDs is given in Chapter 3.

Besides ensuring that the non-linearity is preserved across the entire I-V, the polynomial representation also offers a low-complexity, non-computationally intensive way of including devices with arbitrary I-Vs in a circuit simulator. Another advantage is that it allows for quick and easy manipulation of the I-V, which can be used as a way to emulate changes in the physical parameters of a device, such as size and barrier parameters. Finally, all parasitic elements can be added as discrete elements and tweaked separately.

Chapter 3

Resonant-Tunnelling Diode Sub-Harmonic Mixers

This Chapter presents and discusses the investigative work completed at the University of Leeds into the suitability of RTDs as non-linear elements in sub-harmonic mixers. Initially, the model used to represent the diodes in a circuit simulator is further described and illustrated. Following that, the types of mixer circuits used to test the RTDs are introduced and their peculiarities explained. A thorough description of the design methodology employed rounds off the first half of this Chapter.

The second half consists of a detailed report on the results obtained from simulating different circuits and different diodes. A large parameter space was studied, aiming to identify how the different semiconductor layer composition and device size affect conversion performance. Furthermore, different substrates with different transmission line parameters were used in these simulations, in order to quantify their contribution to the overall mixer performance.

The simulation results presented include 2nd and 4th harmonic mixers at different frequency ranges, and testing several circuit designs. The diodes used for these mixers are the RTDs described in Chapter 2, as well as scaled version of these diodes.

3.1 Resonant-Tunnelling Diode Simulation Approach

The method of representing an RTD in a circuit simulator, used for the work presented in this thesis, was introduced in Chapter 2. It is based on using a polynomial, fit to a measured I-V, with the inclusion of various parasitic elements represented by discrete components, connected either in series or in parallel. An example of such a fit is presented in Fig. 3.1. The graph shows that the fit matches the overall I-V shape very well. The order of the polynomial used to obtain a good fit was varied in such a way as to minimise the sum of squared errors (SSE), and was generally around 30. Despite this, in the NDR region the polynomial may not always extend to the peak and similarly, the valley transition may not be as sharp. This region is generally discontinuous. The other thing that should be noted is that the fit can have sinusoidal-like oscillatory behaviour, as illustrated in Fig. 3.2. This can be explained by the difficulty of fitting a single polynomial to an I-V with sudden transitions. This behaviour was identified early on in the modelling process, and to

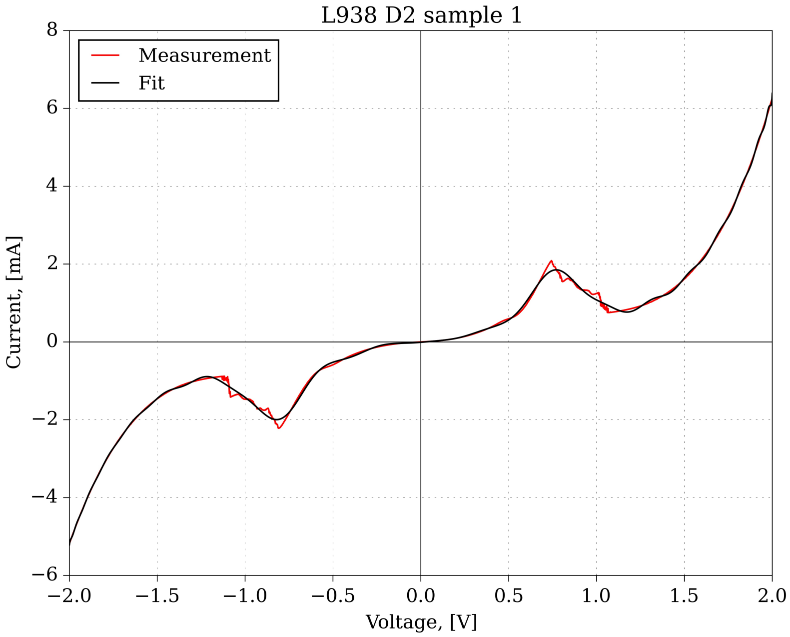

Figure 3.1: A visual comparison between a measured I-V of an RTD with area of $60\mu m^2$ and the polynomial fit to it.

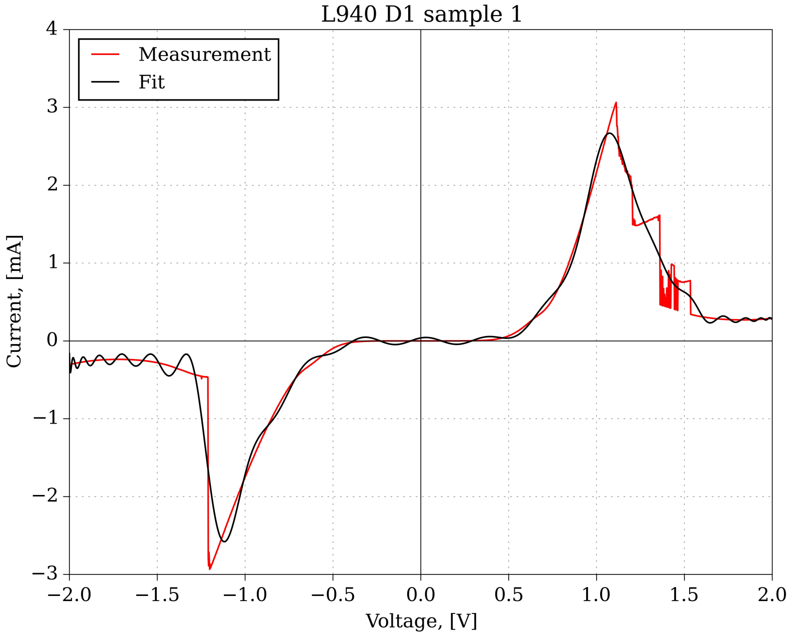

Figure 3.2: A fit exhibiting sinusoidal behaviour as a result of using a polynomial of high degree. The I-V of this particular L940 diode with an area of $30\mu m^2$ was measured at 77 K.

address it, a sectored approach was adopted and used for all diodes tested in this Chapter and Chapter 4. That is, the individual regions of the I-V were extracted and separate polynomials fit to them. This eliminates the sharp transitions between the PDR and NDR regions and results in more stable and linear fits.

After a good fit is found, the coefficients of the polynomial are imported into ADS and an SDD representing a particular diode is created. At this point, additional components such as capacitors, inductors, etc., can be added to better model the real-world behaviour of the diodes. For the purposes of this thesis, a parallel capacitor with value equal to C_{j0} is connected in parallel to the SDD. The final model is shown in Fig. 3.3. The model could be further improved by substituting the static value of the capacitor with one representing the measured C-V characteristic. Unfortunately, we were unable to make such measurements before the end of this project. However given that a typical RTD C-V has the shape shown in Fig. 3.4, it can be argued that using just C_{j0} corresponds to a worst-case scenario, as that

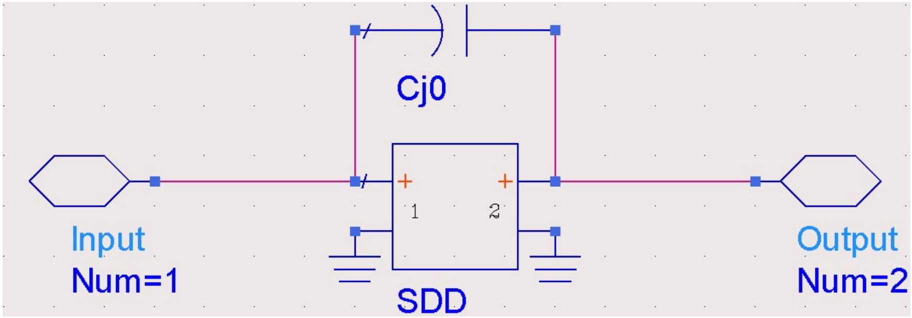

Figure 3.3: Model used to represent RTDs in ADS. Consists of an SDD for the I-V of the device and a parallel capacitor for C_{j0}.

is the value at 0 V, and the capacitance decreases steadily until the NDR region is reached. Another way to improve this model would be to take S-parameter measurements of the RTD at higher frequencies and use those. At the time of writing, work was under way to do that.

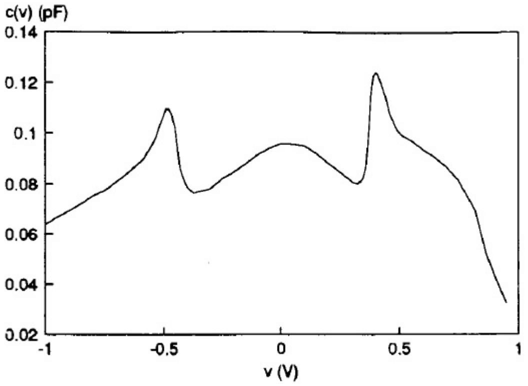

Figure 3.4: A typical shape of an RTD's capacitance-voltage characteristic, in this case of a device with an area of $50\mu m^2$[138].

The polynomial fit approach has been successfully used to model devices in the past[137, 139, 140]. One way to check how well this model performs is to use it for a device that already has a built-in model in ADS. Specifically, a simple mixer circuit using commercially available Schottky diodes was simulated and its conversion loss performance recorded. Afterwards, the I-V characteristic of the diode pair is generated using the schematic shown in Fig. 3.5, and a polynomial is fit to it. The built-in model is then replaced in the mixer circuit by an SDD model of the Schottky diode and the conversion loss performance is again simulated. The

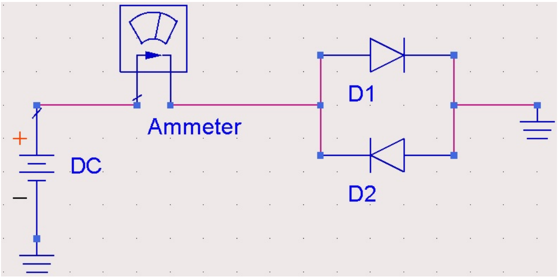

Figure 3.5: ADS circuit used to capture the I-V of an APDP of Schottky diodes.

ADS mixer circuits used for this comparison are presented in Fig. 3.6. A conversion loss comparison between the two methods is shown in Fig. 3.7. This comparison was made for a large range of applied LO power, over which the Schottky APDP transitions from an *off* state to a mixing one, and the full results are shown for completeness. It can be argued that the diode pair is sufficiently pumped by the local oscillator starting at 7 dBm up to about 40 dBm. After that, Agilent ADS reports errors for the built-in model and it can be assumed that the incredibly large LO power, in this case above 40 dBm, drives the diodes beyond the recommended limits for which the model is well-defined. Below 7 dBm, the conversion loss performance of the built-in model quickly deteriorates, as the power supplied is not enough to push the quiescent point into the non-linear region of the APDP's current-voltage characteristic. The comparison graph shows good agreement between the SDD

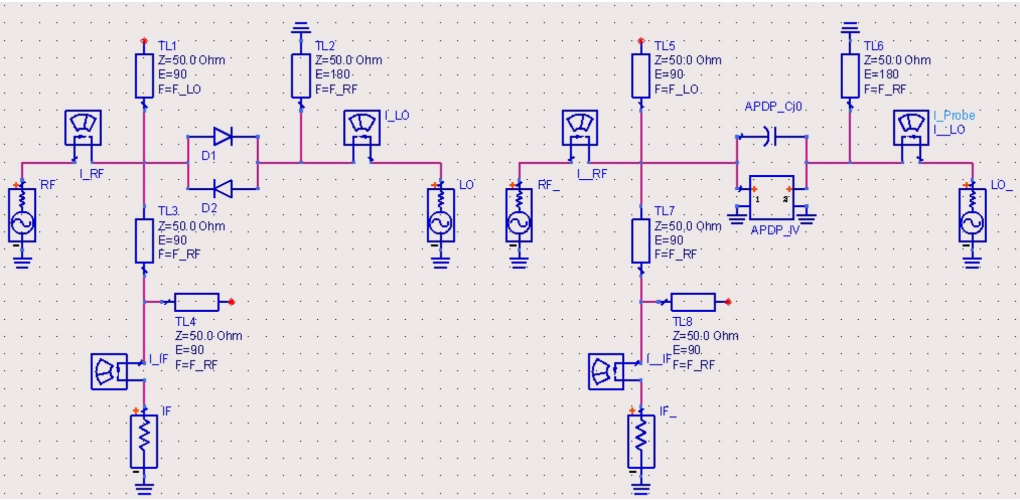

Figure 3.6: ADS circuits used to compare the behaviour of the built-in Schottky diode model (left) and the model using SDD and parallel capacitor (right).

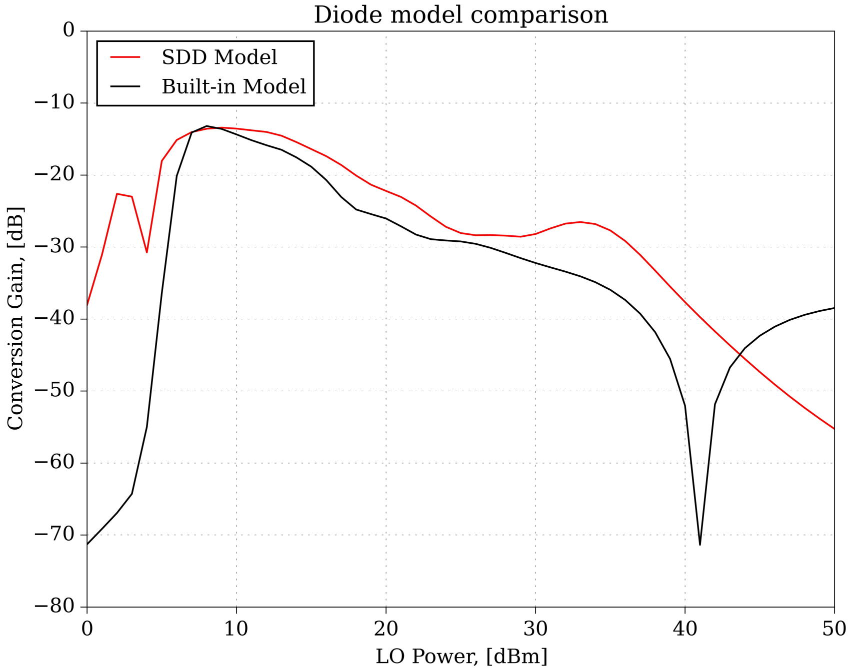

Figure 3.7: A comparison between the conversion loss obtained from using two different diode models and identical mixer circuits.

model and the built-in one over the 7 dBm – 40 dBm power range, where frequency mixing occurs. Above 40 dBm the CL of the SDD steadily decreases as it does not have the same limitations as the Schottky diode model. There is, however a large discrepancy between the two approaches at LO powers below 7 dBm. This can be attributed to the absence of several of the additional elements present in the built-in model equivalent circuit. Furthermore, while the built-in model guarantees zero current through the pair at voltages below the turn-on one, the same cannot be said for the SDD, and this is likely a contributing factor to the difference.

However, none of the measured RTD I-Vs has a large zero current region, meaning that even small applied LO would immediately drive the diode into its non-linear, frequency mixing region, where the SDD model provides sufficient accuracy.

3.2 Sub-Harmonic Mixer Circuit Types

There are multiple ways to implement a circuit for sub-harmonic frequency mixing, though all of them share common core characteristics. For example, it is important to provide virtual grounds for the RF and LO signals in order to improve port-to-port isolation. Additionally, a way to suppress the fundamental mode of the LO is needed.

For the work presented in this thesis two major circuit variants were investigated, a sub-harmonic mixer using the 2nd and the 4th harmonic of the LO generator. Both of them are essentially single-ended mixers in that they use a single diode, featuring two back-to-back junctions. It is possible however, to implement them in a balanced configuration, though in practice this is rarely done due to increased power requirements and circuit complexity.

3.2.1 2nd Sub-Harmonic Mixer Circuits

Circuits using the 2nd harmonic of the LO signal are the most widespread type of sub-harmonic mixer. The most commonly used circuit realising an $n = 2$ SHM was introduced in Chapter 1 (Fig. 1.18) and is expanded upon in Fig. 3.8. Here, an anti-parallel Schottky diode pair is used as a non-linear element to provide frequency mixing. As stated in Chapter 1, it can be demonstrated that currents containing

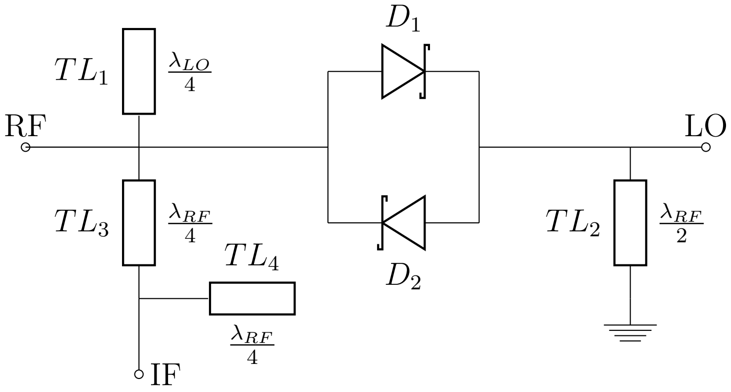

Figure 3.8: The most common circuit implementing an $n = 2$ SHM, using Schottky diodes.

the fundamental or odd harmonics of the LO signal are suppressed by the diode pair and are not present at the IF or RF ports. The two stubs, TL_1 and TL_2 provide terminations for the LO and RF signals respectively. TL_1 presents a short circuit at the LO frequency, while acting as an open at the RF one, due to $f_{RF} \cong 2f_{LO}$. Similarly, TL_2 presents a short to the RF signal, while the LO signal sees it as an open circuit. Finally, the two $\frac{\lambda_{RF}}{4}$ transmission lines prevent both the RF and LO from leaking to the IF port.

This is the most basic form of an $n = 2$ SHM. Filters and matching circuits can be added to improve their performance, as illustrated by Fig. 1.8.

Another way to implement a sub-harmonic mixer is shown in Fig. 3.9. Here, instead of having a diode pair connected in series to the rest of the circuit, it is connected in parallel[82]. Additional circuitry is added to allow for individual biasing

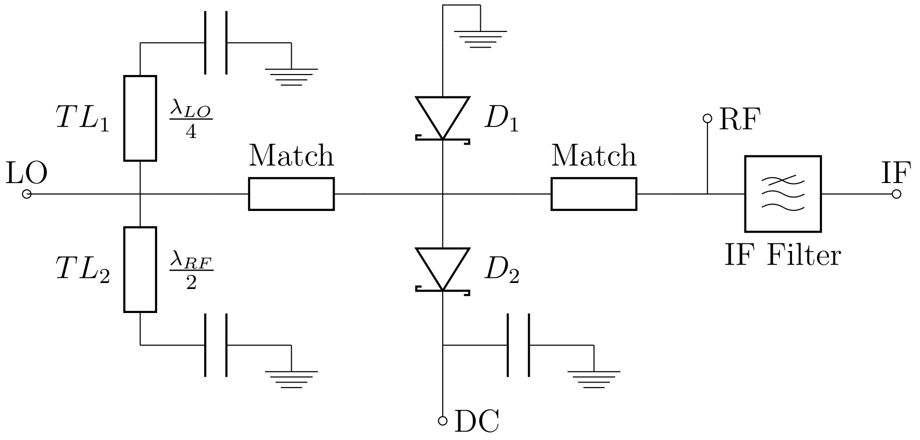

Figure 3.9: Alternative topology for an $n = 2$ SHM, which favours DC biasing of its diodes. Used at higher frequencies and waveguide mixers as a solution to high LO drive requirements.

of the two diodes. This type of circuit is used at sub-millimetre wave frequencies, when the available LO power is insufficient to drive the diodes into their non-linear region and applying DC bias helps address this. Unfortunately, this leads to increase in the noise generated by the diodes, and thus a trade-off needs to be made.

3.2.2 4^{th} Sub-Harmonic Mixer Circuits

The $n = 4$ SHM, as the name implies, uses the 4^{th} harmonic of the LO signal. A typical circuit[71, 62] implementing such a mixer is presented in Fig. 3.10. The only differences are the addition of TL_5, which provides port termination for the $2f_{LO}$ component, and the change of TL_2 from $\frac{\lambda_{RF}}{2}$ to λ_{RF}. This particular type of mixer is used when the RF signal is at such a high frequency that LO generators either do not exist or cannot provide adequate power for an $n = 2$ sub-harmonic mixer.

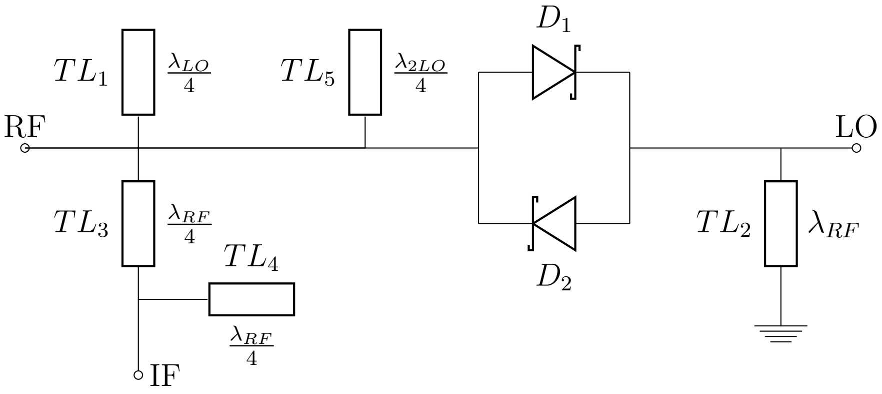

Figure 3.10: The most common circuit implementing an $n = 4$ SHM, using Schottky diodes.

3.3 Design Methodology

The methodology employed follows a somewhat standard work flow, that is widely used in both academia and industry to design sub-harmonic mixer circuits[63, 73, 78, 86]. There are several steps, and the design process itself is an iterative one. A brief description of each stage, together with illustrating figures is presented next.

Diode selection

Diode selection is a major part of the design procedure, and is usually the starting point. Different diodes are rated by manufacturers for use at different frequency ranges. They key parameters that determine what frequency bands a particular diode or an anti-parallel diode pair are suitable for, are the junction capacitance C_{j0} and the series resistance R_s.

The RTDs fabricated at the University of Leeds were designed with the goal of operating at the millimetre-wave frequency range, however they were also tested at both lower and higher frequencies. These diodes have the smallest area that could be produced at the time without the use of Electron-beam Lithography (EBL).

LO power level

The performance of a diode as a non-linear element providing frequency mixing is heavily dependent on the amount of LO power supplied. Other metrics of the mixers, such as port impedances, are also a function of the LO power. There is usually an optimal amount of LO power needed for good performance. Too little would mean that the quiescent point does not reach the non-linear *knee* of a diode's I-V, and too much would result in the point overshooting.

In the case of RTDs, the optimal LO power level was not known *a priori*, so simulations were run over a large range of LO powers. However, once a certain power level has been found to provide good initial mixing performance, the impedances that the diode or diode pair presents at all three frequencies, RF, LO, and IF; can be determined, and matching circuits designed, if needed.

Matching circuits

The inclusion of matching networks improves performance by increasing the amount of RF power delivered to the diode, and thereby decreasing conversion loss. Often a few iterations are needed before the desired level of VSWR is reached. It may not always be possible to achieve good match at all ports for all frequencies. In such cases, the match at the RF port for the RF signal is given priority. It should also be noted that the inclusion of port termination stubs in sub-harmonic mixers affects the impedances to which the networks should match. Therefore, matching circuits are usually placed after any filters but before port termination stubs.

Various circuit topologies can be used to implement matching networks. Two-stub networks, such as the one shown in Fig. 3.11 are the most widely used[52]. The choice of whether to use a short or an open for the stub TL_2 is generally determined by the type of planar technology used, e.g. short circuits are easier to implement in coplanar waveguide, but open circuits are more straightforward in microstrip. Generally, matching networks are narrowband structures and can act as a sort of a filter, in the sense that the reflection coefficient is high for signals outside of the frequency for which the matching circuit has been designed. At the frequencies of interest, i.e. W-band and beyond, this is not necessarily a problem, since even a few per cent bandwidth translate to tens of GHz. Another reason is that the types of signals that will be detected are usually also narrowband in their nature, e.g. gas absorption lines, etc.

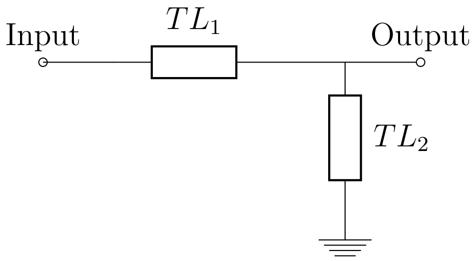

Figure 3.11: A generic schematic of a two stub matching network. TL_2 can be either open or short circuited.

Circuit simulation

The main tool used for mixer design is a circuit simulator package, such as Agilent Advanced Design System (ADS). Initially, circuits are designed and tested using ideal models for any components, be they transmission lines, lumped elements, or others. While ADS has built-in models for Schottky diodes, it lacks one for resonant-tunnelling devices. This necessitates the use of SDDs to represent RTDs. This constitutes the first iteration of a mixer design.

The second iteration replaces the ideal transmission lines with analytical models of the technology that would be used for the final circuit, i.e. microstrip, CPWG[1], etc. Even though the behaviour of these is not perfectly indicative of the expected actual performance, it is a good approximation. At this stage, tuning and optimisation routines can be run to adjust the parameters of the transmission line elements. A comparison between a mixer circuit using ideal transmission lines and analytical model is given in Fig. 3.12.

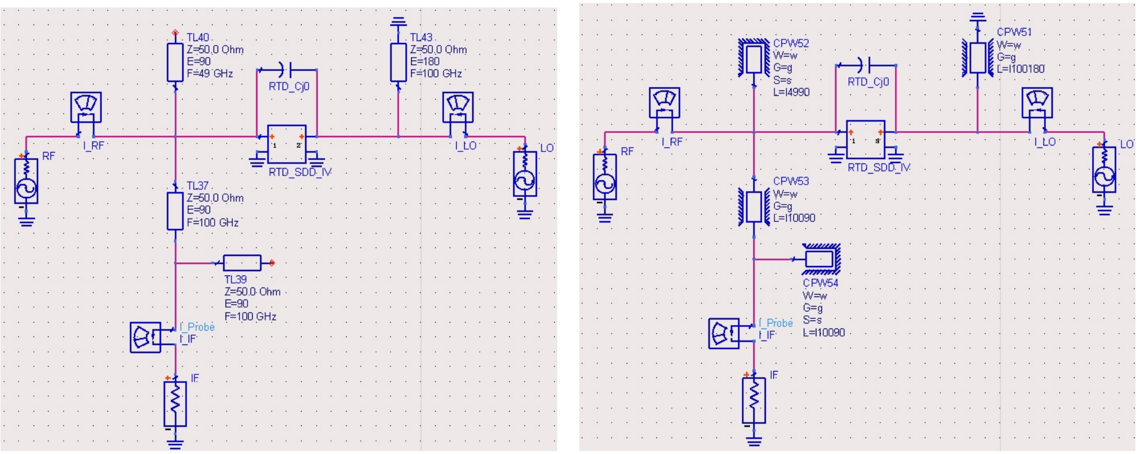

(a) Using ideal transmission lines.

(b) Using CPWG transmission lines.

Figure 3.12: ADS circuits showing the first two stages of mixer design, i.e. using ideal and analytical models of transmission lines.

The next step consists of using a 3D Finite Element Method (FEM) electromagnetic simulator, such as Ansoft's High Frequency Structural Simulator (HFSS), to obtain a more accurate representation of their real world performance. Additional elements, such as air-bridges, are added to CPWG circuits to suppress odd mode propagation and to improve the overall field distribution. An example of an HFSS model of a sub-harmonic mixer circuit is presented in Fig. 3.13. The result of the FEM simulations are files with the computed S-parameters of the structure at specified frequencies. These are imported back in ADS, as shown in Fig. 3.14, for a final simulation pass.

---

[1] Coplanar Waveguide with Ground plane

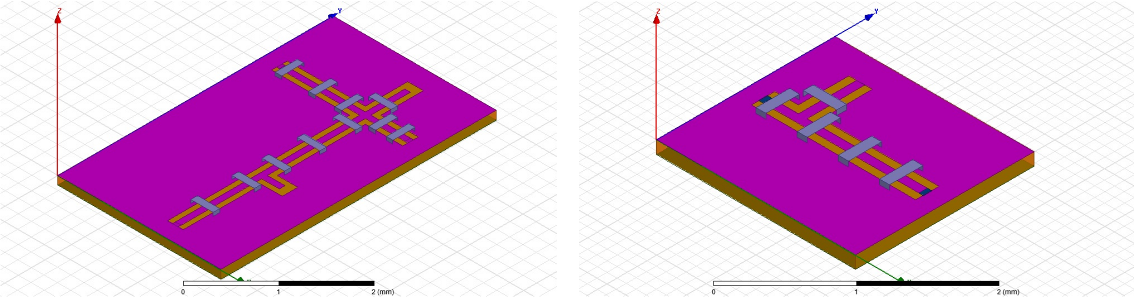

(a) RF port to RTD.

(b) LO port to RTD.

Figure 3.13: Models of SHM circuit halves used in HFSS for 3D FEM simulations.

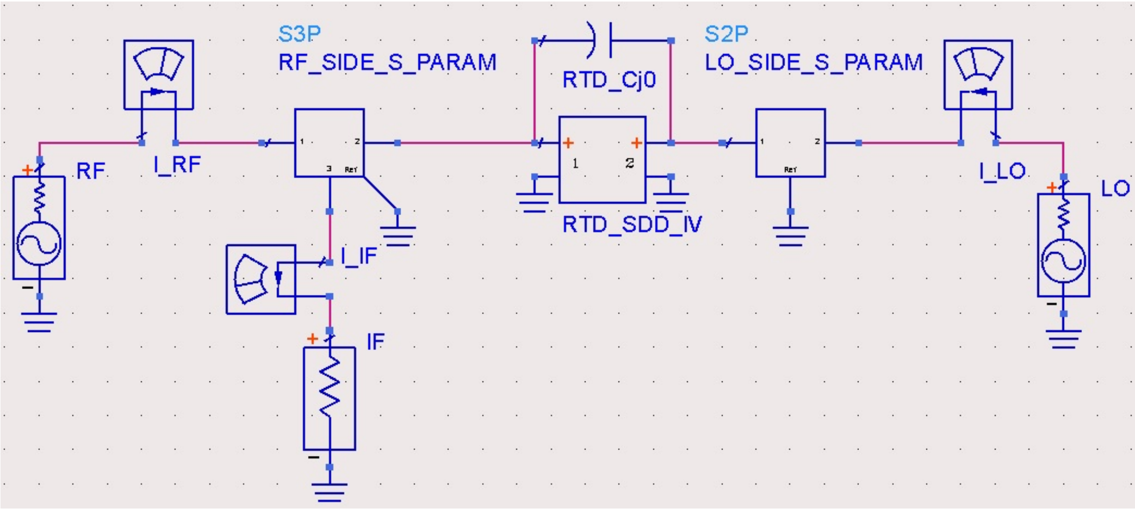

Figure 3.14: Mixer circuit in ADS using S-parameters obtained from HFSS simulations.

Some of the steps described above are iteratively repeated to achieve as good performance as possible. For example, after importing the S-parameter files back into ADS and re-running the circuit simulator, additional tuning of the transmission lines might be required, due to differences such as the ones illustrated in Fig. 3.15. In addition to this, different substrates can and should be tested, as well as different topologies, to ensure that the optimal performance is squeezed out of the non-linear element. This is a time consuming process, although necessary prior to fabrication to minimise differences induced during the realisation of these physical circuits.

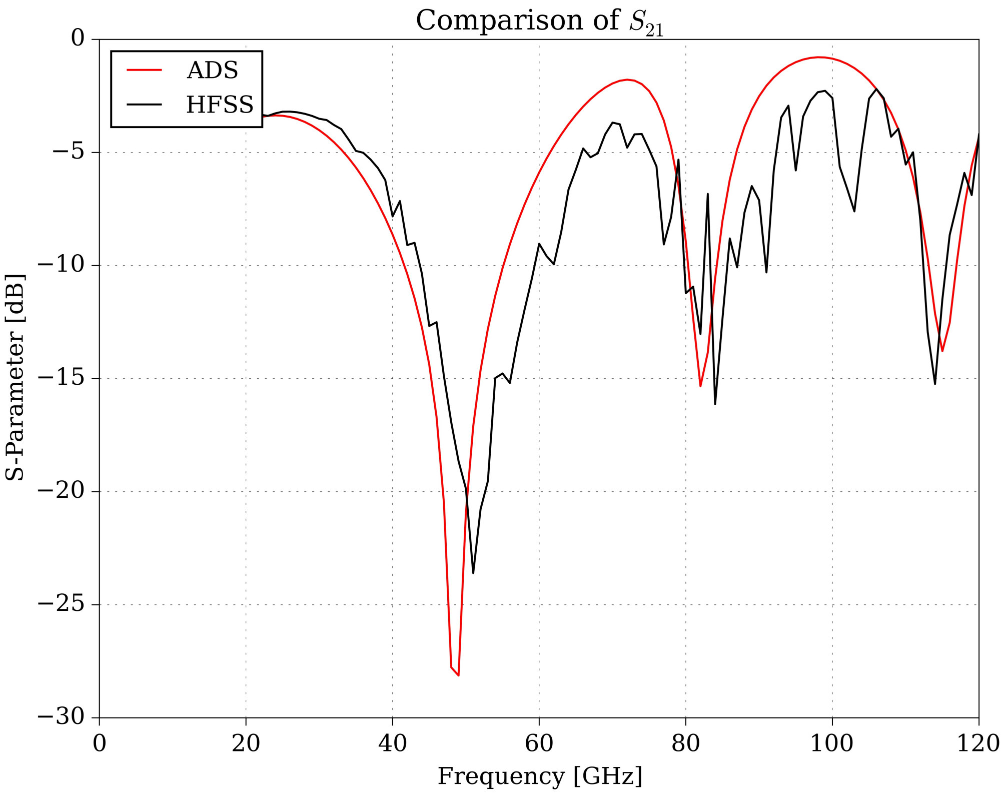

Figure 3.15: A comparison between the results for the S_{21} parameter of the circuit in Fig. 3.13a obtained from Agilent ADS and Ansoft HFSS.

3.4 Designed Circuits

Several different circuits were designed for the purposes of investigating the performance of RTDs as sub-harmonic mixer elements. Both 2$^{\text{nd}}$ and 4$^{\text{th}}$ harmonic SHMs were designed, utilising different planar media technologies on different substrates. Different combinations of RF and LO frequencies were studied for both types of sub-harmonic mixers.

Overall, the mixer designs can be grouped into low frequency ones with RF of 20 GHz, and high frequency ones, with RF of 100 GHz and 424 GHz. Both the 20 GHz and 100 GHz were chosen as a good starting point for future circuit scaling, while receivers at 424 GHz are used by the Met Office to study ice clouds in the Earth's atmosphere[141].

In the beginning, the choice of substrate for these circuits was governed by local availability. Hence, semi-insulating GaAs ($\epsilon_r = 12.9$ up to 40 GHz[142]) was used for the high frequency designs, and Duroid5880 ($\epsilon_r = 2.2$ up to 40 GHz[143]) for the low frequency ones. Duroid5880 was readily available at the University's Electronics Service Workshop as a substrate for RF and microwave circuits, with thickness of $787\mu m$, and GaAs wafers were already being used as host substrates by the MBE team and facilities.

However, simulations of circuits designed for Duroid5880 showed poor expected performance. These results, combined with the realisation that the GaAs wafers available were conducting instead of semi-insulating, led to the selection of alternative set of substrates.

For the low frequency designs, a 254 μm thick Duroid4350B ($\epsilon_r = 3.48$ at 10 GHz[144]) was found to be a good candidate with a combination of good performance and resulting transmission line dimensions suitable for rapid manufacture at the Electronics Service Workshop at the University of Leeds. A different substrate from the same manufacturer, Duroid6010 ($\epsilon_r = 10.2$ up to 40 GHz[145]), with a thickness of 127 μm was used for the high frequency designs, due to the similar performance it offered in comparison to GaAs. Additionally, 100 μm thin quartz, a low-loss substrate with low dielectric constant ($\epsilon_r = 3.8$ up to W-band[146]), was also used as an alternative for the 100 GHz designs. Designs were undertaken for all these alternatives.

Graphs showing a comparison between the S-parameters obtained from Agilent ADS and Ansoft HFSS for all designed mixer circuits are included in Appendix C.

3.4.1 Second Harmonic Mixers

As a first step, mixers with RF of 20 GHz were investigated as initial design, while also allowing for easy scaling for higher frequencies. The circuit topology used in the ADS circuit simulator to initially gauge the diodes' performance was the same as Fig. 3.8, using a single RTD instead of an APDP. However, it was found that the addition of two new stubs, marked TL_{N1} and TL_{N2} in Fig. 3.16, improved the conversion loss by about 6 dB on average. These two stubs achieve this improvement by ensuring that both the RF and LO voltage waveforms are at a maximum across the RTD's terminals.

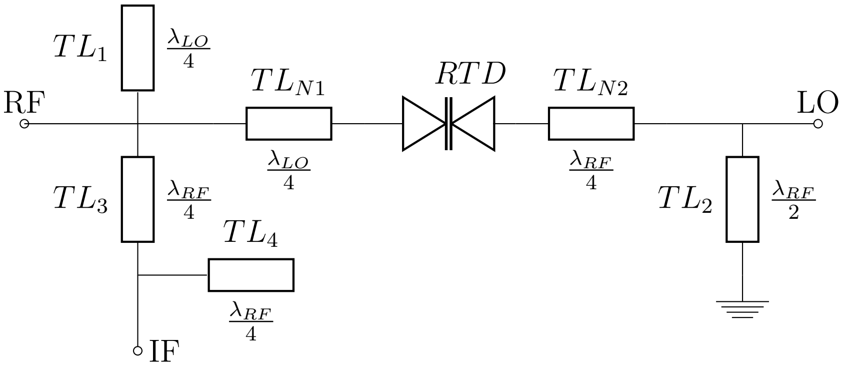

Figure 3.16: A schematic showing the two additional stubs added to the $n = 2$ SHM circuit.

As was previously mentioned, the 20 GHz circuits were designed to be implemented on a 254 μm thick Duroid4350B substrate with an ϵ_r of 3.48. The technology used was CPWG, with microstrip transitions to coaxial SMA connectors. A photograph of one of the fabricated circuits is given in Fig. 3.17. The same additional stubs were also added to the 100 GHz circuits, where their inclusion led to a similar boost in performance.

The 100 GHz 2^{nd} harmonic mixer circuits are the main focus of the investigative work into the suitability of RTDs as an element of a SHM. Two different substrates were used for circuit simulation, Duroid6010 and quartz, with CPWG being the planar transmission line technology of choice. The reasons for this choice are the lower losses offered by the CPWG technology, as well as the easier realisation of short circuit elements[147]. Furthermore, due to the high dielectric constant of Duroid6010, narrower and shorter transmission lines were possible, requiring less substrate space, and providing good containment of the propagating EM field.

Three sub-variants of the Duroid6010 were tested, with the difference being in the width of the central conductor W, the gap between it and the ground planes

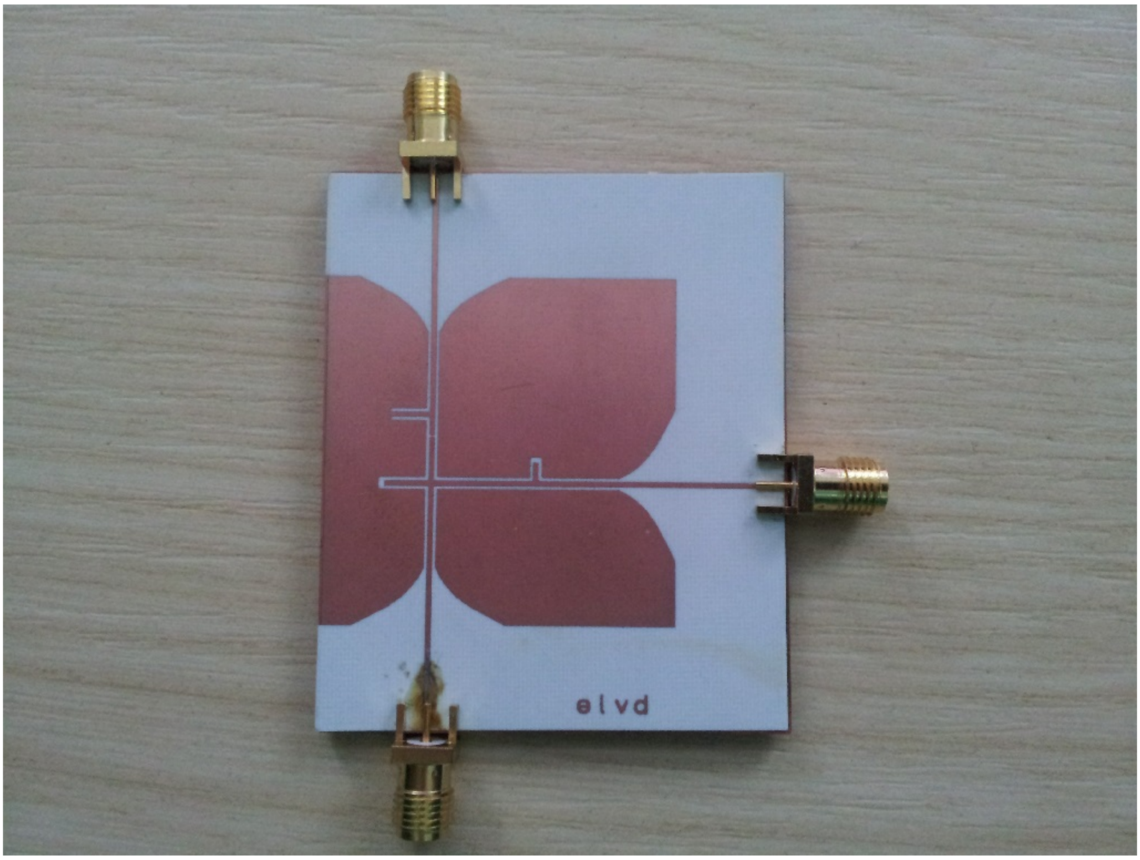

Figure 3.17: An example of a 20 GHz SHM circuit, implemented on Duroid4350B, with SMA connectors.

G, and the thickness of the metal conductor T. While the Duroid substrates come pre-plated with copper, the quartz pieces were metallised in-house with gold. A summary of the different substrate parameters and their designations used later in this Chapter is given in Table 3.1. These parameters were calculated as to produce a 50 Ω transmission line. Care was taken to ensure that the five skin depths rule for conductor thickness was observed. Due to the higher frequencies of operation,

Substrate	Designation	Thickness [μm]	ϵ_r	W [μm]	G [μm]	T [μm]
Quartz	Quartz	100	3.8	170	50	2
Duroid6010	Duroid 1	127	10.2	29	20	5
Duroid6010	Duroid 2	127	10.2	46	25	1
Duroid6010	Duroid 3	127	10.2	75	50	1

Table 3.1: A summary of the substrate and circuit parameters used for 100 GHz $n = 2$ SHMs.

air-bridges had to be added to the 100 GHz SHM circuits to stabilise and improve the EM fields in said circuits.

3.4.2 Fourth Harmonic Mixers

The 4^{th} harmonic mixer circuits designed follow a similar philosophy to the 2^{nd} harmonic ones. Initially, a circuit with an RF of 100 GHz, the same one as the main $n = 2$ discussed previously, was designed in CPWG technology using the Duroid 1 substrate specifications in Table 3.1. The motivation for this design was two-fold. First, to study whether the I-V characteristics of the available RTDs exhibit enough non-linearity to allow for sub-harmonic mixing with the 4^{th} harmonic of the LO signal. The other reason was to attempt to quantify the decrease in conversion performance by comparing an $n = 2$ and $n = 4$ SHM with the same RF input signal.

Following the 100 GHz design, one using ideal transmission lines, operating at an RF of 424 GHz, was used to gain insight into the RTDs' performance at sub-millimetre frequencies, and what modifications to the diodes might be needed to achieve good conversion loss.

While the starting circuit used for these designs was the same as Fig. 3.10, additional stubs, just like the ones in Fig. 3.16, were included here as well.

3.5 Simulation Results

All the available diodes were simulated with all circuit designs, using both S-parameters obtained from Agilent ADS and from simulating the mixer circuits in Ansoft HFSS. The results presented in this Section are comparative ones, illustrating the dependence of conversion loss on device size, semiconductor layer composition, circuit topology and substrate used, and supplied LO power. These comparisons are made for all frequency ranges, mentioned earlier in this Chapter.

The graphs shown here, while not all of the produced ones, give the typical obtained performance and emerged trends. Furthermore, unless explicitly noted otherwise, all graphs are obtained using S-parameters from ADS simulations.

Finally, a note on the limits used in the figures presented should be made. Since one of the primary drivers of this investigative study was to produce SHMs with low power requirements, the supplied LO power in the simulations was swept to a minimum of -20 dBm. As a result, obtained CL performance decreases to values below 40 dB. While in practice such results would not be meaningful, they are kept in the presented graphs to give a fuller picture of the overall CL trends and to better identify the minimum needed LO power for best available performance.

3.5.1 20 GHz

Before embarking on evaluating and comparing the different sized devices from the three layers (L938, L939, and L940), a single circuit topology has to be selected. By using the same circuit and just swapping one diode for another a fair and accurate picture of the overall performance can be achieved.

The SHM circuit that was eventually chosen is the one in Fig. 3.16, as opposed to the more traditional one in Fig. 3.8. The reason for this is the significantly improved performance, as illustrated by the comparison in Fig. 3.18. These graphs

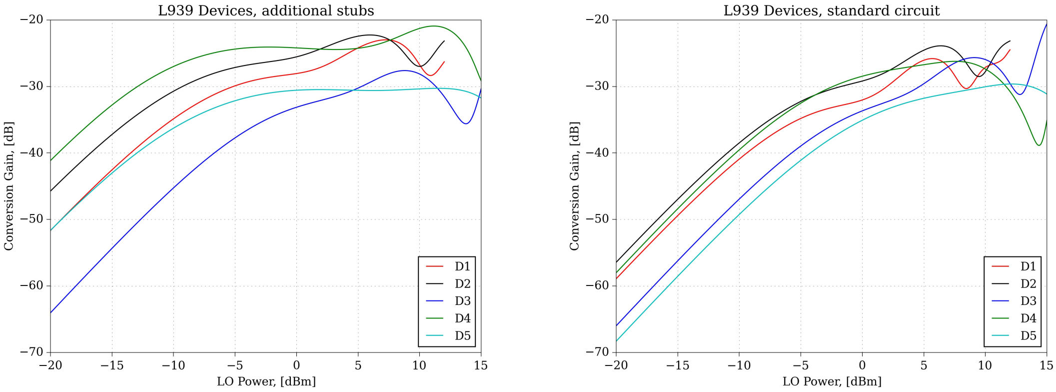

(a) Circuit with additional stubs

(b) Standard circuit

Figure 3.18: A comparison between a circuit with additional stubs vs a regular SHM circuit.

show that the addition of the two new stubs improves the performance of the smaller devices (D1, $30\mu m^2$ – D3, $110\mu m^2$) by about 5 dB at LO powers of 0 dBm or more, and provides an even greater boost in the region of -5 dBm LO to 0 dBm LO. While ample power is available at these microwave frequencies, when designing a SHM for the millimetre and sub-millimetre wave ranges, such an improvement can be quite significant and valuable if carried through to these higher frequencies.

The next step was to examine how devices of the same size, but fabricated from different semiconductor layers, compare to one another. Again, the same circuit was used, however instead of using the analytical transmission line models offered by ADS, S-parameters obtained from HFSS simulations of the mixer circuits were used. The results of this comparison for the smallest and largest devices of all three layers are shown in Fig. 3.19. For the smallest devices, L939 clearly has an advantage over L938/L940, largely due to its higher current density and stronger non-linearity. At the other end of the spectrum, RTDs from all three layers have similar CL performance. This can be explained by the large C_{j0} of these devices, and losses there are the determining factors. Larger diodes, however, allow for higher LO pump power, bringing L938/L940 D5 devices to the same CL as an L939 D1. It should also be noted that L938/L940 diodes perform almost identically, which

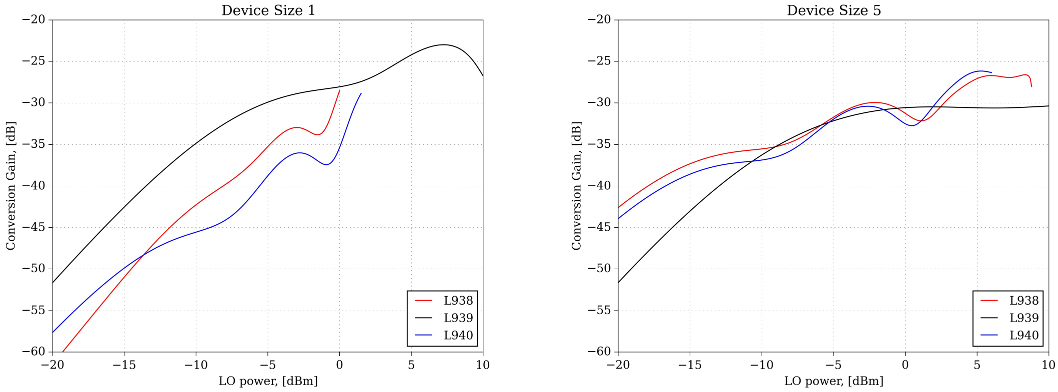

(a) Device Size 1, area of $30\mu m^2$ (b) Device Size 5, area of $450\mu m^2$

Figure 3.19: Performance comparison between same size devices from different semiconductor layers.

is to be expected given that their layer compositions are the same. This is good confirmation that designs based on RTD layers can be highly reproducible.

The final stage of the preliminary investigation at 20 GHz is to evaluate the effect of using S-parameters obtained from HFSS. As explained in Section 3.3, employing a 3D FEM simulator provides a more accurate estimation of expected real-world behaviour, due to solving Maxwell's equations in the entirety of the circuit structure. This allows the simulator to capture phenomena such as odd mode propagation, metal losses, etc. As a result, some degradation in performance is expected, as ideal representations of transmission lines will no longer be used.

A comparison between using a SHM circuit simulated in ADS and one in HFSS for two different sized L939 devices is given in Fig. 3.20. As may be expected, there is a degradation of the CL performance, of up to 5 dB in this case, when HFSS results are used. This could be partially mitigated by better selection of substrate and planar transmission line parameters, coupled with optimisation in HFSS. Unfortunately, this is a very time-consuming process and is usually undertaken as a last design step. Nevertheless, it illustrates the merit of using HFSS where appropriate.

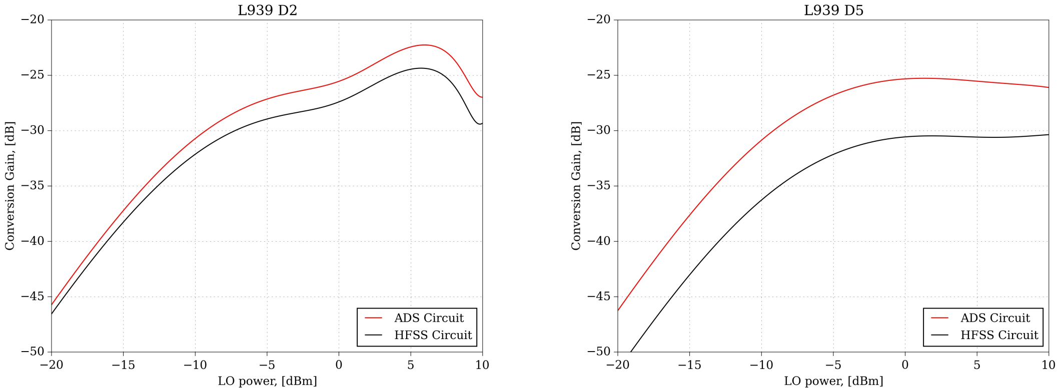

(a) L939 D2, area of $60\mu m^2$ (b) L939 D5, area of $450\mu m^2$

Figure 3.20: An illustration of the effect of using S-parameters obtained from HFSS.

3.5.2 100 GHz, n=2

As previously stated, the $n = 2$ SHM circuits operating with an RF of 100 GHz and an LO of 49 GHz form the majority of design work carried out for this thesis. As such, a more extensive comparative study was conducted, also partly due to the increased design space as a result of testing multiple different circuits on two different substrates.

The first round of comparisons is to check which of the investigated circuits and substrates offer the best performance. In Fig. 3.21 and Fig. 3.22 the results of simulating the smallest and largest device from L939 with both ADS and HFSS circuits for all substrates are presented. While the difference in peak performance between D1 ($30\mu m^2$) and D5 ($450\mu m^2$) is small, i.e. around 2 dB, the largest devices achieve that with about 5 dBm less LO power at the LO frequency of 49 GHz. Continuing the trend from the 20 GHz mixers, there is a 5 dB deterioration in the performance of circuits implemented in Duroid6010 when using HFSS S-parameters, with Duroid 2 seemingly offering the best performance. Further investigation of the mixers using HFSS obtained S-parameters, revealed that Duroid 2 consistently performed best. Looking at the S-parameter comparison graphs in Section C.2, a conclusion can be made that despite the higher expected losses for Duroid 2 due to

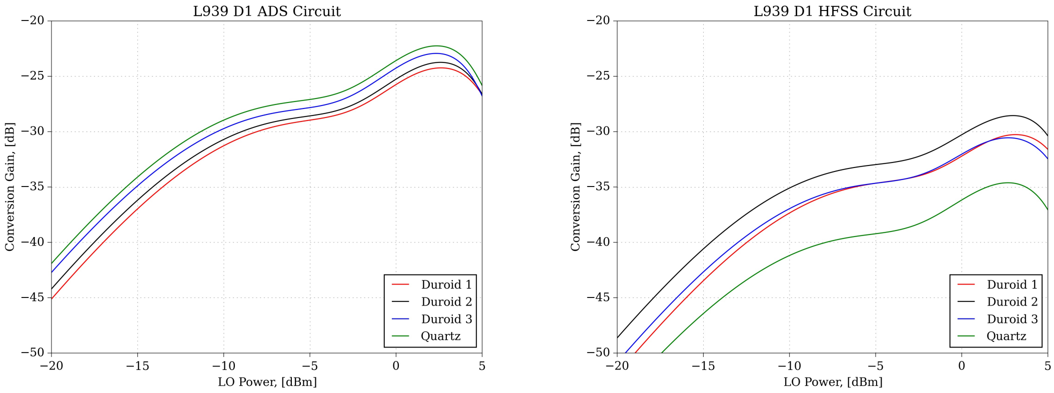

(a) ADS S-parameters (b) HFSS S-parameters

Figure 3.21: L939 Device Size 1 ($30\mu m^2$) conversion loss performance, showing effect of HFSS S-parameters.

its higher aspect ratio[148, 149], the EM field is more stable, in addition to close agreement between the ADS and HFSS simulations for that substrate variant.

There is a much bigger drop for the quartz-based circuits, on the order of 12 dB – 15 dB. Looking at the S-parameters of the quartz mixer circuit, given in Section C.2, it can be argued that a slotline mode propagating in the channels between the central conductor and the adjacent ground planes is responsible for the behaviour of the circuit at 100 GHz. Attempts to rectify that via the use of air-bridges were unsuccessful.

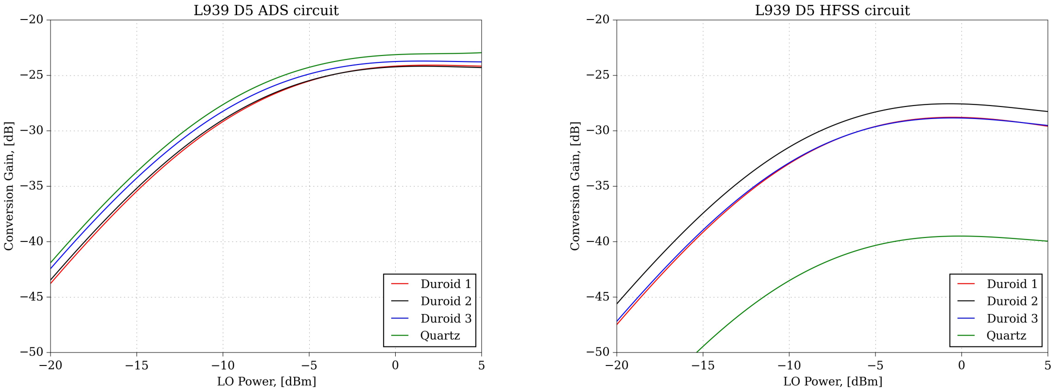

(a) ADS S-parameters (b) HFSS S-parameters

Figure 3.22: L939 Device Size 5 ($450\mu m^2$) conversion loss performance, showing effect of HFSS S-parameters.

An overall encouraging result, however, is the fact that the conversion loss performance peaks at between -3 dBm and 3 dBm LO power, which at the frequency in this case, 49 GHz, should be manageable to obtain.

The next point of interest is the effect of device size on CL performance. Results for mixers using L938 and L940 devices are presented in Fig. 3.23. The comparison is shown for circuits implemented on Duroid 2 substrate. Looking at these graphs, it is evident that diodes from these two layers exhibit similar general behaviour, which is in line with expectations and results reported so far. Performance appears to be proportional to device area at LO powers less than 0 dBm, with diodes with largest area (D5, $450\mu m^2$) having up to 10 dB better CL than those with smallest

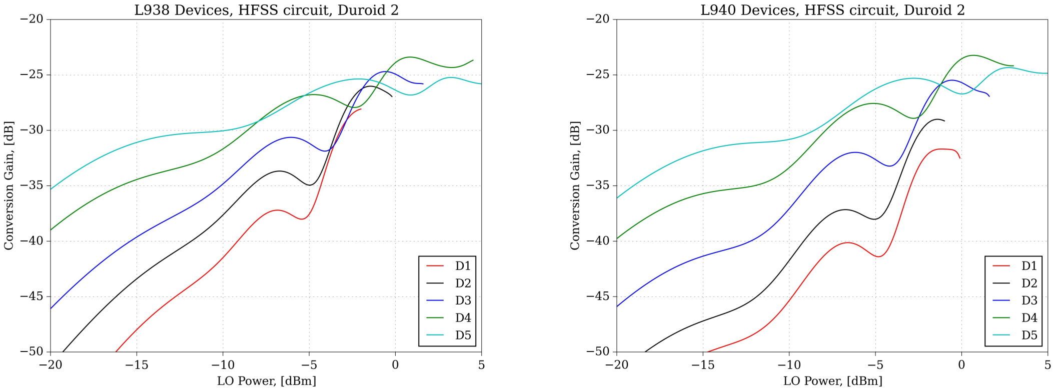

(a) L938, Duroid 2

(b) L940, Duroid 2

Figure 3.23: Effect of device size on conversion loss performance. Two different layers on same substrate.

area (D1, $30\mu m^2$. However, in the region of 0 dBm – 3 dBm, device size 4 with area $225\mu m^2$ offers the best CL by a factor of roughly 4 dB, while still operating at the same combination of RF frequency (100 GHz) and LO frequency (49 GHz).

The same sort of comparison, this time for L939 devices, is shown in Fig. 3.24. Here there is also a secondary contrast between circuits on Duroid 2 and Duroid 3, further illustrating Duroid 2's slightly better performance. Due to the L939's devices having their first PDR region over a larger voltage range, it was possible to drive the SHMs using them with higher LO, up to 10 dBm in this case. Here again,

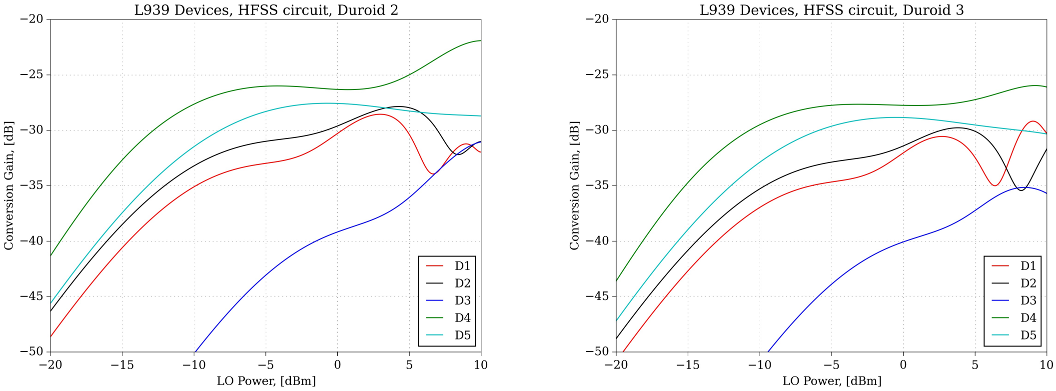

(a) Duroid 2

(b) Duroid 3

Figure 3.24: Effect of substrate parameters on L939 devices' conversion loss performance.

mixer circuits using device size 4 perform the best, with a similar margin of 3 dB.

Compared to L938 and L940 diodes however, L939 reach peak performance at lower LO powers, -5 dBm as opposed to 0 dBm. Increasing the LO pump level to 10 dBm leads to a further 2 dB improvement in peak CL in the case of L939 D4 on Duroid 2, when compared to L938/L940 D4 diodes. Notably, simulations of device size 3 ($110\mu m^2$) of L939 suggest exceptionally poor performance and does not follow the same trend as L938 and L940. One reason for this could be the less linear I-V those devices have.

Finally, the difference in performance in same sized devices from different layers is investigated. A comparison for the smallest devices, using circuits on Duroid 1 and Duroid 2 substrates, is shown in Fig. 3.25. The Duroid 2 circuits outperform the Duroid 1 by comparable margin as they do the Duroid 3 ones. Here it is evident that the small differences in the I-V of the L938 and L940 devices play a more important role at this high frequency of operation, leading to about 3 dB – 4 dB difference in their conversion losses. Overall shape of CL is however the same. Furthermore, the L939 diode offers the same peak performance as the L938 one, albeit at a higher applied LO power. This can be explained by decreased non-linearity of the L939's I-V with higher voltages.

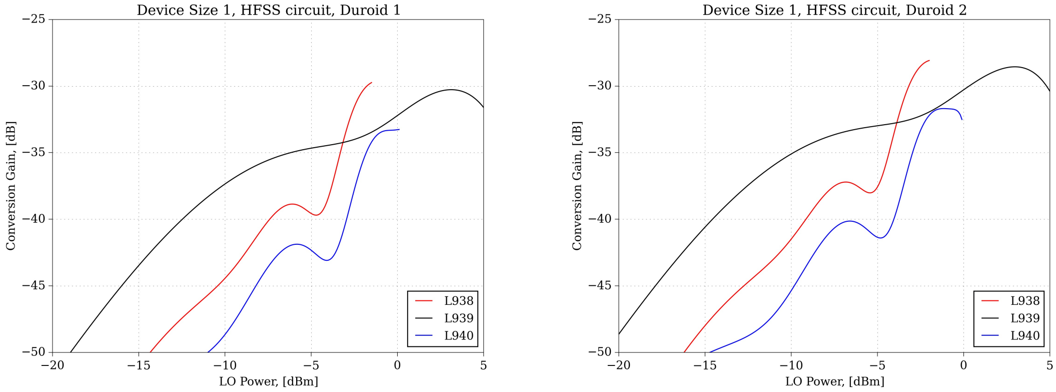

(a) Duroid 1

(b) Duroid 2

Figure 3.25: Performance comparison between smallest ($30\mu m^2$) devices from the three different layers.

Another layer comparison, this time for the device size 4 ($225\mu m^2$) on Duroid

2 and Duroid 3 substrates, is given in Fig. 3.26. The differences between L938 and L940 are not as pronounced here, with both layers having same best CL. The RTD fabricated from L939 outperforms them only at LO powers above 5 dBm and between -5 dBm and 0 dBm, by no more than 4 dB in each case.

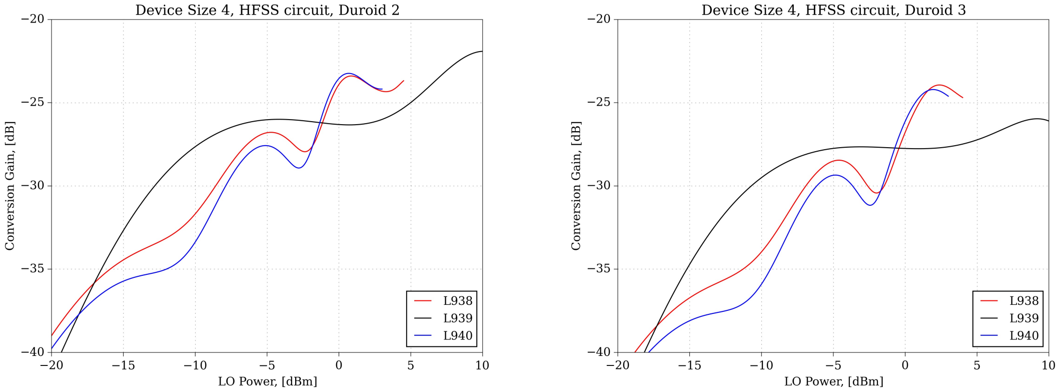

(a) Duroid 2

(b) Duroid 3

Figure 3.26: Performance comparison between largest devices from the three different layers.

Intermediate Conclusions

The results obtained for the 100 GHz $n = 2$ mixers, presented and discussed so far, form a good starting point for future investigation and evaluation of RTDs. Patterns have emerged, mainly the observed best performance by device size 4 and the circuits implemented on Duroid 2 substrate, as well as the unexpectedly poor results offered by the circuits on quartz substrate.

As was stated, it is believed that a slotline mode is excited and propagated in the channels between the centre conductor and the ground planes. Further HFSS simulations revealed that this is the case. A circuit with different parameters might take better advantage by the low dielectric losses usually associated with this substrate.

3.5.3 100 GHz, n=4

A 4th harmonic mixer with an RF of 100 GHz and an LO of 24 GHz was designed and investigated as a precursor to an $n = 4$ SHM operating with an RF of 424 GHz and an LO of 100 GHz. Since the RF was chosen to be the same as the $n = 2$ SHMs previously discussed, a direct comparison between the two can be made, in order to evaluate the effect of using a higher harmonic on the conversion loss performance. To aid this, an $n = 4$ CPWG circuit was designed, using the Duroid 1 parameters.

In a similar vein to the 2nd harmonic circuits, the addition of two $\frac{\lambda}{4}$ stubs on either side of the RTD led to a decrease of conversion loss. The comparison between the two circuits is given in Fig. 3.27 for L939 diodes. While the performance of D1 and D2 at higher LO powers is not significantly affected, all the other device sizes show substantial improvement when the stubs are added, e.g. CL at LO between 0 dBm and 5 dBm is decreased by up to 20 dB.

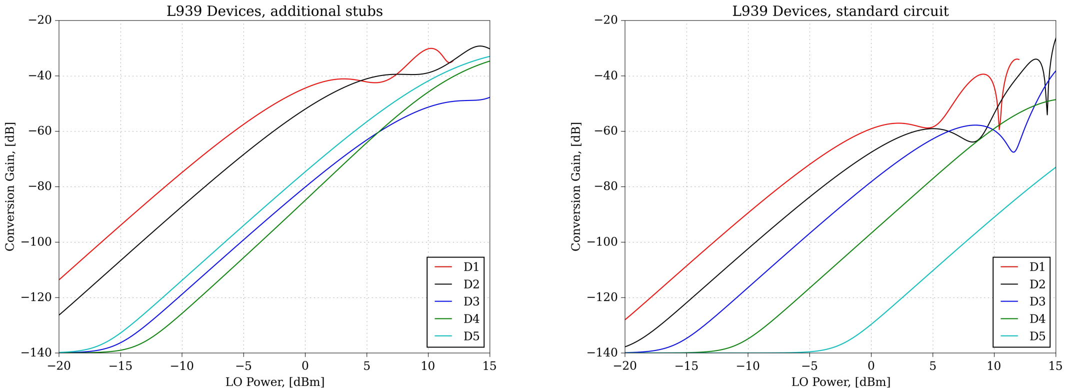

(a) Circuit with additional stubs

(b) Standard circuit

Figure 3.27: A comparison between a circuit with additional stubs vs a regular $n = 4$ SHM circuit.

Previously, it was demonstrated that device size 4 offers the best CL for all device layers for the $n = 2$ 100 GHz mixer. Graphs showing a comparison between the different diode sizes for L938 and L939 are shown in Fig. 3.28. L940 is not included for brevity, as results obtained from those devices closely match L938 ones. It can be seen that the same is true for $n = 4$ 100 GHz SHM circuits, with D4

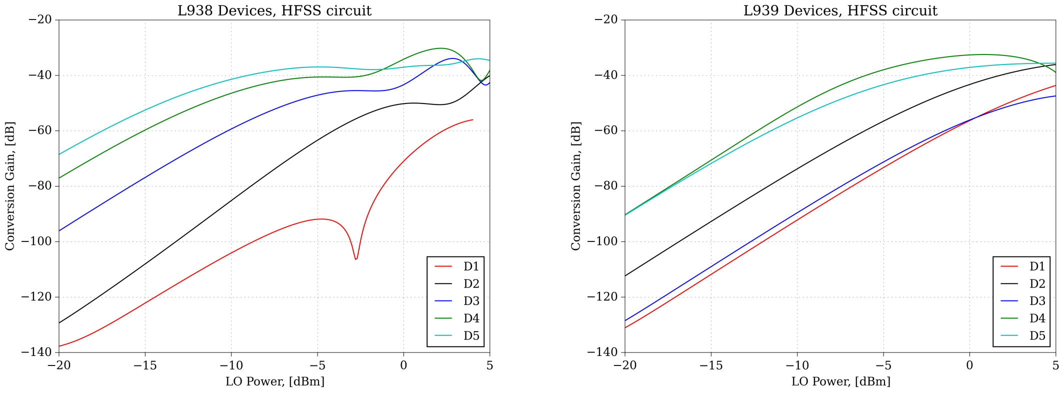

(a) L938

(b) L939

Figure 3.28: Effect of device size on conversion loss performance. Two different layers on same substrate.

from both layers exhibiting best CL, though at slightly higher LO powers than their $n = 2$ counterparts.

As opposed to the $n = 2$ 20 GHz and 100 GHz circuits, here the effect of semiconductor layer composition is not as pronounced, as evidenced by Fig. 3.29. This is likely due to the non-linearity of the I-V being the determining factor, with larger current density playing a smaller role. Similarly to the 2nd harmonic circuits, L939 devices reach peak performance at lower applied LO than L938/L940.

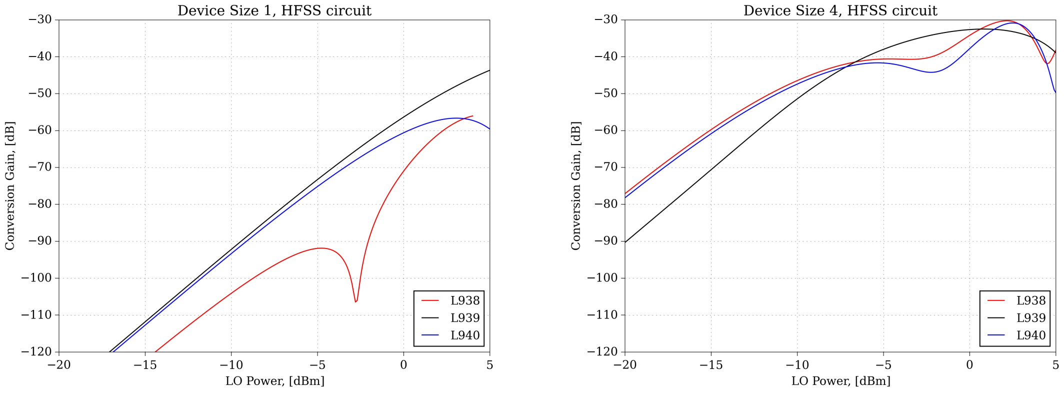

(a) Device Size 1, area of $30\mu m^2$)

(b) Device Size 4, area of $225\mu m^2$)

Figure 3.29: Conversion loss performance of two device sizes for all three layers.

Finally, the difference in using the 2nd and 4th harmonic is explored by comparing circuits implemented on the same substrate, and with the same RTD device. The result of this comparison, for D4 devices from L938 and L939 layers, is shown in Fig. 3.30. The graphs show that at sufficiently high LO power levels, the CL increase is on the order of 10 dB. Performance also deteriorates faster for the 4th harmonic mixers.

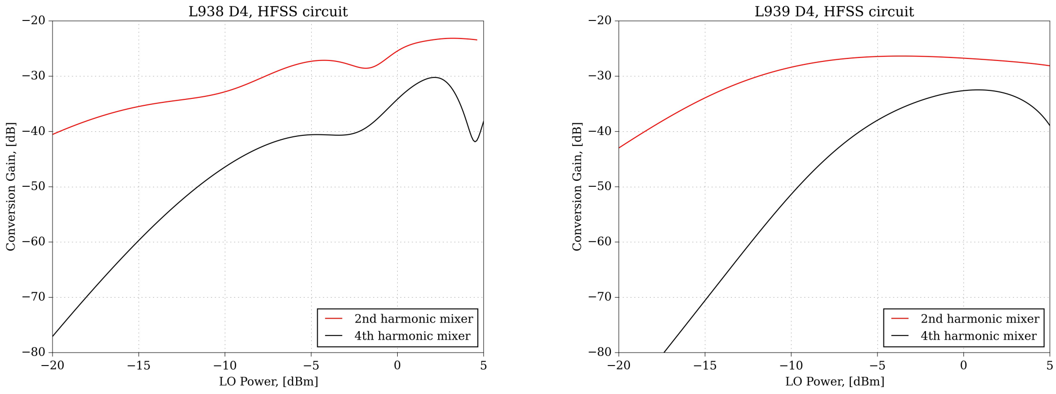

(a) L938 D4

(b) L939 D4

Figure 3.30: A comparison between $n = 2$ and $n = 4$ mixer circuits, using same size devices, size 4 ($225\mu m^2$), from two different layers.

These results show that it is feasible to design and make $n = 4$ SHMs using RTDs, although the increase in their exhibited conversion loss would require some mitigation via signal amplification.

3.5.4 424 GHz, n=4

One application of sub-millimetre waves is in the fields of atmospheric science and meteorology. In order to study whether RTD devices can be a viable candidate for receivers at 424 GHz, an $n = 4$ SHM, using the schematic in Fig. 3.10, with ideal transmission lines was investigated with the current crop of diodes. Therefore, the results presented are considered an optimistic best-case scenario. In practice, such a circuit would need to be implemented in waveguide technology, using finline transitions. These are further discussed in Chapter 5.

Following the same reporting order as the 100 GHz mixers, CL comparisons for L938 and L939 devices of all five sizes are presented in Fig. 3.31. These results

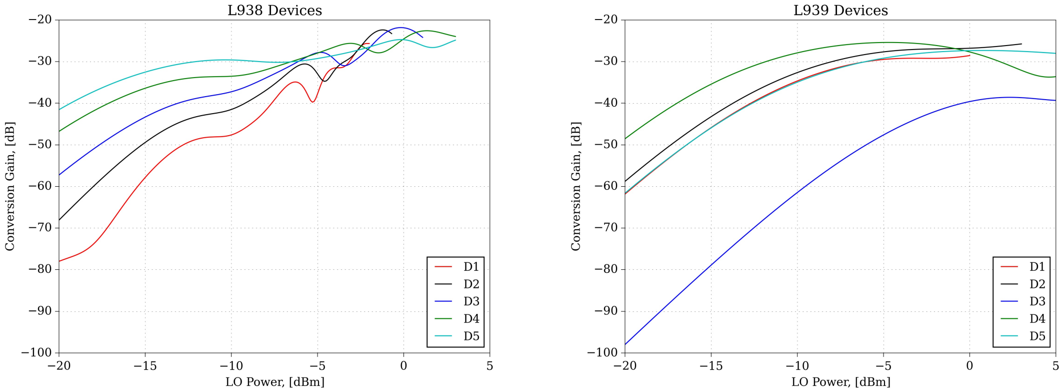

(a) L938 Devices

(b) L939 Devices

Figure 3.31: Conversion loss performance of different size devices for L938 and L939 layers.

somewhat echo those for previously discussed designs. Best achieved performance is by L938 D3 (0 dBm LO) and L939 D4 (-5 dBm LO). Although L938 D3 outperforms L939 D4 by a few dB, given that the LO frequency is 100 GHz, the L939 diode might still be the better choice due to the lower power requirement.

A direct layer effect comparison for device sizes 2 and 4 is given in Fig. 3.32. Continuing the trend for size 4 devices, L939 exhibits peak performance at lower LO

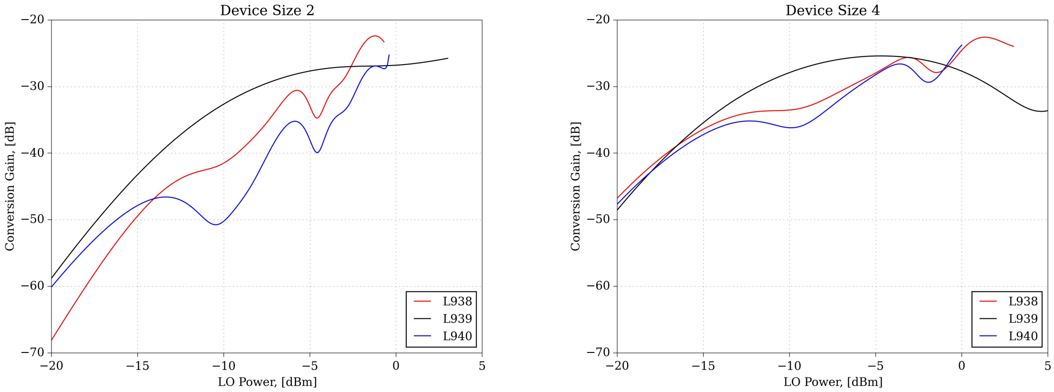

(a) Device Size 2, area of $60\mu m^2$

(b) Device Size 4, area of $225\mu m^2$

Figure 3.32: Layer comparison for two different device sizes.

power than L938/L940, which in turn offer better CL by about 3 dB. An interesting result is that there is little difference in peak CL obtained by size 2 and size 4 devices. This can be explained by the really high frequency of operation, where performance is limited by the large C_{j0} of the diodes.

Intermediate Conclusions

Mixers using the 4th harmonic of the LO could feasibly be realised using RTDs. The currently available ones could potentially operate at 100 GHz, although they would need assistance from an amplifier to address the 10 dB of expected CL degradation.

The results for the 424 GHz one are also encouraging, however they are for an ideal scenario with ideal transmission lines. Diodes with smaller capacitance, higher current density and non-linearity in their I-V characteristics would certainly be needed when the transition to real-world transmission lines is made.

3.5.5 Scaled Diodes

The results obtained from simulating the sub-harmonic RTD mixers at both 20 GHz and 100 GHz, while good and promising, point to the conclusion that the currently available devices, while having sufficient current density, might have too large C_{j0} to provide optimum performance at sub-millimetre wave frequency range.

Ideally, devices with same or similar current density, but smaller capacitance, would be used at these higher frequencies. One way to emulate these smaller diodes without the expense of growing new layers and fabricating them first is to numerically alter both the I-V and the C_{j0}. To do so, custom scripts were written in Python. The source code for these is printed in Appendix B. Using these scripts, it was possible to imitate both the effect of scaling the active area of the current RTDs by altering both their I-V and C_{j0}; and using different material system, via preserving the current density and changing just the junction capacitance. The results obtained from using these scaled devices are presented next.

The main circuits of interest where the effect of scaling was investigated are the 2nd harmonic 100 GHz one and the 4th harmonic 424 GHz one. For the 100 GHz SHM circuit, the comparison in performance of smallest and largest L938 diodes is given in Fig. 3.33. When both the I-V and the C_{j0} are scaled by the same factor of

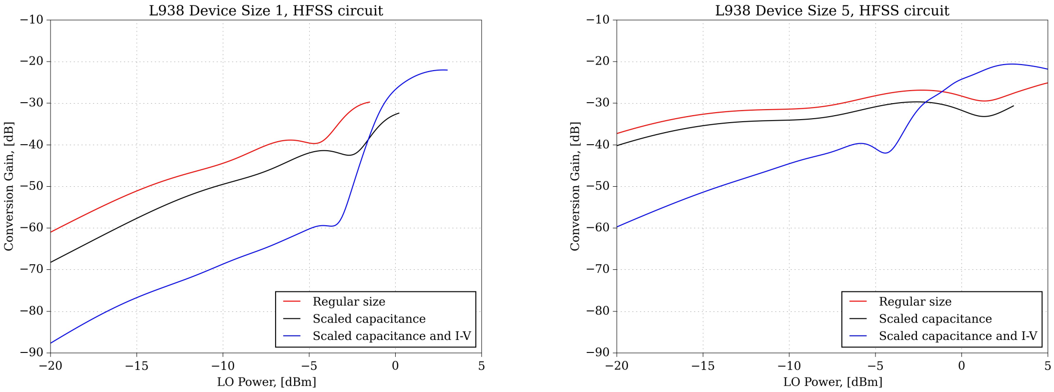

(a) L938 D1 ($30\mu m^2$)

(b) L938 D5 ($450\mu m^2$)

Figure 3.33: Effect of scaling on L938 devices, 100 GHz $n = 2$ SHM circuits.

10, in effect representing a device 10 times smaller, there is a marked improvement of 10 dB in the CL performance for both D1 and D5. At the same time, the LO power at which the peak performance is achieved has increased from 0 dBm to 3 dBm.

A similar increase, of about 10 dB, is also observed in the scaled L938 and L940 devices used in the $n = 4$ 424 GHz mixer circuit, as shown by Fig. 3.34[2].

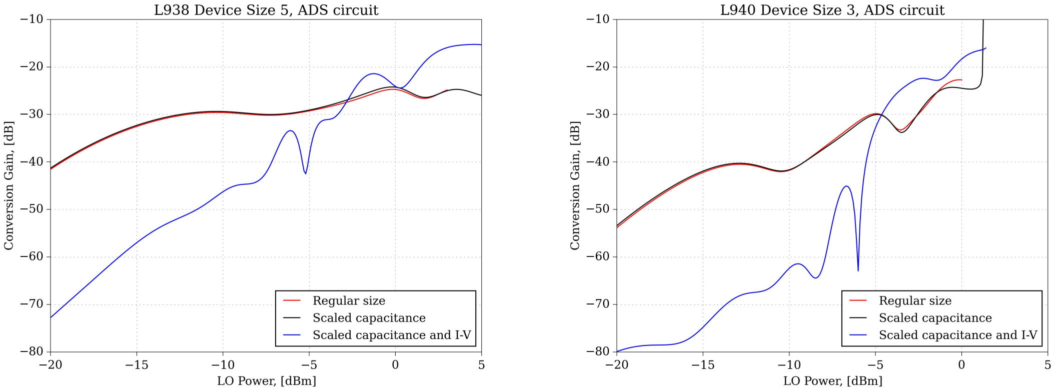

(a) L938 D5 ($450\mu m^2$)

(b) L940 D3 ($110\mu m^2$)

Figure 3.34: Effect of scaling on L938 and L940 diodes, 424 GHz $n = 4$ SHM circuit.

---

[2] The sudden spike in CL to -10 dB is a data processing artefact and not actual result

3.5.6 Summary

There are several conclusions that can be drawn from the results presented in this Chapter about the potential performance of the currently available RTDs at the University of Leeds, and their applicability to sub-harmonic mixer circuits.

Firstly, the similarity in performance obtained across different frequency ranges for L938 and L940 devices meets the expectations due to the same semiconductor layer structure that these devices have.

Next, devices fabricated from L939, the layer with AlAs barriers and higher current density, can offer better performance at the cost of increased power requirements. In some cases, as much as 5 dBm additional power is required. However, most L939 devices reach a plateau in their CL performance at lower powers, e.g. -5 dBm for L939 vs 0 dBm for L938/L940.

The effect of device size on CL is generally linear, with CL decreasing as size, and therefore current density, increases. A notable exception is the inversion between D4 (active area of $225\mu m^2$) and D5 (active area of $450\mu m^2$) performance, with D4 having the best one across different layers and frequency ranges. This can be explained by size 4 providing the best trade-off between current density and junction capacitance.

The switch from using the 2^{nd} to 4^{th} harmonic of the LO is found to lead to an increase of at least 10 dB in the CL. It was also found that the performance of the diodes as part of $n = 4$ SHM circuits is mainly limited by their non-linearity, especially at 424 GHz. At that frequency, the large C_{j0} also plays a big limiting role, as evidenced by both D2 ($60\mu m^2$) and D4 ($225\mu m^2$) from all three layers having the same best CL.

The obtained results for conversion loss themselves are not as good as many of the previously reported circuits operating at the same RF frequency, with minimum CL around 22 dB. These can be explained by insufficient non-linearity and current density offered by the RTDs that were used, together with the dominating effect of the large junction capacitance C_{j0}, associated with their active areas, which are as large as $450\mu m^2$.

However, the trends that have emerged would be useful for future layer design. The reported expected effect of scaling the currently available diodes provide further pointers as to what to look for in the next iteration of RTDs fabricated at the University of Leeds.

Chapter 4

Resonant-Tunnelling Diode Amplifiers

The initial motivation for this project was to investigate the performance of resonant-tunnelling diodes as potential non-linear elements in a sub-harmonic mixer circuit. This potential application focused on the part of the I-V that is formed by the first PDR regions, arising from the tunnelling current.

Another potentially unique application of RTDs, related to low level signal detection at THz frequencies, is in amplifier circuits, where their NDR region can be used to provide gain. This has been used in the past with Esaki tunnel diodes[150, 151, 152], and in this case with RTDs it may be possible to revive the principle, such that an appropriately designed wafer could provide a technologically attractive integrated approach to form a very low loss sub-millimetre wave mixer. Possible use includes a stand-alone amplifier for high-frequency signals, a combination of a sub-harmonic mixer preceded by an amplifier, or a straight-forward active mixer. Therefore, these prospects were investigated via two different types of amplifiers, a reflection based one and an active distributed transmission line. Simulation results for both types at different frequency ranges are presented in this Chapter.

The overall work flow when designing these amplifiers is similar to the one used for SHMs in Chapter 3. The same RTD model is used in Agilent ADS, with the same design stages, i.e. initial design in ADS using ideal transmission lines, subsequent change to a particular technology like microstrip or CPWG, S-parameter simulation in HFSS, and final simulation pass in ADS.

4.1 Reflection Based Amplifier

The reflection based amplifier was the first type of amplifier using resonant-tunnelling diodes that was investigated and as a result was studied a bit more extensively. Circuits implementing this design at two different frequency ranges were fabricated, however at the time of writing measurements are still to be performed.

4.1.1 Principle of Operation

As the name implies, the signal to be amplified is reflected at some point in the circuit. A sample circuit schematic using ideal transmission lines is presented in Fig. 4.1. The amplifier circuit can be divided into several distinct parts. A branchline coupler, acting as a 3 dB power splitter, forms the core of the circuit. Unlike the sub-harmonic mixers discussed in Chapter 3, the amplifier circuit requires two RTDs, which are separated from the coupler by two DC blocking capacitors.

The diodes are biased in the middle of their respective NDR regions. Both diodes can be biased in the same quadrant, or they can be biased using both positive and negative DC voltage. The two most often used bias points are shown in Fig. 4.2. It should be noted that the device pictured was grown with a symmetrical layer structure, as its main intended application was for sub-harmonic mixers. In practice, RTDs for amplifiers and oscillators can have an asymmetrical semiconductor layer structure, maximising the PVCR and ensuring an NDR region over a larger voltage range. Since the NDR region can be approximated as a straight line, it essentially

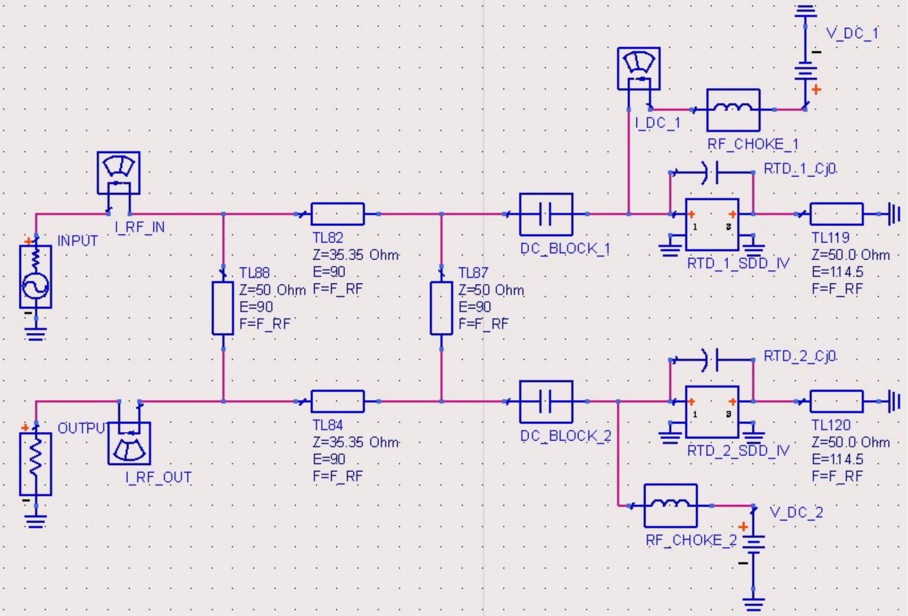

Figure 4.1: A circuit realising a reflection based amplifier using ideal transmission lines and components.

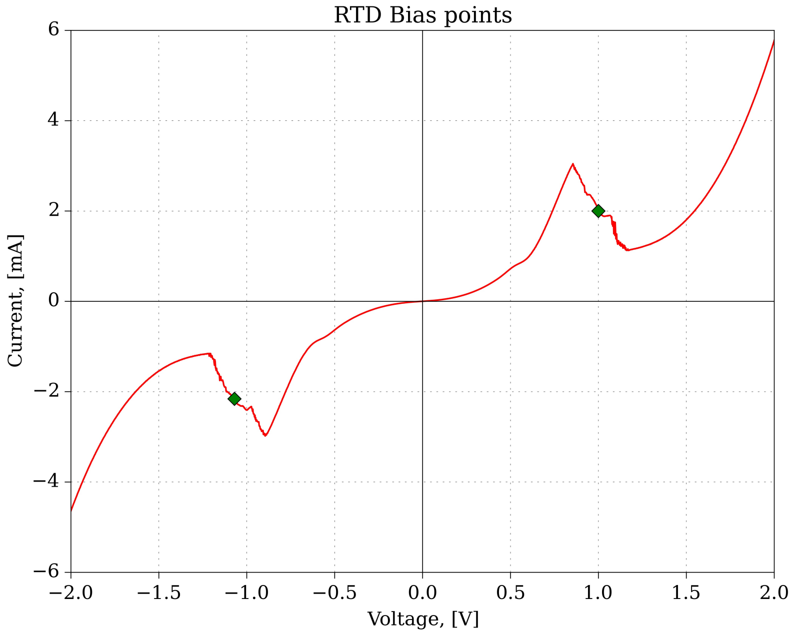

Figure 4.2: An illustration of where an RTD is usually biased when used in reflection based amplifiers. Diode used is L938 D2, with an area of $60\mu m^2$.

fulfils the role of a negative resistor.

The DC power source is decoupled from the RF circuitry via two RF chokes. The final part of the circuit are two pieces of transmission line that end in a discontinuity, such as an open or short circuit. In Fig. 4.1 they are labelled TL_{119} and TL_{120}, and their impedance and electrical length are used to fine tune the circuit.

A signal flow diagram is presented in Fig. 4.3. The input RF signal is applied to port 1 of the circuit. It is then equally split by the branch coupler and fed to the two diodes, themselves connected to ports 2 and 3. Due to the nature of the coupler, these two signals are 90° out of phase with each other, or rather the signal at port 3 is 90° behind the signal at port 2. Said signals are amplified by the resonant-tunnelling diodes and then reflected by the discontinuity. They can now be considered input signals to the branchline coupler. The signal at port 2 is delayed by 90°, allowing it to be combined in-phase with the signal coming from port 3, at the output port 4. Overall, the phase difference between the input and the amplified output signal is 270°.

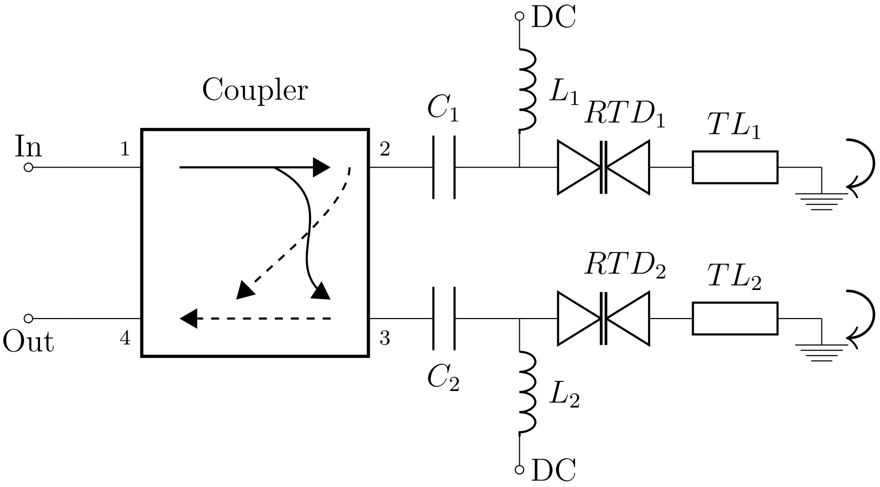

Figure 4.3: A diagram illustrating the signal flow in a reflection based RTD amplifier.

One potential advantage of such a circuit is the ability to connect several of them in a chain, thereby providing a larger overall gain, at the expense of the composite circuit having a narrower bandwidth. An example consisting of two such *cells* is given in Fig. 4.4. Unfortunately, this type of amplifier offers no port-to-port isolation, which necessitates the use of circulators and good matching networks at both the input and output port.

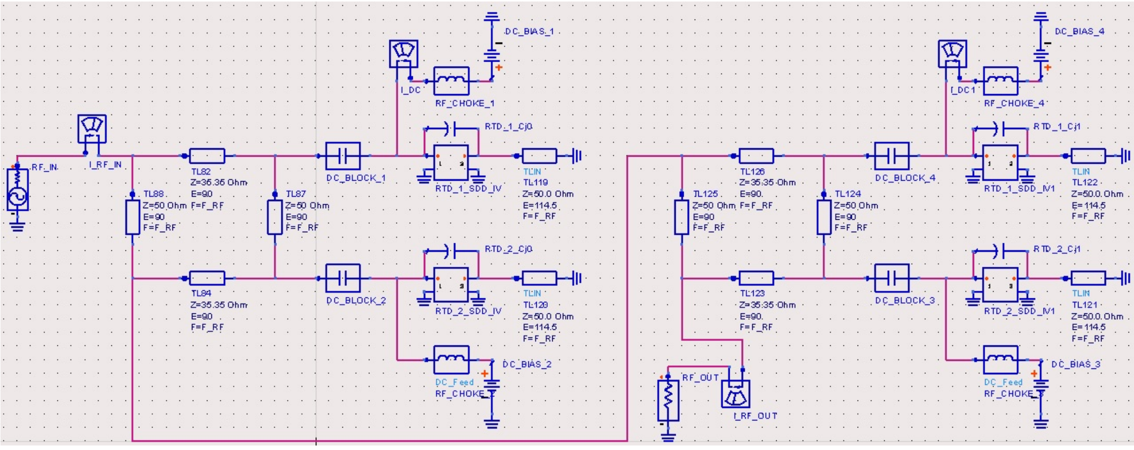

Figure 4.4: Reflection based amplifier with two cells connected in series.

This amplifier concept was tested at two different centre frequencies, 20 GHz and 100 GHz. The long term goal was to develop a way to amplify signals at sub-millimetre wave frequencies, potentially integrating an RTD amplifier with an RTD mixer. When running simulations, the performance indicators that were monitored were power gain, input and output port reflection, and input-to-output isolation. Both S-parameter and harmonic balance simulations were used to obtain these.

Since this was an exploratory concept, other important parameters such as noise performance, SFDR, third-order intercept point, etc., were not studied initially as the focus was on determining whether the circuit can provide sufficient gain to be considered feasible and to justify further research. In addition, the input signals were expected to be of such low power that compressions issues were not anticipated to be a problem. The results of this initial investigation are presented in the following sections.

4.1.2 20 GHz

The circuits designed for the 20 GHz centre frequency were the first attempts at making an RTD based reflection amplifier at the University of Leeds. They were realised in microstrip technology, using discrete capacitors as DC blocking elements and a radial stub as an RF choke. The branchline coupler is implemented using the double-box variant, and a photograph of the entire circuit is shown in Fig. 4.5. The main challenge was optimising the branchline coupler's dimensions to provide even power split. The first few iterations were implemented using the low ϵ_r (2.2) substrate Duroid5880 with a thickness of 787 μm. This led to wide and short transmission lines, as illustrated by Fig. 4.6. HFSS simulations of these structures showed that there was a large degree of energy coupling between parallel branches of the coupler, leading to uneven power split and high reflection at the input port. One attempted solution was to use a double-box branchline coupler with a higher Z_0, on the order of 70 Ω. The result was the structure shown in Fig. 4.6, and its S-parameters are given in Fig. 4.7. These show that while the coupler provides some form of power split, it is not even and the combination of higher impedance lines and impedance transformers increases the losses. To solve this, a thinner substrate with a higher ϵ_r (3.48) was used, namely a 254 μm thick Duroid4350B. Unfortunately, this was not sufficient, as the 35 Ω lines were still too wide and the power split provided was not equal, in addition to large losses from coupling between the lines.

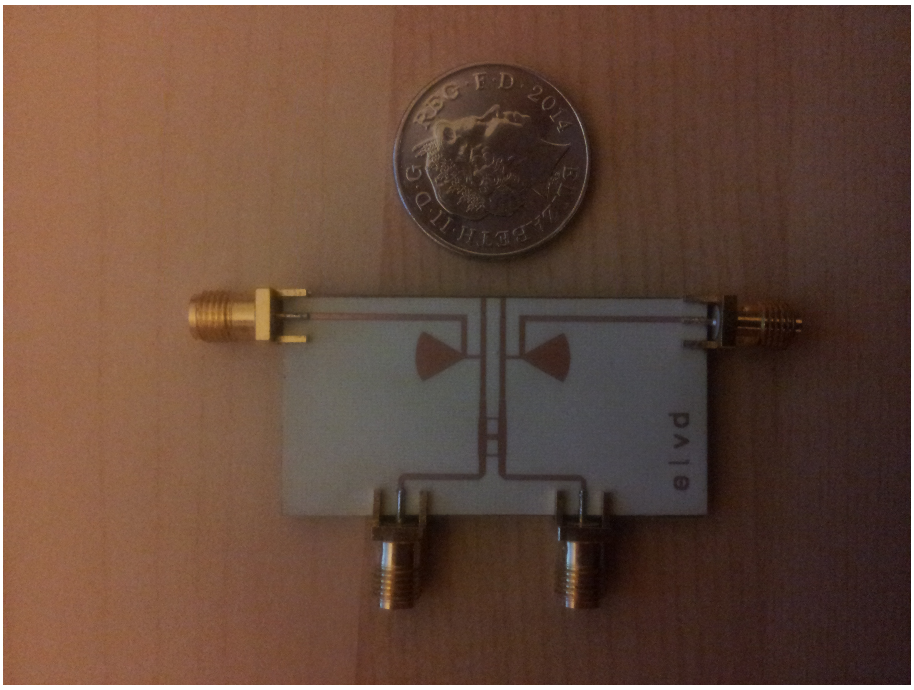

Figure 4.5: A photograph of a 20 GHz reflection based amplifier, fabricated on Duroid4350B substrate and using a double-box branchline coupler.

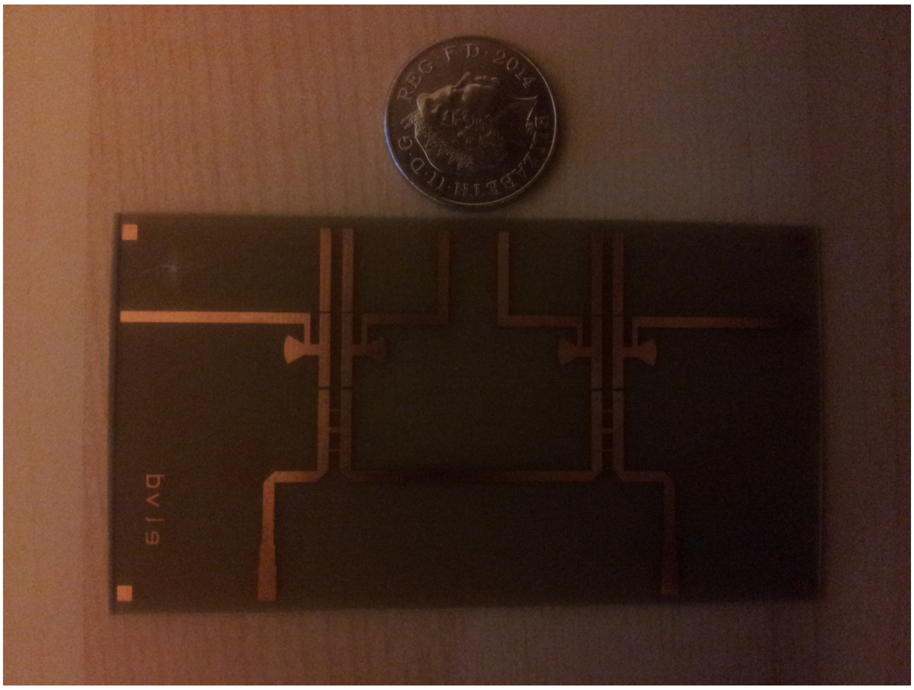

Figure 4.6: A photograph of a two cell RTD reflection based amplifier, illustrating the thick transmission lines on Duroid5880.

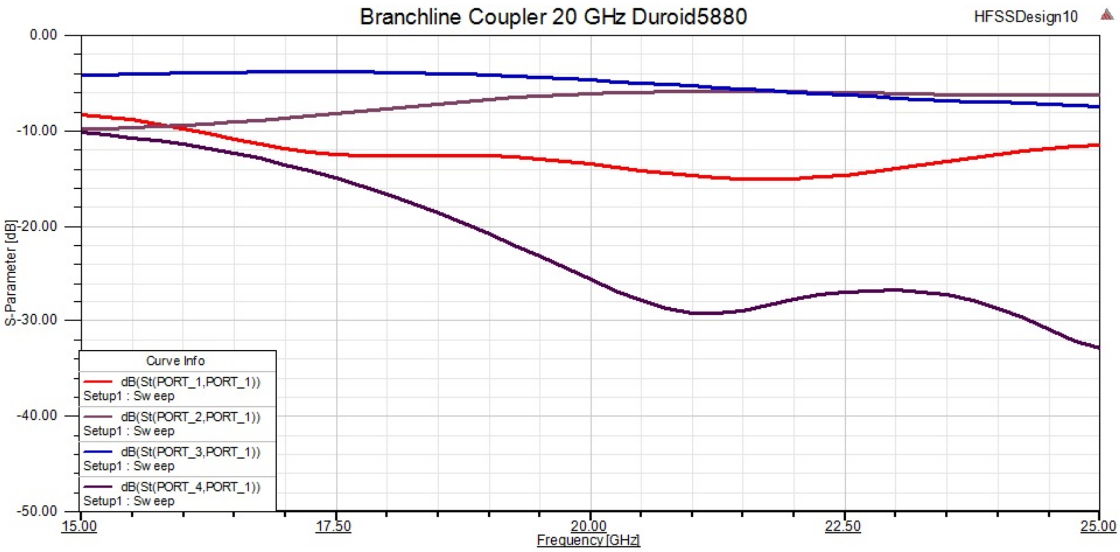

Figure 4.7: S-parameters for a double-box branchline coupler realised on Duroid5880 substrate.

Therefore, a double-box structure was used instead. A schematic using ideal lines is shown in Fig. 4.8.

One advantage of a double-box branchline coupler is the wider bandwidth. The

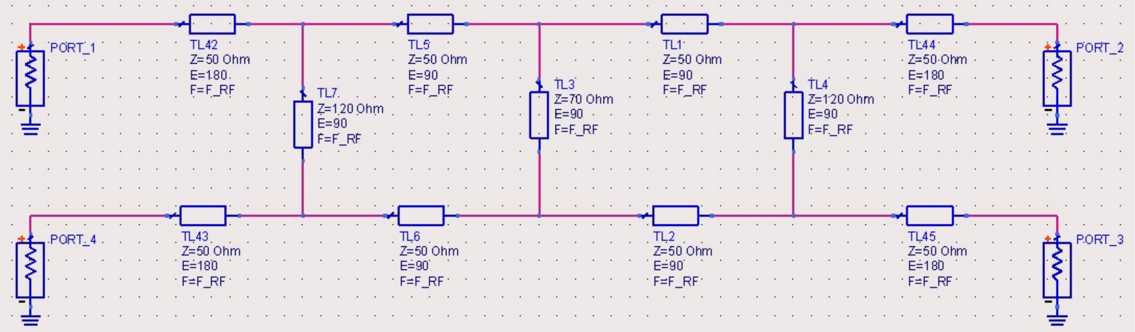

Figure 4.8: A branchline coupler implemented with ideal transmission lines.

higher impedance lines in a double-box coupler translated to significantly thinner lines and better coupler performance, as demonstrated by Fig. 4.9. The power split is close to even over a larger bandwidth, in addition to both input reflection and isolated port attenuation being less than -20 dB. Once the amplitude performance

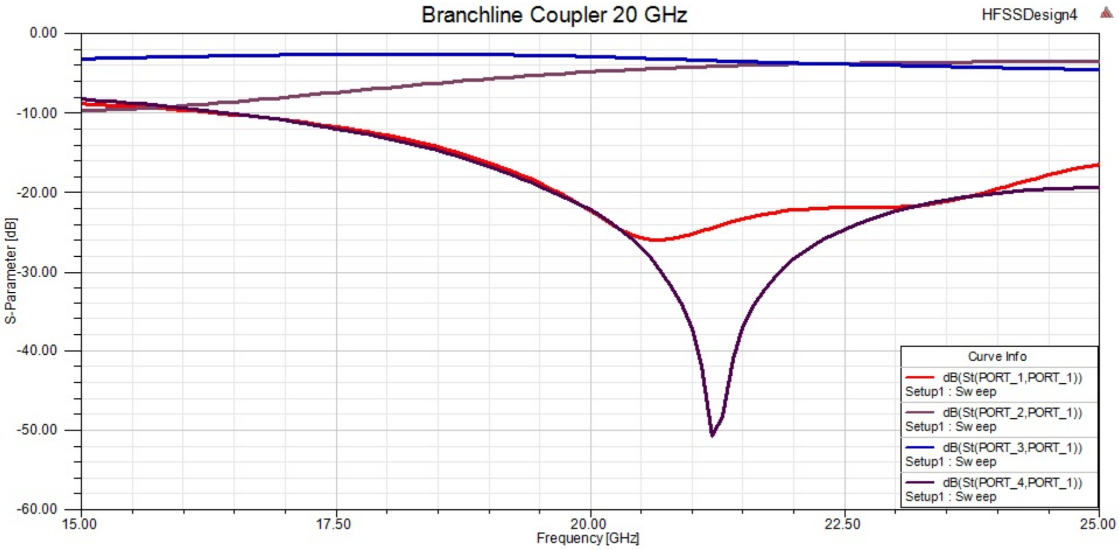

Figure 4.9: S-parameters for a double-box branchline copler realised on Duroid4350B substrate.

of the couplers has been obtained, the phase relationship between the two ports that are connected to RTDs, ports 2 and 3, should be investigated. It is integral to the operation of the circuit that these are as close to being 90° out-of-phase as possible. The results for the two 20 GHz couplers are presented in Fig. 4.10 and show that both circuits provide very good phase performance at the centre frequency of 20 GHz, as well as part of the frequency range over which there is an even power split. However, the better amplitude S-parameters of the coupler implemented on Duroid4350B led to it being selected for further investigation. The excellent phase difference this circuit offers in the range 20 GHz – 25 GHz, combined with an even power split, suggests that good amplification performance could be expected in this frequency span.

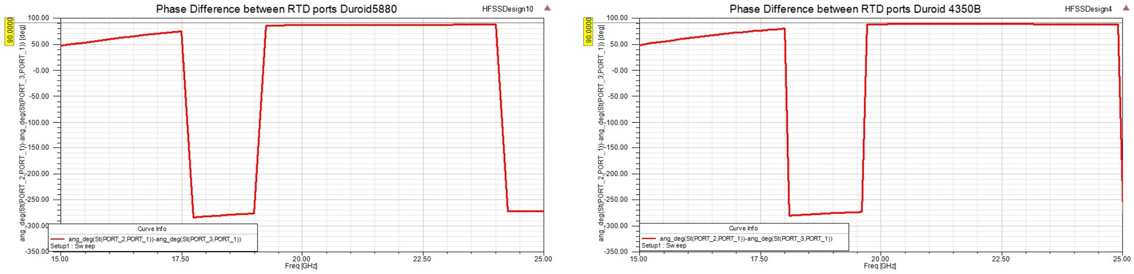

(a) Coupler on Duroid5880

(b) Coupler on Duroid4350B

Figure 4.10: Plots of phase difference between ports 2 and 3 of the 20 GHz couplers. Ideal difference is 90°.

The final parts of the amplifier left to design are the radial stubs that provide RF choke functionality. They were implemented as open-ended radial stubs, with an initial Z_0 of 70 Ω, and an experimentally determined length. The stub itself is connected to the main transmission line via a 70 Ω transmission line. The final design of the RF chokes, along with their S-parameters, is shown in Fig. 4.11. The obtained S-parameter results show that there is very little RF power transfer to the

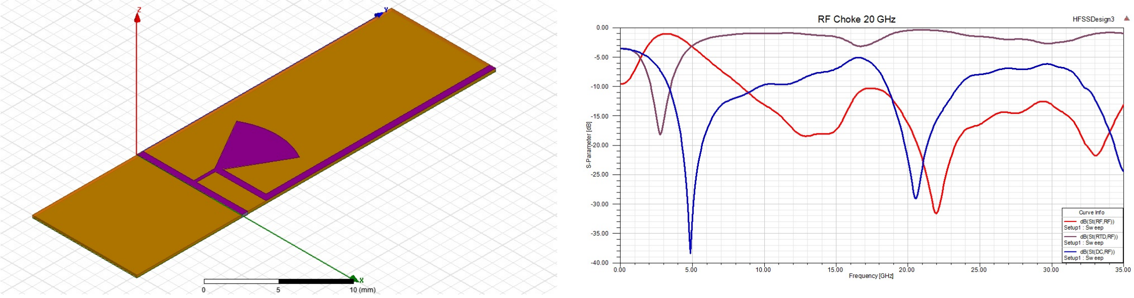

(a) HFSS Model

(b) S-parameters

Figure 4.11: HFSS model of an RF choke circuit for 20 GHz reflection based amplifiers, along with its simulated S-parameters.

DC port over the frequency range of interest, i.e. 20 GHz – 25 GHz. The reflection on the input port is less than -15 dB over this range, while the RF leakage to the DC port has a minimum at 20 GHz and is less than -15 dB up to about 22.5 GHz. These results mean that the DC power source will be relatively isolated from the RF signals.

4.1.3 100 GHz

Following the promising results obtained at lower frequencies, a design was developed for 100 GHz centre frequency. This was considered as the next logical step on the path to designing an RTD amplifier at sub-millimetre wave range as it complements the sub-harmonic mixers described in Chapter 3, and it would allow for easy scaling.

There are a few differences that have been introduced due to the higher frequency of operation. First of all, the discrete DC blocking capacitors have been replaced by intedigital ones, which, as shown in Fig. 4.12a, are realised as part of the centre conductor in a CPWG circuit. This capacitance should be big, so as not to present a high impedance to the incoming RF signal. The S-parameters for this structure are given in Fig. 4.12b. Even though the main interest is within a narrow span around 100 GHz, the losses in this capacitor are small (-1 dB) over a much wider range, 70 GHz – 105 GHz, with a corresponding reflection coefficient of less than -10 dB in the same range. As frequency increases beyond 105 GHz, the structure exhibits resonant behaviour and losses increase, however this is not the intended application region, and results are shown for completeness.

Next, the RF choke is implemented using $\frac{\lambda_g}{4}$ open-ended resonator stubs. An HFSS model of them, together with their simulated S-parameters, is given in Fig. 4.13. Again, a large frequency span is shown for completeness.

The RF transmission losses are again close to being constant, at about -1 dB, over a wide frequency range. While the isolation between the main transmission line and the DC port is not as good as the 20 GHz one, its level is still less than -10

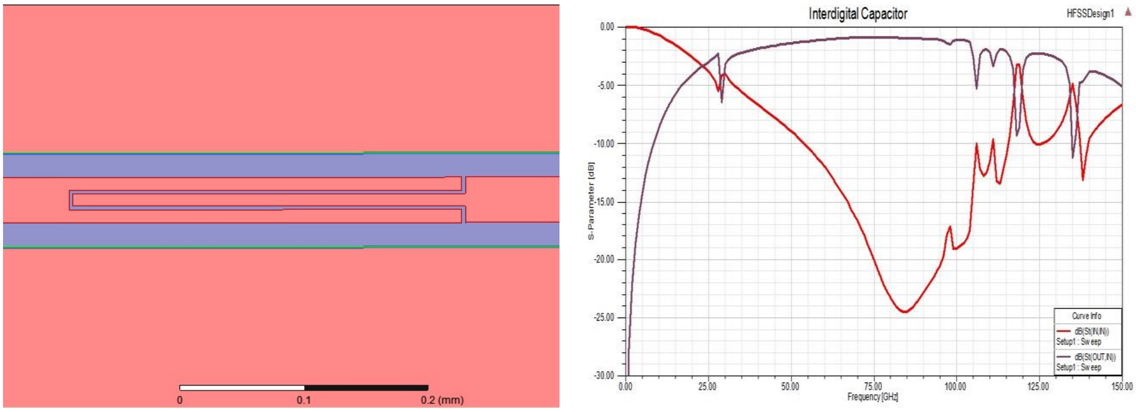

(a) HFSS Model (b) S-parameters

Figure 4.12: HFSS model of an interdigital capacitor for 100 GHz reflection based amplifiers, along with its simulated S-parameters.

dB at the main frequency of interest, 100 GHz. Overall, both the input reflection and DC port isolation are below -10 dB in a wide range, 95 GHz – 120 GHz. The good values for these parameters around 112.5 GHz mean that that frequency can be viewed as a secondary point of interest.

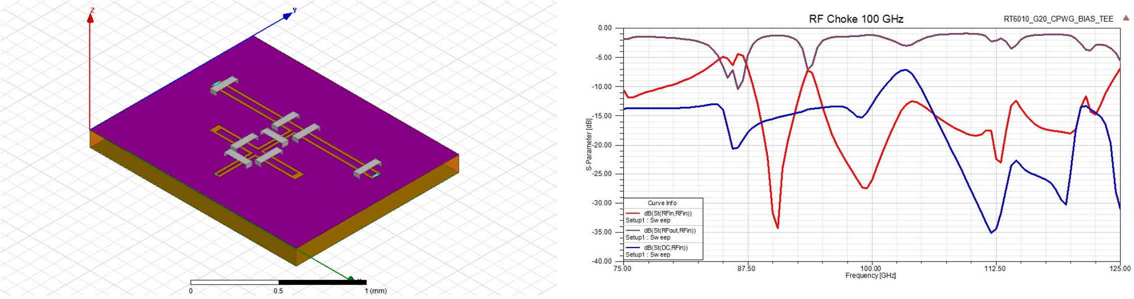

(a) HFSS Model (b) S-parameters

Figure 4.13: HFSS model of an RF choke for 100 GHz reflection based amplifiers, along with its simulated S-parameters.

Unlike the 20 GHz variant, two different substrates were used for the 100 GHz amplifiers, the same ones used for the SHM circuits in Chapter 3. One is a 100 μm thick quartz substrate, and the other is a thin (127 μm) Duroid6010. While the interdigital capacitors and the RF chokes were straightforward to adapt between substrates, the central coupler required more work and individual design tuning. The resultant transmission line sizes necessitated that the amplifier circuit designed for quartz substrate uses a double-box branchline coupler, while the one meant for

Duroid6010 utilises a single-box one.

The HFSS models of both couplers are shown in Fig. 4.14 and the results from their S-parameter simulations are presented in Fig. 4.15. The S-parameters are again shown over a much wider frequency range than the immediate region around the 100 GHz centre frequency for two reasons. On one hand for completeness, on the other to better illustrate the overall behaviour of the circuit and to help identify where good amplification should be expected. Both circuits are realised using CPWG technology. As was previously mentioned, air-bridges are added to improve field distribution and suppress the propagation of odd modes. The S-parameters obtained are later imported back in ADS for final circuit simulation, in a similar manner to the procedure described for SHMs in Chapter 3.

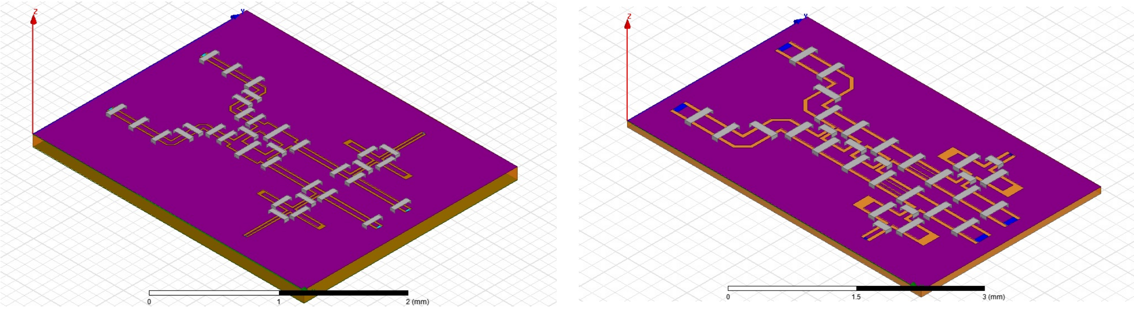

(a) 100 GHz coupler on Duroid6010

(b) 100 GHz coupler on quartz

Figure 4.14: HFSS models of couplers for 100 GHz reflection based amplifiers on Duroid6010 and quartz substrates. Models include additional circuitry such as interdigital capacitors and RF chokes.

The results of the HFSS simulations show that the designed couplers can provide even power split, albeit in a small frequency range. This is not deemed an issue, however, because the purpose of these amplifiers is to complement the SHMs, discussed in Chapter 3, and to help offset their conversion loss.

The circuit implemented on Duroid6010 substrate has an even power split in the range 100 GHz – 110 GHz, with both reflection and isolation parameters below -10 dB. Higher dielectric and ohmic losses at these frequencies have led to the power split to be about -5 dB, rather than the -3 dB observed in the case of the circuit

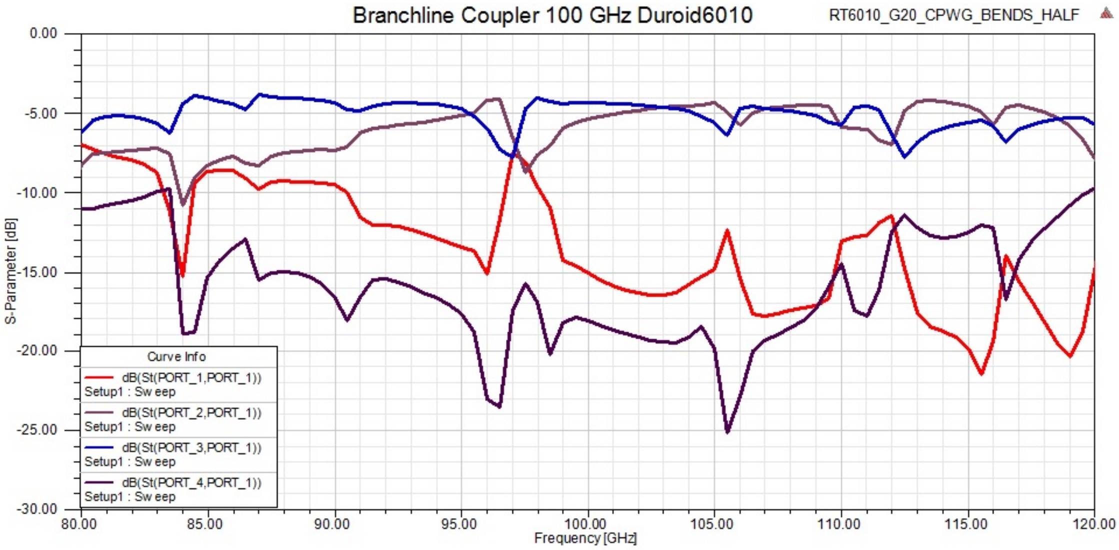

(a) 127 μm Duroid6010 Coupler S-parameters

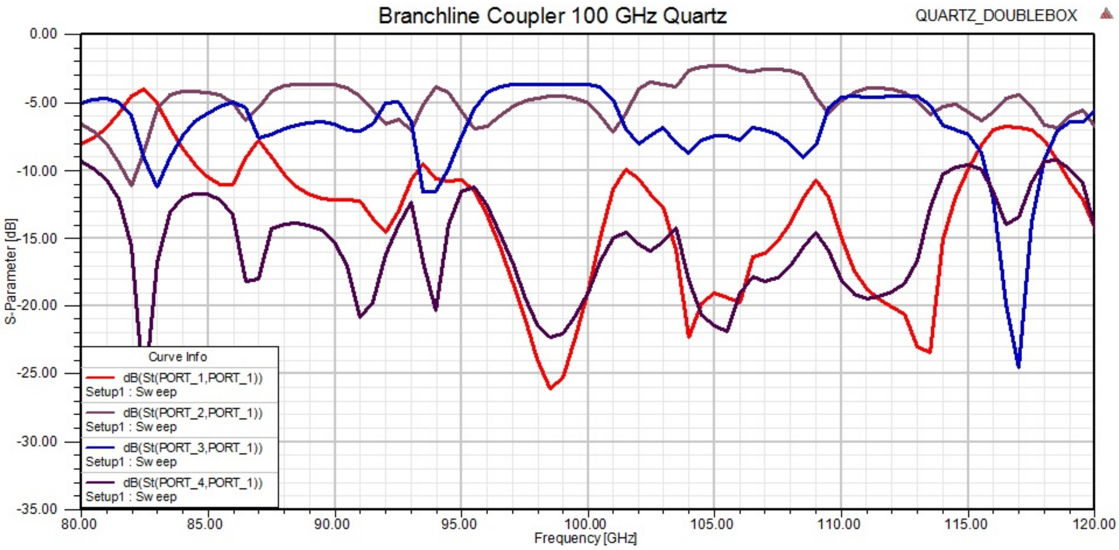

(b) 100 μm Quartz Coupler S-parameters

Figure 4.15: Simulated S-parameters for branchline couplers implemented on Duroid6010 and quartz substrates for 100 GHz reflection based amplifiers.

designed to operate at 20 GHz case. The quartz based circuit, on the other hand, has adequate performance roughly in the 5 GHz span between 95 GHz and 100 GHz. Even then, the power split is uneven. This poor performance can again be attributed to slotline mode excitation, as well as energy coupling between adjacent transmission lines in the main region of the coupler. Overall, these circuits are narrowband in their nature, however both cover the main point of interest, 100 GHz.

Analogously to the 20 GHz mixers, the phase performance of the 100 GHz couplers is presented in Fig. 4.16. These show that the coupler realised on Duroid6010 exhibits phase difference of 90° a prerequisite for the proper operation of the reflection amplifier circuit, in the range 99 GHz – 104 GHz. This overlaps with the range over which the same coupler provides even power split and as a result, the results for the full amplifier circuits based on this coupler will focus on performance in the range 95 GHz – 105 GHz.

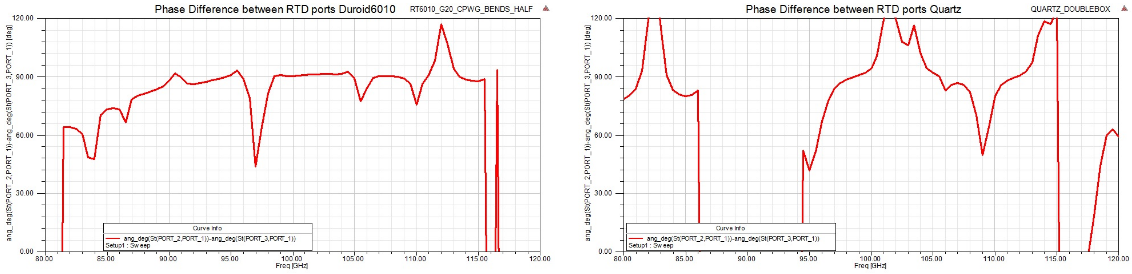

(a) 127 μm Duroid6010 Coupler

(b) 100 μm Quartz Coupler

Figure 4.16: Plots of phase difference between ports 2 and 3 of the 100 GHz couplers. Ideal difference is 90°.

The quartz coupler on the other hand has very erratic phase behaviour and as a consequence the amplifier based on it is expected to perform poorly. Nevertheless, those amplifier circuits were still tested to confirm these assumptions.

The higher transmission losses in planar media at these frequencies, along with poor phase performance of the couplers, and other undesired effects such as excitation of odd modes, could seriously hamper the performance of reflection based amplifiers. An alternative way of implementing 3 dB couplers in waveguide media is investigated in Chapter 5.

4.2 Reflection Based Amplifiers Simulation Results

Since one of the motivating reasons behind investigating RTD amplifiers is to pair them with the sub-harmonic mixers discussed in Chapter 3, circuits operating at 20 GHz and 100 GHz centre frequencies were studied. Presented results are grouped by frequency range, with a focus on comparative graphs. Similarly to the SHM study, the aim here was to undertake a parametric type review of the comparative merits of device and material characteristics.

While all three semiconductor layers were studied, only devices with active areas of $30\mu m^2$ (size 1), $60\mu m^2$ (size 2), and $110\mu m^2$ (size 3) were simulated with these circuits. The reasoning behind this restriction is that the capacitance of the larger diodes, those with areas of $225\mu m^2$ (size 4) and $450\mu m^2$ (size 5), was found to be too large, and that some of these devices had a reduced or non-existent NDR region at room temperature due to self-heating.

It is also expected that the characteristics of these amplifiers will be dominated by the behaviour of the 3 dB couplers previously discussed.

4.2.1 20 GHz

The first step is to investigate the difference, if any, in performance between the separate RTD layers. Such a comparison is given in Fig. 4.17 for device sizes 1 and 3. The graphs include both S_{11} and S_{21} parameters over a broad frequency range, however the main interest is the centre frequency of 20 GHz. For the smallest devices, the overall obtained gain is similar for L938 and L939, with L938 having slightly better S_{11}. The larger size 3 devices show a clear distinction between the two layers, largely due to the smaller NDR region of L939 D3. However, the S_{11} of the circuit with that device is much better, remaining under -10 dB over a larger frequency range, while having a flat gain. Both D1 and D3 based amplifiers exhibit

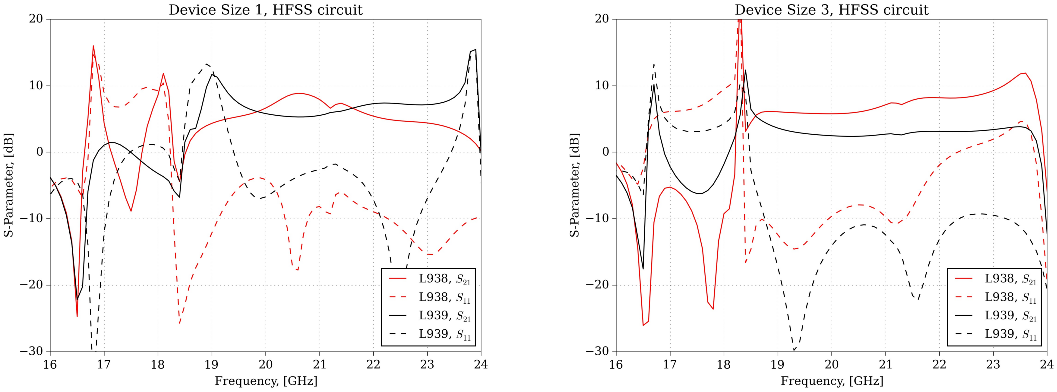

(a) Device Size 1, area of $30\mu m^2$ (b) Device Size 3, area of $110\mu m^2$

Figure 4.17: Layer comparison for two different device sizes for a 20 GHz reflection based amplifier circuit.

good performance between 20 GHz and 23 GHz, which overlaps with frequency range over which the 20 GHz coupler, implemented on Duroid4350B, has a good power split, and more importantly, a 90° phase difference between the two RTD ports.

The next step is to take a look at the effect of device size, and therefore junction capacitance, on the S_{21} and S_{11} parameters of the tested circuits. This is presented for L938 and L939 in Fig. 4.18. For both layers, the smallest devices offer the highest gain, at the cost of high S_{11}. Device size 2 ($60\mu m^2$) from L939 could be an optimum choice here, combining steady gain with excellent S_{11}. The difference in gain between D1 and D2/D3 is small, and of the order of 3 dB.

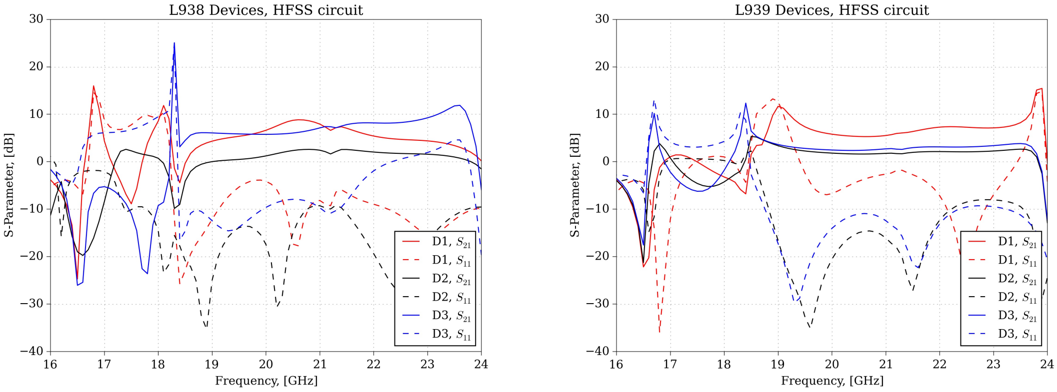

(a) L938 (b) L939

Figure 4.18: Effect of device size on amplifier performance for L938 and L939 semiconductor layers.

The previously mentioned idea of connecting two reflection based amplifier cells in series was also tested at 20 GHz, using L939 D2 ($60\mu m^2$) and L939 D3 ($110\mu m^2$). Comparison graphs between a single circuit and a two cell one are shown in Fig. 4.19. As could be expected, there is around 3 dB increase in the overall gain of the two cell circuit. L939 D2 again offers the best characteristics here, with minimum deterioration of its S_{11}.

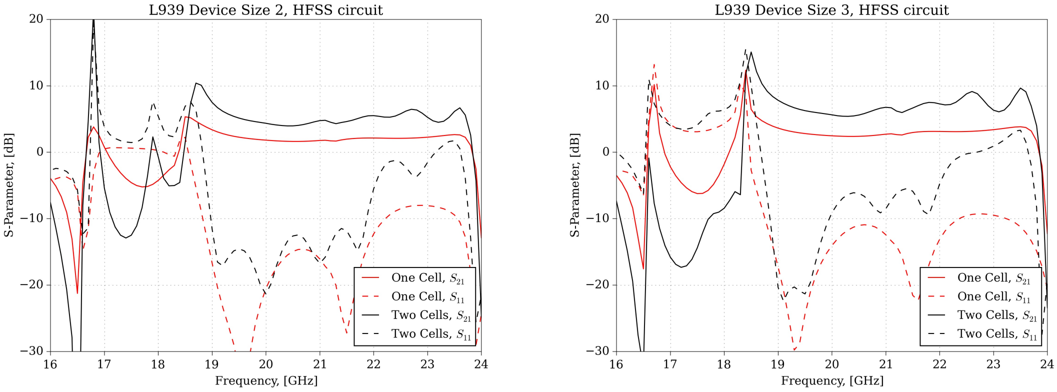

(a) L939 D2

(b) L939 D3

Figure 4.19: Comparison of amplifier gain between circuits with different number of cells for L939 devices.

4.2.2 100 GHz

All the S-parameter results presented for the 100 GHz amplifiers focus on a small frequency range around the centre frequency, 90 GHz – 110 GHz. This is due to the intention of using these circuits together with the SHMs also operating at 100 GHz and the narrow-band nature of the signals that would be detected at this frequency.

Similarly to the SHM circuits with an RF of 100 GHz, both Duroid6010 and quartz substrates were used for the 100 GHz RTD amplifiers. Judging by the coupler S-parameters and phase performance given in Fig. 4.15 and Fig. 4.16 the expectation would be for relatively poor performance of quartz based circuits.

An example comparison between the Duroid and quartz circuits is shown in Fig. 4.20 for size 2 diodes from all three layers. Due to the increased transmission

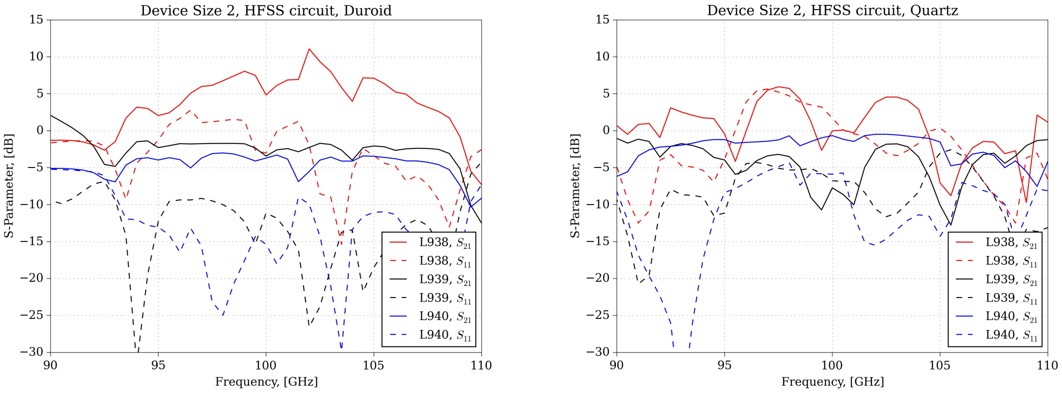

(a) Circuit on Duroid substrate

(b) Circuit on quartz substrate

Figure 4.20: Layer comparison for Device Size 2 ($60\mu m^2$) diodes on two different substrates, 100 GHz reflection based amplifier circuit.

line losses at 100 GHz, only L938 D1 ($30\mu m^2$) on a Duroid substrate offers any amplification, peaking at a respectable 10 dB at about 103 GHz. Furthermore, the S_{11} of that circuits is less than 0 dB in a very narrow range around 105 GHz. Whilst L939 and L940 offer satisfactory S_{11} performance, any gain that they provide is negated by the transmission line losses.

A similar comparison, this time for diodes size 3 ($110\mu m^2$), is given in Fig. 4.21. Here, the device from L940 is the one that produces observable positive gain, while

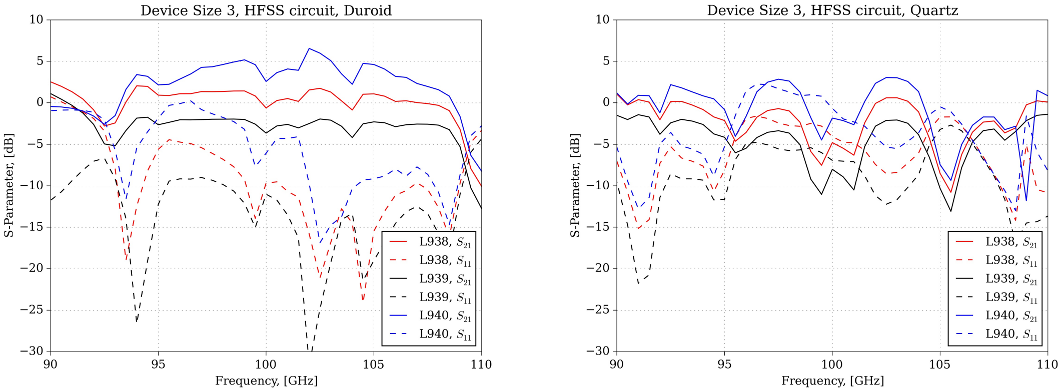

(a) Circuit on Duroid substrate

(b) Circuit on quartz substrate

Figure 4.21: Layer comparison for Device Size 3 ($110\mu m^2$) diodes on two different substrates, 100 GHz reflection based amplifier circuit.

L938 offers 1 dB to 2 dB amplification in the same frequency range. Gain on this order is generally insignificant and not considered worth the effort.

The peak amplification from the L940 D3 based circuit is less than the L938 D1 by about 3 dB. This could be explained by the capacitive losses in the C_{j0} outweighing any gains provided by the increased current density.

Finally, the effect of device size on the S-parameters of the amplifier circuits is shown for L938 and L939 devices in Fig. 4.22. The results confirm that the smaller devices offer better performance, due to smaller junction capacitance and more pronounced NDR regions. It is also evident that the diodes fabricated from L938 exhibit higher gain, likely because of a less steeper NDR region.

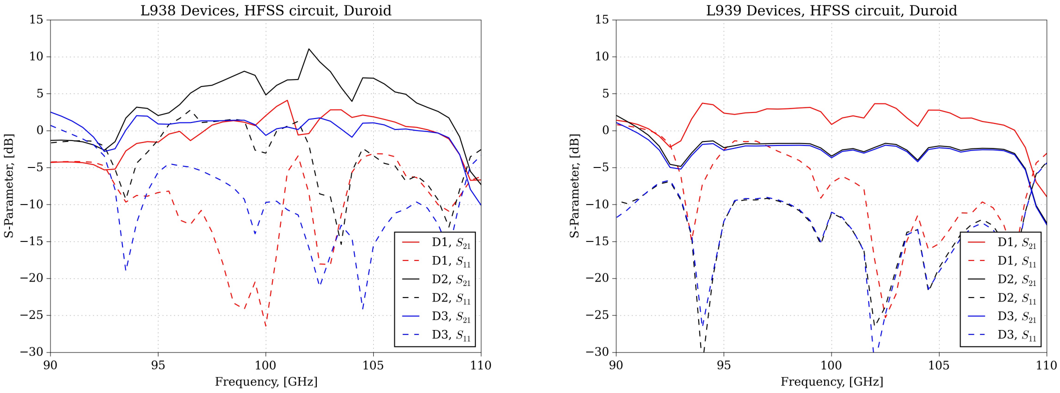

(a) L938

(b) L939

Figure 4.22: Effect of device size on amplifier performance for L938 and L939 semiconductor layers.

While none of the three layers investigated was designed as either oscillating or amplifying layers, where high current density and an NDR over a large voltage range are a prerequisite, the study was warranted in case there was access, in principle, to such devices.

4.2.3 Scaled Diodes

Similarly to the RTD mixers, the results obtained so far point to the conclusion that the currently available devices at the University of Leeds might be too big to provide good performance at millimetre and sub-millimetre wave frequencies. However, using the same method of scaling diodes' C_{j0} and current density as described in Chapter 3, it was possible to investigate in what ways the use of smaller diodes would improve the reflection based amplifiers.

The results obtained for scaled Device Size 3 ($110\mu m^2$) from both L938 and L939, in comparison to non-scaled performance, are given in Fig. 4.23 for the same frequency range as the one used in the previous Section. It can be seen that scaling just the capacitance of the devices offers a very small advantage, while an L939 D3 with both I-V and C_{j0} scaled now has similar peak performance as L938 D2, the diode with best available gain so far.

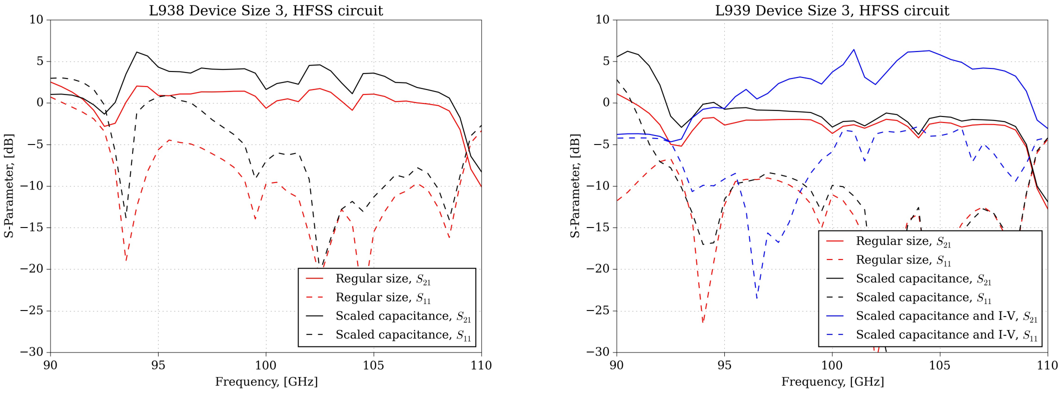

(a) L938 D3

(b) L939 D3

Figure 4.23: Effect of scaling on L938 D3 and L939 D3, 100 GHz amplifier circuit.

4.2.4 Summary

The overall conclusion that can be made from the results presented in this Section is that reflection based amplifiers using resonant-tunnelling diodes could be a viable circuit. Smaller devices generally seem to offer better performance, due to a good combination of junction capacitance and a well-formed NDR region, i.e. an appreciable value of NDR or a low negative conductance and hence higher potential gain.

Highest exhibited gain by both the 20 GHz and 100 GHz circuits is around 10 dB, with some devices at 20 GHz providing a flat 5 dB – 6 dB gain over a larger bandwidth. While neither of these results can compare with gain achieved by power amplifiers at 20 GHz, the result at 100 GHz is quite positive, especially given the possibility for combined use with sub-harmonic mixer circuits. The narrow-band behaviour of the 100 GHz circuits is not an issue, as any signals that would be detected at this frequency will be just as narrow-band. This sort of circuits can help offset and improve the conversion loss performance of the SHMs presented in Chapter 3.

Both L938 and L939 layers offer at least one device that is suitable for reflection based amplifier circuits, providing respectable gain in the range 95 GHz – 105 GHz, while not suffering from stability issues as a consequence of having a positive S_{11}.

4.3 Active Transmission Line

The second type of RTD amplifier that was investigated is based on the active transmission line concept. This type of amplifier has been studied by other research teams in the past and their findings have generally been positive and optimistic about its viability[117, 153, 154]. The reasoning for this study is to explore the possibilities of this approach for use at much higher frequeinces where the complexities of 3-terminal devices hamper their easy use.

Resonant-tunnelling diodes are again used for their NDR region, fulfilling the role of negative resistors. Unlike the reflection based amplifiers, no circuits were fabricated, and all simulation work was done using ideal transmission lines. This was due to the study being a proof of concept and time limited constraints, although there are plans to expand on this work in the future.

4.3.1 Distributed Transmission Line

It is well known that any transmission line can be modelled using lumped elements, namely series resistance and inductance and shunt capacitance and conductance, as illustrated in Fig. 4.24[147]. Using this model, the attenuation per unit length in

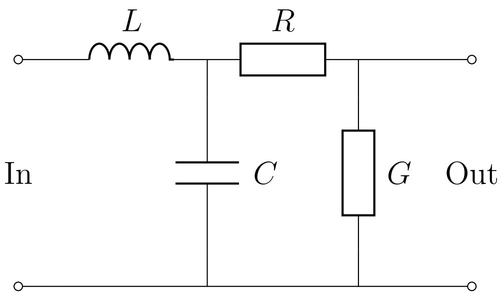

Figure 4.24: A single section of a generalised lumped element model of a transmission line.

Nepers is given by the following formula for the attenuation constant:

$$\alpha \approx \frac{1}{2}\left(\frac{R}{Z_0} + GZ_0\right) \tag{4.1}$$

Therefore, if a negative resistor were to be introduced in the place of the element G, the transmission line could have a negative attenuation constant, i.e. it will be providing gain[155]. It is for this reason that an RTD device can be used to synthesise a transmission line from lumped components, as demonstrated by Fig. 4.25. Generally, a series inductive element connected to a shunt RTD forms one unit length of such a transmission line. The diode's junction capacitance C_{j0} is absorbed by its role as the element C in the transmission line model, and thus a broad impedance match is achievable.

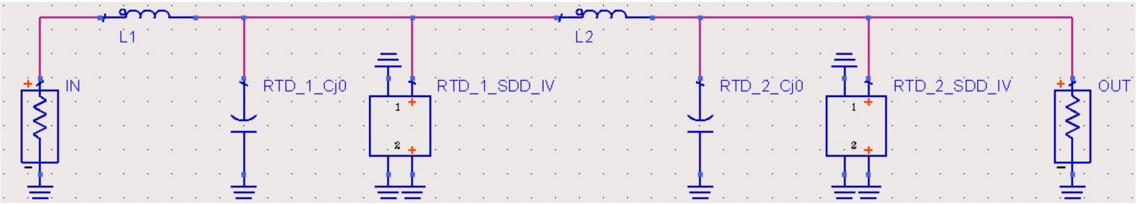

Figure 4.25: An ADS model of a synthesised active transmission line using RTDs.

There are a couple possible ways to implement such a design, both of which have been investigated and are presented in the next section.

4.3.2 Design Types

Regardless of implementation, the way the inductive element is realised is an important design decision. At the first stage of simulation, an ideal lumped inductor can be used. However, a more realistic way would be to use a high impedance length of transmission line. While it is also possible to use other types of inductors such as spiral ones, their manufacture becomes increasingly difficult as the frequency of operation increases.

The high impedance transmission strips are synthesised to present certain inductance at the centre frequency of operation of the distributed transmission line. The value of the inductance is chosen so as to satisfy the condition $Z_0 = \sqrt{\frac{L}{C}}$, where $C = C_{j0}$.

There are two main ways of using RTDs to synthesise an active transmission line. The first one is illustrated in Fig. 4.25 and follows the ideas presented so far, where the junction capacitance of the diode is used together with an inductive element to form a transmission line; with gain being provided by the diode's NDR region. The diode itself is biased in the middle of its NDR. It is possible to use two diodes per segment, as shown in Fig. 4.26, in order to provide more gain. However this leads to doubling of the capacitance and therefore the inductance needed, leading to thinner lines which are either difficult to manufacture, or under certain circumstances cannot be physically realised at all. The other way is to provide separate bias to two RTDs connected in parallel in order to form a composite I-V with the form shown in Fig. 4.27. An example circuit implementing this is given in Fig. 4.28. One advantage of this approach is a larger input signal dynamic range. Unfortunately, this also comes at the price of increased capacitance that needs to be compensated by a high impedance transmission line.

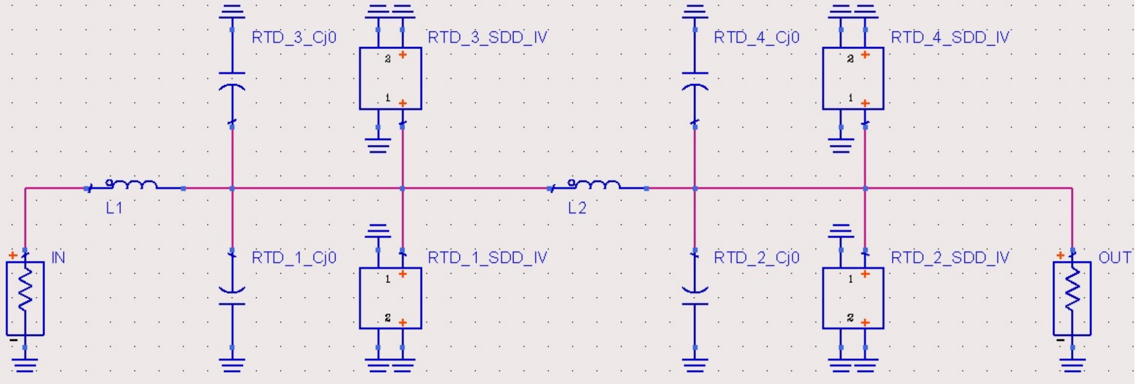

Figure 4.26: An ADS model of an active transmission line, showing the use of two diodes per segment.

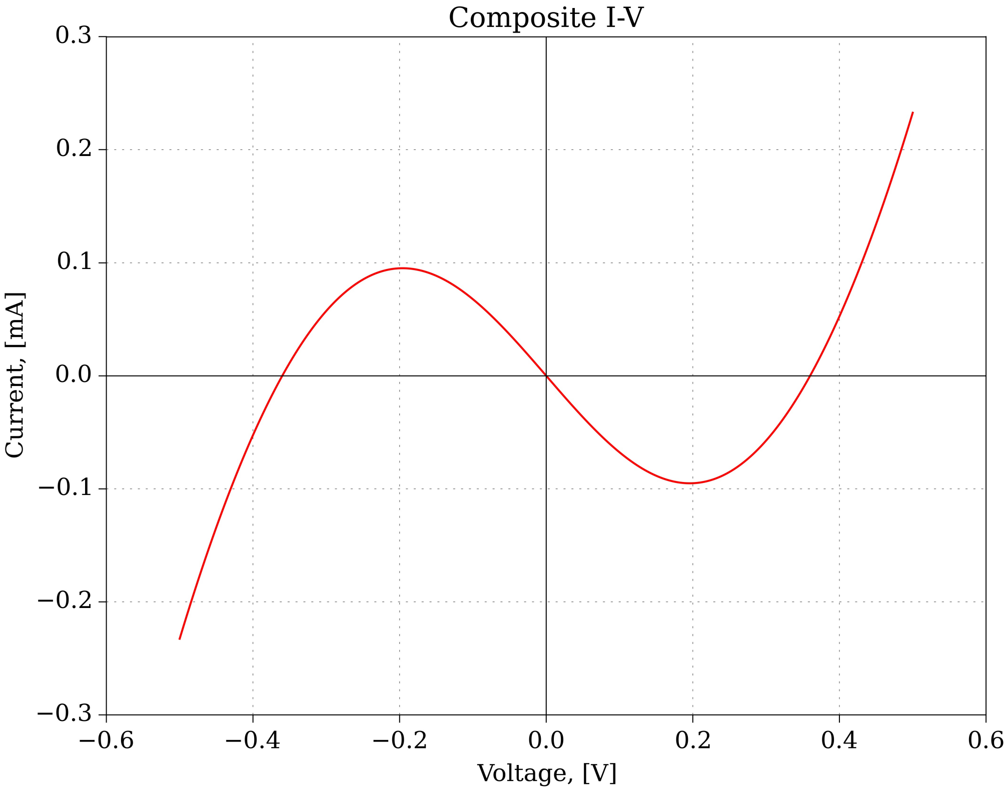

Figure 4.27: A composite I-V formed by individually biasing two RTDs, connected in parallel.

4.4 Active Transmission Line Simulation Results

In contrast to all the other circuits presented and discussed so far in the thesis, the active transmission line ones are not grouped by frequency. The reason for that is that they are expected to operate at a much wider frequency range, rather than

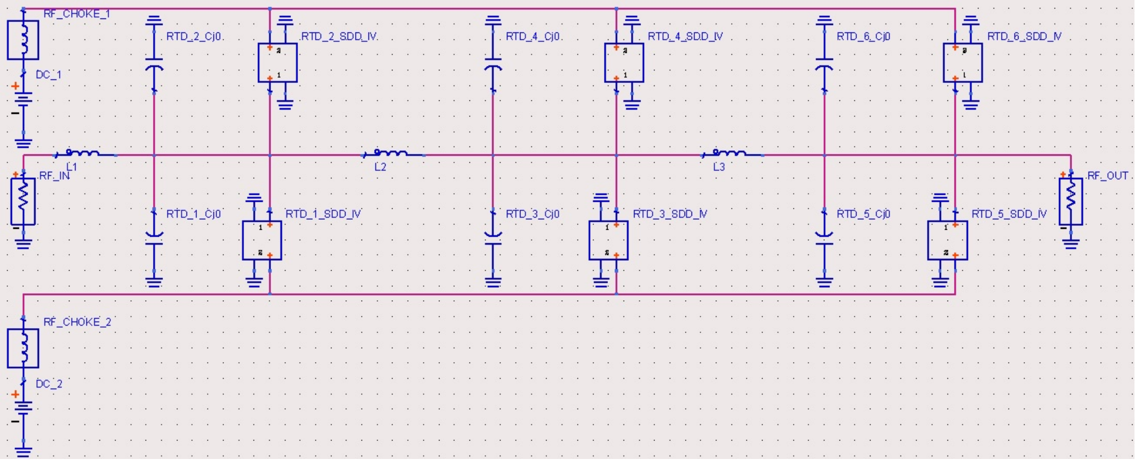

Figure 4.28: An ADS model of an active transmission line using double DC bias and a composite I-V.

a single central one. In some respects this is useful as it may accommodate any frequency shifts due to fabrication differences.

The simulation results are mainly grouped by circuit type. The design in Fig. 4.25 would be referred to as *Single bias* from now on, whereas the circuit in Fig. 4.28 as *Double bias*. All the simulations were done in ADS, using ideal transmission lines to represent the inductance needed to achieve a Z_0 of 50 Ω, when combined with the RTD's C_{j0}.

Both of these were simulated with devices size 1 ($30\mu m^2$) from the three different layers, with a varying number of transmission line segments and number of diodes per segment. Larger devices were found to offer worse performance, and in some cases, due to increased capacitance, required transmission lines that would be impossible to physically implement.

4.4.1 Single Bias

The order of evaluating and examining the active transmission lines closely follows that of SHM circuits and reflection based amplifiers. The initial comparisons made are between identical circuits with diodes from different layers. Results are presented in Fig. 4.29 for lines with 3 and 6 segments and 1 device per segment. Devices from

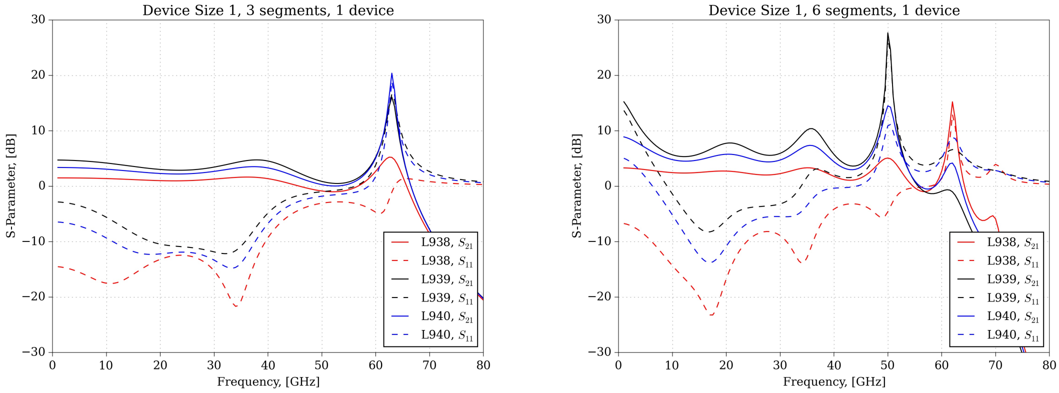

(a) 3 segments (b) 6 segments

Figure 4.29: Comparison between Device Size 1 ($30\mu m^2$) diodes from all three layers, for a line with 3 and 6 segments and 1 device per segment.

all layers seem to exhibit low, i.e. between 1 dB and 5 dB, but flat broadband gain up to 40 GHz, though the 6 segment circuit is unstable in the low frequency range, up to about 10 GHz. Observed difference in gain between separate layers is about 1 dB to 2 dB, with L939 giving the highest gain of about 5 dB.

The effect of adding multiple segments is better illustrated in Fig. 4.30, where the results for L938 are shown. Predictably, the overall transmission line gain sees an increase at the cost of worse S_{11} behaviour. Furthermore, the resonance at the end of the band is more pronounced, and the ripples of the frequency response close to the resonance are somewhat reminiscent of the transfer characteristic of a Chebyshev filter[156].

The final parameter for the Single bias circuit that was studied is the number devices per segment. Results for 3 and 6 segment transmission lines using L938 diodes are given in Fig. 4.31. The observed trend is for a 2 dB to 3 dB increase in gain, while the maximum frequency at which the circuit is still stable and amplifying is roughly halved.

Overall, the behaviour and performance of the active transmission lines presented so far, is limited and defined by the low-pass filter that is formed by the series inductor and parallel capacitor. Any increase in the total capacitance per segment

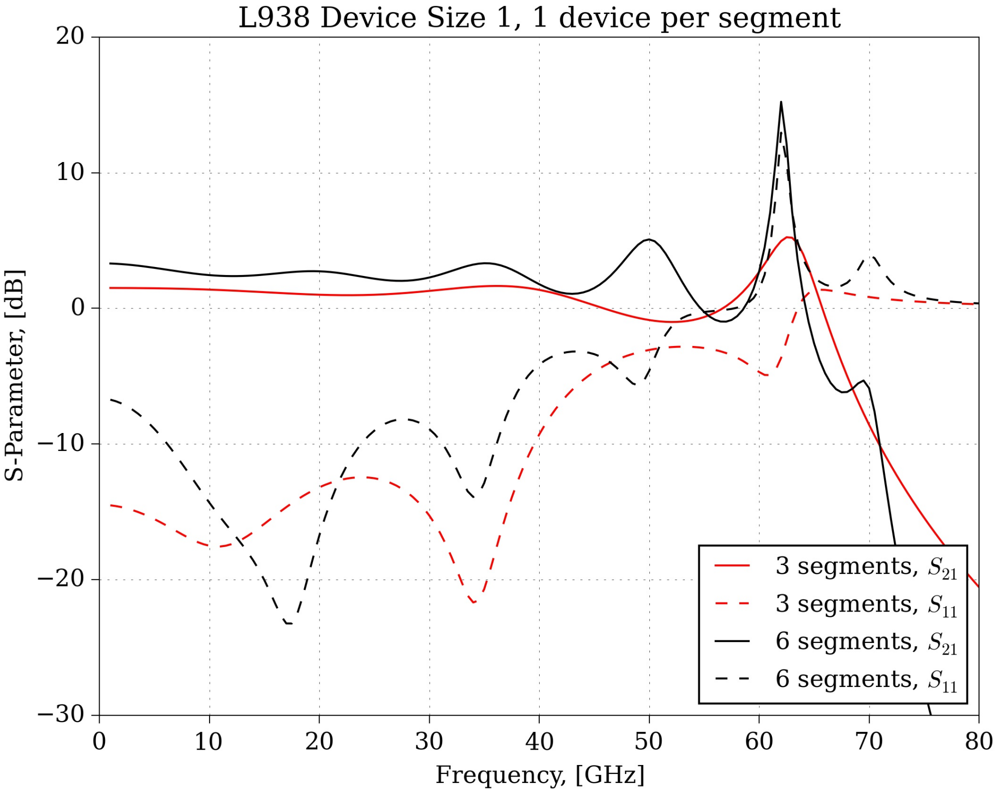

Figure 4.30: Comparison between an active transmission line with 3 segments vs one with 6, using an identical RTD.

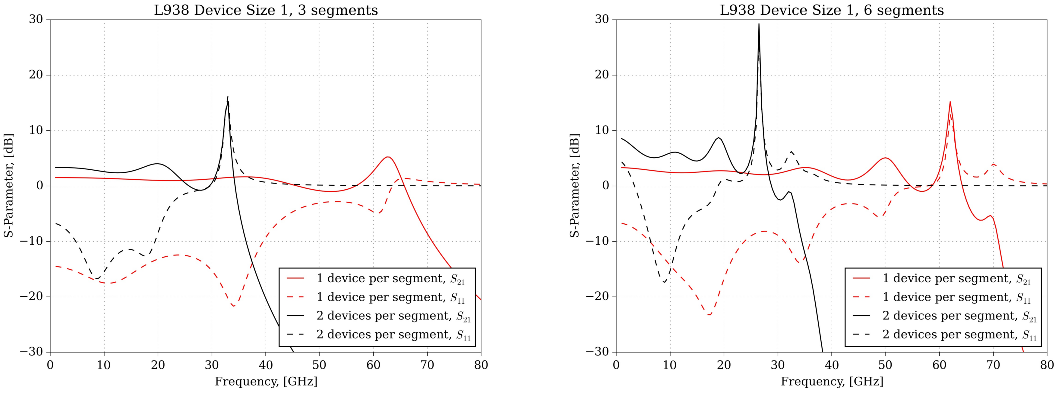

(a) 3 segments (b) 6 segments

Figure 4.31: Comparison between an active transmission line with 1 device per segment vs one with 2, using an identical RTD.

leads to a corresponding change in the inductance and decrease in overall bandwidth. Furthermore, there is a very high gain resonance at the cut-off frequency, which could be utilised by other narrow-band circuits.

4.4.2 Double Bias

The Double bias circuit, by its very nature, always requires 2 diodes per segment. As a result, a frequency performance and bandwidth similar to those of Single bias 2 devices/segment transmission line is expected. A potential difference between the two would be the greater dynamic range of the input signal that could be handled by the Double bias line, and possibly higher gain before saturation.

A layer comparison between L938 and L939 size 1 ($30\mu m^2$) devices for a 3 segment Double bias circuit is presented in Fig. 4.32. The frequency bandwidth obtained is consistent with stated expectations, however the shape of the gain is more resonant and virtually non-existent at frequencies below 10 GHz. Layer L939 again offers better gain, although the stability here is far worse than that of Single bias analogues.

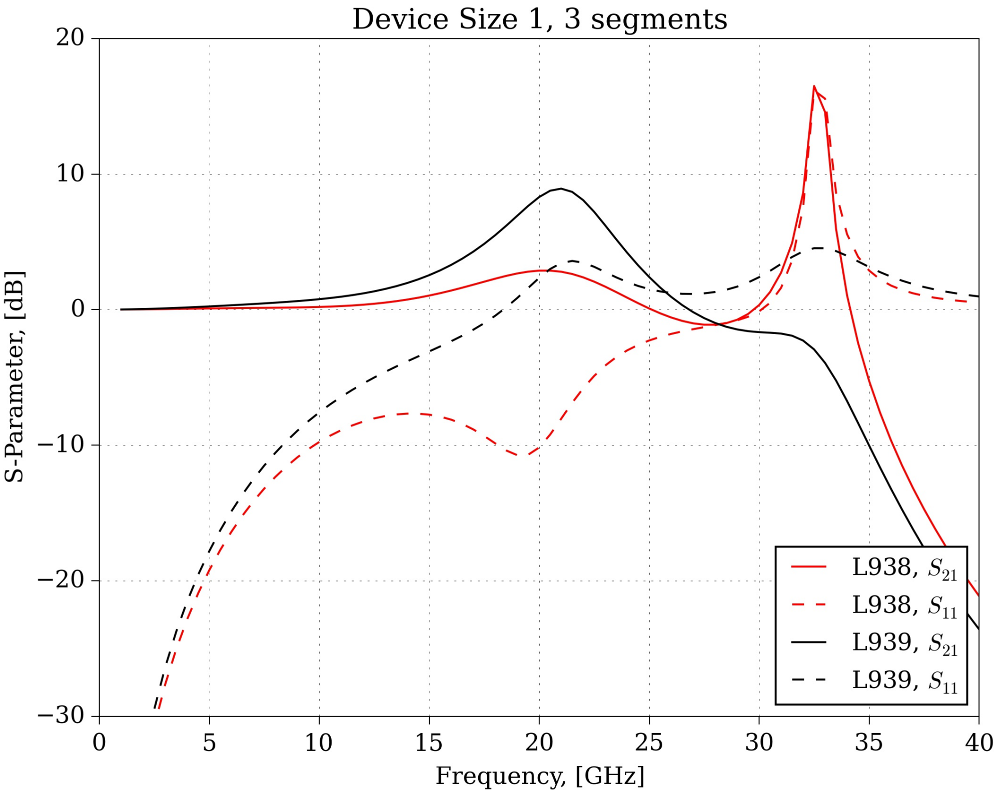

Figure 4.32: Comparison between double bias active transmission line using same size devices from different layers.

The addition of more segments, while increasing the overall gain, especially over the lower end of the frequency bandwidth, further reduces the maximum frequency at which amplified transmission is still present. The comparison graph is shown in Fig. 4.33. Resonant peaks in frequency response imply gains of at least 15 dB, which if preserved at higher frequencies, would be very useful.

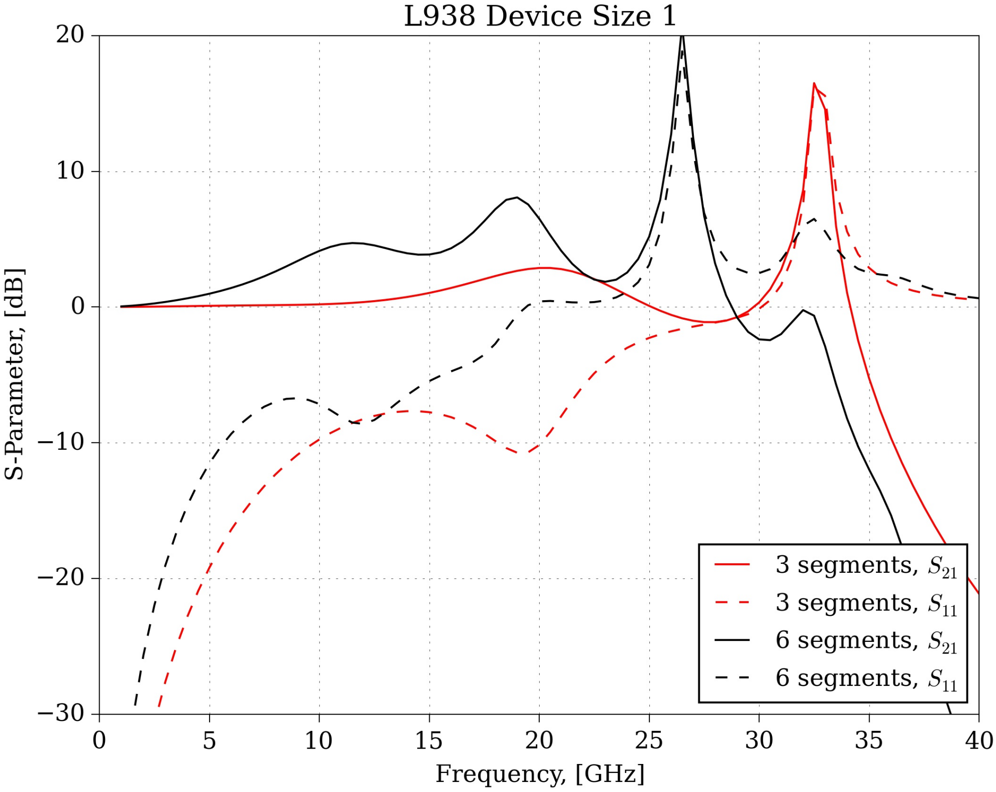

Figure 4.33: Comparison between a double bias active transmission line with 3 segments vs one with 6, using an identical RTD.

Finally, a direct comparison is made between a Single bias transmission line with two devices per segment and a Double bias one. The results for 3 and 6 segments are displayed in Fig. 4.34. These results show that the two variants have virtually identical frequency bandwidths, as defined by the series inductance/parallel capacitance combination. The Single bias circuit offers better gain, especially at lower frequencies, while the Double bias one has better stability.

Overall, the Double bias approach for extended gain and dynamic range does not justify the extra complexity, while the approach of Single bias 3 segments or 6

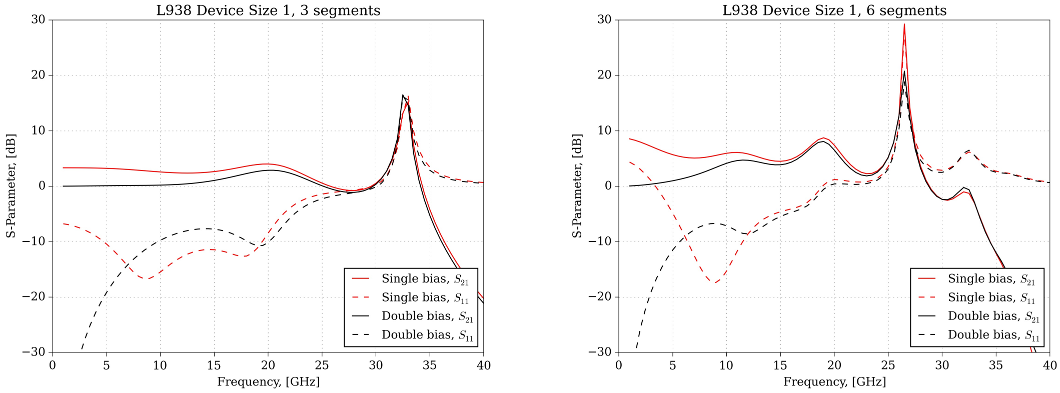

(a) 3 segments

(b) 6 segments

Figure 4.34: Active transmission line performance comparison between a single bias design vs a double bias one, using L938 D1 diode.

segments can be used to improve the CL of the SHMs presented in Chapter 3.

4.4.3 Scaled Diodes

Despite their promising apparent performance at frequencies up to about 50 GHz, the currently available RTDs yet again prove that they have too large junction capacitances in order to be used efficiently at higher frequencies. Similarly to the mixer circuits discussed in Chapter 3, scaled versions of the diodes used in this Chapter were investigated.

The effect of this scaling is shown in Fig. 4.35 for L938 D1 in Single bias transmission line with 3 and 6 segments and 1 device per segment. The major factor is the capacitance, with the current density scaling having almost negligible effect. The smaller C_{j0}, when combined with the smaller corresponding inductance, essentially shifts the maximum frequency of the resulting low-pass structure to a few hundred GHz. Overall gain is reduced to less than 2 dB. For both 3 and 6 segment circuits, there is a peak of S_{21} at about 650 GHz, which is paired with a minimum of S_{11}.

Similar effects are observed for Single bias circuits with 2 devices per segment, as illustrated by Fig. 4.36. Just like their non-scaled counterparts, doubling the number of devices per segment roughly halves the maximum frequency. Gain is

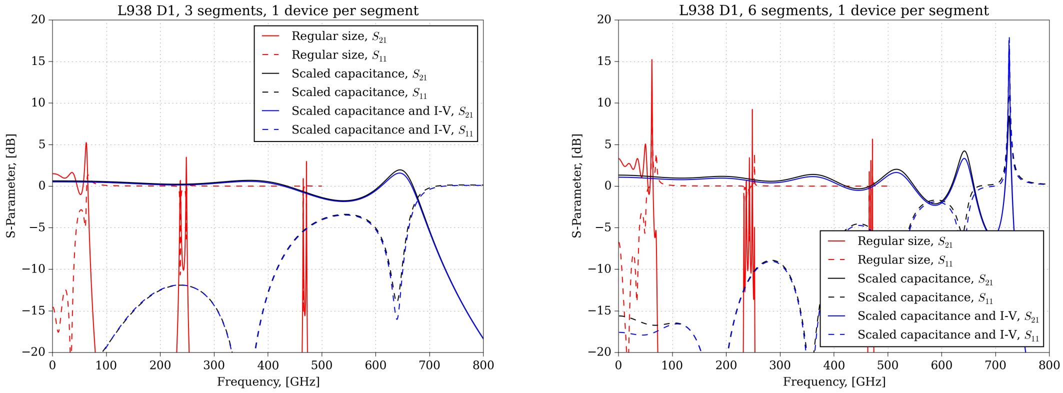

(a) 3 segments

(b) 6 segments

Figure 4.35: Effect of diode scaling on single bias active transmission line with 1 device per segment.

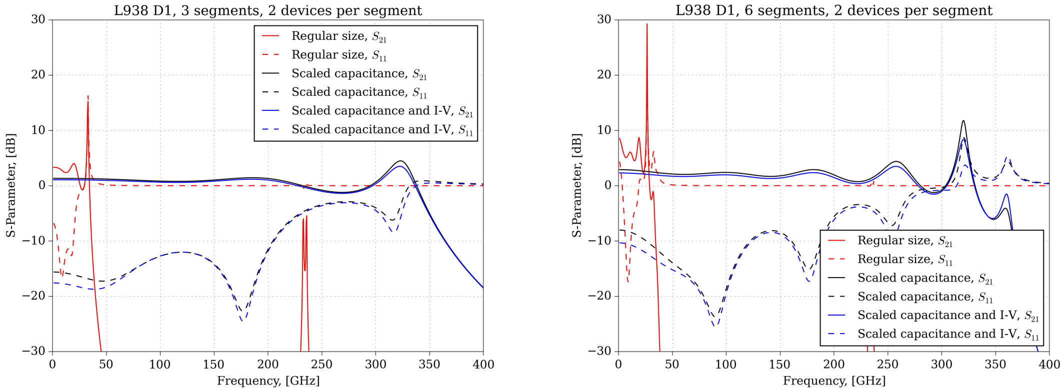

(a) 3 segments

(b) 6 segments

Figure 4.36: Effect of diode scaling on single bias active transmission line with 2 devices per segment.

similarly reduced to no more than a few dB.

The effect of scaling the I-V is much more pronounced for the Double bias circuits, as evidenced by Fig. 4.37. While the 6 segment Double bias active transmission line seem to offer staggering 10 dB gain at 250 GHz, it is not stable at frequencies higher than 200 GHz. The region of interest here is the 100 GHz – 150 GHz span, where the predicted gain is about 3 dB. However, this corresponds to a diode with the same current density as the currently available L938 devices, but with 10 times smaller capacitance.

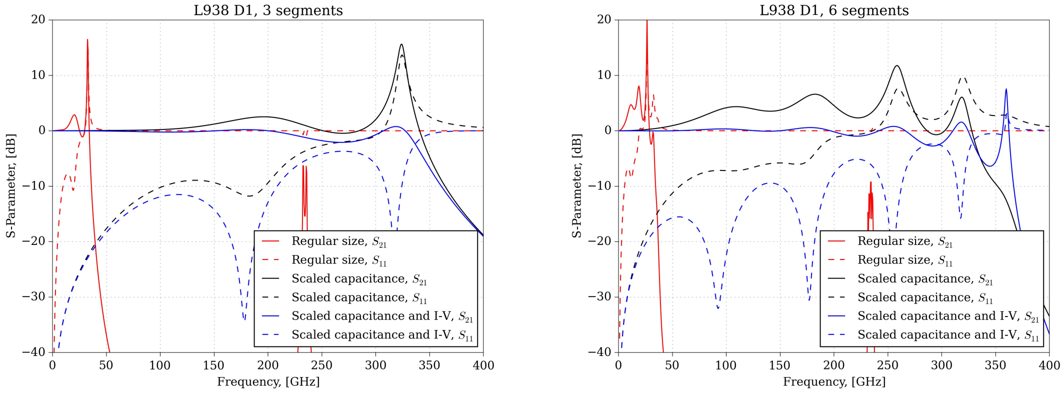

(a) 3 segments

(b) 6 segments

Figure 4.37: Effect of diode scaling on double bias active transmission line.

4.4.4 Summary

The active transmission line with resonant-tunnelling diodes is arguably a viable and promising circuit concept. The preliminary simulation results presented in this Section show that a broadband amplifying transmission line up to 40 GHz could be feasible. The possibility exists to use more than 6 segments to boost the gain beyond the current 2 dB – 3 dB range, however the stability of the circuit needs to be carefully monitored.

Going further, by designing and fabricating smaller diodes from the same layers, a transmission line that offers positive gain up to 350 GHz – 400 GHz could potentially be realised. This is a very promising and encouraging prospect, as any amplification at sub-millimetre wave frequencies is hard to achieve and such a circuit would be welcome.

Another more appealing option is to use these circuits for their narrow-band resonant peaks, which could potentially offer up to 10 dB gain at frequencies as high as 300 GHz. If these amplifier circuits are deliberately designed to emphasise this peak gain, then for a small number of segments a usefully high gain of 20 dB can be achieved. This would be extremely useful as a complementary circuit to SHMs and detectors operating at millimetre and sub-millimetre wave frequencies. The positive S_{11} associated with these resonant peaks is not considered an issue, as any reflected signal back into the antenna system would be quickly attenuated by atmospheric absorption.

Chapter 5

Waveguide Circuits

The circuits that have been presented so far were designed and implemented in planar technology to facilitate accurate measurements by on-wafer CPW probes, and as a consequence can only operate up to the upper portion of the W-band frequency range as limited by presently affordable probes. There are several reasons why planar media are not used at higher frequencies. The main one is the increased dielectric loss of the substrate. Furthermore, said substrates need to be very thin to satisfy the condition $H \leq \frac{\lambda_g}{4}$, where H is the substrate height[49, 157]. Propagation of higher order modes is also a limiting factor.

As a result, many passive high Q circuits and components such as filters, directional couplers, impedance matching networks, attenuators, etc; are preferably implemented in waveguide technology[158, 159, 160]. There are a few favoured ways of doing this. Waveguide circuits can be machined directly as split blocks and then joined together via screws and bolts, while filters and attenuators can be implemented as E-plane metal inserts[161, 162, 163, 164]. Finally, a variety of other circuits can be made using finline and other waveguide to planar media transitions[165, 166, 167].

Sub-harmonic frequency mixers are often realised in waveguide technology when operating at frequencies above 100 GHz, in so-called mixer blocks[79, 168]. Reflection based amplifiers require a 3 dB coupler with low transmission losses, and while this can be achieved in planar transmission media at lower frequencies, at W-band and above a waveguide implementation of such a coupler would be expected to give better performance through lower losses.

Therefore, in order to eventually be able to manufacture such blocks at the University of Leeds, the fabrication capabilities of the facilities available here need to be explored and tested. To that end, a few different waveguide blocks were designed and fabricated. The results are presented and discussed in this Chapter.

5.1 Waveguide Blocks

Waveguide blocks are usually machined from brass, copper, aluminium, bronze, or other material with high electrical conductivity. A common type of waveguide blocks is the E-plane split waveguide block, where the waveguide cavity is formed by two halves joined together in the middle of the wide waveguide wall[169]. A 3D SolidWorks drawing of a straight-through waveguide realised using this technology is shown in Fig. 5.1. This is the preferred method for implementing split blocks, since a discontinuity across the wide wall minimally affects performance, as there is no current flow. The cavity in each block half can be manufactured by using either a slitting saw, or via traditional milling techniques.

(a) Isometric view

(b) One half

Figure 5.1: SolidWorks model of split block waveguide, including flange detail and holes for alignment pins and fastening screws.

An advantage of this method is that a small pocket can be cut out where planar circuits or metal inserts can be dropped. An example of such a pocket is illustrated in Fig. 5.2. This ensures that the position of the dropped circuit relative to the rest of the waveguide stays the same, and is perfect for quickly testing different iterations of the same circuit. A simple straight-through waveguide block was designed and manufactured at the University of Leeds for calibration purposes in waveguide frequency band WR-3 (220 GHz – 325 GHz). Made from bronze using a slitting saw, a photograph of this block is shown in Fig. 5.3a. Additionally, an aluminium block with a pocket for a planar circuit has been previously fabricated, and is shown in Fig. 5.3b.

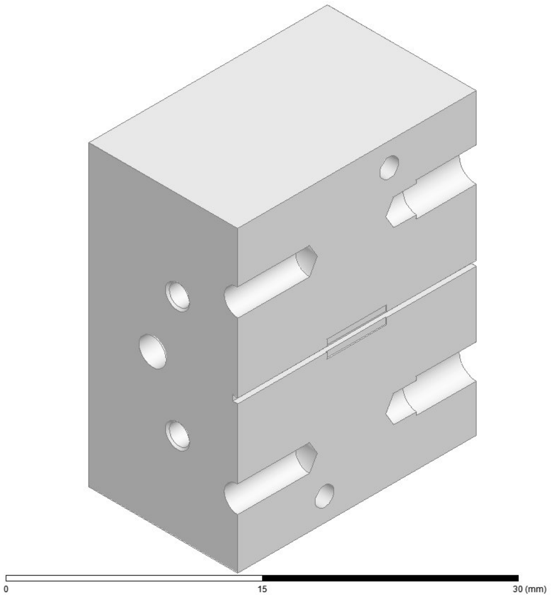

Figure 5.2: A model of a waveguide with a pocket for a planar circuit. Pocket depth is usually equal to substrate thickness.

5.2 Finlines

A lot of circuits and components can be realised with just waveguide transmission media. However, when said circuits require the use of semiconductor devices, a transition to planar transmission lines needs to be incorporated. A widespread way of doing that is by using finline transitions[170].

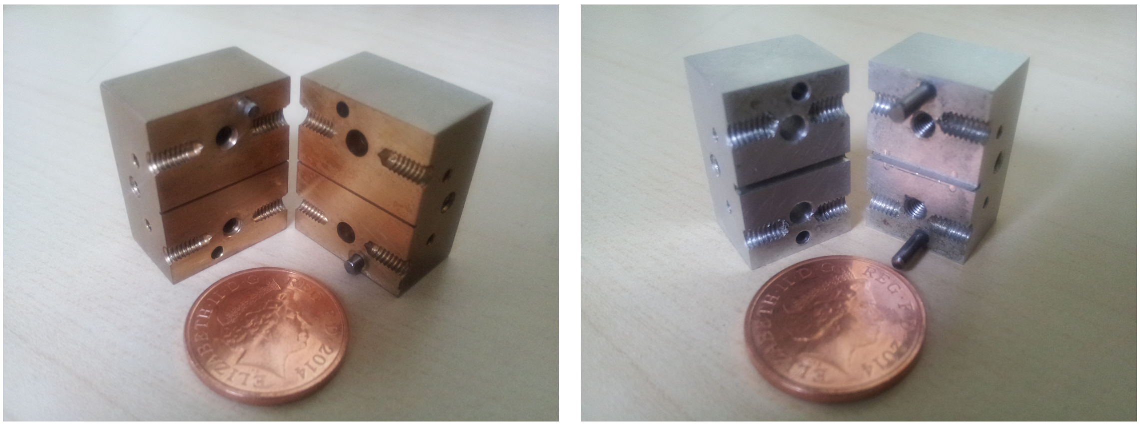

(a) A bronze WR-3 straight through waveguide.

(b) Aluminium waveguide block with a pocket cut-out

Figure 5.3: Photographs of waveguide blocks fabricated at the University of Leeds using two different materials.

There are several subtypes of these transitions, with the most common one, the unilateral transition, illustrated in Fig. 5.4[171]. Usually the transition is to slotline or coplanar waveguide. These are more suitable for surface mounted devices, such as diodes and transistors, and do more readily provide ground planes.

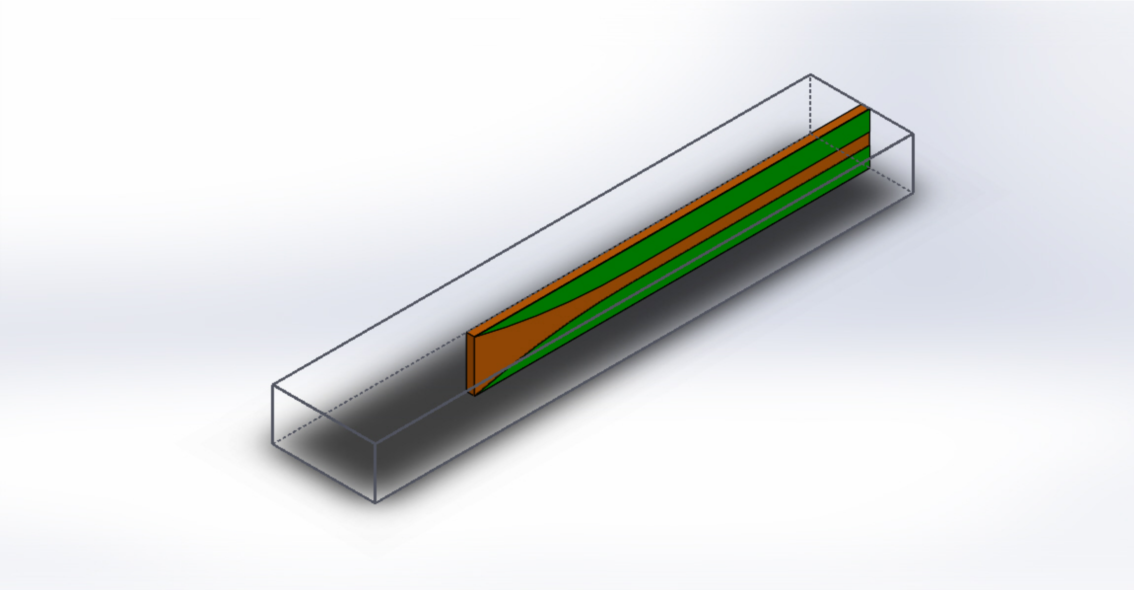

Figure 5.4: A sketch of a unilateral finline transition to slotline in a rectangular waveguide. Metallisation, shown in green is only present on one side of the substrate.

The finline transition is placed in the middle of a rectangular waveguide, where the electric field intensity $\vec{E}$ is at a maximum. The transition itself consists of thin (up to $\sim 100\ \mu m$) dielectric substrate with metallisation on one or both sides, depending on the type of finline used. The dielectric is usually one with low dielectric constant, in order to minimise losses and loading of waveguide[172]. The metallisation pattern can be divided into two parts, the transition taper and the actual planar circuit. The tapered section acts as an impedance transformer, and the shape of its profile can be optimised for different requirements, such as length, reflection coefficient, etc. As a result, the characteristic impedance Z_0 of the planar transmission line can be as high as 300 Ω[173, 174].

Mixers, triplers, and other circuits operating at frequencies above 100 GHz can be readily implemented in waveguide using finline transitions[73, 79]. In the case of mixers, both the RF and the LO signals are supplied to the circuit via waveguide, while the low frequency IF signal is extracted via planar transmission lines. An example of a sub-harmonic mixer realised as a finline circuit is presented in Fig. 5.5. This sort of transition enables use of mixers well into the sub-millimetre wave range.

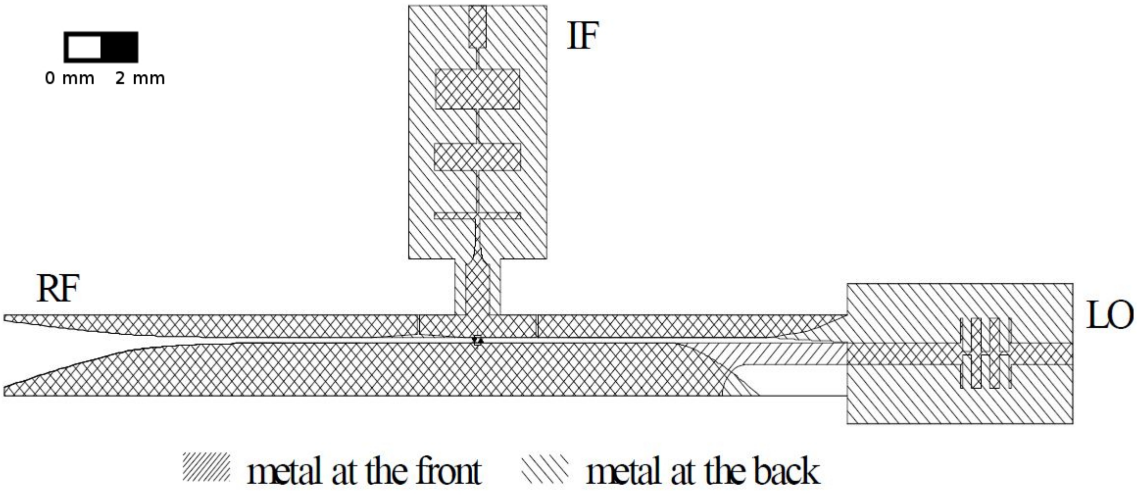

Figure 5.5: A sub-harmonic mixer in a planar circuit using finline transitions[175].

Another model of a waveguide mixer is shown in Fig. 5.6, where the planar circuit is again positioned in the middle of the waveguide wide wall and parts of it act as probes. In this case, the LO signal is fed through a waveguide with a transition to a reduced-height configuration, while the RF signal is picked up by a finline transition. Finally, the IF signal is extracted through a microstrip circuit.

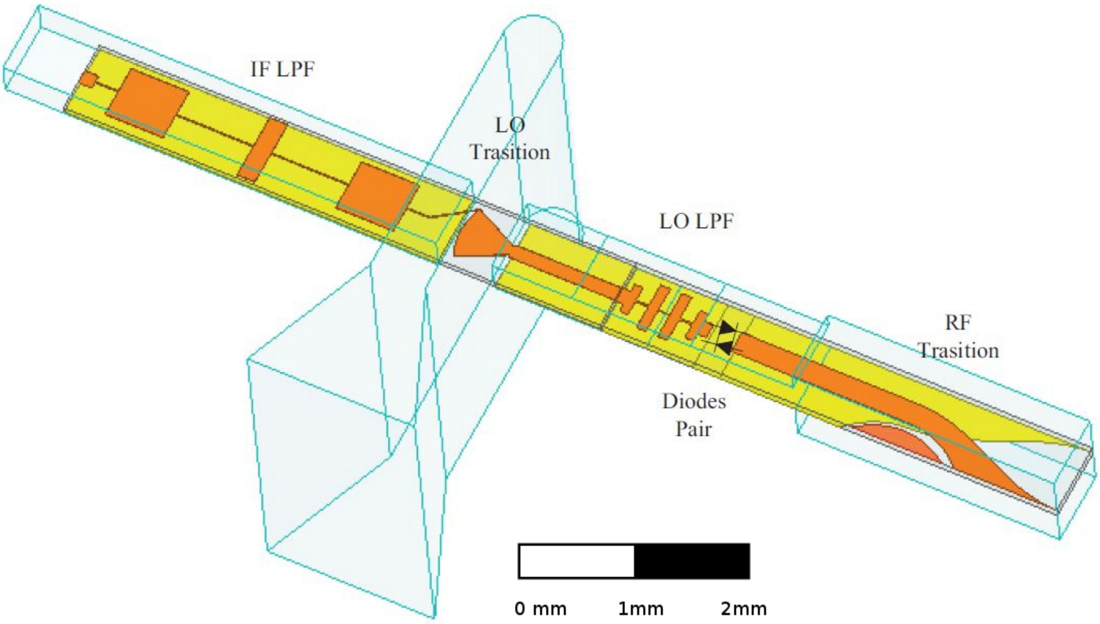

Figure 5.6: A model of a waveguide mixer for electromagnetic simulation purposes[62].

This sort of approach can be used with the microstrip and CPWG based SHMs discussed in Chapter 3, and incorporate them with a finline transition to construct mixers operating at millimetre and sub-millimetre wave frequencies, using rectangular waveguide as a low-loss transmission media.

5.3 Narrow-Wall Couplers

As was previously mentioned, a 3 dB coupler with low transmission losses is essential for the good performance of an RTD based reflection amplifier. Results reported in Chapter 4 suggest that such an amplifier could be designed for W-band frequencies and above. If the coupler is realised in waveguide, then the diodes themselves can be connected to its ports using stepped impedance transformers, or short waveguide to finline transitions.

Indeed, the complete mixer circuit and amplifier circuit can be designed on a single substrate and integrated with the 3 dB coupler to provide a mixer with a conversion gain. If this principle worked well, perhaps even the LO signal could be amplified if the dynamic range of the amplifiers would permit it.

A new facility has recently been opened at the University of Leeds, offering state-of-the-art water-jet guided laser cutter manufacturing capabilities. As a first step towards implementing RTD reflection based amplifiers in waveguide technology, 3 dB narrow-wall waveguide couplers were designed and manufactured for several different frequency bands.

5.3.1 Coupler Design

The couplers designed are single-aperture narrow-wall couplers. This type is well studied, and despite being the simplest form of a coupler, can provide an even power split with good isolation over a large bandwidth[176, 177].

The general shape of such a coupler is presented in Fig. 5.7, and the individual dimensions for four different designs are given in Table 5.1. The dimensions were optimised using Ansoft HFSS to allow for a 3 dB power split over as wide bandwidth as possible.

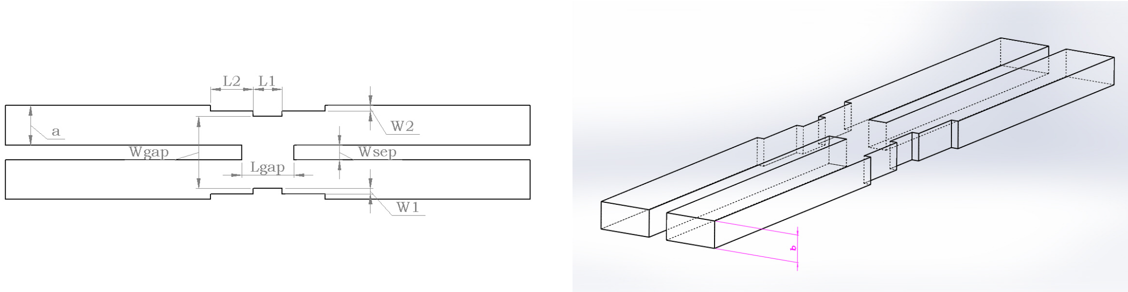

(a) Top-down view (b) Isometric view

Figure 5.7: A mechanical drawing of the general shape of a narrow-wall waveguide coupler, with dimensions used for design.

The frequency band over which the coupler has good performance is determined

Parameter	E-band	G-band	WR-3	WR-1
Frequency span	60 – 90 GHz	140 – 220 GHz	220 – 325 GHz	0.75 – 1.1 THz
a, $[mm]$	3.0988	1.2954	0.8636	0.254
b, $[mm]$	1.5494	0.6477	0.4318	0.127
L_{gap}, $[mm]$	4	1.7	1.14	0.33
W_{sep}, $[mm]$	1	0.47	0.28	0.08
$W_1 = W_2$, $[mm]$	0.5	0.18	0.14	0.04
L_1, $[mm]$	2	0.94	0.56	0.16
L_2, $[mm]$	3	1.4	0.86	0.25

Table 5.1: Optimised dimensions for narrow-wall waveguide couplers. The dimension W_{gap} is not given since it can be calculated from the other parameters.

by the TE_{20} and the TE_{30} modes' cut-off frequencies[178, 179]

$$2f_c\left(TE_{10}\right) < f < 3f_c\left(TE_{10}\right), \text{ or} \tag{5.1}$$

$$f_c\left(TE_{20}\right) < f < 1.5f_c\left(TE_{20}\right) \tag{5.2}$$

The length of the aperture of a narrow-wall coupler is $\sim \lambda_g$, whereas the width W_{gap} is sized to support TE_{20} but not TE_{30} mode. The additional stepped sections are added for bandwidth improvement.

5.3.2 Simulation Results

Initially, the four couplers were simulated in HFSS without including connecting circuits or modelling the waveguide blocks that would eventually house these couplers. These models, along with simulation results are shown in Fig. 5.8 and Fig. 5.9. The S-parameters are shown over the entire frequency range covered by each band. As can be seen, the designed structures have a very good 3 dB power split over a large bandwidth. Reflected power and attenuation to isolated port are maintained at -15 dB or less, making these couplers suitable for use. When compared to the planar transmission line couplers presented in Chapter 4, the waveguide ones offer superior performance. The next steps would be to design the waveguide block structures and manufacture them.

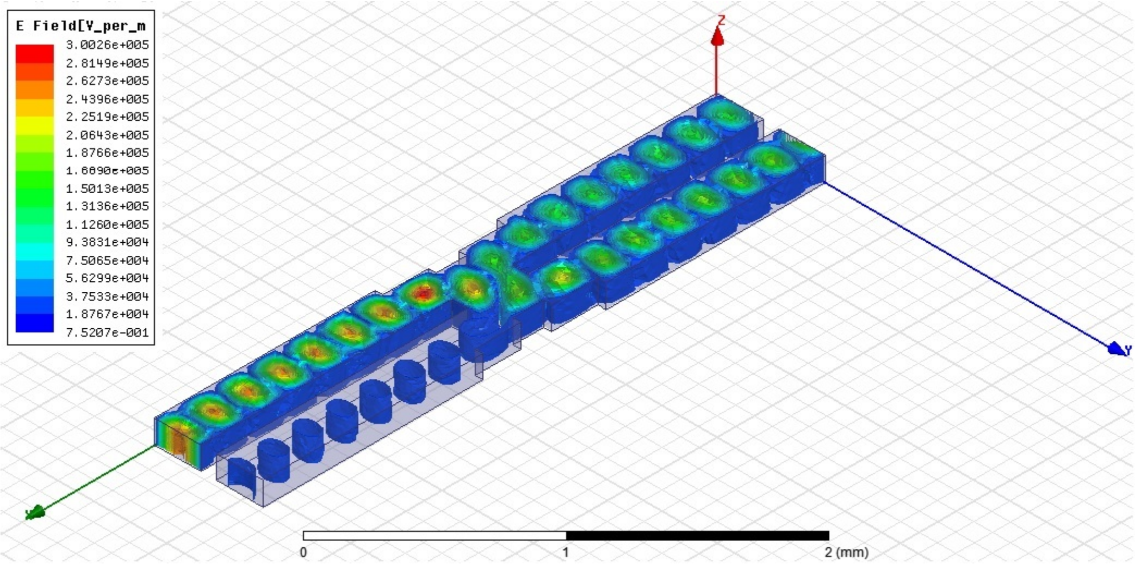

Figure 5.8: The model used for 3D FEM simulations, showing the electrical field inside the structure.

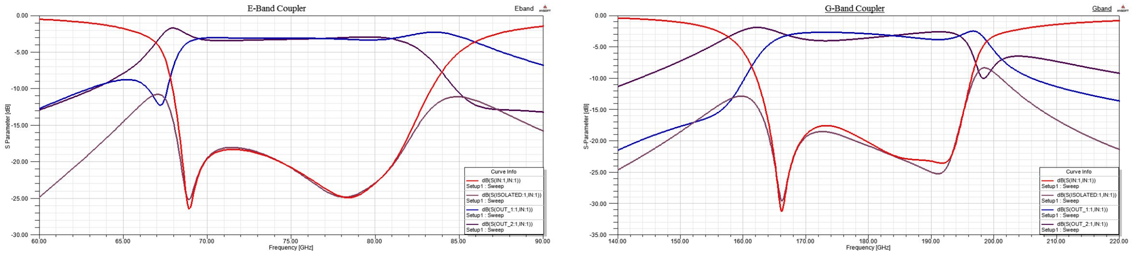

(a) E-Band Coupler (b) G-Band Coupler

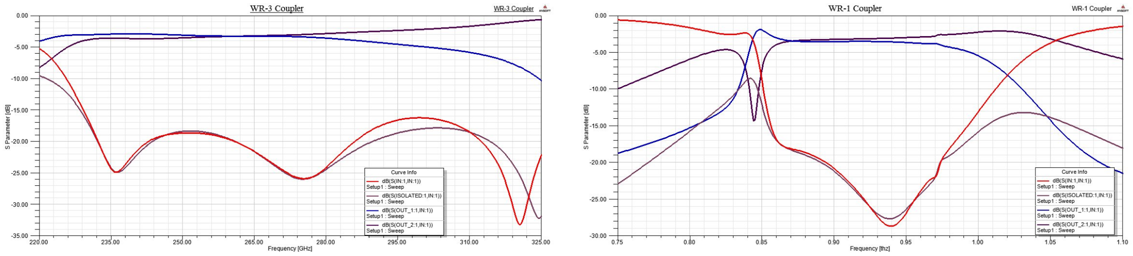

(c) WR-3 Band Coupler (d) WR-1 Band Coupler

Figure 5.9: Simulated S-parameters for narrow-wall waveguide couplers.

5.3.3 Block Design

An experimental approach was taken to the design of the waveguide coupler blocks. Because of the bends and the step transitions, using a slitting saw to fabricate an E-plane split block is not suitable. Instead, a metal shim sandwiched between two metal blocks is used. The waveguide topology is cut out in a metal sheet with a thickness equal to the narrow wall of the waveguide. Thus, when later the sheet is mounted between two metal blocks, the full waveguide is formed. A mechanical drawing for the one of these blocks is shown in Fig. 5.10. The top half of the split metal block is shown transparent. The shim itself is shown in green, and consists of the coupler area, together with connecting waveguide structure, and holes for alignment pins and tightening screws. In the manufacturing process, the shim would be wider and longer than the clamping blocks, and the excess would be cut out after the shim is sandwiched and the fastened in place.

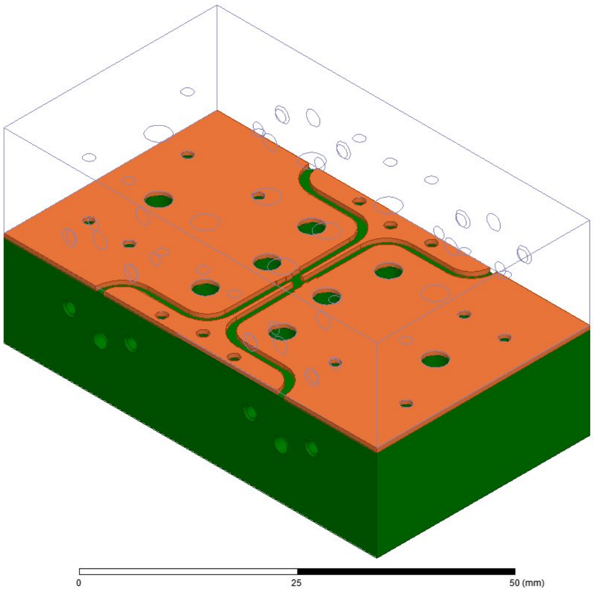

Figure 5.10: A 3D mechanical drawing of a G-band waveguide coupler, including middle shim.

One important issue that is caused by using this approach is the potential performance degradation from having a discontinuity along the narrow waveguide walls. To gauge the extent to which performance would deteriorate, small separations were introduced between the three components of the waveguide block before re-running the simulations. The results are summarised in Fig. 5.11. It can be seen that this type of waveguide block configuration is very sensitive to air gaps between the shim and the two clamping blocks, with even a small gap leading to the coupler becoming non-functional. However, as can be seen in Fig. 5.11a, if a good seal is achieved,

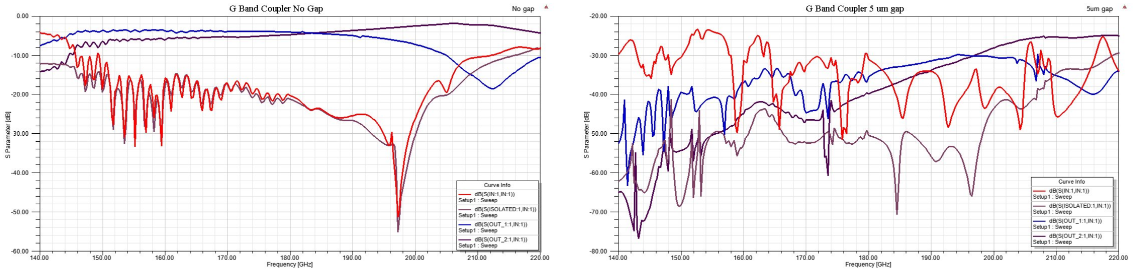

(a) No air gap

(b) 5 μm air gap

Figure 5.11: Simulated effect of an air gap between waveguide coupler block components on coupler performance.

the coupler block would still have good performance, albeit with some increase in loss. While the split is still somewhat even over a large bandwidth and the S_{11} and S_{41} parameters are below -15 dB, the additional transmission losses affect the power delivered to the two output ports.

To ensure a good interface contact between the shim and the two blocks, a couple of features were introduced to the design. Additional screws were added, to ensure tight fits between all three components. Furthermore, shoulders running parallel to the waveguide structure were added to both metal halves. Their height is 750 μm, and some part of it will act as a sacrificial layer in a polishing process, to ensure a smooth interface and as small a gap as possible. The final version of the waveguide block design is presented in Fig. 5.12. Only the bottom half of the block is shown. Additional length is added to the connecting waveguide structure, to ensure that there is sufficient space between the ports on each side for attaching waveguide heads of a vector network analyser (VNA). At the time of writing, the coupler shims and coupler blocks were still being fabricated.

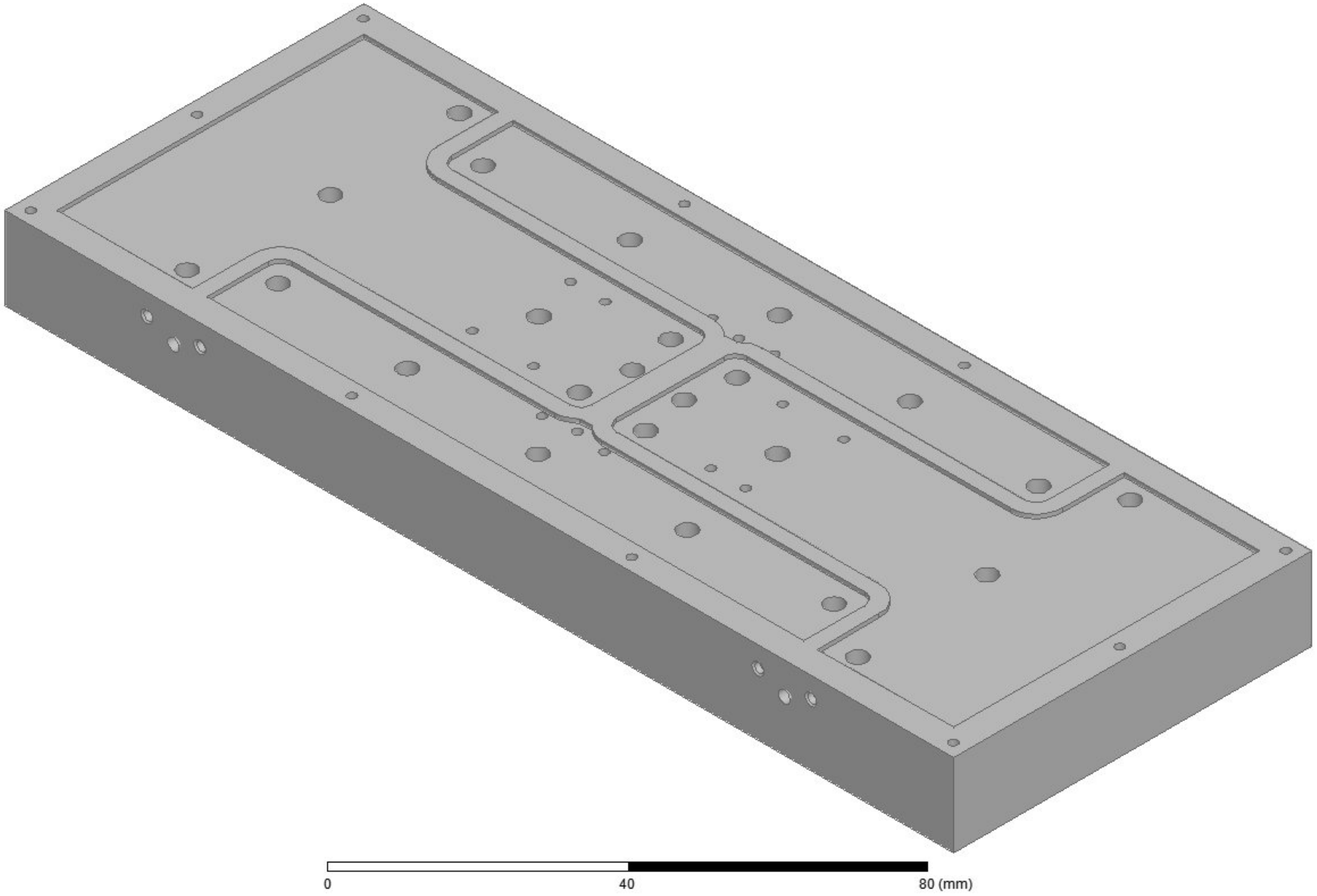

Figure 5.12: Bottom half of final design of waveguide coupler block, illustrating the shoulder structure.

5.4 Summary

The waveguide blocks presented in this Chapter would be instrumental in implementing the mixer and amplifier circuits, discussed in Chapter 3 and Chapter 4, at sub-millimetre wave frequencies and beyond. The split blocks, in combination with the finline transitions and circuits, can be used to accommodate the semiconductor devices into the low loss waveguide media.

The 3 dB narrow-wall couplers, which again offer lower losses and better performance than their CPWG counterparts, can be combined with the finline transitions to implement narrow-band RTD based amplifiers with high gain, in order to improve the conversion loss performance of RTD base mixers.

The limiting factors to the improvement offered by waveguide circuits over planar ones have mainly to do with fabrication tolerances and metals used. Especially in the case of waveguide blocks with a split in the H-plane, which are demonstrated to be sensitive to gaps, surface roughness parameters and fastening methods need to be carefully selected and used. Longer fabrication times would also necessitate extensive optimisation routines carried out first.

Chapter 6

Conclusion and Future Work

The final Chapter of this thesis fulfils a dual role. On one hand, it provides a brief summary of the work presented in Chapters 3 through 5, together with the main conclusions drawn from the results discussed in said chapters. On the other hand, ideas and directions for future work, that builds on what has been done so far, are given here.

6.1 Summary and Conclusions

Extensive studies and simulations were performed using the resonant-tunnelling diodes fabricated at the University of Leeds from three different semiconductor layers, also grown here. This was done at two main frequency ranges, centred around 20 GHz and 100 GHz, with the main purpose of determining the devices' suitability for use in sub-harmonic mixer circuits, and later, in amplifiers. This was paired with device measurements and modelling in the commercially available software packages Agilent ADS and Ansoft HFSS. Furthermore, waveguide circuits and manufacturing capabilities were also investigated in preparation for circuit design at sub-millimetre wave frequencies.

A parametric study of the effect of current density and junction capacitance, i.e. different layers and different device sizes, on potential performance was carried out, as an aid to future design. The results obtained from these simulations can be summarised as promising and encouraging. Even though the current best predicted performance is outmatched by industry's very best performing analogues, there are plenty of parameters to tune in order to improve. In particular, the aim was to investigate the use of simple two terminal devices as mixers and amplifiers elements, that have been relatively easily fabricated to provide frequency mixing and amplification at millimetre and sub-millimetre wave range.

The sub-harmonic mixers, designed for an RF frequency of 100 GHz, exhibit average overall frequency conversion loss of about 20 dB. A couple of options for boosting that into the 10 dB range have been suggested in this thesis, namely via optimised circuit design, and via device size scaling. Scaled devices would also be needed if a sub-harmonic mixer circuit design is attempted at the other centre frequency of interest, 424 GHz.

Both the reflection based amplifiers and the active transmission line concepts that were presented in Chapter 4 could produce positive results with the currently available devices. Achieving even several dB of RF signal amplification at frequencies of 100 GHz and more will be incredibly beneficial. Even higher gain, on the order of 15 dB – 20 dB, can be accomplished via use of narrow-band resonant peaks in the frequency response of these circuits. Even here, there is room for improvement through diode scaling and better circuit design, namely 90° coupler design.

As for the devices themselves, the main desired characteristics are high non-linearity in the first PDR region, close to 0 V bias, in the case of mixers; and a large and linear NDR region, in the case of amplifying circuits. While high current density would be beneficial for both applications, separate layers might need to be grown for amplifiers and mixers. Small junction capacitance is also preferable to both. Of the currently available devices, L939 D4 is the best performing diode for the purposes of sub-harmonic mixing, while L938 D1, D2; and L939 D1 are the ones that offer good amplifier gain.

Finally, specific approaches to utilising waveguide transmission media have been studied, with prototype components for sub-harmonic mixers and reflection based amplifiers fabricated, or in the process of fabrication, as a way to further improve performance and pave the way to RTD circuits at sub-millimetre wave frequencies.

6.2 Directions and Ideas for Future Work

The next logical step of the study of RTDs will be to fabricate the designed circuits, mount devices in them, and perform measurements. These will be crucial to the device model validation and further circuit design. At the time of writing, a mask set had been designed by the author and made by Compugraphics Inc., and circuit fabrication was about to begin. This mask also includes calibration structures in accordance with the TRL model[180] for diode measurements and equivalent circuit modelling, as an alternative to the ADS SDD model currently used.

Manufacturing smaller resonant-tunnelling diodes will follow, in order to push for circuits operating in the sub-millimetre wave range. This could be done via optical scaling of currently available lithographic masks, although the practical limit would be widths $\sim 0.7\mu m$ and lengths of perhaps $0.5\ \mu m$ – $1\ \mu m$. Nonetheless this represents a reduction in size, compared with present smallest devices, of close to 100. This would be more than enough to realise the scaled diodes investigated in Chapter 3 and Chapter 4.

Alternatively, cutting and slicing existing diodes using a focused Ion Beam instrument can be employed, although the electrical consequences of this process are difficult to predict. Another option would be to use an EBL machine.

Some of the foundation for circuit design at sub-millimetre frequencies, where waveguide circuits would need to be employed, has already been established. Further work in this area would include the design and optimisation of planar media to waveguide transitions, which is ongoing with a fellow PhD student.

Finally, alternative semiconductor layer structures for RTDs can be explored. Adjusting the barrier thicknesses, as well as material composition, could result in significantly better performing devices. Trying other material combinations besides GaAs/AlGaAs is also an avenue that can be pursued.

Overall, it can be argued that the results obtained so far are sufficiently good to warrant pursuit of these ideas and justify continuing research into resonant-tunnelling diodes application to millimetre and sub-millimetre wave circuits and subsystems.

Bibliography

[1] R. Tsu and L. Esaki, “Tunneling in a finite superlattice,” *Applied Physics Letters*, vol. 22, no. 11, pp. 562–564, 1973.

[2] J. Chen, J. G. Chen, C. H. Yang, and R. A. Wilson, “The IV characteristics of doublebarrier resonant tunneling diodes: Observation and calculation on their temperature dependence and asymmetry,” *Journal of Applied Physics*, vol. 70, no. 6, pp. 3131–3136, 1991.

[3] K. Arai and M. Yamamoto, “Experimental demonstration of single peak IV characteristics in a novel resonant tunneling diode,” *Electron Device Letters, IEEE*, vol. 17, no. 10, pp. 491–493, 1996.

[4] M. Cohn, J. E. Degenford, and B. A. Newman, “Harmonic Mixing with an Antiparallel Diode Pair,” *Microwave Theory and Techniques, IEEE Transactions on*, vol. 23, no. 8, pp. 667–673, 1975.

[5] E. R. Carlson, M. V. Schneider, and T. F. McMaster, “Subharmonically Pumped Millimeter-Wave Mixers,” *Microwave Theory and Techniques, IEEE Transactions on*, vol. 26, no. 10, pp. 706–715, 1978.

[6] S. A. Maas, *Microwave Mixers*, 2nd ed. Artech House, 1993.

[7] ——, *Nonlinear Microwave and RF Circuits*, 2nd ed. Artech House, 2003.

[8] D. P. Steenson, “The relevance of quantum barrier devices to millimetre wave systems,” in *Proc. IEE Colloquium Terahertz Technology.*

[9] V. P. Dragunov and D. V. Boldyrev, "Calculations of electrical characteristics of resonant tunneling structures," in *Electronic Instrument Engineering Proceedings, 1998. APEIE-98. Volume 1. 4th International Conference on Actual Problems of*, pp. 442–446.

[10] M. A. Remnev, I. Y. Kateev, and V. F. Elesin, "Effect of Spacer Layers on CurrentVoltage Characteristics of Resonant Tunneling Diode," *Semiconductors*, vol. 44, no. 8, pp. 1034–1039, 2010.

[11] A. Matiss, W. Brockerhoff, A. Poloczek, W. Prost, and F. J. Tegude, "Low-Temperature DC and RF Measurement and Modelling of InGaAs-InAlAs Resonant Tunneling Diodes down to 15 K," in *European Microwave Integrated Circuits Conference, 2006. The 1st*, pp. 344–347.

[12] D. Lippens, E. Barbier, and P. Mounaix, "Fabrication of high-performance $Al_xGa_{1-x}As/In_yGa_{1-y}As/GaAs$ resonant tunneling diodes using a microwave-compatible technology," *Electron Device Letters, IEEE*, vol. 12, no. 3, pp. 114–116, 1991.

[13] J. H. Smet, T. P. E. Broekaert, and C. G. Fonstad, "Peak-to-valley current ratios as high as 50:1 at room temperature in pseudomorphic $In_{0.53}Ga_{0.47}As/AlAs/InAs$ resonant tunneling diodes," *Journal of Applied Physics*, vol. 71, no. 5, pp. 2475–2477, 1992.

[14] W. Lian, "Resonant Tunneling Diode Mixer and Multiplier," Ph.D. dissertation, 1994.

[15] N. V. Alkeev, S. V. Averin, V. E. Lyubchenko, E. I. Golant, and A. B. Pashkovskii, "Resonant-Tunneling Diode as an Active Element of Lownoise Terahertz Subharmonic Mixer," in *Proc. Int. Conf. Microwaves, Radar & Wireless Communications MIKON 2006*, pp. 889–892.

[16] N. Alkeev, S. Averin, A. Dorofeev, N. Gladysheva, and M. Torgashin, "GaAs/AlAs resonant-tunneling diode for subharmonic mixers," *Russian Microelectronics*, vol. 39, no. 5, pp. 331–339, 2010.

[17] 686 WG – Terminology Working Group, "521-2002 - IEEE Standard Letter Designations for Radar-Frequency Bands," 2009.

[18] L. Belov, S. Smolskiy, and V. Kochemasov, *Handbook of RF, Microwave, and Millimeter-Wave Components.* Artech House, 2012.

[19] ITU Radio Regulations, "Volume 1, Article 2," 2008. [Online]. Available: http://life.itu.int/radioclub/rr/art02.htm

[20] D. M. Sheen, D. L. McMakin, and T. E. Hall, "Active millimeter-wave and sub-millimeter-wave imaging for security applications," in *Infrared, Millimeter and Terahertz Waves (IRMMW-THz), 2011 36th International Conference on*, pp. 1–3.

[21] K. S. J. Murphy, R. Appleby, G. Sinclair, A. McClumpha, K. Tatlock, R. Doney, and I. Hutcheson, "Millimetre wave aviation security scanner," in *Security Technology, 2002. Proceedings. 36th Annual 2002 International Carnahan Conference on*, pp. 162–166.

[22] L. Hai-Bo, H. Zhong, N. Karpowicz, Y. Chen, and Z. Xi-Cheng, "Terahertz Spectroscopy and Imaging for Defense and Security Applications," *Proceedings of the IEEE*, vol. 95, no. 8, pp. 1514–1527, 2007.

[23] X. Feifei, S. Hongyan, and X. Yong, "Terahertz imaging system for remote sensing and security applications," in *Antennas and Propagation (APCAP), 2014 3rd Asia-Pacific Conference on*, pp. 1335–1338.

[24] R. Appleby and R. N. Anderton, “Millimeter-Wave and Submillimeter-Wave Imaging for Security and Surveillance,” *Proceedings of the IEEE*, vol. 95, no. 8, pp. 1683–1690, 2007.

[25] P. H. Siegel, “Terahertz Technology in Biology and Medicine,” *Microwave Theory and Techniques, IEEE Transactions on*, vol. 52, no. 10, 2004.

[26] E. Pickwell and V. P. Wallace, “Biomedical applications of terahertz technology,” *Journal of Physics D: Applied Physics*, vol. 39, no. 17, p. R301, 2006.

[27] I. McAuley, L. Young, M. Gradziel, W. Lanigan, C. O’Sullivan, J. A. Murphy, R. Mahon, R. May, and N. Trappe, “Millimetre-wave and Terahertz Imaging Systems with Medical Applications,” in *Infrared Millimeter Waves and 14th International Conference on Teraherz Electronics, 2006. IRMMW-THz 2006. Joint 31st International Conference on*, pp. 371–371.

[28] P. H. Siegel, “IRMMW-THz in space: The golden age,” in *Infrared and Millimeter Waves, 2007 and the 2007 15th International Conference on Terahertz Electronics. IRMMW-THz. Joint 32nd International Conference on*, pp. 106–108.

[29] D. Vavriv, “MM-wave meteoradars: development, design, and research data,” in *Applied Electromagnetics and Communications, 2003. ICECom 2003. 17th International Conference on*, pp. 13–17.

[30] M. Lucente, A. Salome, E. Limiti, M. Ferri, L. Fiorani, W. R. Saleh, C. Stallo, M. Ruggieri, and G. Codispoti, “PLATON: Satellite remote sensing and telecommunication by using millimetre waves,” in *Satellite Telecommunications (ESTEL), 2012 IEEE First AESS European Conference on*, pp. 1–6.

[31] S. C. Reising, T. C. Gaier, S. Padmanabhan, L. Boon, P. Kangaslahti, S. T. Brown, and J. Bosch-Lluis, “Microwave and millimeter-wave radiometers for

CubeSat deployment for remote sensing of the earth's atmosphere," in *Infrared, Millimeter, and Terahertz waves (IRMMW-THz), 2014 39th International Conference on*, pp. 1–1.

[32] J. Yang, W. L. Shan, S. C. Shi, Q. J. Yao, Y. X. Zuo, S. H. Chen, A. Q. Cao, and Z. H. Lin, "The Superconducting Spectroscopic Array Receiver (SSAR) for Millimeter-wave Radio Astronomy," in *Millimeter Waves, 2008. GSMM 2008. Global Symposium on*, pp. 177–179.

[33] T. Kleine-Ostmann and T. Nagatsuma, "A Review on Terahertz Communications Research," *Journal of Infrared, Millimeter, and Terahertz Waves*, vol. 32, no. 2, pp. 143–171, 2011.

[34] S. Ho-Jin and T. Nagatsuma, "Present and Future of Terahertz Communications," *Terahertz Science and Technology, IEEE Transactions on*, vol. 1, no. 1, pp. 256–263, 2011.

[35] R. Waterhouse and D. Novack, "Realizing 5G: Microwave Photonics for 5G Mobile Wireless Systems," *Microwave Magazine, IEEE*, vol. 16, no. 8, pp. 84–92, 2015.

[36] Z. Gao, L. Dai, D. Mi, Z. Wang, M. Imran, and M. Shakir, "MmWave massive-MIMO-based wireless backhaul for the 5G ultra-dense network," *Wireless Communications, IEEE*, vol. 22, no. 5, pp. 13–21, 2015.

[37] T. Rappaport, S. Sun, R. Mayzus, H. Zhao, Y. Azar, K. Wang, G. Wong, J. Schulz, M. Samimi, and F. Gutierrez, "Millimeter Wave Mobile Communications for 5G Cellular: It Will Work!" *Access, IEEE*, vol. 1, pp. 335 – 349, 2013.

[38] B. Schuppert, "Analysis and Design of Microwave Balanced Mixers," *Microwave Theory and Techniques, IEEE Transactions on*, vol. 34, no. 1, pp. 120–128, 1986.

[39] N. V. Alkeev, S. V. Averin, A. A. Dorofeev, E. I. Golant, and A. B. Pashkovskii, "New Terahertz Mixer Based on Resonant-Tunneling Diode," in *Proc. Sixth Int. Kharkov Symp. Physics and Engineering of Microwaves, Millimeter and Submillimeter Waves and Workshop Terahertz Technologies MSMW '07*, vol. 1, pp. 192–194.

[40] T. Shiode, T. Mukai, M. Kawamura, and T. Nagatsuma, "Giga-bit wireless communication at 300 GHz using resonant tunneling diode detector," in *Microwave Conference Proceedings (APMC), 2011 Asia-Pacific*, pp. 1122–1125.

[41] S. Sze, *Physics of Semiconductor Devices.* Wiley-Interscience, 1969.

[42] D. Vakhshoori and S. Wang, "Resonant tunneling diodes with AlAs barrier: Guides for improving room-temperature operation," *Journal of Applied Physics*, vol. 62, no. 8, pp. 3474–3476, 1987.

[43] P. H. Siegel, "Terahertz technology," *Microwave Theory and Techniques, IEEE Transactions on*, vol. 50, no. 3, pp. 910–928, 2002.

[44] C. Armstron, "The Truth About Terahertz," 2012. [Online]. Available: http://spectrum.ieee.org/aerospace/military/the-truth-about-terahertz

[45] L. Li, L. Chen, J. Zhu, J. Freeman, P. Dean, A. Valavanis, A. Davies, and E. Linfield, "Terahertz quantum cascade lasers with ¿1 W output powers," *Electronics Letters*, vol. 50, no. 4, pp. 309–311, 2014.

[46] M. Feiginov, H. Kanaya, S. Suzuki, and M. Asada, "Operation of resonant-tunneling diodes with strong back injection from the collector at frequencies up to 1.46 THz," *Applied Physics Letters*, vol. 104, no. 24, 2014. [Online]. Available: http://scitation.aip.org/content/aip/journal/apl/104/24/10.1063/1.4884602

[47] J. Wang, A. Ofiare, K. Alharbi, R. Brown, A. Khalid, D. Cumming, and E. Wasige, “MMIC resonant tunneling diode oscillators for THz applications,” in *Ph.D. Research in Microelectronics and Electronics (PRIME), 2015 11th Conference on*, 2015, pp. 262–265.

[48] R. Letizia, M. Mineo, and C. Paoloni, “Photonic Crystal-Structures for THz Vacuum Electron Devices,” *Electron Devices, IEEE Transactions on*, vol. 62, no. 1, pp. 178–183, Jan 2015.

[49] U. L. Rohde and D. P. Newkirk, *RF/microwave circuit design for wireless applications.* John Wiley, 2000.

[50] *Radio broadcasting systems; Very High Frequency (VHF), frequency modulated, sound broadcasting transmitters*, Online, European Telecommunications Standards Institute Std. ETS 300 384, January 1995.

[51] Philips Semiconductors, “TDA1596T IF amplifier/demodulator for FM radio receivers,” Online, April 1991.

[52] G. D. Vendelin, A. M. Pavio, and U. L. Rohde, *Microwave circuit design using linear and nonlinear techniques.* Wiley, 2005.

[53] E. Chan, “Design of a 5-6 GHz single balanced Schottky diode mixer,” in *Applied Electromagnetics, 2003. APACE 2003. Asia-Pacific Conference on*, pp. 67–71.

[54] H. I. Fujishiro, Y. Ogawa, T. Hamada, and T. Kimura, “SSB MMIC mixer with subharmonic LO and CPW circuits for 38 GHz band applications,” *Electronics Letters*, vol. 37, no. 7, pp. 435–436, 2001.

[55] G. Bryant, *Principles of Microwave Measurements.* Peter Peregrinus Ltd., 1993.

[56] A. R. Kerr, “Noise and Loss in Balanced and Subharmonically Pumped Mixers: Part I–Theory,” *Microwave Theory and Techniques, IEEE Transactions on*, vol. 27, no. 12, pp. 938–943, 1979.

[57] ——, “Noise and Loss in Balanced and Subharmonically Pumped Mixers: Part II–Application,” *Microwave Theory and Techniques, IEEE Transactions on*, vol. 27, no. 12, pp. 944–950, 1979.

[58] A. Przadka, K. J. Webb, and D. B. Janes, “Two-port noise and impedance measurements for two-terminal devices with a resonant tunneling diode example,” *Microwave Theory and Techniques, IEEE Transactions on*, vol. 46, no. 9, pp. 1215–1220, 1998.

[59] B. Thomas, A. Maestrini, J. Ward, E. Schlecht, G. Chattopadhyay, J. Gill, C. Lee, R. Lin, and I. Mehdi, “Terahertz cooled sub-harmonic Schottky mixers for planetary atmospheres,” 2009.

[60] X. Mei, W. Yoshida, M. Lange, J. Lee, J. Zhou, P.-H. Liu, K. Leong, A. Zamora, J. Padilla, S. Sarkozy, R. Lai, and W. Deal, “First Demonstration of Amplification at 1 THz Using 25-nm InP High Electron Mobility Transistor Process,” *Electron Device Letters, IEEE*, vol. 36, no. 4, pp. 327–329, April 2015.

[61] M. W. Chapman and S. Raman, “A 60 GHz uniplanar MMIC 4X subharmonic mixer,” in *Microwave Symposium Digest, 2001 IEEE MTT-S International*, vol. 1, pp. 95–98 vol.1.

[62] C. Ling, M. Jingchao, X. Mingming, Y. Weihua, and L. Xin, “Design of a 220GHz 4X subharmonical mixer using terahertz GaAs Schottky diodes BITD1530A,” in *Microwave and Millimeter Wave Technology (ICMMT), 2012 International Conference on*, vol. 4, pp. 1–4.

[63] S. Raman, F. Rucky, and G. M. Rebeiz, “A high-performance W-band uniplanar subharmonic mixer,” *Microwave Theory and Techniques, IEEE Transactions on*, vol. 45, no. 6, pp. 955–962, 1997.

[64] R. S. Tahim, T. Pham, and K. Chang, “Millimetre-wave microstrip subharmonically pumped mixer,” *Electronics Letters*, vol. 21, no. 19, pp. 861–862, 1985.

[65] R. G. Hicks and P. J. Khan, “Numerical Analysis of Subharmonic Mixers Using Accurate and Approximate Models,” *Microwave Theory and Techniques, IEEE Transactions on*, vol. 30, no. 12, pp. 2113–2120, 1982.

[66] W. Y. Liu and D. P. Steenson, “Investigation of subharmonic mixer based on a quantum barrier device,” *Microwave Theory and Techniques, IEEE Transactions on*, vol. 48, no. 4, pp. 757–763, 2000.

[67] P. M. Smith, D. R. Conn, and J. Xu, “The limits of resonant tunneling diode subharmonic mixer performance,” *Journal of Applied Physics*, vol. 66, no. 3, pp. 1454–1458, 1989.

[68] J. Hesler, “The Design and Analysis of Antiparallel Schottky Diode Mixers,” 2000.

[69] I. Mehdi, S. M. Marazita, D. A. Humphrey, L. Trong-Huang, R. J. Dengler, J. E. Oswald, A. J. Pease, S. C. Martin, W. L. Bishop, T. W. Crowe, and P. H. Siegel, “Improved 240-GHz subharmonically pumped planar Schottky diode mixers for space-borne applications,” *Microwave Theory and Techniques, IEEE Transactions on*, vol. 46, no. 12, pp. 2036–2042, 1998.

[70] L. Che-Hung, L. Yu-Ann, C. Jui-Chieh, and W. Yeong-Her, “A 23-37 GHz Miniature MMIC Subharmonic Mixer,” *Microwave and Wireless Components Letters, IEEE*, vol. 17, no. 9, pp. 679–681, 2007.

[71] M. W. Chapman and S. Raman, "A 60-GHz uniplanar MMIC 4x subharmonic mixer," *Microwave Theory and Techniques, IEEE Transactions on*, vol. 50, no. 11, pp. 2580–2588, 2002.

[72] S. Sarkar, P. Sen, S. Pinel, L. Chang-Ho, and J. Laskar, "Si-based 60GHz 2X Subharmonic Mixer for Multi-Gigabit Wireless Personal Area Network Application," in *Microwave Symposium Digest, 2006. IEEE MTT-S International*, pp. 1830–1833.

[73] S. Marsh, B. Alderman, D. Matheson, and P. de Maagt, "Design of low-cost 183 GHz subharmonic mixers for commercial applications," *Circuits, Devices & Systems, IET*, vol. 1, no. 1, pp. 1–6, 2007.

[74] T. Waliwander, M. Crowley, M. Fehilly, D. Lederer, J. Pike, L. Floyd, and D. O'Connell, "Sub-millimeter Wave 183 GHz and 366 GHz MMIC membrane sub-harmonic mixers," in *Microwave Symposium Digest (MTT), 2011 IEEE MTT-S International*, pp. 1–4.

[75] J. V. Siles, J. Grajal, and A. Di Carlo, "Design of Submillimeter Schottky Mixers Under Flat-Band Conditions Using an Improved Drift-Diffusion Model," *Microwave and Wireless Components Letters, IEEE*, vol. 19, no. 3, pp. 167–169, 2009.

[76] B. Thomas, A. Maestrini, and G. Beaudin, "A low-noise fixed-tuned 300-360-GHz sub-harmonic mixer using planar Schottky diodes," *Microwave and Wireless Components Letters, IEEE*, vol. 15, no. 12, pp. 865–867, 2005.

[77] J. Treuttel, A. Maestrini, B. Alderman, H. Wang, D. Matheson, and P. De Maagt, "Design of a Combined Tripler-Subharmonic Mixer at 330 GHz for Multipixel Application Using European Schottky Diodes," 2010.

[78] H. Yu, Y. Mengxia, and M. Wei, “Simulation design of submillimeter wave subharmonic mixer,” in *Microwave Technology and Computational Electromagnetics, 2009. ICMTCE. International Conference on*, pp. 231–234.

[79] B. Thomas, B. Alderman, D. Matheson, and P. de Maagt, “A Combined 380 GHz Mixer/Doubler Circuit Based on Planar Schottky Diodes,” *Microwave and Wireless Components Letters, IEEE*, vol. 18, no. 5, pp. 353–355, 2008.

[80] J. Hesler, K. Hui, S. He, and T. Crowe, “A FIXED-TUNED 400 GHz SUB-HARIVIONIC MIXER USING PLANAR SCHOTTKY DIODES,” 1999.

[81] B. Thomas, J. Gill, A. Maestrini, C. Lee, R. Lin, S. Sin, A. Peralta, and I. Mehdi, “An integrated 520-600 GHz sub-harmonic mixer and tripler combination based on GaAs MMIC membrane planar Schottky diodes,” in *Infrared Millimeter and Terahertz Waves (IRMMW-THz), 2010 35th International Conference on*, pp. 1–2.

[82] E. Schlecht, J. Gill, R. Dengler, R. Lin, R. Tsang, and I. Mehdi, “A Unique 520-590 GHz Biased Subharmonically-Pumped Schottky Mixer,” *Microwave and Wireless Components Letters, IEEE*, vol. 17, no. 12, pp. 879–881, 2007.

[83] J. Schur, M. Ruf, and L. P. Schmidt, “Design of a 4th harmonic Schottky diode mixer for THz frequencies,” in *Infrared and Millimeter Waves, 2007 and the 2007 15th International Conference on Terahertz Electronics. IRMMW-THz. Joint 32nd International Conference on*, pp. 756–757.

[84] I. Mehdi, T. H. Lee, D. A. Humphrey, S. C. Martin, R. J. Dengler, J. E. Oswald, A. Pease, R. P. Smith, and P. H. Siegel, “600 GHz planar-Schottky-diode subharmonic waveguide mixers,” in *Microwave Symposium Digest, 1996., IEEE MTT-S International*, vol. 1, pp. 377–380 vol.1.

[85] I. Mehdi, P. H. Siegel, D. A. Humphrey, T. H. Lee, R. J. Dengler, J. E. Oswald, A. Pease, R. Lin, H. Eisele, R. Zimmermann, and N. Erickson, “An all solid-

state 640 GHz subharmonic mixer," in *Microwave Symposium Digest, 1998 IEEE MTT-S International*, vol. 2, pp. 403–406 vol.2.

[86] J. V. Siles, J. Grajal, and V. Krozer, "Design of Subharmonically Pumped Schottky Mixers for Submillimetre-wave Applications," in *European Microwave Integrated Circuits Conference, 2006. The 1st*, pp. 145–148.

[87] P. Wilkinson, M. Henry, H. Wang, H. Sanghera, B. Alderman, P. Steenson, and D. Matheson, "A 664 GHz Sub-Harmonic Schottky Mixer," in *Twenty-First International Symposium on Space Terahertz Technology*, p. 413.

[88] B. Thomas, A. Maestrini, D. Matheson, I. Mehdi, and P. de Maagt, "Design of an 874 GHz biasable sub-harmonic mixer based on MMIC membrane planar schottky diodes," in *Infrared, Millimeter and Terahertz Waves, 2008. IRMMW-THz 2008. 33rd International Conference on*, pp. 1–2.

[89] T. W. Crowe, R. J. Mattauch, H. P. Roser, W. L. Bishop, W. C. B. Peatman, and X. Liu, "GaAs Schottky diodes for THz mixing applications," *Proceedings of the IEEE*, vol. 80, no. 11, pp. 1827–1841, 1992.

[90] T. Ishii, *Handbook of Microwave Technology: Components and Devices.* Elsevier Science, 2013.

[91] K. Du and M. Swamy, *Wireless Communication Systems: From RF Subsystems to 4G Enabling Technologies.* Cambridge University Press, 2010.

[92] O. Berger, "Gaas mesfet, hemt and hbt competition with advanced si rf technologies." [Online]. Available: http://www.gaas.org/Digests/1999/PDF/59.pdf

[93] T. K. Johansen, J. Vidkjr, V. Krozer, A. Konczykowska, M. Riet, F. Jorge, and T. Djurhuus, "A High Conversion-Gain Q-Band InP DHBT Subharmonic

Mixer Using LO Frequency Doubler," *Microwave Theory and Techniques, IEEE Transactions on*, vol. 56, no. 3, pp. 613–619, 2008.

[94] M. Varonen, M. Karkkainen, J. Riska, P. Kangaslahti, and K. A. I. Halonen, "Resistive HEMT mixers for 60-GHz broad-band telecommunication," *Microwave Theory and Techniques, IEEE Transactions on*, vol. 53, no. 4, pp. 1322–1330, 2005.

[95] T. SOLLNER, E. BROWN, and H. LE, "Microwave and Millimeter-Wave Resonant-Tunneling Devices," *The Lincoln Laboratory Journal*, vol. 1, 1988.

[96] E. R. Brown, J. R. Soderstrom, C. D. Parker, L. J. Mahoney, K. M. Molvar, and T. C. McGill, "Oscillations up to 712 GHz in InAs/AlSb resonant-tunneling diodes," *Applied Physics Letters*, vol. 58, no. 20, pp. 2291–2293, 1991.

[97] S. Sakr, E. Warde, M. Tchernycheva, and F. H. Julien, "Ballistic transport in GaN/AlGaN resonant tunneling diodes," *Journal of Applied Physics*, vol. 109, no. 2, p. 023717, 2011.

[98] W. Jubadi, M. Md Zawawi, and M. Missous, "Simulative study on physical modelling of submicrometer highly-strained In0.8Ga0.2As/AlAs resonant tunnelling diode," in *Advanced Semiconductor Devices Microsystems (ASDAM), 2014 10th International Conference on*, 2014.

[99] A. Fedyay and V. Moskaliuk, "Modeling of resonant-tunneling diode with Quant ST," in *Modern Problems of Radio Engineering Telecommunications and Computer Science (TCSET), 2012 International Conference on*, Feb 2012, pp. 455–456.

[100] S. Jian Ping, G. I. Haddad, P. Mazumder, and J. N. Schulman, "Resonant tunneling diodes: models and properties," *Proceedings of the IEEE*, vol. 86, no. 4, pp. 641–660, 1998.

[101] L. L. Chang, L. Esaki, and R. Tsu, “Resonant tunneling in semiconductor double barriers,” *Applied Physics Letters*, vol. 24, no. 12, pp. 593–595, 1974.

[102] M. Tsuchiya and H. Sakaki, “Dependence of resonant tunneling current on well widths in AlAs/GaAs/AlAs double barrier diode structures,” *Applied Physics Letters*, vol. 49, no. 2, pp. 88–90, 1986.

[103] K. Araki, “Analysis of barrier transmission in resonant tunneling diodes,” *Journal of Applied Physics*, vol. 62, no. 3, pp. 1059–1069, 1987.

[104] A. Evtukh, N. Goncharuk, V. Litovchenko, and H. Mimura, “Electron emission Si-based resonant-tunneling diode,” in *Proc. 24th Int. Vacuum Nanoelectronics Conf. (IVNC)*, pp. 85–86.

[105] V. Mitin, V. Kochelap, and M. Stroscio, *Introduction to Nanoelectronics: Science, Nanotechnology, Engineering, and Applications.* Cambridge University Press, 2008.

[106] T. Wei and S. Stapleton, “Effect of spacer layers on capacitance of resonant tunneling diodes,” *Journal of Applied Physics*, vol. 76, no. 2, pp. 1287–1290, 1994.

[107] D. Neculoiu, I. Sztojanov, and T. Tebeanu, “An investigation of the I-V relationship of double barrier resonant tunneling diodes in oscillating conditions,” in *Proc. Int Semiconductor Conf. CAS ’97*, vol. 2, pp. 345–348.

[108] F. W. Sheard and G. A. Toombs, “Space-charge effects and ac response of resonant tunneling double-barrier diodes,” *Solid-State Electronics*, vol. 32, no. 12, pp. 1443–1447, 1989.

[109] E. T. Koenig, C. I. Huang, and B. Jogai, “Independence of peak current from emitter spacer layer width in AlGaAs/GaAs resonant tunneling diodes,” *Journal of Applied Physics*, vol. 68, no. 11, pp. 5905–5907, 1990.

[110] N. Alkeev, S. Averin, A. Dorofeev, P. Velling, E. Khorenko, W. Prost, and F. Tegude, “Sequential mechanism of electron transport in the resonant tunneling diode with thick barriers,” *Semiconductors*, vol. 41, no. 2, pp. 227–231, 2007.

[111] A. Ouacha, M. Willander, H. Brugger, and U. Meiners, “Influence of the barrier thickness on the noise performance of AlAs/GaAs/AlAs double barrier resonant tunneling diodes,” *Journal of Applied Physics*, vol. 77, no. 11, pp. 6026–6030, 1995.

[112] A. Campbell, V. Kesan, T. Block, G. Crook, D. Neikirk, and B. Streetman, “Influence of MBE growth temperature on GaAs/AlAs resonant tunneling structures,” *Journal of Electronic Materials*, vol. 18, no. 5, pp. 585–588, 1989.

[113] M. Asada and S. Suzuki, “Compact THz oscillators with resonant tunneling diodes and application to high-capacity wireless communications,” in *Applied Electromagnetics and Communications (ICECom), 2013 21st International Conference on*, pp. 1–5.

[114] ——, “Resonant tunneling diodes for room-temperature terahertz oscillators,” in *Microwave Conference Proceedings (APMC), 2013 Asia-Pacific*, pp. 345–347.

[115] T. Hori, T. Ozono, N. Orihashi, and M. Asada, “Frequency mixing characteristics of room temperature resonant tunneling diodes at 100 and 200 GHz,” *Journal of Applied Physics*, vol. 99, no. 6, p. 064508, 2006.

[116] G. Millington, R. E. Miles, R. D. Pollard, D. P. Steenson, and J. M. Chamberlain, “A resonant tunnelling diode self-oscillating mixer with conversion gain,” *Microwave and Guided Wave Letters, IEEE*, vol. 1, no. 11, pp. 320–321, 1991.

[117] J. Mata-Contreras, T. M. Martin-Guerrero, and C. Camacho-Penalosa, “Active composite right/left-handed transmission line-based mixers,” in *Elec-*

trotechnical Conference, 2006. MELECON 2006. IEEE Mediterranean, pp. 276–279.

[118] K. Maezawa, K. Kasahara, and M. Mori, “A traveling wave amplifier based on composite right/left handed (CRLH) transmission lines periodically loaded with resonant tunneling diode pairs,” in *Indium Phosphide & Related Materials (IPRM), 2010 International Conference on*, pp. 1–4.

[119] L. Jongwon, L. Jooseok, K. Maengkyu, and Y. Kyounghoon, “Negative-differential-conductance RTD amplifier MMIC with record foms of gain-to-dc power ratio and noise figure,” in *Indium Phosphide and Related Materials (IPRM), 26th International Conference on*, pp. 1–2.

[120] A. Suminokura, K. Tsuruda, T. Mukai, M. Fujita, and T. Nagatsuma, “Integration of resonant tunneling diode with Terahertz photonic-crystal waveguide and its application to gigabit terahertz-wave communications,” in *Microwave Photonics (MWP) and the 2014 9th Asia-Pacific Microwave Photonics Conference (APMP), 2014 International Topical Meeting on*, pp. 419–422.

[121] P. Mazumder, S. Kulkarni, M. Bhattacharya, J. P. Sun, and G. I. Haddad, “Digital circuit applications of resonant tunneling devices,” *Proceedings of the IEEE*, vol. 86, no. 4, pp. 664–686, 1998.

[122] R. E. Miles, G. Millington, R. D. Pollard, D. P. Steenson, J. M. Chamberlain, and M. Henini, “Accurate equivalent circuit model of resonant tunnelling diodes,” *Electronics Letters*, vol. 27, no. 5, pp. 427–428, 1991.

[123] J. P. Sun, G. I. Haddad, P. Mazumder, and J. N. Schulman, “Resonant tunneling diodes: models and properties,” *Proceedings of the IEEE*, vol. 86, no. 4, pp. 641–660, 1998.

[124] J. M. Gering, D. A. Crim, D. G. Morgan, P. D. Coleman, W. Kopp, and H. Morkoc, “A small-signal equivalent-circuit model for $GaAs - Al_xGa_{1-x}As$

resonant tunneling heterostructures at microwave frequencies," *Journal of Applied Physics*, vol. 61, no. 1, pp. 271–276, 1987.

[125] D. Neculoiu, T. Tebeanu, and I. Sztojanov, "A new large-signal model for double barrier resonant tunneling diodes for frequency multiplier applications," in *Proc. Int Semiconductor Conf. CAS '97*, vol. 2, pp. 349–352.

[126] Z. Peiji, C. Hong Liang, D. L. Woolard, K. L. Jensen, and F. A. Buot, "Equivalent circuit parameters of resonant tunneling diodes extracted from self-consistent Wigner-Poisson simulation," *Electron Devices, IEEE Transactions on*, vol. 48, no. 4, pp. 614–627, 2001.

[127] M. Long, H. Ying-Long, Z. Yang, W. Liang-Chen, Y. Fu-Hua, and Z. Yi-Ping, "A Small Signal Equivalent Circuit Model for Resonant Tunneling Diode," *Chinese Phys. Lett*, vol. 23, 2006.

[128] D. Neculoiu and T. Tebeanu, "SPICE implementation of double barrier resonant tunnel diode model," in *Proc. Int. Semiconductor Conf.*, vol. 1, pp. 181–184.

[129] M. Bhattacharya and P. Mazumder, "Augmentation of SPICE for simulation of circuits containing resonant tunneling diodes," *Computer-Aided Design of Integrated Circuits and Systems, IEEE Transactions on*, vol. 20, no. 1, pp. 39–50, 2001.

[130] A. Sellai, H. Al-Hadhrami, S. Al-Harthy, and M. Henini, "Resonant tunneling diode circuits using Pspice," *Microelectronics Journal*, vol. 34, pp. 741–745, 2003.

[131] S. F. Nafea and A. A. S. Dessouki, "An accurate large-signal SPICE model for Resonant Tunneling Diode," in *Proc. Int Microelectronics (ICM) Conf*, pp. 507–510.

[132] J. N. Schulman, H. J. De Los Santos, and D. H. Chow, “Physics-based RTD current-voltage equation,” *Electron Device Letters, IEEE*, vol. 17, no. 5, pp. 220–222, 1996.

[133] J. P. Mattia, A. L. McWhorter, R. J. Aggarwal, F. Rana, E. R. Brown, and P. Maki, “Comparison of a rate-equation model with experiment for the resonant tunneling diode in the scattering-dominated regime,” *Journal of Applied Physics*, vol. 84, no. 2, pp. 1140–1148, 1998.

[134] H. Kosina, M. Nedjalkov, and S. Selberherr, “Comparison of numerical quantum device models,” in *Simulation of Semiconductor Processes and Devices, 2003. SISPAD 2003. International Conference on*, pp. 171–174.

[135] A. Fediai and V. Moskaliuk, “Modeling of resonant-tunneling diode with uniform and graded emitter,” in *Electronics and Nanotechnology (ELNANO), 2013 IEEE XXXIII International Scientific Conference*, pp. 107–111.

[136] C. Yuxiong, J. Zhi, G. Ji, S. Yongbo, and L. Xinyu, “A symbolically defined InP double heterojunction bipolar transistor large-signal model,” *Journal of Semiconductors*, vol. 30, no. 12, 2009.

[137] W. Xiao and X. Hongxi, “Characterization and modeling of 18-40GHz mm-wave tunneling diode detector,” in *Computer Research and Development (ICCRD), 2011 3rd International Conference on*, vol. 3, pp. 362–365.

[138] T. Wei, S. Stapleton, and E. Berolo, “Equivalent circuit and capacitance of double barrier resonant tunneling diode,” *Journal of Applied Physics*, vol. 73, no. 2, pp. 829–834, 1993.

[139] B. Thomas, E. Schlecht, A. Maestrini, J. Ward, G. Chattopadhyay, R. Lin, J. Gill, C. Lee, and I. Mehdi, “Sub-millimeter wave MMIC Schottky subharmonic mixer testing at passive cooling temperatures,” 2009.

[140] J. Wood, D. E. Root, and N. B. Tufillaro, “A behavioral modeling approach to nonlinear model-order reduction for RF/microwave ICs and systems,” *Microwave Theory and Techniques, IEEE Transactions on*, vol. 52, no. 9, pp. 2274–2284, 2004.

[141] P. Brown and J. P. Taylor, “Observation-based research on atmospheric physical processes,” November 2013.

[142] S. Adachi, *GaAs and Related Materials: Bulk Semiconducting and Superlattice Properties.* World Scientific, 1994.

[143] Rogers Corporation. (2015) RT/duroid 5870/5880 High Frequency Laminates. [Online]. Available: https://www.rogerscorp.com/documents/606/acm/RT-duroid-5870-5880-Data-Sheet.pdf

[144] ——. (2015) RO4000 Series High Frequency Circuit Materials. [Online]. Available: https://www.rogerscorp.com/documents/726/acm/RO4000-Laminates---Data-sheet.pdf

[145] ——. (2015) RT/duroid 6006/6010LM High Frequency Laminates. [Online]. Available: http://www.rogerscorp.com/documents/612/index.aspx

[146] V. Murthy, S. Sundaram, and B. Viswanathan, *Microwave Materials.* Springer Berlin Heidelberg, 2013.

[147] R. Simons, *Coplanar Waveguide Circuits, Components, and Systems*, ser. Coplanar Waveguide Circuits, Components, and Systems, 2002, coplanar Waveguide Circuits, Components, and Systems.

[148] R. Jackson, “Considerations in the use of coplanar waveguide for millimeter-wave integrated circuits,” *Microwave Theory and Techniques, IEEE Transactions on*, vol. 34, no. 12, pp. 1450–1456, Dec 1986.

[149] T. Kitazawa and T. Itoh, “Propagation characteristics of coplanar-type transmission lines with lossy media,” *Microwave Theory and Techniques, IEEE Transactions on*, vol. 39, no. 10, pp. 1694–1700, Oct 1991.

[150] J. Bandler, “Stability and gain prediction of microwave tunnel-diode reflection amplifiers,” *Microwave Theory and Techniques, IEEE Transactions on*, vol. 13, no. 6, pp. 814–819, Nov 1965.

[151] H. Okean, “Synthesis of negative resistance reflection amplifiers, employing band-limited circulators,” *Microwave Theory and Techniques, IEEE Transactions on*, vol. 14, no. 7, pp. 323–337, Jul 1966.

[152] ——, “Microwave amplifiers employing integrated tunnel-diode devices,” *Microwave Theory and Techniques, IEEE Transactions on*, vol. 15, no. 11, pp. 613–622, November 1967.

[153] M. Koichi, K. Naoki, K. Shigeru, M. Takashi, and A. Kazuhiro, “Improved Bias Stability of the Resonant Tunneling Diode Pair Oscillators Integrated on an AlN Ceramic Substrate,” *Japanese Journal of Applied Physics*, vol. 48, no. 4S, p. 04C084, 2009.

[154] M. Koichi, S. Tomoya, K. Koji, and M. Masayuki, “Possibility of Terahertz Amplification by Active Transmission Lines Loaded with Resonant Tunneling Diode Pairs,” *Japanese Journal of Applied Physics*, vol. 48, no. 12R, p. 124503, 2009.

[155] K. K. N. Chang, “Theory of a NegativeResistance Transmission Line Amplifier with Distributed Noise Generators,” *Journal of Applied Physics*, vol. 31, no. 5, pp. 871–875, 1960.

[156] I. Hunter and I. of Electrical Engineers, *Theory and Design of Microwave Filters*, ser. Electromagnetics and Radar Series. Institution of Engineering and Technology, 2001.

[157] P. A. R. Holder, “X-band microwave integrated circuits using slotline and coplanar waveguide,” *Radio and Electronic Engineer*, vol. 48, no. 1.2, pp. 38–42, 1978.

[158] M. Surdin, “Directive couplers in wave guides,” *Electrical Engineers - Part IIIA: Radiolocation, Journal of the Institution of*, vol. 93, no. 4, pp. 725–736, 1946.

[159] R. Vahldieck, “Quasi-planar filters for millimeter-wave applications,” *Microwave Theory and Techniques, IEEE Transactions on*, vol. 37, no. 2, pp. 324–334, 1989.

[160] A. Ismail, M. S. Razalli, M. A. Mahdi, W. N. I. Wan Darman, R. S. A. Raja Abdullah, and M. M. Isa, “Micromachined W-band Integrated Rectangular Waveguide Filter Utilising SU-8,” in *Microwave Conference, 2007. APMC 2007. Asia-Pacific*, pp. 1–4.

[161] M. Politi, G. B. Stracca, A. Melloni, G. Macchiarella, and G. G. Gentili, “An Equivalent Circuit for the Design of E-Plane Metal-Insert Filters in Millimeter-Wave Applications,” in *Microwave Conference, 1990. 20th European*, vol. 2, pp. 1257–1262.

[162] Leo, A. n, A. Casanueva, and A. Mediavilla, “Novel topologies for finline E-plane filters using split ring resonators,” in *Microwave Conference Proceedings (APMC), 2010 Asia-Pacific*, pp. 1162–1165.

[163] G. Shimonov, K. Garb, and R. Kastner, “Mode matching analysis and design of waveguide E-plane filters and diplexers,” in *Antenna Technology (iWAT), 2010 International Workshop on*, pp. 1–4.

[164] O. Glubokov and D. Budimir, “Novel inline waveguide E-plane filters using dual-mode extracted pole section,” in *Microwave Conference (EuMC), 2011 41st European*, pp. 99–102.

[165] P. Espes, P. F. Combes, J. M. Goutoule, and B. Theron, "Asymmetrical finline for space applications using millimeter waves," *Microwave Theory and Techniques, IEEE Transactions on*, vol. 37, no. 2, pp. 289–298, 1989.

[166] J. de Mingo, A. Moliner, and A. Comeron, "Waveguide-to-coupled fin-line transition in Ka band," *Microwave and Guided Wave Letters, IEEE*, vol. 6, no. 10, pp. 363–365, 1996.

[167] W. Thiel and W. Menzel, "Full-wave design and optimization of mm-wave diode-based circuits in finline technique," *Microwave Theory and Techniques, IEEE Transactions on*, vol. 47, no. 12, pp. 2460–2466, 1999.

[168] P. J. Sobis, N. Wadefalk, A. Emrich, and J. Stake, "A Broadband, Low Noise, Integrated 340 GHz Schottky Diode Receiver," *Microwave and Wireless Components Letters, IEEE*, vol. 22, no. 7, pp. 366–368, 2012.

[169] R. Vahldieck, J. Bornemann, F. Arndt, and D. Grauerholz, "Optimized Waveguide E-plane Metal Insert Filters For Millimeter-wave Applications," *Microwave Theory and Techniques, IEEE Transactions on*, vol. 31, no. 1, pp. 65–69, 1983.

[170] P. J. Meier, "Integrated Fin-Line Millimeter Components," *Microwave Theory and Techniques, IEEE Transactions on*, vol. 22, no. 12, pp. 1209–1216, 1974.

[171] A. M. K. Saad and K. Schunemann, "Design of Fin-Line Tapers, Transitions, and Couplers," in *Microwave Conference, 1981. 11th European*, pp. 305–308.

[172] A. M. K. Saad, "Analysis of fin-line tapers and transitions," *Microwaves, Optics and Antennas, IEE Proceedings H*, vol. 130, no. 3, pp. 230–235, 1983.

[173] R. N. Simons, "Analysis of millimetre-wave integrated fin line," *Microwaves, Optics and Antennas, IEE Proceedings H*, vol. 130, no. 2, pp. 166–169, 1983.

[174] C. Schieblich, J. K. Piotrowski, and J. H. Hinken, “Synthesis of Optimum Finline Tapers Using Dispersion Formulas for Arbitrary Slot Widths and Locations,” *Microwave Theory and Techniques, IEEE Transactions on*, vol. 32, no. 12, pp. 1638–1645, 1984.

[175] D. Yuliang, B. Rui, X. Jun, and X. LiangJin, “Wideband subharmonic mixer in bilateral finline at U-band,” in *Microwave and Millimeter Wave Technology, 2008. ICMMT 2008. International Conference on*, vol. 2, pp. 850–853.

[176] L. W. Hendrick and R. Levy, “Design of waveguide narrow-wall short-slot couplers,” *Microwave Theory and Techniques, IEEE Transactions on*, vol. 48, no. 10, pp. 1771–1774, 2000.

[177] U. Rosenberg and K. Beis, “Improved Narrow-Wall Short Slot Coupler Design Exhibiting Significant Increased Bandwidth and Low Cost Production,” in *Microwave Conference, 2001. 31st European*, pp. 1–4.

[178] L. T. Hildebrand, “Results for a simple compact narrow-wall directional coupler,” *Microwave and Guided Wave Letters, IEEE*, vol. 10, no. 6, pp. 231–232, 2000.

[179] F. Yufeng and Y. Xuequan, “Design of waveguide narrow-wall 3dB coupler for 3mm-wave frequency band,” in *Millimeter Waves (GSMM), 2012 5th Global Symposium on*, pp. 166–169.

[180] J. Fleury and O. Bernard, “Designing and Characterizing TRL Fixture Calibration Standards for Device Modeling,” *Applied Microwave & Wireless*, 2003.

Appendix A

RTD I-V Plots

A.1 L938

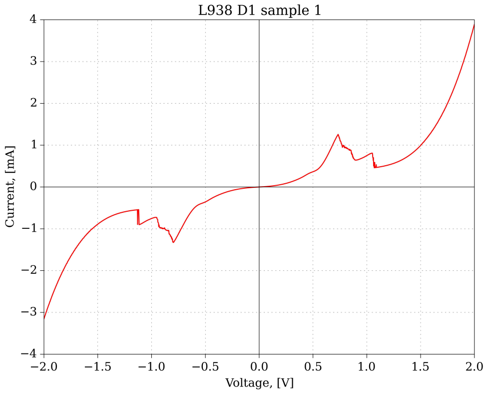

(a) Device Size 1, Wafer Sample 1

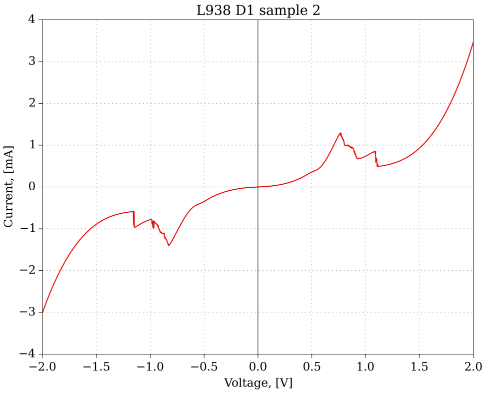

(b) Device Size 1, Wafer Sample 2

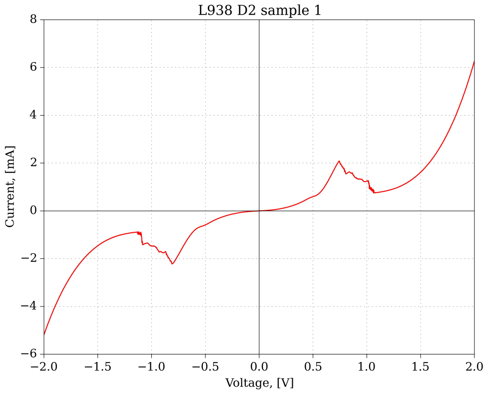

(c) Device Size 2, Wafer Sample 1

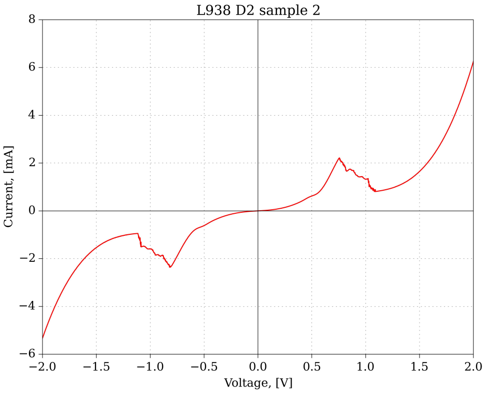

(d) Device Size 2, Wafer Sample 2

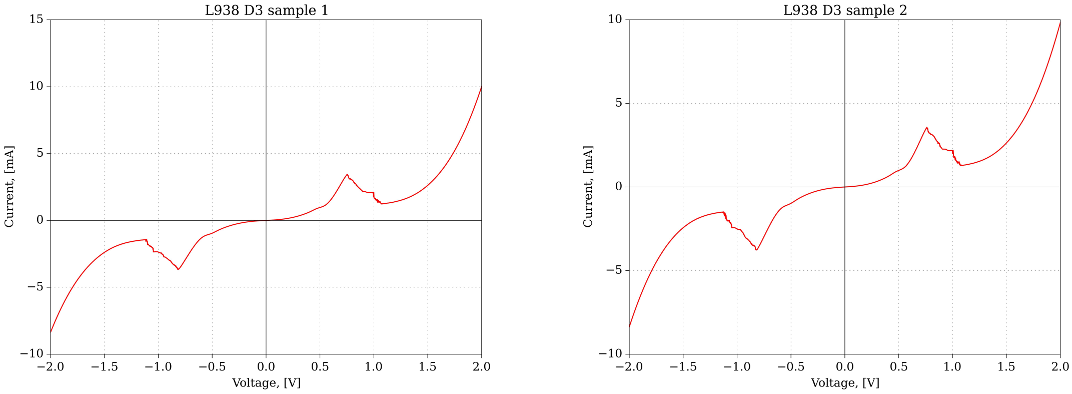

(e) Device Size 3, Wafer Sample 1

(f) Device Size 3, Wafer Sample 2

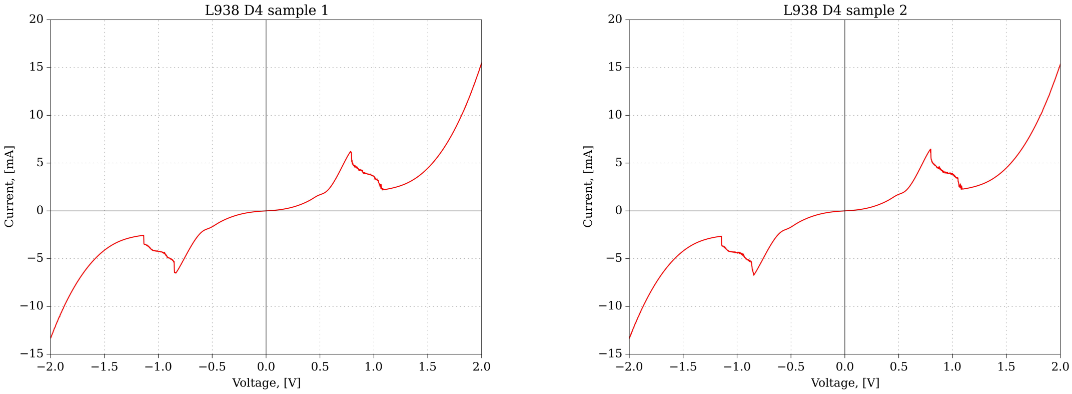

(g) Device Size 4, Wafer Sample 1

(h) Device Size 4, Wafer Sample 2

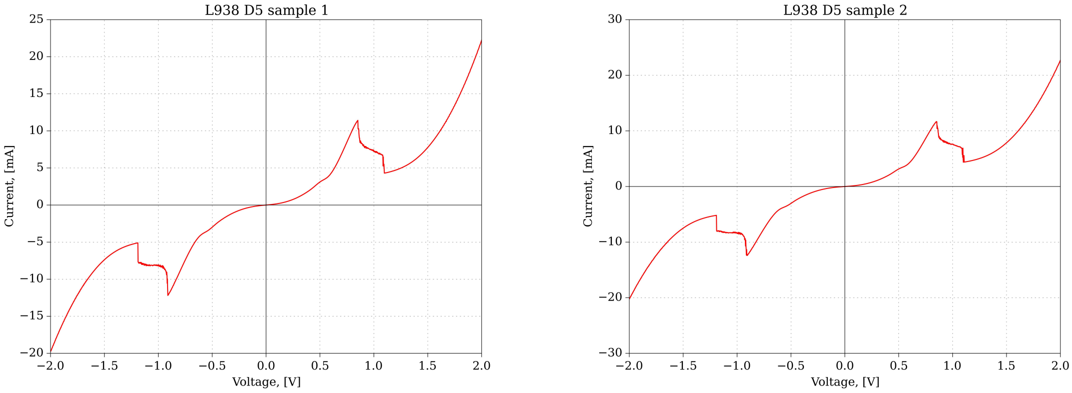

(i) Device Size 5, Wafer Sample 1

(j) Device Size 5, Wafer Sample 2

Figure A.1: Current-voltage characteristics of L938 RTD devices.

These I-Vs were measured from devices made during the initial fabrication run. It can be seen that diodes from the two wafer samples have virtually identical characteristics, signifying good manufacturing repeatability.

Measurements of devices made during the second production run are shown in

Fig. A.2. This time, the voltage range was extended to $-3V$ to $3V$, in order to

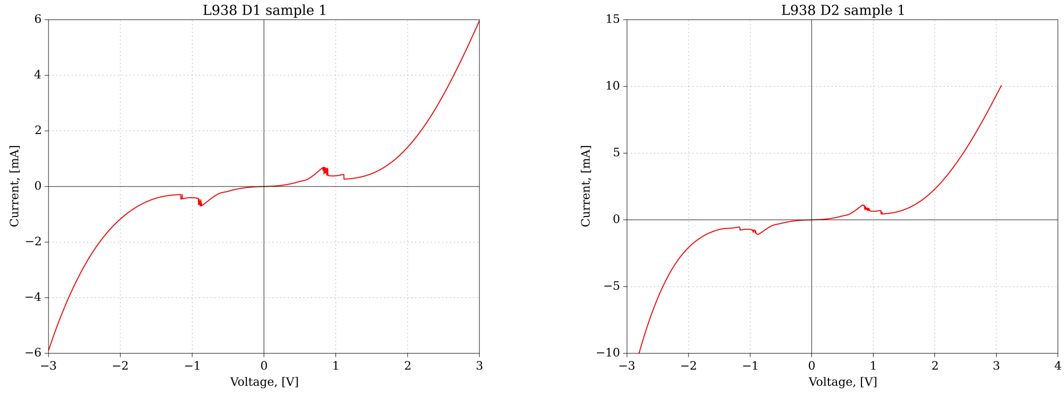

(a) Device Size 1

(b) Device Size 2

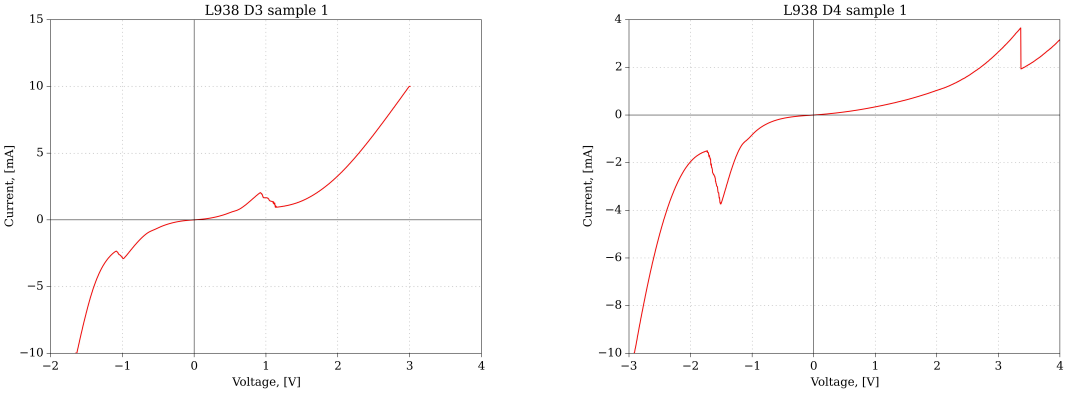

(c) Device Size 3

(d) Device Size 4

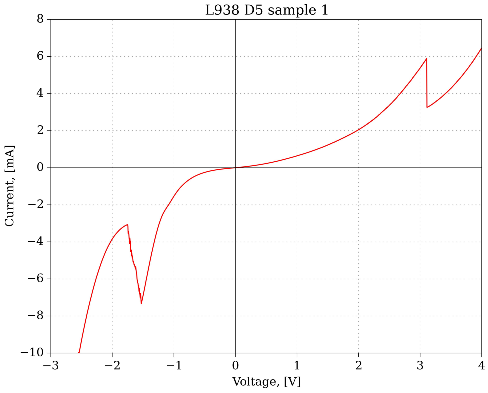

(e) Device Size 5

Figure A.2: Current-voltage characteristics of L938 RTD devices.

explore how the diodes perform at higher voltage, and what their power handling capabilities are. Devices of smaller sizes have similar I-Vs to those in Fig. A.1; while D3, D4, and D5 deviate away from perfect anti-symmetry. The first PDR region is extended, and the NDR region is still present. This can be explained by increased contact resistance from uneven metallisation, and heating from current passing through the quantum barrier structure.

A.2 L939

L939 differs significantly from L938 and L940 with respect to the composition of the quantum barriers, leading to expectations of higher current density and NDR region presence at higher voltages.

Initial L939 diode measurements however did not reveal resonant tunnelling behaviour. These I-Vs are given in Fig. A.3. Some measurements from the first sample were not included, because the devices' active area was shorted imperfect metallisation. However, from the devices that worked, it is evident that L939 does have higher current density.

During the second manufacturing run, the voltage range was extended, and I-Vs with an NDR region were captured. These are given in Fig. A.4. Even though the NDR region is well pronounced in the smaller devices, heating of the quantum barrier structure reduces the resonant-tunnelling current.

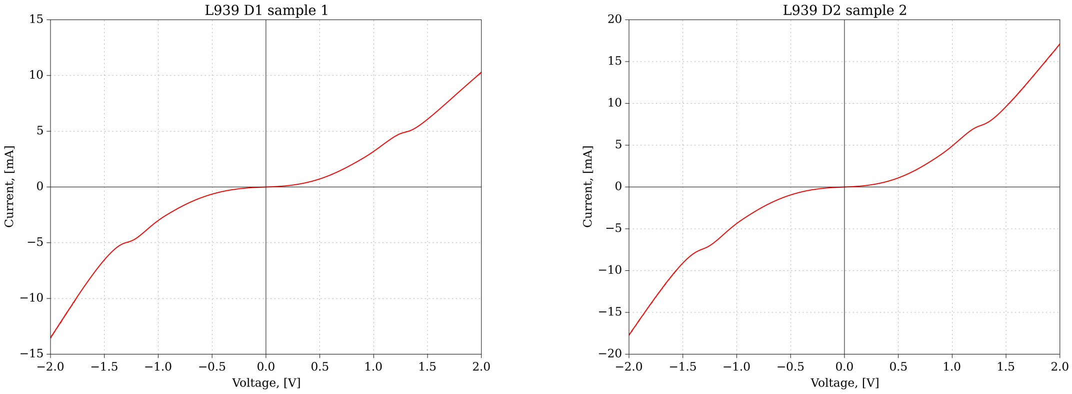

(a) Device Size 1 (b) Device Size 2

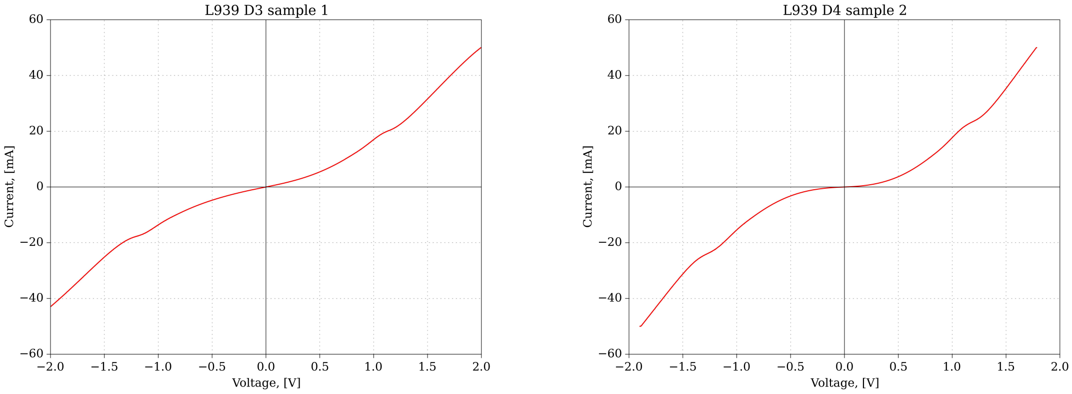

(c) Device Size 3 (d) Device Size 4

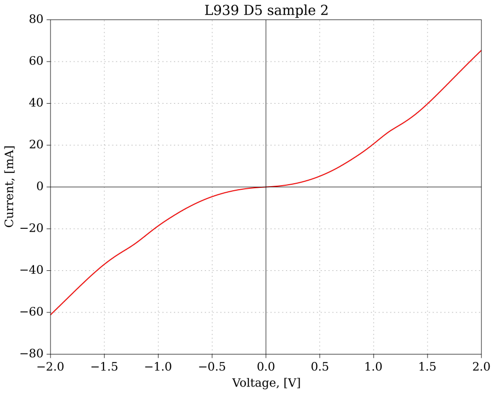

(e) Device Size 5

Figure A.3: Current-voltage characteristics of L939 RTD devices.

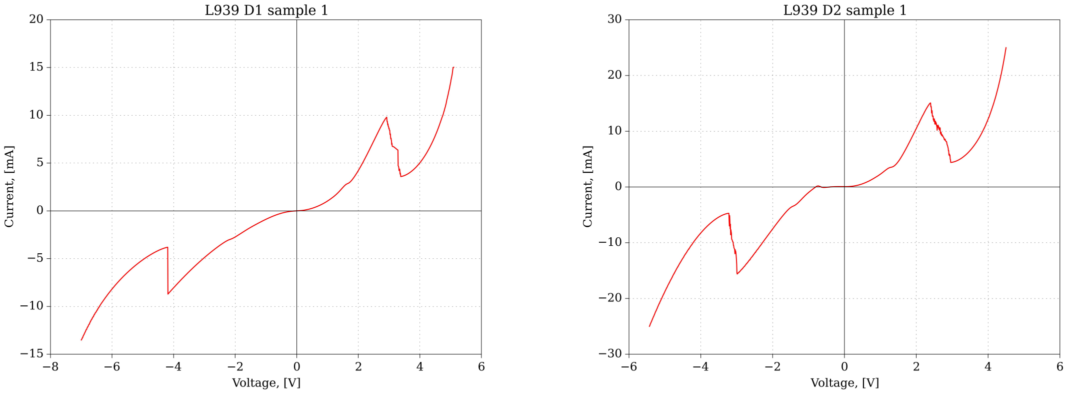

(a) Device Size 1 (b) Device Size 2

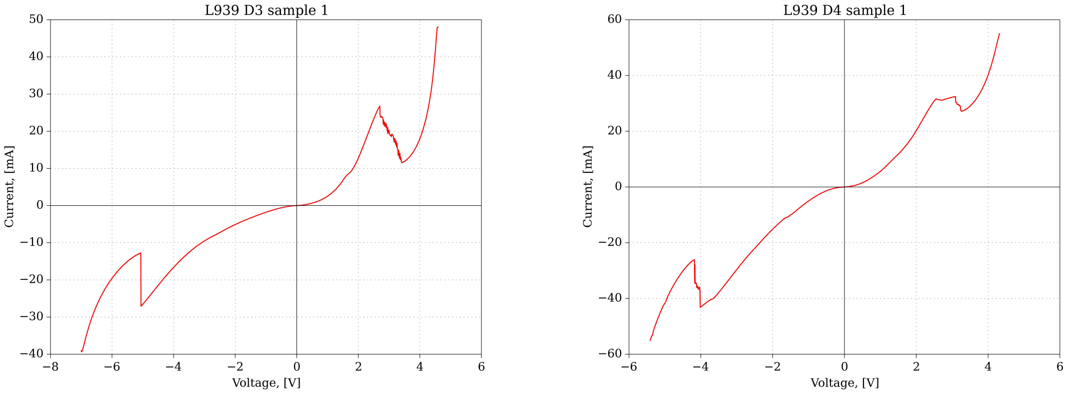

(c) Device Size 3 (d) Device Size 4

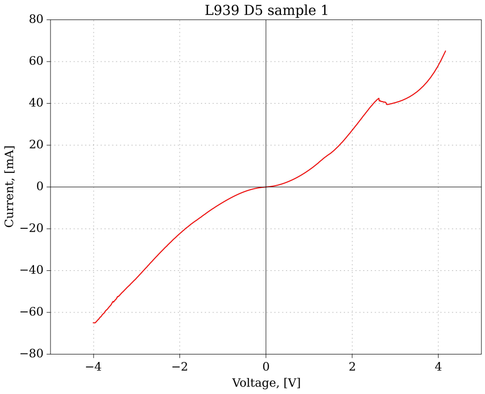

(e) Device Size 5

Figure A.4: Current-voltage characteristics of L939 RTD devices.

A.3 L940

Similarly to L938 devices, the initial L940 diodes show good repeatability and their I-V characteristics are shown in Fig. A.3.

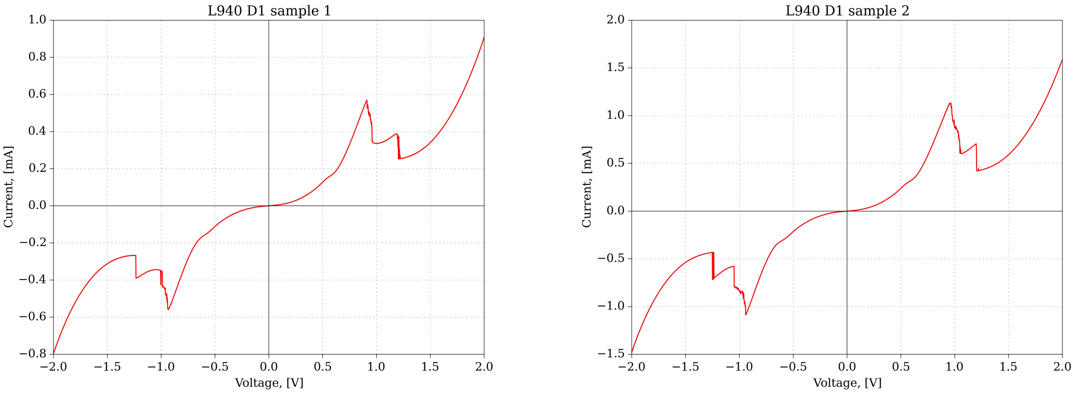

(a) Device Size 1, Wafer Sample 1

(b) Device Size 1, Wafer Sample 2

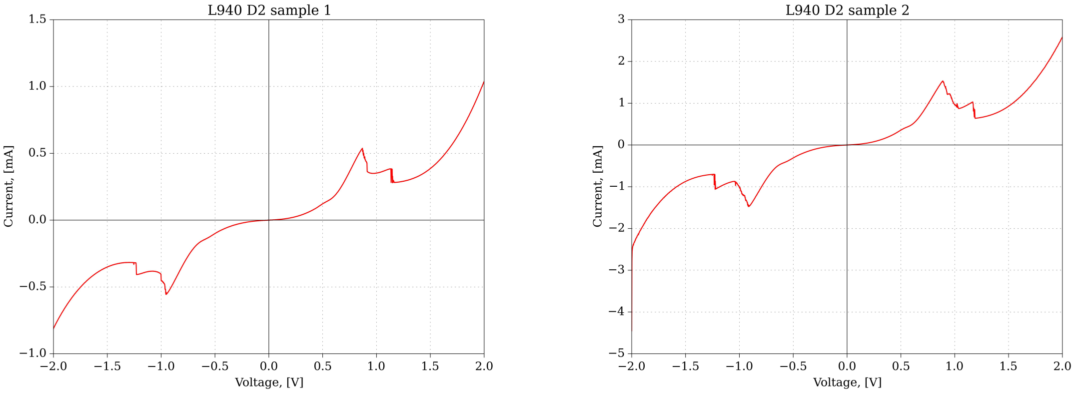

(c) Device Size 2, Wafer Sample 1

(d) Device Size 2, Wafer Sample 2

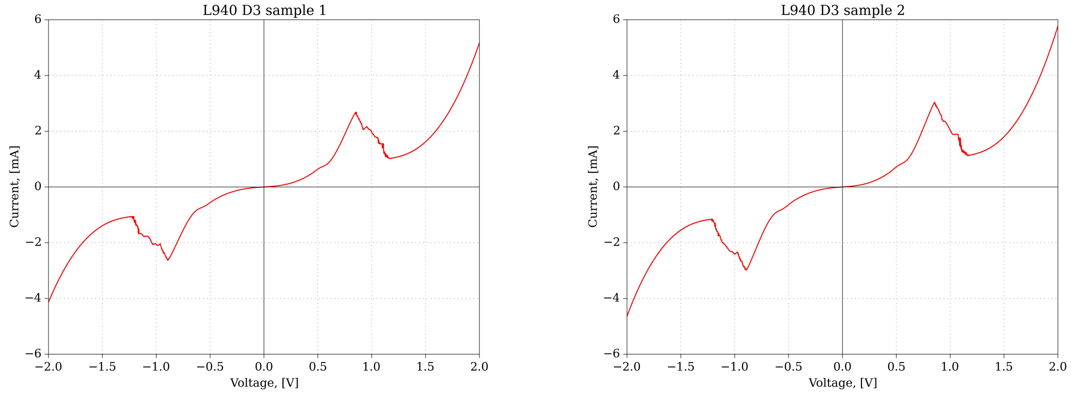

(e) Device Size 3, Wafer Sample 1 (f) Device Size 3, Wafer Sample 2

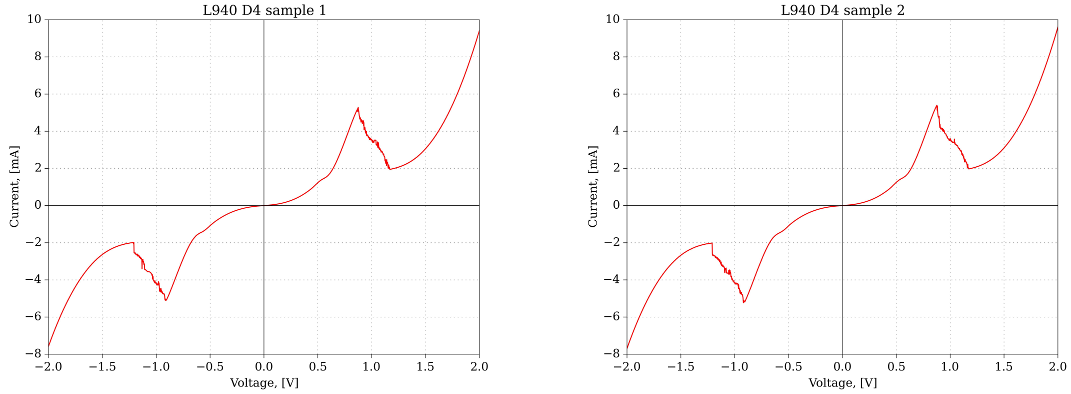

(g) Device Size 4, Wafer Sample 1 (h) Device Size 4, Wafer Sample 2

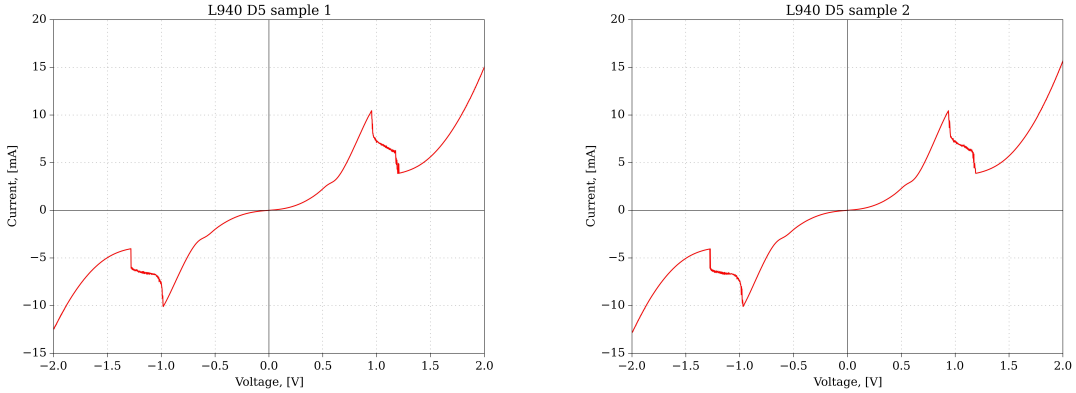

(i) Device Size 5, Wafer Sample 1 (j) Device Size 5, Wafer Sample 2

Figure A.5: Current-voltage characteristics of L940 RTD devices.

Since L938 and L940 have the same semiconductor layer structure, diodes from the two layers with the same size have almost identical current-voltage characteristics.

Measurements taken during the second manufacturing run show similar phenomena as those with L938, and the I-Vs are presented in Fig. A.6.

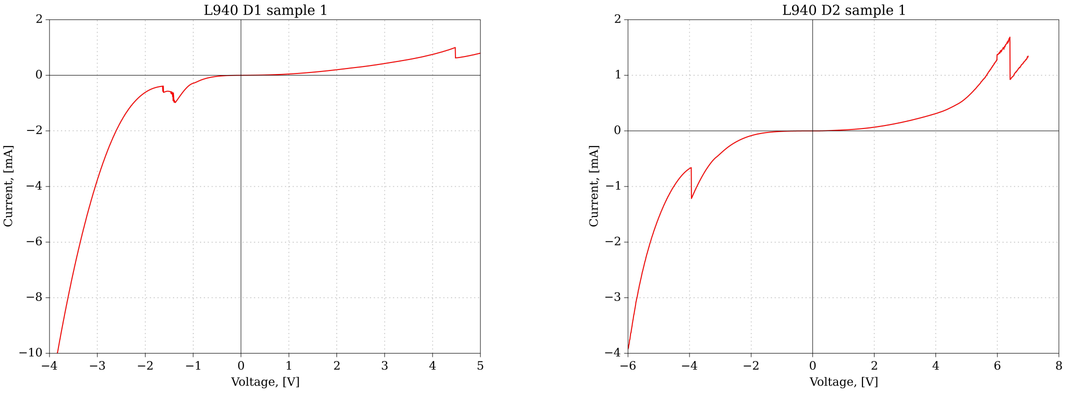

(a) Device Size 1 (b) Device Size 2

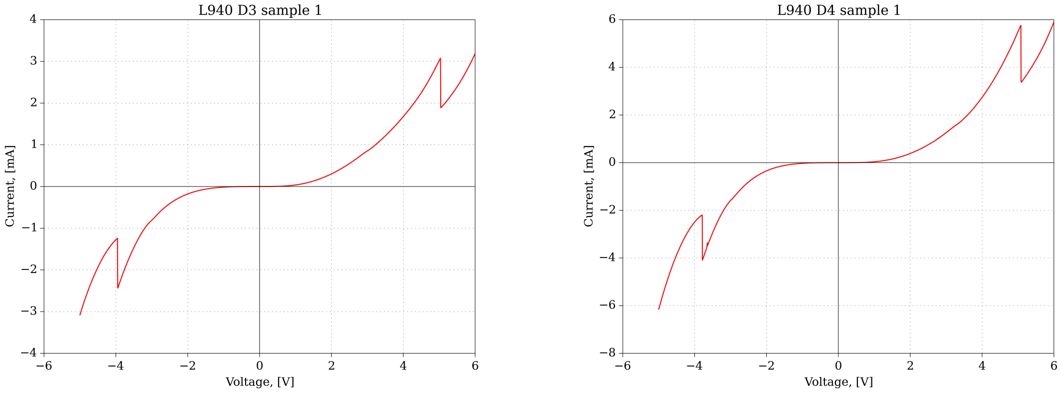

(c) Device Size 3 (d) Device Size 4

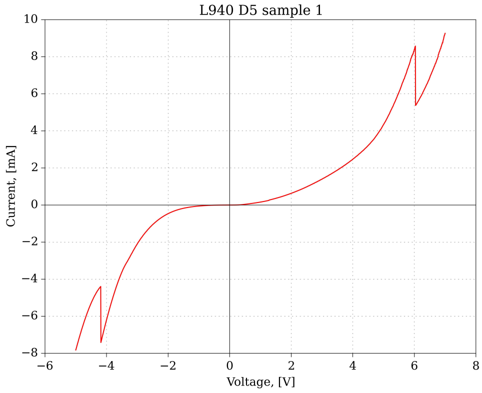

(e) Device Size 5

Figure A.6: Current-voltage characteristics of L940 RTD devices.

Appendix B

Python Scripts

The full source code of all Python scripts used for this thesis is available at http://github.com/elvd/phd_helper.

B.1 Polynomial Generation

The fitting of polynomials to measured current-voltage characteristics is accomplished via the following two python functions:

```
# -*- coding: utf-8 -*-
"""
A module to hold all auxiliary, all-purpose, functions.

Functions contained in module.
------------------------------
- fit_poly(data, degree)
- poly_to_ads_string(coeffs)
- custom_plot(data, xlabel='X axis', ylabel='Y axis', title='
   Plot title',
                legend=None, mode='linear')
```

```
Individual documentation can be accessed by using the
   following commands:
>>> import elvd_tools
>>> print elvd_tools.<function_name>.__doc__  # or
>>> help(elvd_tools.<function_name>)

Created on Wed Aug 13 16:10:18 2014
@author: elvd

"""

from __future__ import print_function
import numpy as np
import matplotlib.pyplot as plt


def fit_poly(data, degree):
    """
    Fits an array of [x, y] data to a polynomial of a
       specified
    degree. Used with measured I-V data.

    Parameters:
    -----------
    data : numpy.ndarray
        I-V data of one device.
    degree : int
        The degree of polynomial to which the data is to be
           fitted.
```

```
    Returns:
    --------
    fit : numpy.ndarray
        The original x data, bundled with the fitted y data.
    coeffs : numpy.ndarray
        The coefficients of the fitted polynomial, highest order first.

    Notes:
    ------
    Requires an installation of NumPy.

    """

    coeffs = np.polyfit(data[:, 0], data[:, 1], degree)
    fit = np.polyval(coeffs, data[:, 0])
    # combine original data and fit into a single array
    fit = np.array([data[:, 0], fit])
    fit = fit.T

    return (fit, coeffs)


def poly_to_ads_string(coeffs):
    """
    Converts the numerical representation of a polynomial to a string one, to
    be used in Agilent/Keysight ADS as an SDD element.

    Parameters:
```

```
    -----------
    coeffs : numpy.ndarray
        Coefficients of the polynomial to be converted.

    Returns:
    --------
    polynom : string
        The string representation of the polynomial, to be
           used as the
        non-linear relationship between I and V in a 2-port
           SDD element.

    """

    coeffs = coeffs[::-1]
    # convert to Agilent ADS SDD format
    polynom = [’(%e)*((_v1+_v2)^%d)+’ % (j, i) for (i, j) in
       enumerate(coeffs)]
    polynom = ’’.join(polynom)

    return polynom


def custom_plot(data, xlabel=’X axis’, ylabel=’Y axis’, title
   =’Plot title’,
                legend=None, mode=’linear’):
    """
    Plots data, with labels, title, and legend. Used to make
       sure all graphs
    have the same style. Datapoints must be in columns.
```

```
Parameters:
-----------
data : numpy.ndarray
    I-V data of one or more device; alternatively, the
       measured and fitted
    data of one device.
xlabel, ylabel : string
    X and Y axis labels.
title : string
    Plot title.
legend : array_like, optional
    The lalbes for the different sets of data, to appear
       in the legend box.
mode : {'linear', 'log'}, optional
    Scaling of the Y axis.

Returns:
--------
fig : matplotlib.figure.Figure
    A matplotlib figure, containing the plots of the data
        passed to the
    function.

Raises:
-------
IndexError
    In case there is insufficient data, or data is not
       organised in
    columns.
```

```
Notes:
------
Requires an installation of NumPy and Matplotlib. Figure
   is not displayed,
just created and its parameters set. It is up to the
   calling function to
display and/or save the figure.

Example:
--------
>>> import elvd_tools
>>> data1 = [[0, 0], [1, 1], [2, 2]]
>>> data2 = [[0, 0], [1, 1], [2, 4]]
>>> data3 = [[0, 0], [1, 1], [2, 8]]
>>> data_comb = elvd_tools.np.array([data1, data2, data3
   ])
>>> label1 = 'Test X label'
>>> label2 = 'Test Y label'
>>> title = 'Test Title'
>>> legend = ['Test item 1', 'Test item 2', 'Test item
   3']
>>> try:
...     test_fig = elvd_tools.custom_plot(data_comb,
   label1, label2,
                                          title, legend)
...     elvd_tools.plt.show()
... except IndexError as e:
...     print e.message
```

```
"""

fig = plt.figure()
ax1 = fig.add_subplot(111)  # just one plot
# different colours for the different datasets
ax1.set_color_cycle(['r', 'k', 'b', 'g', 'c', 'm'])

if np.ndim(data) == 2:  # one set of data
    if np.size(data, 0) >= np.size(data, 1) and np.size(
       data, 1) > 1:
        ax1.plot(data[:, 0], data[:, 1], lw=1.0)
    else:
        raise IndexError('Incorrect format. Datapoints
           must be in columns')
elif np.ndim(data) == 3:  # two or more sets
    if np.size(data, 1) >= np.size(data, 2) and np.size(
       data, 2) > 1:
        for datum in data:
            ax1.plot(datum[:, 0], datum[:, 1], lw=1.0)
    else:
        raise IndexError('Incorrect format. Datapoints
           must be in columns')
else:
    raise IndexError('Missing data')

# set labels, title
ax1.set_yscale(mode)
ax1.set_xlabel(xlabel)
ax1.set_ylabel(ylabel)
ax1.set_title(title)
```

```
    if legend is not None:
        ax1.legend(legend, loc='lower left')

    # cosmetic stuff, make it look pretty
    ax1.set_axisbelow(True)
    ax1.grid(which='both', axis='both', color='0.1', ls=':',
       lw=0.2)
    ax1.tick_params(direction='out', top='off', right='off',
       width=0.5)

    for spine in ['left', 'top', 'right', 'bottom']:
        ax1.spines[spine].set_linewidth(0.5)

    plt.axhline(y=0, color='0', lw=0.5)
    plt.axvline(x=0, color='0', lw=0.5)

    plt.rc('font', family='serif')

    plt.rc('legend', fontsize=12)
    plt.rc('axes', titlesize=14)
    plt.rc('axes', labelsize=12)
    plt.rc('xtick', labelsize=12)
    plt.rc('ytick', labelsize=12)

    return fig

if __name__ == '__main__':
    print(__doc__)
```

These are used to process all measurement files and obtain a string representation of the polynomial, suitable for use in the definition of an SDD in Agilent ADS environment.

B.2 I-V Manipulation

These are the scripts that were used to alter the devices' I-V in order to simulate change in the physical dimensions.

```
# -*- coding: utf-8 -*-
"""
Functions to manipulate and modify measurement data for RTD
   current-voltage
characteristics.


Functions contained in module.
------------------------------
- make_symmetric(data, quadrant)
- scale(data, factor)
- extract_region(data, region)

Individual documentation can be accessed by using the
   following commands:
>>> import iv_manipulate
>>> print iv_manipulate.<function_name>.__doc__  # or
>>> help(iv_manipulate.<function_name>)

Created on Tue Aug 19 17:01:45 2014
@author: Viktor Doychinov

"""
```

```
from __future__ import print_function
import numpy as np
import scipy.signal as spsig


def make_symmetric(data, quadrant=’pos’):
    """
    Takes an I-V and makes it anti-symmetric, i.e. odd, with respect to
    the origin, by taking one half of the I-V and rotating it around the
    origin.

    Parameters:
    -----------
    data : numpy.ndarray
        I-V data of one device.
    quadrant : {’pos’, ’neg’}, optional
        Signifies which quadrant is to be used for ‘symmetrising’ the I-V.

    Returns:
    --------
    new_data : numpy.ndarray
        The newly symmetric I-V, with datapoints in different rows.

    Raises:
    -------
```

```
IndexError
    In case the data array has more than 2 dimensions, i.
       e. data for more
    than one device.
ValueError
    In case an invalid parameter is specified for the `
       quadrant` variable.

Notes:
------
Requires an installation of NumPy. Data is returned as an
    array, further
processing is up to calling function.

"""

if np.ndim(data) != 2:  # only process one I-V dataset at
    a time
    raise IndexError('Incorrect data format')

if np.size(data, 0) < np.size(data, 1):
    data = data.T  # make sure data is in columns

new_data = data.copy()  # do not change original data

# create a boolean mask to extract region
if quadrant == 'pos':
    elements_mask = np.where(new_data[:, 0] >= 0.0)
elif quadrant == 'neg':
    elements_mask = np.where(new_data[:, 0] <= 0.0)
```

```
    else:
        raise ValueError('Invalid value for quadrant')

    elements_mask = elements_mask[0]
    new_data = new_data[elements_mask]

    mirror_data = new_data * -1
    mirror_data = np.flipud(mirror_data)

    # newly symmetric I-V
    if quadrant == 'pos':
        new_data = np.concatenate((mirror_data, new_data))
    else:
        new_data = np.concatenate((new_data, mirror_data))

    return new_data



def scale(data, factor):
    """
    Scales an I-V by multiplying they measured `y` data by a
       factor.
    Performs a type conversion before scaling.

    Parameters:
    -----------
    data : numpy.ndarray
        I-V data of one device.
    factor : float
        The factor by which to scale the I-V.
```

```
    Returns:
    ---------
    new_data : numpy.ndarray
        The newly scaled I-V, with datapoints in different
           rows.

    Raises:
    -------
    IndexError
        In case the data array has more than 2 dimensions, i.
           e. data for more
        than one device.

    Notes:
    ------
    Requires an installation of NumPy. Data is returned as an
        array, further
    processing is up to calling function.
    Variable `factor` should be [0, Inf).

    """

    if np.ndim(data) != 2:  # only process one IV dataset at
       a time
        raise IndexError('Incorrect data format')

    if np.size(data, 0) < np.size(data, 1):
        data = data.T  # make sure data is in columns
```

```
    # match data types for float multiplication/division
    new_data = data.copy().astype(float)

    new_data[:, 1] *= factor

    return new_data


def extract_region(data, region='pdr'):
    """
    Extracts a part of the measured I-V that is of interest. Possible
    regions are either the initial Positive Differential Resistance one, or the
    Negative Differential Resistance regions plus the second PDR regions.

    Parameters:
    -----------
    data : numpy.ndarray
        I-V data of one device.
    region : {'pdr', 'ndr'}, optional
        Which region of the RTD's I-V to extract.

    Returns:
    ---------
    new_data : numpy.ndarray
        The extracted region, with datapoints in different rows.
```

```
Raises:
-------
IndexError
    In case the data array has more than 2 dimensions, i.
       e. data for more
    than one device.
ValueError
    In case an invalid parameter is specified for the ‘
       region‘ variable.

Notes:
------
Requires an installation of NumPy and SciPy. Data is
   returned as an array,
further processing is up to calling function.
Region extraction works in the following way. First,
   local minima and
maxima are identified and their ‘x‘ values saved, going
   from smallest to
largest. Using those, the ’pdr’ region is defined as the
   data between the
last minimum before ‘x‘ = 0, and the first maximum after
   ‘x‘ = 0.
When extracting the ’ndr’ region, two parts of the I-V
   are actually
concatenated together. The first part spans from the
   value with smallest
‘x‘ component to the last minimum before ‘x‘ = 0; and the
    second part is
```

```
from the first maximum after ‘x‘ = 0, up to the value with largest ‘x‘.

"""

if np.ndim(data) != 2:  # only process one IV dataset at a time
    raise IndexError(’Incorrect data format’)

if np.size(data, 0) < np.size(data, 1):
    data = data.T  # make sure data is in columns

new_data = data.copy()  # do not change original data

# find local minima and maxima
local_min_indices = spsig.argrelmin(new_data, order=100)
local_max_indices = spsig.argrelmax(new_data, order=100)

# extract indices from returned data structure
local_min_indices = local_min_indices[0]
local_max_indices = local_max_indices[0]

local_min_values = new_data[local_min_indices]
local_max_values = new_data[local_max_indices]

# split into extrema in I and III quadrant
neg_mins_indices = np.where(local_min_values[:, 0] <= 0.0)
neg_mins_indices = neg_mins_indices[0]
neg_mins_indices = local_min_indices[neg_mins_indices]
```

```
    pos_max_indices = np.where(local_max_values[:, 0] >= 0.0)
    pos_max_indices = pos_max_indices[0]
    pos_max_indices = local_max_indices[pos_max_indices]

    if region == 'pdr':
        first_peak = neg_mins_indices[-1]
        second_peak = pos_max_indices[0]
        new_data = new_data[first_peak:second_peak, :]
    elif region == 'ndr':
        first_ndr = new_data[:neg_mins_indices[-1], :]
        second_ndr = new_data[pos_max_indices[0]:, :]
        new_data = np.concatenate((first_ndr, second_ndr))
    else:
        raise ValueError('Region should be either pdr or ndr'
           )

    return new_data

if __name__ == '__main__':
    print(__doc__)
```

B.3 Transmission Probability

A Python translation of a FORTRAN programme developed by Dr Paul Steenson to calculate the transmission probability function of a resonant-tunnelling diode.

```
# -*- coding: utf-8 -*-
from __future__ import print_function
import numpy as np
```

```
def dbtx_calc(fractE, fractC, Lw, Lbe, Lbc):
    """
    A Python translation of a Matlab script to calculate
       electron transmission
    probability for a GaAs/AlGaAs Resonant-Tunneling Diode.

    Parameters:
    -----------
    fractE : float
        Mole fraction of Aluminium in emitter barrier.
    fractC : float
        Mole fraction of Aluminium in collector barrier.
    Lw : float
        Well length in Angstroms.
    Lbe : float
        Emitter barrier length in Angstroms.
    Lbc : float
        Collector barrier length in Angstroms.

    Returns:
    --------
    E : array_like
        Electron energy levels for which the transmission
           probability `Tx` has
        been calculated.
    Tx : array_like
        Transmission probabilty as function of electron
           energy.
```

```
Notes:
------
Output is returned as a NumPy array, with E and Tx being
   two rows in it.
Calling function is responsible for graphically
   displaying the result.

Example:
--------
>>> import matplotlib.pyplot as plt
>>> import dbrttx
>>> import elvd_tools
>>> fractE = 1.0
>>> fractC = 1.0
>>> Lw = 50
>>> Lbe = 17
>>> Lbc = 17
>>> results = dbrttx.dbtx_calc(fractE=fractE, fractC=
   fractC, Lw=Lw,
                               Lbe=Lbe, Lbc=Lbc)
>>> results = results.T
>>> try:
...     graph = elvd_tools.custom_plot(data=results,
   xlabel='',
                                       ylabel='Electron
                                          energy, [eV]',
                                       title='
                                          Transmission
                                          probability',
```

```
                                              mode='log')
...       plt.savefig('TxE.png')
...       plt.show()
... except IndexError as e:
...       print e.message

Created on Mon Aug 04 13:46:17 2014
@author: elvd

"""


fractE = float(fractE)
fractC = float(fractC)
Lw = float(Lw)
Lbe = float(Lbe)
Lbc = float(Lbc)

# convert to SI units
Lw *= 1e-10
Lbe *= 1e-10
Lbc *= 1e-10

m = 0.91e-30  # effective electron mass
hbar = 1.06e-34  # Planck's constant
q = 1.6e-19  # Electron charge
NI = 25000  # number of steps
Mw = 0.067
Me = Mw
Mc = Mw
Mbe = (0.083*fractE + 0.067)
```

```
Mbc = (0.083*fractC + 0.067)
Vbe = (80*fractE) / 100
Vbc = (80*fractC) / 100
de = (Vbc - 0.001) / NI
Ve = 0
Vw = 0
Vc = 0

# initialise empty lists
Tx = list()
E = list()

for n in range(NI):
    E.append((n + 1) * de)
    mult = np.sqrt(2 * m * q / (hbar**2))

    ke = mult * np.sqrt(Me * (E[n] - Ve))
    kbe = mult * np.sqrt(Mbe * (Vbe - E[n]))
    kw = mult * np.sqrt(Mw * (E[n] - Vw))
    kbc = mult * np.sqrt(Mbc * (Vbc - E[n]))
    kc = mult * np.sqrt(Mc * (E[n] - Vc))

    a = (kbe * Me) / (ke * Mbe)
    b = (kw * Mbe) / (kbe * Mw)
    c = (kbc * Mw) / (kw * Mbc)
    d = (kc * Mbc) / (kbc * Mc)

    e = complex(0, kw*Lw)
    N11 = complex(1, a)
    N12 = complex(1, -a)
```

```
        O11 = complex(1, -b) * np.exp(kbe * Lbe)
        O12 = complex(1, +b) * np.exp(kbe * Lbe)
        O21 = complex(1, +b) * np.exp(-kbe * Lbe)
        O22 = complex(1, -b) * np.exp(-kbe * Lbe)
        P11 = complex(1, +c) * np.exp(-e)
        P12 = complex(1, -c) * np.exp(-e)
        P21 = complex(1, -c) * np.exp(e)
        P22 = complex(1, +c) * np.exp(e)
        Q11 = complex(1, -d) * np.exp(kbc * Lbc)
        Q21 = complex(1, +d) * np.exp(-kbc * Lbc)

        T11 = (N11*O11 + N12*O21) * (P11*Q11 + P12*Q21) + \
            (N11*O12 + N12*O22) * (P21*Q11 + P22*Q21)

        Tx.append(16 * kc / (ke * (T11 * np.conj(T11))))

    E = np.abs(E)
    Tx = np.abs(Tx)

    return np.array([E, Tx])  # combined in a numpy array

if __name__ == '__main__':
    print(dbtx_calc.__doc__)
```

B.4 Inductor Calculator

This is a custom script to calculate the electrical and physical parameters of a transmission line that provides a given inductance.

```
# -*- coding: utf-8 -*-
```

```python
from __future__ import print_function
import numpy as np


def tline_ind(ind, freq, er, z0l):
    """
    A quick script to calculate the parameters of a transmission line, used to
    represent an inductive element.

    Parameters:
    -----------
    ind : float
        Value of inductance in pH.
    freq : float
        Centre frequency in GHz.
    er : float
        Effective dielectric constant of substrate material.
    z0l : float
        Desired impedance of the transmission line.

    Returns:
    --------
    l_elec : float
        Electrical length of an ideal transmission line, used to represent the
        inductance `ind`.
    l_phys : float
        Corresponding physical length in um.
    c_par : float
```

```
    Total parasitic capacitance in fF.

Raises:
-------
ValueError
    In case requested inductance cannot be formed using a
        line of the
    specified impedance and/or the frequency specified is
        too high.

Notes:
------
Requires an installation of NumPy. Pretty display of
   results is up to
calling function.

Example:
--------
>>> import ind_calculator
>>> results = ind_calculator.tline_ind(225, 50, 10.2,
   100)
>>> print results
[44.979873297640133, 2.3472907724095448e-10,
   1.3178277694076776e-29]

Created on Wed Jun 25 16:20:35 2014
@author: Viktor Doychinov

"""
```

```
    # convert to basic units, i.e. Hz and H
    freq *= 1e9
    ind *= 1e-12

    # calculate guide wavelength
    lambda_g = (3e8 / freq) / np.sqrt(er)
    norm_impedance = 2 * np.pi * freq * ind / z01
    if norm_impedance > 1:
        raise ValueError('Line impedance too low or frequency
            too high')

    else:
        l_phys = (lambda_g / (2 * np.pi)) * np.arcsin(
           norm_impedance)

        l_elec = ((2 * np.pi / lambda_g) * l_phys) * (180 /
           np.pi)

        c_par = (1 / (2 * np.pi * z01 * freq)) * \
            np.tan(np.pi * l_phys / lambda_g)

        # convert to output units
        l_phys /= 1e-6
        c_par /= 1e-15

    return [l_elec, l_phys, c_par]  # returns as a list

if __name__ == '__main__':
    print(tline_ind.__doc__)
```

Appendix C

Expanded S-parameter graphs

C.1 20 GHz Mixer circuits

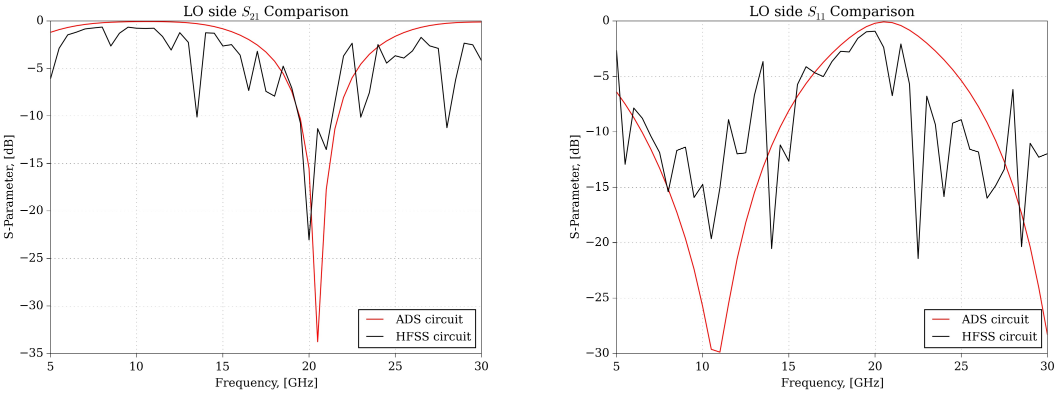

(a) LO side S_{21} (b) LO side S_{11}

Figure C.1: Comparison between the S-parameters obtained by ADS and HFSS for the LO side of a 20 GHz SHM circuit.

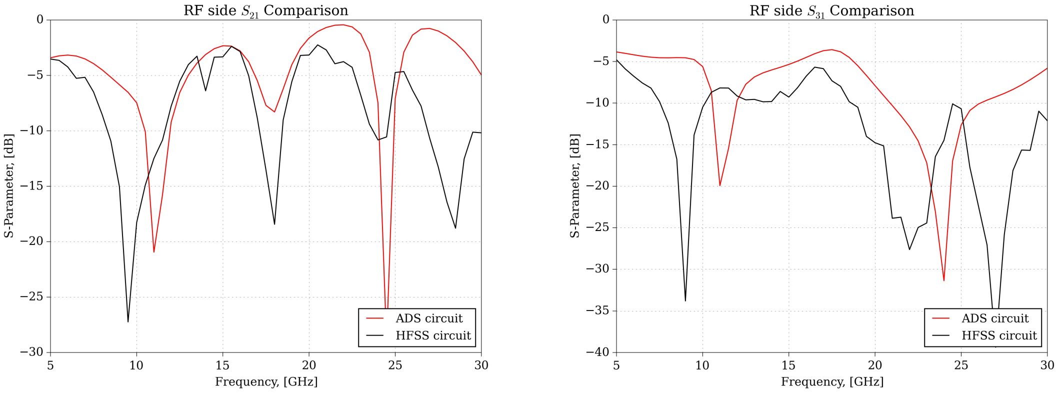

(a) RF side S_{21}

(b) RF side S_{31}

Figure C.2: Comparison between the S-parameters obtained by ADS and HFSS for the RF side of a 20 GHz SHM circuit.

C.2 100 GHz 2$^{\text{nd}}$ harmonic mixer circuits

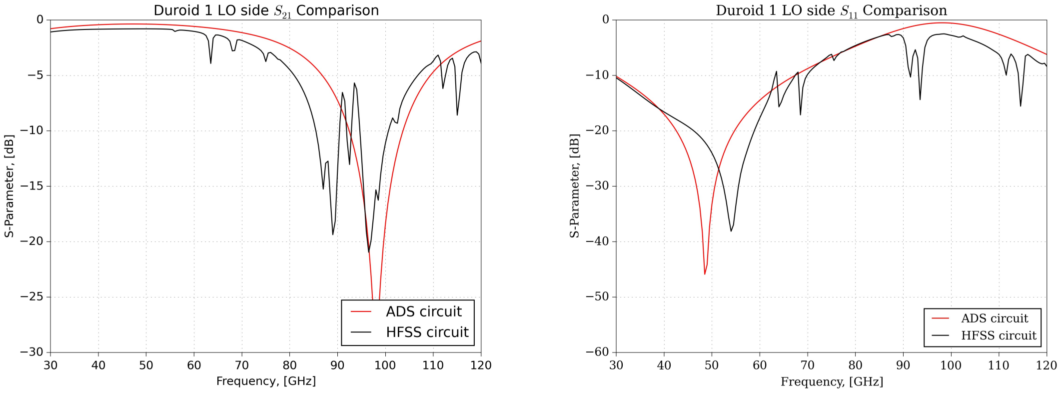

(a) LO side S_{21}

(b) LO side S_{11}

Figure C.3: Comparison between the S-parameters obtained by ADS and HFSS for the LO side of a 100 GHz SHM circuit, implemented on Duroid 1 substrate.

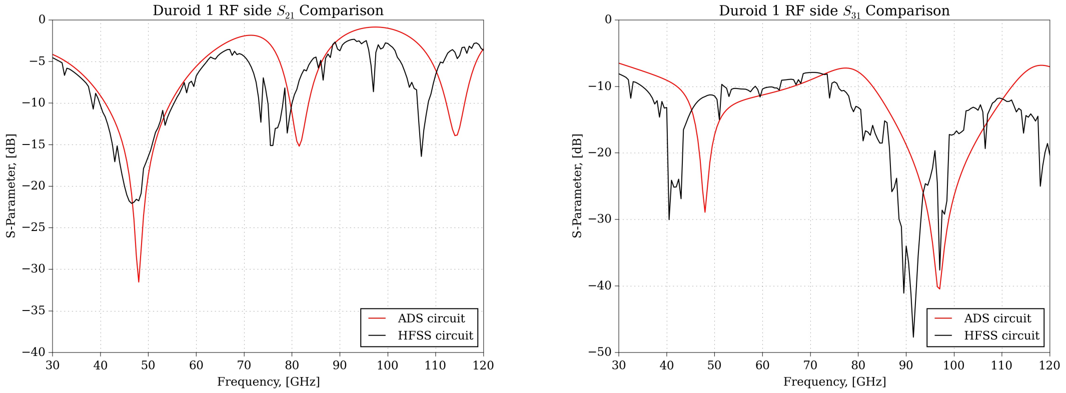

(a) RF side S_{21} (b) RF side S_{31}

Figure C.4: Comparison between the S-parameters obtained by ADS and HFSS for the RF side of a 100 GHz SHM circuit, implemented on Duroid 1 substrate.

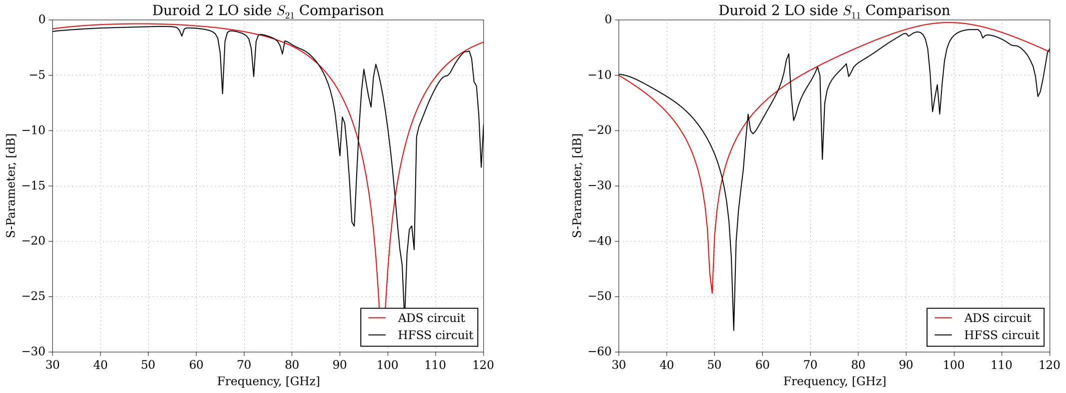

(a) LO side S_{21} (b) LO side S_{11}

Figure C.5: Comparison between the S-parameters obtained by ADS and HFSS for the LO side of a 100 GHz SHM circuit, implemented on Duroid 2 substrate.

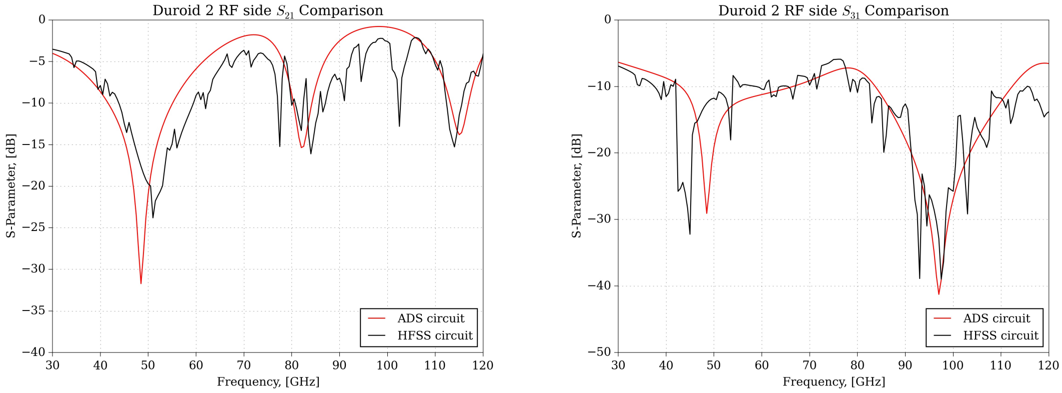

(a) RF side S_{21} (b) RF side S_{31}

Figure C.6: Comparison between the S-parameters obtained by ADS and HFSS for the RF side of a 100 GHz SHM circuit, implemented on Duroid 2 substrate.

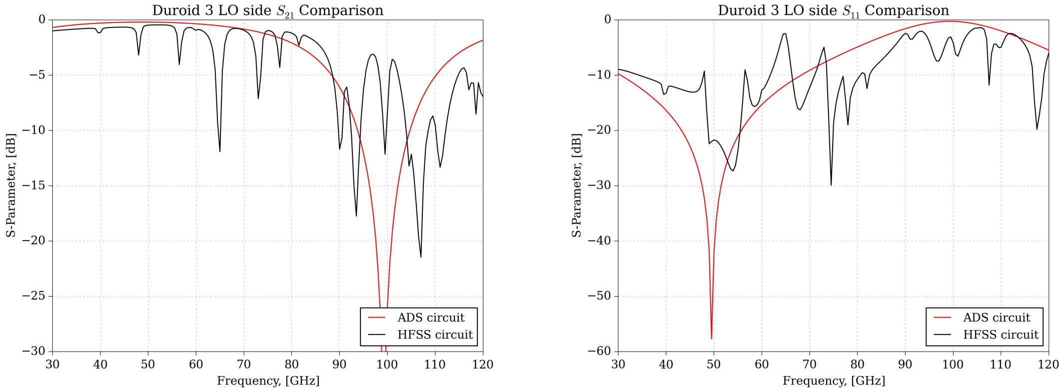

(a) LO side S_{21} (b) LO side S_{11}

Figure C.7: Comparison between the S-parameters obtained by ADS and HFSS for the LO side of a 100 GHz SHM circuit, implemented on Duroid 3 substrate.

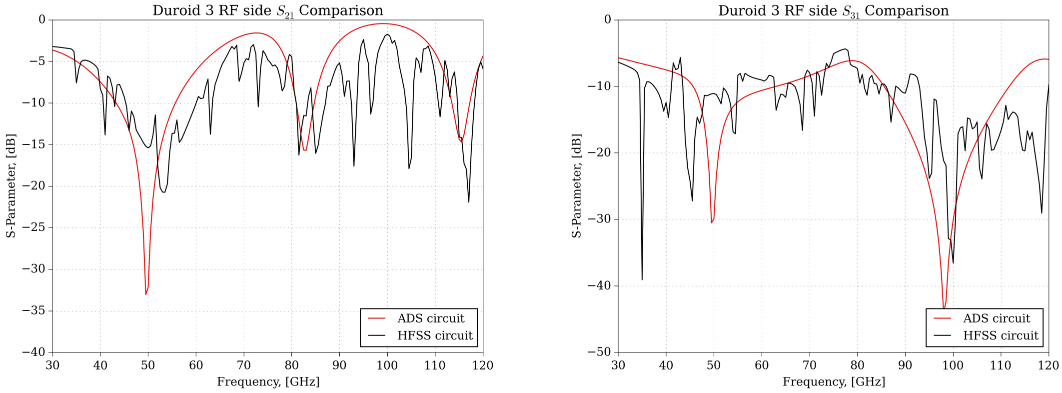

(a) RF side S_{21} (b) RF side S_{31}

Figure C.8: Comparison between the S-parameters obtained by ADS and HFSS for the RF side of a 100 GHz SHM circuit, implemented on Duroid 3 substrate.

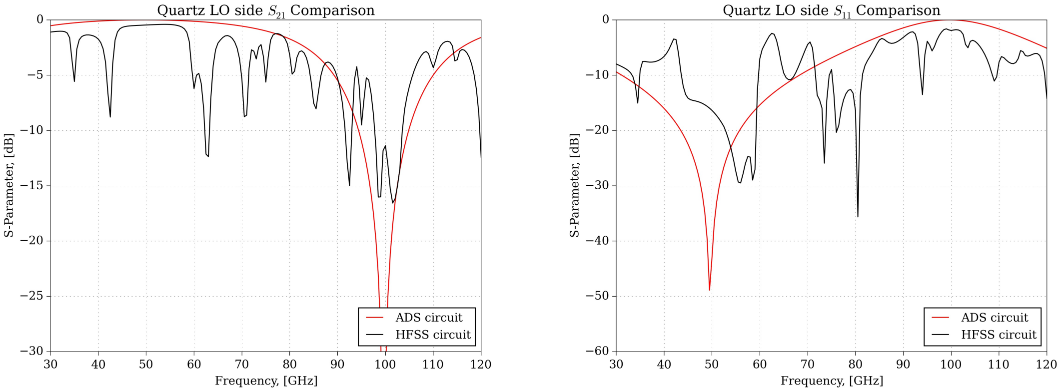

(a) LO side S_{21}

(b) LO side S_{11}

Figure C.9: Comparison between the S-parameters obtained by ADS and HFSS for the LO side of a 100 GHz SHM circuit, implemented on Quartz substrate.

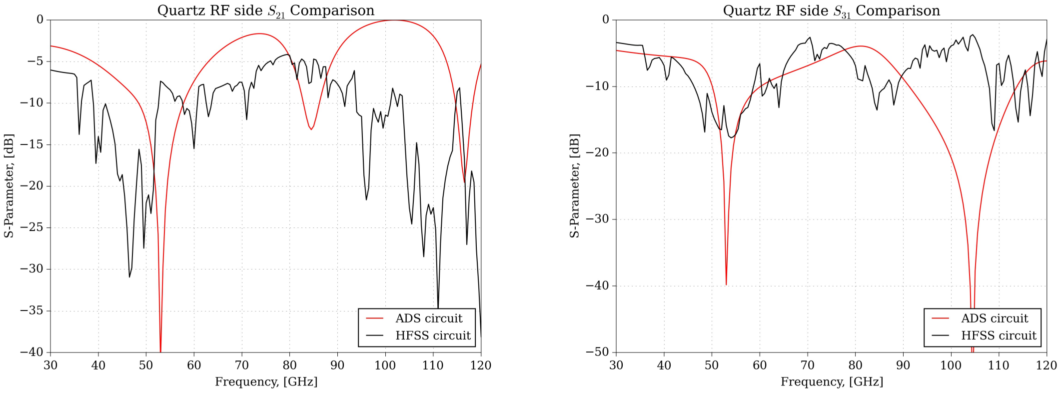

(a) RF side S_{21}

(b) RF side S_{31}

Figure C.10: Comparison between the S-parameters obtained by ADS and HFSS for the RF side of a 100 GHz SHM circuit, implemented on Quartz substrate.

C.3 100 GHz 4th harmonic mixer circuits

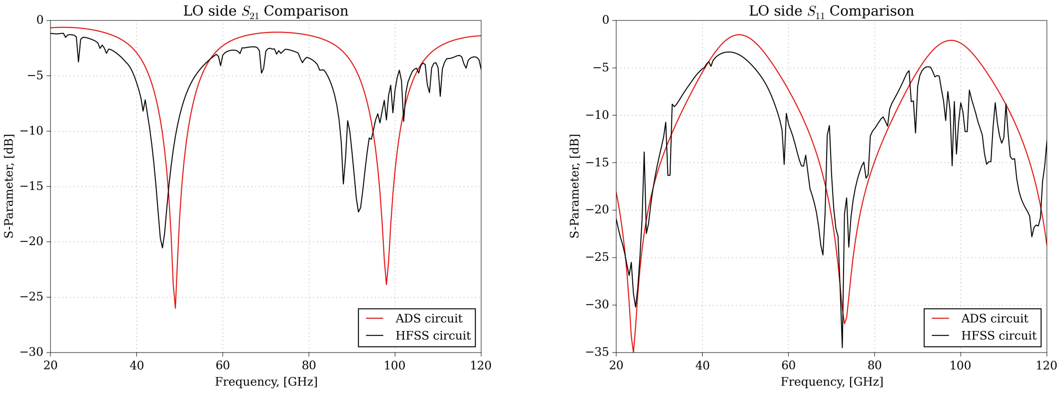

(a) LO side S_{21} (b) LO side S_{11}

Figure C.11: Comparison between the S-parameters obtained by ADS and HFSS for the LO side of a 100 GHz n=4 SHM circuit.

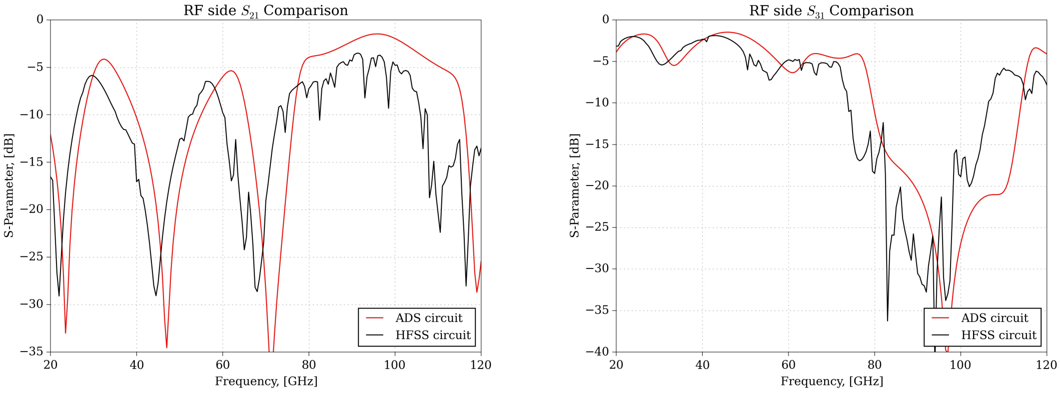

(a) RF side S_{21} (b) RF side S_{31}

Figure C.12: Comparison between the S-parameters obtained by ADS and HFSS for the RF side of a 100 GHz n=4 SHM circuit.

C.4 20 GHz Amplifier circuits

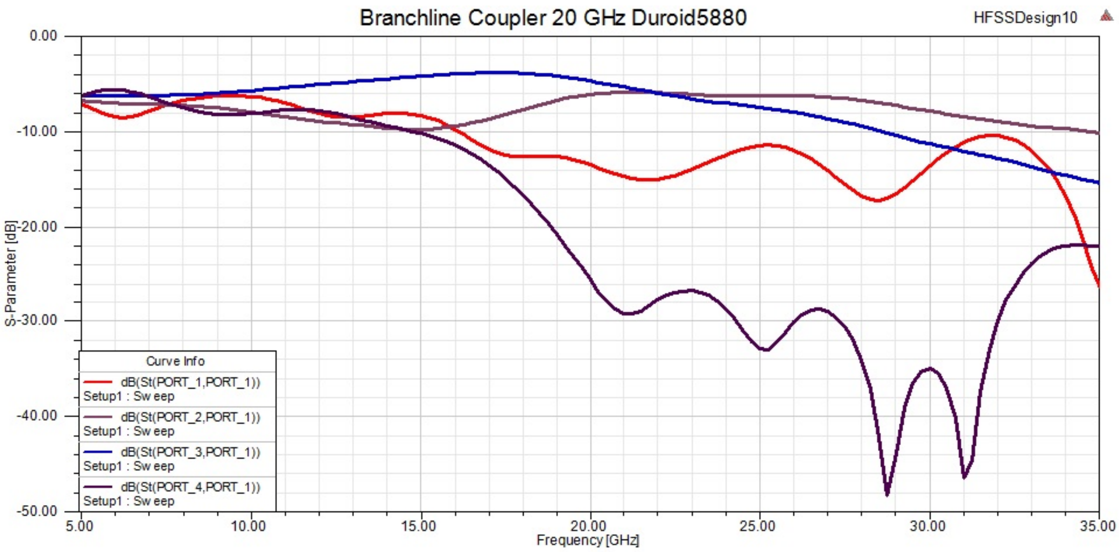

(a) S-Parameters

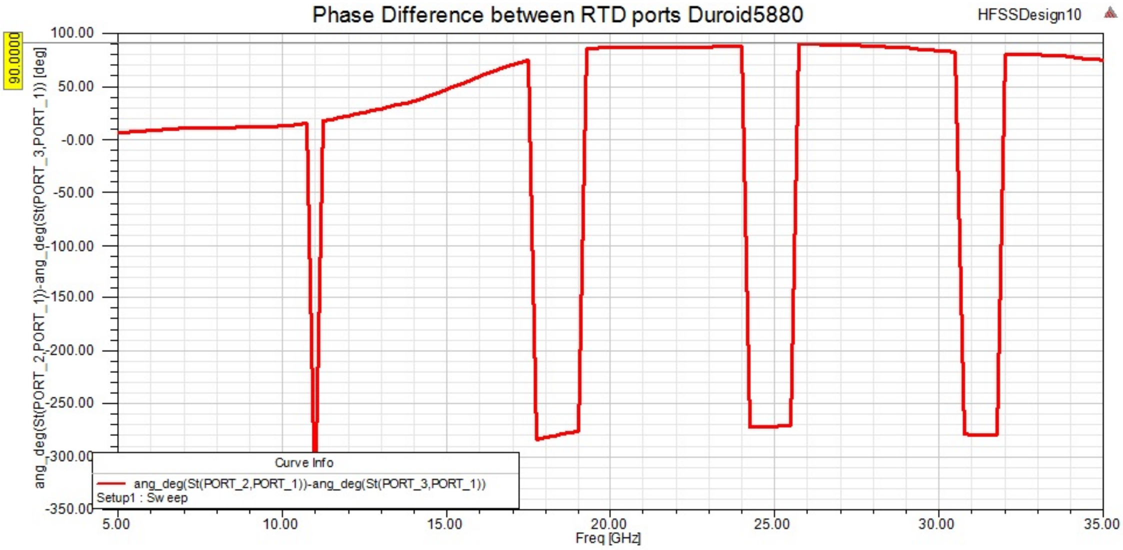

(b) Port phase difference

Figure C.13: Coupler for 20 GHz reflection based amplifiers, implemented on Duroid5880

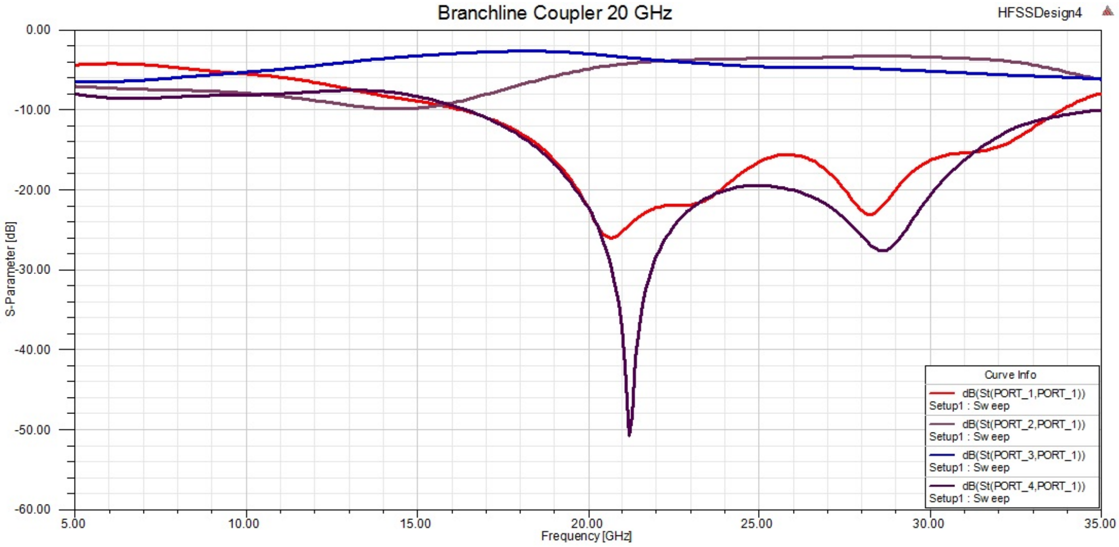

(a) S-Parameters

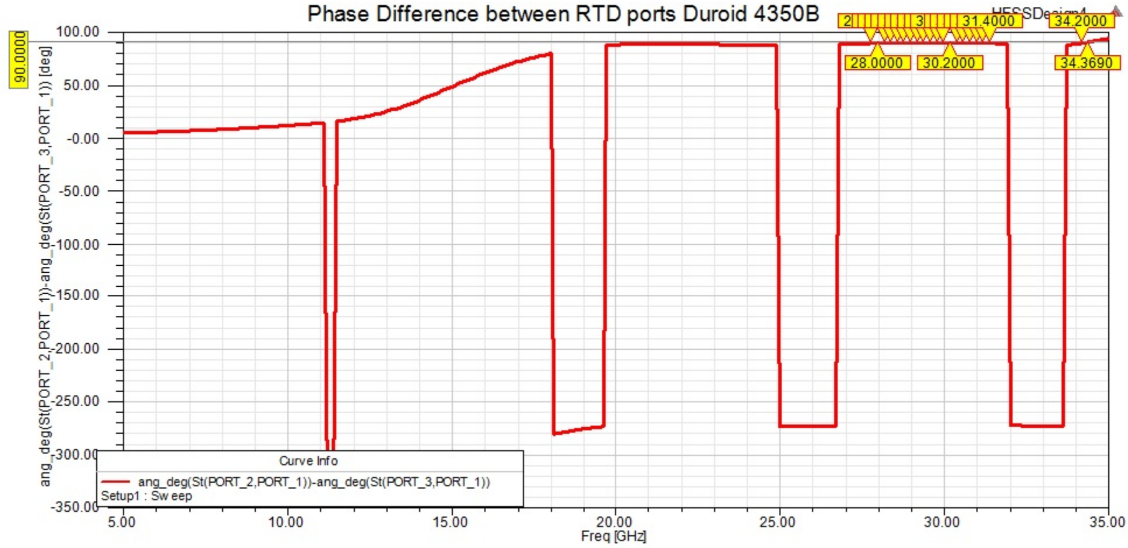

(b) Port phase difference

Figure C.14: Coupler for 20 GHz reflection based amplifiers, implemented on Duroid4350

C.5 100 GHz Amplifier circuits

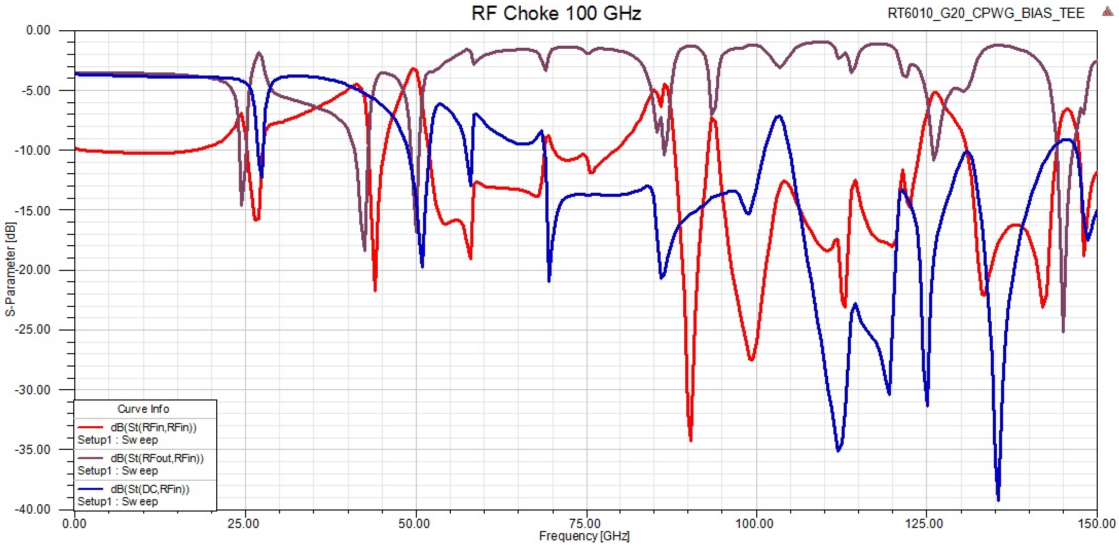

Figure C.15: RF choke for 100 GHz RTD reflection based amplifiers.

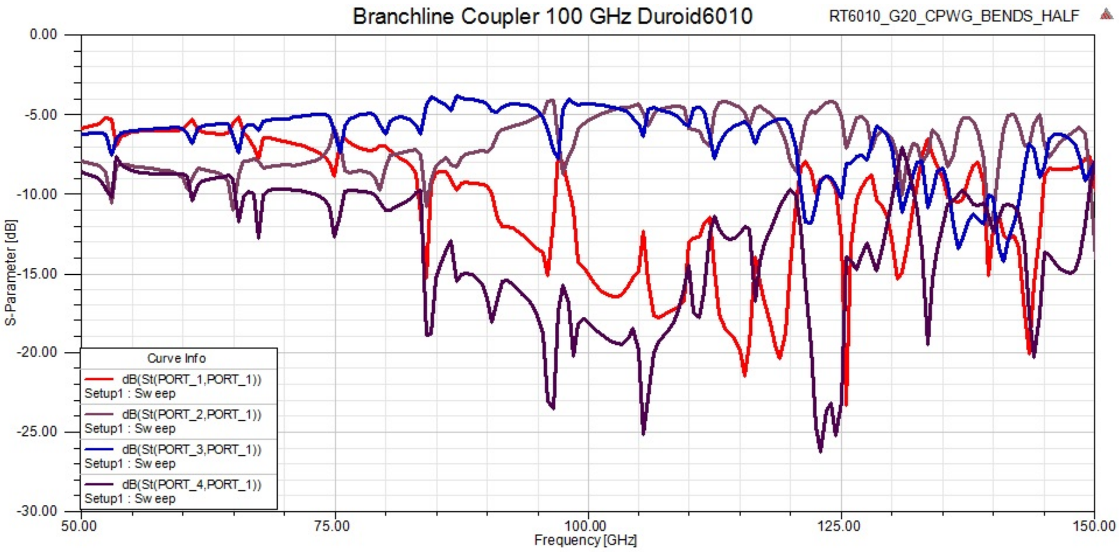

(a) S-Parameters

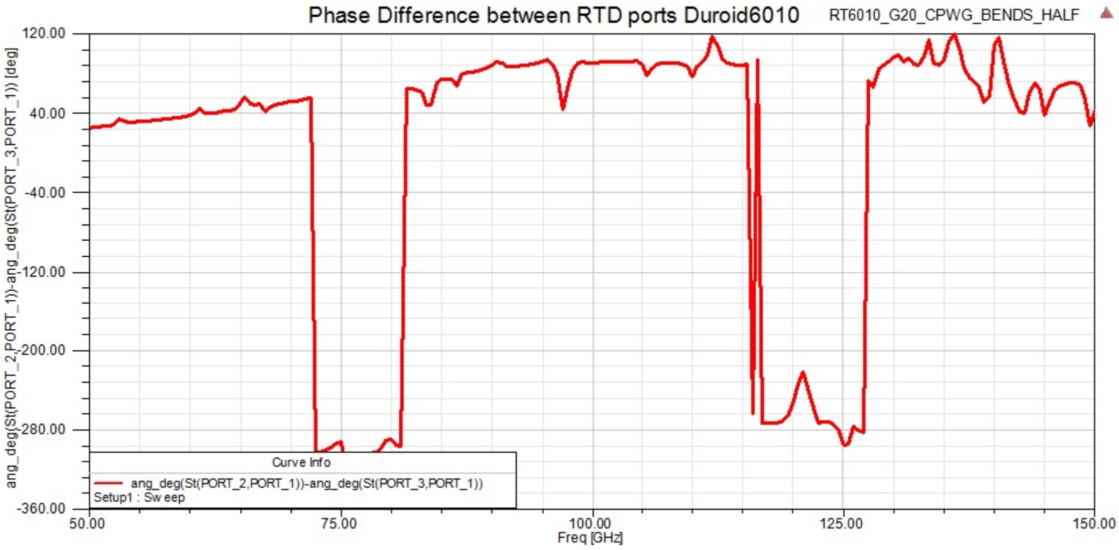

(b) Port phase difference

Figure C.16: Coupler for 100 GHz reflection based amplifiers, implemented on Duroid6010

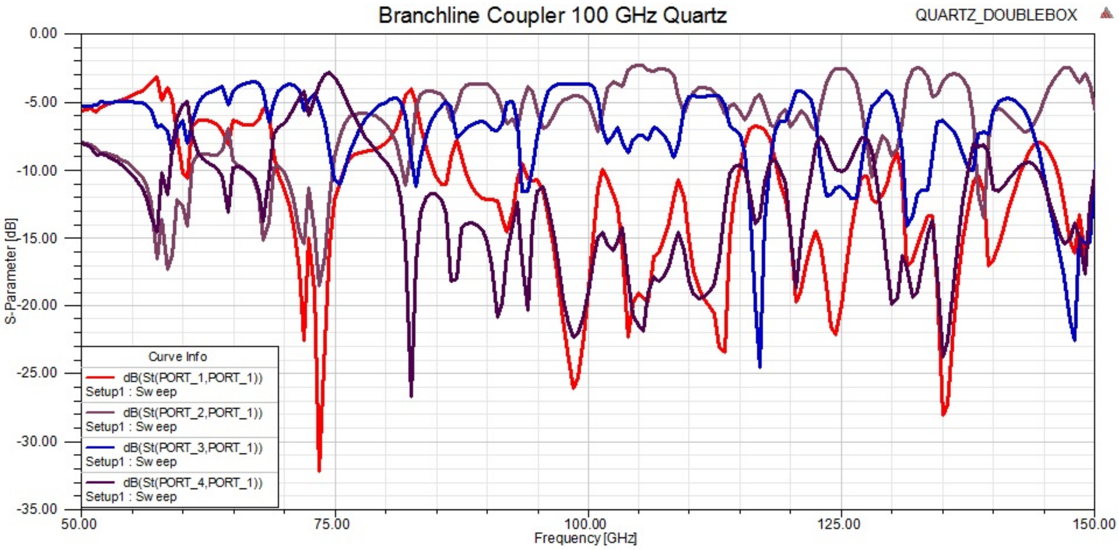

(a) S-Parameters

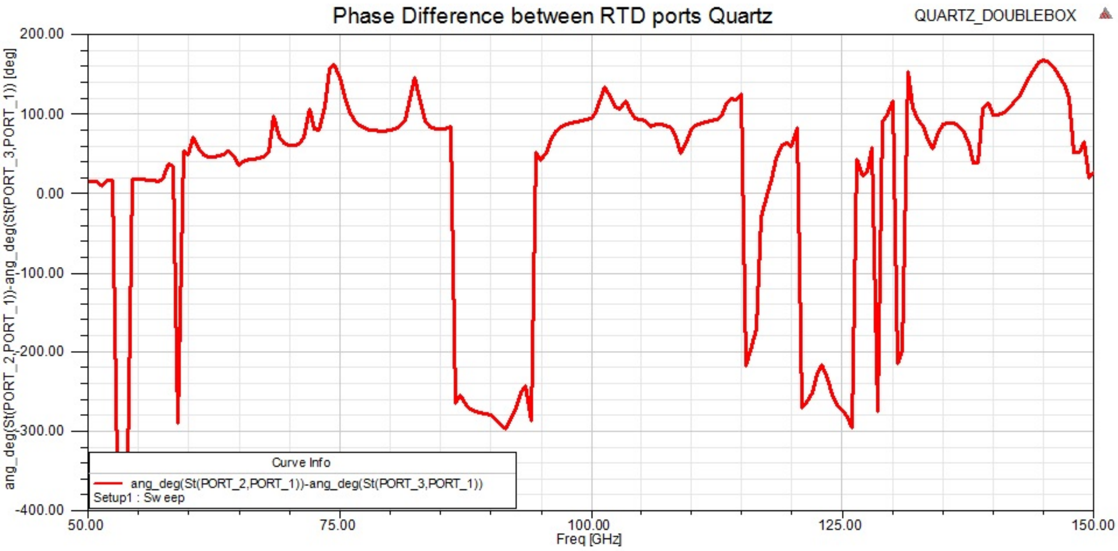

(b) Port phase difference

Figure C.17: Coupler for 100 GHz reflection based amplifiers, implemented on quartz